Magnetism of $3d$ Frustrated Magnetic Insulators: α-$CaCr_2O_4$, β-$CaCr_2O_4$ and Sr_2VO_4

vorgelegt von
Diplom-Physiker
Sándor Tóth

von der Fakultät II - Mathematik und Naturwissenschaften
der Technischen Universität Berlin
zur Erlangung des akademischen Grades
Doktor der Naturwissensschaften
Dr. rer. nat.

g e n e h m i g t e D i s s e r t a t i o n

Promotionsausschuss:
Vorsitzender: Prof. Dr. M. Kneissl
Gutachterin: Prof. Dr. B. Lake
Gutachter: Prof. Dr. N. Shannon
Gutachter: Prof. Dr. D. A. Tennant

Tag der wissenschaftlichen Aussprache: 30.07.2012

Berlin 2012

D 83

Acknowledgements

During the years of research and thesis writing I got help from many people. I would like to thank them in the following lines.
First of all I would like to thank my supervisor Bella Lake for her support and encouragement, for teaching me so much science, for showing me how to do research with patience and humility, for giving me direction. Also I would like to thank all present and past group members of M-A2 for the good atmosphere and fruitful discussions and for paying my lunch in the canteen. Thank you Diana for being a friend and being here every day since I am in Berlin. Thank you Elisa for all the discussions which are still only a phone call away. Thank you Oliver for all the fun and for the couch! Thank you Konrad for sharing with me all the practical knowledge of experimental physics. Thank you Manfred for teaching me crystallography. Thank you Patricia, Anup and Christian for all the fun we had since you are here.
My research would not have been possible without samples. The growth of α-$CaCr_2O_4$ single crystal was a heroic act, thank you Nazmul! Thank you Simon for providing me the β-$CaCr_2O_4$ sample and data and all the motivating discussions. Special thanks to Oksana for teaching me spherical polarimetry in 85 emails. I would like to thank all the local contacts, who made the experiments possible and relaxed: Klaudia Hradil, Kirrily Rule, Tatiana Guidi, Adrian Hill, Andrey Podlesnyak, Andrew Walters, Illya Glavatskyy, Nikolaos Tsapatsaris, Sylvain Petit. I would like to thank Igor Zaliznyak for fruitfull discussions and Samir El Shawish for the simulations. I would like to thank Peter Lemmens and Joachim Deisenhofer for the collaboration and sharing their results. I would like to thank Duc Lee for all the help in programming and Markos for cheering me up any time. I would also like to express gratitude to Alan Tennant and Nic Shannon for agreeing to examine this thesis.
Köszönet szüleimnek hogy végig támogattak ez alatt az idő alatt és hogy mindig elérhetem őket ha szükségem van rájuk!
Finally, thank you Kathi for all the love and care!

Abstract

This thesis is about the experimental investigation of three magnetic insulators with magnetic $3d$ transition metal ions: α-$CaCr_2O_4$, β-$CaCr_2O_4$ and Sr_2VO_4. Both α-$CaCr_2O_4$ and β-$CaCr_2O_4$ have the same stoichiometry and the magnetic spin-3/2 Cr^{3+} ions are in the same octahedral environment. The comparison of these two compounds shows, how different crystal symmetry combined with frustration can lead to different magnetic behaviour. Both of them develop magnetic long range order which contrasts with the short range ordered dimer ground state of Sr_2VO_4.

The first part of the thesis deals with the triangular lattice antiferromagnet α-$CaCr_2O_4$. Detailed analysis of the crystal structure and magnetic structure is presented. The low temperature magnetically ordered state of α-$CaCr_2O_4$ is a helical spin arrangement, where on the triangular planes the angles between nearest neighbour spins are 120°. This structure is surprising considering that the triangular lattice is distorted and there are four different nearest neighbour exchange interactions. The analysis of the classical zero temperature phase diagram of α-$CaCr_2O_4$ confirmed that the 120° structure is stable for this type of distortion from triangular symmetry. Single crystals were grown to perform detailed inelastic neutron scattering. The experiments revealed spin wave excitations in the ordered phase with soft modes and roton like minima. The exchange parameters were obtained by fitting the spectra using linear spin wave theory. The fitted parameters put α-$CaCr_2O_4$ close to the edge of this 120° phase. β-$CaCr_2O_4$ is a spin-chain compound where spins build up zig-zag chains with weakly ferromagnetic rungs and strongly antiferromagnetic leg couplings. Furthermore significant interchain superexchange interactions are expected through edge sharing oxygen atoms. It develops helical magnetic order at low temperatures. The thorough analysis of the magnetic neutron diffraction and the measured spin wave spectra of the ordered phase is described. They reveal helical incommensurate magnetic order within the zig-zag chains suggesting frustrated interactions, while neighbouring chains have opposite chirality due to Dzyaloshinskii-Moriya interactions. The combination of these features effectively decouples the chains as verified by the weak interchain magnon dispersion. Thus β-$CaCr_2O_4$ shows how frustrated interactions can lead to a reduction in dimensionality. Magnetic susceptibility and inelastic neutron scattering on Sr_2VO_4 revealed a dimerised ground state. However the analysis of the crystal structure provides no obvious exchange pathways. Together these three compounds show, how frustration and low dimensionality can lead to complex magnetic behaviour and unconventional states of matter.

Zusammenfassung

Die hier vorliegende Doktorarbeit beschäftigt sich mit der Erforschung dreier magnetischer Isolatoren mit magnetischen $3d$ Übergangsmetall-Ionen, α-$CaCr_2O_4$, β-$CaCr_2O_4$ und Sr_2VO_4. Durch den Vergleich der beiden Verbindungen, α-$CaCr_2O_4$ und β-$CaCr_2O_4$, konnte gezeigt werden, dass trotz gleicher Stöchiometrie und der Tatsache, dass die magnetischen Spin-3/2 Cr^{3+} Ionen dieselbe oktaedrische Umgebung sehen, die unterschiedliche Kristall-Symmetrie kombiniert mit Frustration zu unterschiedlichem magnetischen Verhalten führt. Diese beiden Verbindungen zeigen eine magnetische Fernordnung im Grundzustand, welche im Kontrast zur vorliegenden Nahordnung (Dimere) im Grundzustand der dritten Verbindung Sr_2VO_4 steht.

Der erste Teil der Arbeit beschäftigt sich mit dem antiferromagnetischen Dreiecksgitter α-$CaCr_2O_4$. Hier wird eine detaillierte Analyse der Kristall- und magnetischen Struktur präsentiert. Der magnetisch geordnete Zustand des α-$CaCr_2O_4$ bei tiefen Temperaturen ist ein helixförmiges Spin-Arrangement, wobei die Winkel zwischen den nächsten Nachbarspins auf den dreieckigen Ebenen 120° beträgt. Geht man davon aus, dass das Dreiecksgitter gestört ist und vier verschiedene Austauschwechselwirkungen zwischen den nächsten Nachbarn besitzt, ist diese Struktur überraschend. Für diese Art der Störung der dreieckigen Symmetrie bestätigt die Analyse des klassischen Nulltemperatur-Phasendiagramms von α-$CaCr_2O_4$ die Stabilität der 120° Struktur. Für die Experimente mit inelastischer Neutronenstreuung wurden Einkristalle gezüchtet. Durch die Experimente konnte gezeigt werden, dass die Spinwellen-Anregungen in der geordneten Phase, weiche Moden und Rotonähnliche Minima aufweisen. Die Austauschwechselwirkungen wurden durch das Fitten der Spektren mittels Spinwellen-Theorie bestimmt. Die gefitteten Parameter setzen α-$CaCr_2O_4$ nah an die Grenze dieser 120° Struktur. β-$CaCr_2O_4$ ist eine Spin-Ketten-Verbindung, in der die Spins in einer Zick-Zack-Kette mit schwach ferromagnetischen Sprossen und stark antiferromagnetisch gekoppelten Holmen aneinandergereiht sind. Außerdem erwartet man durch die Sauerstoffatome in dieser Verbindung, welche sich die Ecken teilen, einen signifikanten Superaustausch zwischen den Ketten. β-$CaCr_2O_4$ zeigt eine helikale magnetische Ordnung bei tiefen Temperaturen. In der vorliegenden Arbeit wird die gründliche Analyse der magnetischen Neutronendiffraktions-Ergebnisse, sowie der gemessenen Spinwellen-Spektren dieser geordneten Phase gezeigt. Diese zeigen eine inkommensurate magnetische Ordnung in den Zick-Zack-Ketten, welche auf frustrierte Wechselwirkungen hindeutet. Durch die Dzyaloshinskii-Moriya-Wechselwirkung zeigen die Nachbarketten eine gegensätzliche Chiralität. Die Kombination dieser Eigenschaften entkoppelt die Ketten, wie es durch die schwachen Zwischen-Ketten Magnonen Dispersion verifiziert wurde. Magnetische Suszeptibilität und inelastische Neutronenstreuung an Sr_2VO_4 bestätigen den dimerisierten Grundzustand. Allerdings konnte durch die Analyse der Kristallstruktur kein Hinweis auf offensichtliche Wechselwirkungspfade gefunden werden. Diese drei Verbindungen zeigen, wie Frustration und niedrige Dimension zu einem komplexen magnetischen Verhalten und unkonventionellen Zuständen der Materialien führen kann.

Contents

1 Introduction

Magnetism, despite its inherent quantum physical origin, is often treated as a classical phenomena. Industries which are based on magnetism (like hard disc production) depends on room temperature properties of magnets which are essentially classical. In quantum magnets the effects of quantum fluctuations have to be considered besides thermal fluctuations. Quantum fluctuations are enhanced by low spin, low dimensionality and frustration. Greater interest in quantum magnetism emerged more recently with the discovery of high temperature superconductivity. The elusive mechanism behind this quantum phenomena raised questions about the interplay between superconductivity, spin fluctuations and magnetic order in the cuprates. In the last two decades quantum magnetism research flourished. Researchers have discovered a number of exotic quantum ground states and emergent excitations. Besides their interest to fundamental research, practical applications of quantum magnets are promising as well. Suggested applications include quantum computing [1, 2, 3] and multiferroic materials. [4]

The topic of this thesis is the experimental investigation of three quantum magnets: α-$CaCr_2O_4$, β-$CaCr_2O_4$ and Sr_2VO_4. In all of them the magnetic ion is a $3d$ transition metal, with quenched orbital angular momentum leading to a spin-only magnetic ion. These compounds show several interesting phenomena, which are characteristic of quantum magnets. Disordered magnetic states down to temperatures which are fractions of the Curie–Weiss temperature, short range order, long range helical order and reduction of dimensionality due to frustration.

α-$CaCr_2O_4$ is a distorted triangular lattice antiferromagnet with a unique orthorhombic distortion. The magnetic Cr^{3+} ions have spin $S = 3/2$ and no orbital degeneracy. Due to the geometrical frustration, long range order develops only far below the Curie–Weiss temperature. In the ordered structure nearest neighbour spins are arranged with angles of 120° between them, as found in an undistorted triangular antiferromagnet. The complex magnetic excitation spectrum of the ordered phase seemingly contradicts the highly symmetric magnetic order. The reason for this dichotomy is the interplay of the peculiar structural distortion and the nearest neighbour direct exchange interactions. However the experimentally observed roton like-minima of the magnon spectrum reveals

that the system is close to a quantum phase transition between the 120° phase and an unknown multi-k ordered phase.

β-$CaCr_2O_4$ is a polymorph of α-$CaCr_2O_4$ with the same magnetic Cr^{3+} ions. These magnetic ions build up frustrated zig-zag chains arranged in a honeycomb lattice. As for α-$CaCr_2O_4$, long range helical order develops at temperature far below the Curie–Weiss temperature. The magnetic structure consists of helically ordered zig-zag chains while neighbouring zig-zag chains having opposite chirality. This staggered chirality is the result of the alternating Dzyaloshinskii–Moriya interaction vectors along neighbouring zig-zag chains. The excitation spectrum of the ordered phase corresponds to uncoupled zig-zag chains, which shows that frustration and chiral magnetic order can reduce dimensionality. The observed extended excitation continua suggest the presence of multiparticle excitations. In the disordered high temperature phase gapped excitations are found which require further experimental and theoretical investigation.

Sr_2VO_4 is a magnetic insulator with $S = 1/2$ V^{4+} magnetic ions. Although there are no obvious V^{4+} pairs visible in the crystal structure, the low temperature magnetic ground state is dimerized. Inelastic neutron scattering reveals the expected gapped triplet excitations. Surprisingly magnetic susceptibility shows, that only the half of the V^{4+} ions are magnetic.

The following chapters are organised as follows. Chapter 2 gives a short introduction to the general topic of quantum magnetism with particular emphasis on topics related to the experimental work described in this thesis. It begins with the free magnetic ion, then introduces the interactions between ions, the possible ground states of interacting magnetic systems and finally the magnetic excitations. There is a detailed derivation of linear spin-wave theory for application to incommensurate magnetic structures. Chapter 3 details most of the experimental techniques used in this thesis. The main emphasis is on neutron scattering. Neutron scattering enables the investigation of static and dynamic magnetic properties of solids in the typical energy range of the excitations and throughout the Brillouin zone.

The next four chapters give the experimental results, analysis and discussion on the three compounds. Chapter 4 explains the general magnetic properties of α-$CaCr_2O_4$ together with the analysis of the crystal structure and the low temperature ordered magnetic structure. The stability of the observed 120° structure is discussed within a classical context. Chapter 5 introduces the magnetic excitation spectrum of α-$CaCr_2O_4$ in the ordered phase and discusses in detail the spin-wave analysis of the experimental results and the significance of the extracted exchange interactions. Chapter 6 describes the ordered magnetic structure and excitations of β-$CaCr_2O_4$ and shows how chirality

and frustration decouple the magnetic zig-zag chains. Chapter 7 introduces magnetic susceptibility and inelastic neutron scattering results on Sr_2VO_4 and confirms that it is a weakly coupled dimer antiferromagnet.
Finally the main results on all three compounds are summarised in Chapter 8 and suggestions are made for future research directions.

2 Frustrated magnetism

This chapter provides a short theoretical introduction to magnetism in condensed matter and quantum magnetism. The topics that are focused on here are those most relevant to the investigated compounds α-$CaCr_2O_4$, β-$CaCr_2O_4$ and Sr_2VO_4. These are: single ion properties of $3d$ transition metal ions, magnetic interactions in magnetic insulators, static and dynamic properties of the spin-1/2 dimer, characterisation of magnetic long-range order and spin-wave excitations. Additional details of the points discussed here can be found in the following books and references therein. [5, 6, 7]

2.1 Magnetic ion

The origin of magnetism in insulating solids are atoms and ions with unfilled electronic shell. Of the elements of the periodic table three groups are magnetic: transition metals with the intensively studied $3d$ series and the much less studied $4d$ and $5d$ ions, rare earth elements with partially filled $4f$ subshell and the series of actinides with partially filled $5f$ subshell. The magnetic moment of an ion is the sum of the magnetic moment of its electrons if the small nuclear contribution is neglected. The magnetic moment of a single electron is coupled to its angular momentum, which is the sum of the electron spin ($\hbar/2$) and the orbital angular momentum ($\hbar l$, $l \in \{0, 1, 2...\}$). The description of the electronic orbitals are based on the hydrogen-like solutions of the of Schrödinger equation. These solutions are the electronic orbitals which can be described by 4 quantum numbers and symbolized by the ket $|n, l, m_\mathrm{l}, m_\mathrm{s}\rangle$. This model predicts degenerate orbitals, since the energy depends only on the n principal quantum number which defines the electron shells. The other quantum numbers are l the angular momentum quantum number defining subshells ($l \in \{0(\text{“s”}),\ 1(\text{“p”}),\ 2(\text{“d”}),\ 3(\text{“f”})\}$), m_l the z component of the angular momentum ($m_\mathrm{l} \in \{-l, -l+1, ...l\}$) and m_s the z component of the electron spin ($m_\mathrm{s} \in \{-1/2, 1/2\}$). However this degeneracy is lifted when the Coulomb repulsion between electrons is considered. Furthermore a new term appears in the atomic Hamiltonian called spin-orbit coupling which is a relativistic correction to the Schrödinger equation. It has a form of $\mathcal{H}_\mathrm{so} = V(r)\boldsymbol{L} \cdot \boldsymbol{S}$, where $V(r)$ is the electric potential of the nucleus.

For the heavy rare earth ions spin-orbit coupling is much stronger than for $3d$ transition metals, due to the larger charge of the nucleus and the smaller mean radius of the valence orbitals. According to the Pauli exclusion principle two electron cannot have identical quantum numbers, thus the orbitals are gradually filled starting from the one with lowest energy. The effect of the Coulomb repulsion and the spin-orbit coupling on the energy of the orbitals are described by Hund's rules. These rules for a partially filled subshell are the following: (1) the value of the sum of the electron spins on the subshell is maximal ($S = \sum s_\mathrm{i}$), (2) the value of the sum of the orbital angular momentum is maximal ($L = \sum l_\mathrm{i}$) and (3) if the subshell is less than half full the total angular momentum is $J = |L - S|$, if the subshell is more than half full then $J = L + S$. The third rule is the result of the spin-orbit coupling. According to these rules for example the free Cr^{3+} ion has a spin value of $S = 3/2$, orbital angular momentum of $L = 3$ and total angular momentum of $J = 3/2$, the same values for V^{4+}: $S = 1/2$, $L = 2$ and $J = 3/2$.

If a magnetic ion is in uniform $\boldsymbol{B}$ magnetic field, the leading term in the interaction energy is the Zeeman term:

$$E_\mathrm{Zeeman} = -\mu_\mathrm{B}\boldsymbol{B}\cdot(\boldsymbol{L} + 2\boldsymbol{S}) = -g\mu_\mathrm{B}\boldsymbol{B}\cdot\boldsymbol{J}, \tag{2.1}$$

where μ_B is the Bohr-magneton and g is the Landé g-factor defined as:

$$g = 1 + \frac{J(J+1) + S(S+1) - L(L+1)}{2J(J+1)}. \tag{2.2}$$

For ions with spin-only magnetic moment $g = 2$. Assuming that the level splitting due ot spin-orbit coupling is much greater than the Zeeman level separation (which is often a good approximation), the magnetisation of an ion:

$$m_\mathrm{z} = gJ\mu_\mathrm{B}F_\mathrm{J}(B), \tag{2.3}$$

The $F_\mathrm{J}(B)$ Brillouin function defined as:

$$F_\mathrm{J}(B) = \frac{2J+1}{2J}\coth\left(\frac{(2J+1)g\mu_\mathrm{B}\beta B}{2}\right) - \frac{1}{2J}\coth\left(\frac{g\mu_\mathrm{B}\beta B}{2}\right), \tag{2.4}$$

where $\beta = 1/k_\mathrm{B}T$ is the inverse temperature. If the Zeeman energy is small compared to the thermal energy $k_\mathrm{B}T$, Eq. 2.3 can be approximated with the Curie formula:

$$m_\mathrm{z} = \frac{g^2 J(J+1)\mu_\mathrm{B}^2 B}{3k_\mathrm{B}T}. \tag{2.5}$$

The Curie susceptibility of N paramagnetic ions can be readily obtained:

$$\chi_{\mathrm{C}} = \frac{\partial m_{\mathrm{z}}}{\partial H} = \frac{\mu_0 N g^2 J(J+1)\mu_{\mathrm{B}}^2}{3k_{\mathrm{B}}T} = \frac{\mu_0 N \mu_{\mathrm{eff}}^2}{k_{\mathrm{B}}T}, \tag{2.6}$$

where $\mu_{\mathrm{eff}} = g\sqrt{J(J+1)}\mu_{\mathrm{B}}$ is the effective moment. Experimental susceptibility data is often published in units of $\mathrm{cm}^3/\mathrm{mol}$, the Curie susceptibility in this unit is:

$$\chi_{\mathrm{C}} = \frac{\pi}{2}\frac{g^2 J(J+1)}{T}. \tag{2.7}$$

2.1.1 Crystal field

For rare earth elements the Brillouin formula gives very good agreement with experiment. However for transition metals, the measured magnetisation can only be explained if one assumes $L = 0$ and $J = S$. This is an example of the phenomenon called quenching of the angular momentum. Quenching is the result of the symmetry lowering of the ionic one-electron effective potential due to the charge distribution around the magnetic ion. The electric potential in a crystal is called the crystal field (CF). It can often be approximated by the potential of point charges.

Whether the orbitals are quenched or not depends on the relative strength of the spin-orbit coupling and the crystal field. Spin-orbit coupling favours large L, while the CF favours zero L. In rare earth and actinide ions the CF is weak since f shell electrons are tightly localised around the nucleus therefore they are well shielded. In transition metals the CF is stronger due to the larger mean radius of the d orbitals. Thus for f shell electrons spin-orbit coupling is the dominant interaction, which keeps the orbitals unquenched, while for d electrons the CF dominates and spin-orbit coupling acts as a perturbation which results in a small L.

To mathematically describe the effect of the crystal field on electronic orbitals, the electron wave functions are expressed with a properly chosen set of orthogonal functions. For a free atom with continuous $O(3)$ rotational symmetry the spherical harmonics expansion readily provides the electronic orbitals. These orbitals are eigenfunctions of the atomic Hamiltonian with the weak spin-orbit coupling. The wave function of an electron in a free atom can be written as:

$$\psi_{\mathrm{nlm}}(\boldsymbol{r}) = R_{\mathrm{nl}}(r) Y_{\mathrm{l}}^{\mathrm{m}}(\theta, \varphi), \tag{2.8}$$

where $R_{\mathrm{nl}}(r)$ is the radial part of the wave function and $Y_{\mathrm{l}}^{\mathrm{m}}(\theta, \varphi)$ are the spherical harmonics which describe the angular dependence. For example $Y_2^m(\theta, \phi)$ functions

describe the angular dependence of the amplitude of the d orbitals. These wave functions describe orbitals with non-zero orbital angular momentum and the electron density $|\psi_{\mathrm{nlm}}(\boldsymbol{r})|^2$ is rotation invariant around z. However when the crystal field lowers the continuous rotational symmetry to the discrete point group symmetry of the crystal and this perturbation is stronger than the spin-orbit coupling, the ground state orbitals are not any more pure spherical harmonics but the linear combination of these.

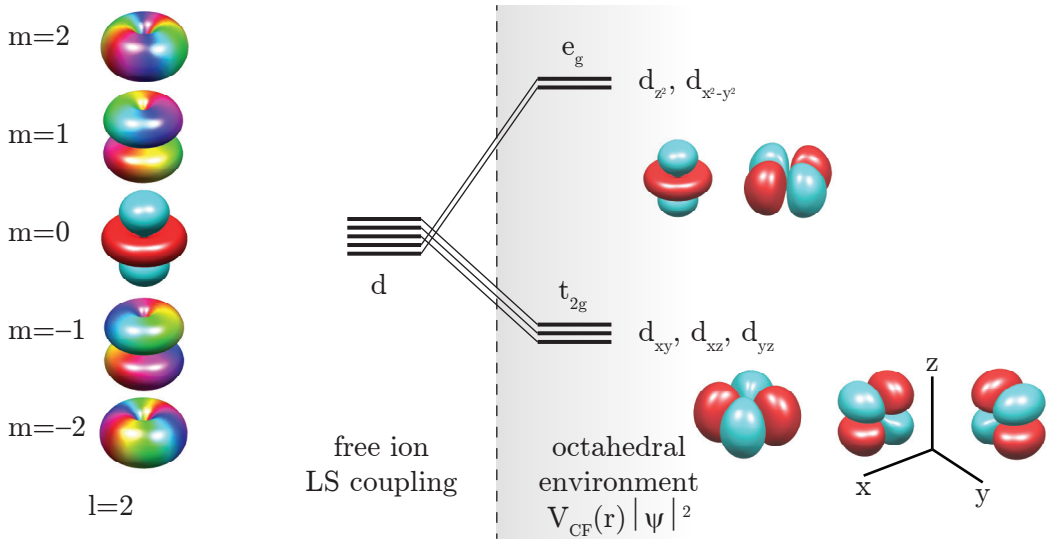

Figure 2.1: Illustration of the splitting of the free ion d orbitals in octahedral crystal field. Left side shows the d orbitals with different z angular momentum component, colour is the phase of the complex amplitude. Right side shows the low lying threefold degenerate $\mathrm{t_{2g}}$ orbitals and the higher energy $\mathrm{e_g}$ orbitals.

For example, the five $3d$ orbitals of a transition metal ion in an octahedral environment (virtual positive charges along $\{x, y, z\}$ axes in positive and negative direction) split into a triplet $\mathrm{t_{2g}}$ and a doublet $\mathrm{e_g}$ orbital, see Fig. 2.1. The $\mathrm{t_{2g}}$ orbitals are called d_{xy}, d_{yz} and d_{xz}, while the $\mathrm{e_g}$ orbitals are $d_{\mathrm{z^2}}$ and $d_{\mathrm{x^2-y^2}}$. For tetrahedral environment, the sign of the splitting is opposite, the e orbitals have lower energy than the t_2 orbitals (the g-"gerade" index is omitted due to the lack of CF inversion symmetry).

For α-$\mathrm{CaCr_2O_4}$ and β-$\mathrm{CaCr_2O_4}$ the $\mathrm{Cr^{3+}}$ ion is in an octahedral environment, therefore the orbital angular momentum is quenched and the three $\mathrm{t_{2g}}$ orbitals are all half-filled. For $\mathrm{Sr_2VO_4}$ the $\mathrm{V^{4+}}$ ions are in tetrahedral environment thus the single valence electron occupies one of the e orbitals ($d_{\mathrm{z^2}}$ or $d_{\mathrm{x^2-y^2}}$).

2.1.2 Single-ion anisotropy

Single-ion anisotropy is the combined result of crystal field and spin-orbit coupling. The details of the mechanism depend on the degree of quenching. Therefore the main distinction is between rare earth $4f$ and iron series $3d$ magnets. [7]

In $4f$ rare earth ions the strong spin orbit coupling keeps the orbital angular moment unquenched and parallel to the spin. The interaction of the ion with the crystal field is due to its non-zero electric quadrupole moment, which is rigidly coupled to the magnetic moment. If the magnetic moment is along the z axis, the electron density of the unquenched orbitals are rotational invariant around the z axis. Therefore the only non-zero element of the quadrupole moment tensor is the Q_{33} term:

$$Q_{33} = \int |\psi_{\mathrm{nlm}}(\boldsymbol{r})|^2 (3z^2 - r^2) d^3\boldsymbol{r}. \tag{2.9}$$

For filled and half filled sub-shells the quadrupole moment is zero, for example Gd^{3+} and La^{3+}. For other rare earth ions the quadrupole moment is non-zero and interacts with the crystal field, which results in easy axis or easy plane anisotropy.

In comparison the anisotropy of the $3d$ transition metals is much weaker. Due to the weakness of the spin-orbit coupling, the orbitals are almost quenched. The small residual orbital moment leads to only small anisotropy. In the Hamiltonian the spin-orbit coupling is a perturbation, the size of this anisotropy appears as a second order term $D_{\mathrm{aniso}} \sim \lambda^2/A$, where λ is the spin orbit coupling constant and A is the CF strength. Therefore only very weak anisotropy is expected to the magnetic ions Cr^{3+} and V^{4+} investigated in this thesis.

2.2 Magnetic interactions

In strongly correlated electron systems, such as many transition metal oxides the electronic and magnetic behaviour cannot be described by an effective one electron model. Each single electron has a complex influence on its neighbours. Strongly correlated materials have electronic structure that are neither effectively free electron like neither completely ionic, but it is somewhere between. The competition between kinetic and Coulomb energies decides which electron states are favoured. The way to describe these systems is to use effective models, which catch some aspects of the complex behaviour.

2.2.1 Hubbard model

The simplest many-particle model, which cannot be reduced to a single-particle theory, is the Hubbard model. [8] It assumes localized electron wave functions on a lattice and that electrons can move ("hop") between sites. The spin of the electron is also considered. Each site can be empty or occupied by one electron with no energy cost. Also two electrons can occupy the same site if they have opposite spins. This configuration has U potential energy due to Coulomb repulsion between electrons. More than two electrons on the same site are not allowed due to the Pauli exclusion principle. The hopping of the electrons from site j to site i is expressed as $t_{\mathrm{ij}}a^{+}_{\mathrm{i}\uparrow}a_{\mathrm{j}\uparrow}$, where t_{ij} is the hopping integral and $a^{+}_{\mathrm{i}\uparrow}$ creates an electron with spin up on site i and $a_{\mathrm{j}\uparrow}$ destroys an electron with spin up on site j. The whole Hamiltonian is:

$$\mathcal{H} = \sum_{\mathrm{i,j}} t_{\mathrm{ij}} \left(a^{+}_{\mathrm{i}\uparrow}a_{\mathrm{j}\uparrow} + a^{+}_{\mathrm{i}\downarrow}a_{\mathrm{j}\downarrow} \right) + U \sum_{\mathrm{i}} n_{\mathrm{i}\uparrow}n_{\mathrm{i}\downarrow}, \tag{2.10}$$

where $n_{\mathrm{i}\uparrow}$ is the number of electron on site i with spin up. This model can describe the transition between conducting and insulating systems with partially filled bands. If the t/U ratio is large, the material is a conductor because electrons can move easily. While for small t/U the material is insulating. These types of insulators are called Mott insulators to distinguish them from the conventional band-gap insulators. α-$CaCr_2O_4$, β-$CaCr_2O_4$ and Sr_2VO_4belong to this family.

2.2.2 Heisenberg interaction

It can be shown that the large-U limit of the Hubbard model for half filled sites has primarily spin excitations at low energies. [8] This effective spin model is called the Heisenberg model, which has the form:

$$\mathcal{H} = \sum_{\mathrm{i>j}} J_{\mathrm{ij}} \boldsymbol{S}_{\mathrm{i}} \cdot \boldsymbol{S}_{\mathrm{j}}, \tag{2.11}$$

where $\boldsymbol{S}_{\mathrm{i}}$ is the spin of the electron on the ith site. The exchange couplings are:

$$J_{\mathrm{ij}} = -4t^2_{\mathrm{ij}}/U. \tag{2.12}$$

In this approximation a negative value of J_{ij} favours ferromagnetic (parallel) alignment of the spins. The Heisenberg model can be also generalised to positive J_{ij} values, which favour antiferromagnetic (antiparallel) spin alignment. For a simple argument lets assume an interaction between two well separated magnetic ion with one-one electron.

According to the Pauli principle, the wave function of two spin-1/2 electrons has to be antisymmetric with respect to the exchange of the two electrons. The two-electron wave function can be written as the product of the spatial $\psi(\boldsymbol{r}, \boldsymbol{r}')$ and spin dependent $\chi(\sigma, \sigma')$ part. Therefore for an antisymmetric spin function the spatial function must be symmetric and vice versa. Including the Coulomb interaction between electrons, the antisymmetric spatial configuration has lower energy than the symmetric one, thus the ground state would be $S = 1$. However if the electrons are allowed to move between the two atoms, the symmetric spatial configuration can be favoured. This would lead to an antisymmetric spin arrangement with $S = 0$. In the two cases the effective coupling would be ferromagnetic or antiferromagnetic respectively.
Since the above argument requires direct overlap of the electronic orbitals of the neighbouring atoms, this type of interaction is called direct exchange. For $3d$ transition metals the electron density overlap vanishes if the distance between two magnetic ions is larger than ~ 3 Å. However strong exchange interactions are also found in compounds, where the distance between magnetic ions is much larger than 3 Åand they are separated by a non-magnetic anion. [9] This is the so called superexchange interaction. Kramers proposed first that the interaction is mediated by the non-magnetic anion. Goodenough and Kanamori [10, 11] developed a set of semi-empirical rules which give the sign and strength of the superexchange interaction depending on the symmetry relations and electron occupancy of the overlapping orbitals. According to the Goodenough-Kanamori rules a 180° superexchange (the magnetic ion–ligand–magnetic ion angle) of two magnetic ions with partially filled d shells is strongly antiferromagnetic, while the 90° superexchange is ferromagnetic and much weaker.

2.2.3 Dzyaloshinskii–Moriya interaction

Another type of magnetic interaction is the antisymmetric Dzyaloshinskii–Moriya (DM) interaction, which appears as a higher order correction from the Dirac equation. It is expressed as:

$$\mathcal{H} = \sum_{\mathrm{i}>\mathrm{j}} \boldsymbol{D}_{\mathrm{ij}} \cdot (\boldsymbol{S}_{\mathrm{i}} \times \boldsymbol{S}_{\mathrm{j}}) \,, \tag{2.13}$$

where $\boldsymbol{D}_{\mathrm{ij}}$ is a vector. In crystals DM interactions are allowed if the centre of the bond connecting $\boldsymbol{S}_{\mathrm{i}}$ and $\boldsymbol{S}_{\mathrm{j}}$ does not have an inversion symmetry. The DM interaction energy is reduced if the angle between interacting spins is 90° and the spins are perpendicular to $\boldsymbol{D}_{\mathrm{ij}}$, therefore it acts as an effective easy plane anisotropy. Furthermore DM interaction favours non-zero chirality of the ground state structure. The DM interaction plays

a significant role in the physics of β-$CaCr_2O_4$ and gives rise to chains ordered with different chiralities.

2.2.4 Mean field theory

The mean field theory (MFT) is an effective way to simplify complicated many-body problems. It approximates the many-body interactions with an effective field. Therefore it neglects fluctuations. It is useful in magnetism to calculate high temperature magnetic properties and it is often the starting point of a more sophisticated calculation. Using mean field theory the high temperature susceptibility of an interacting magnetic system can be well approximated if the $k_\mathrm{B}T$ energy is much larger than then the interatomic exchange. The susceptibility is:

$$\chi_\mathrm{MF} = \frac{\chi_0}{1 + \lambda\chi_0/2}, \tag{2.14}$$

where χ_0 is the susceptibility of the magnetic site and λ is the molecular field (effective field) coupling constant: [12]

$$\lambda = \sum_\mathrm{j} \frac{J_\mathrm{ij}}{Ng^2\mu_\mathrm{B}^2}. \tag{2.15}$$

Substituting the free ion susceptibility for χ_0 one gets the Curie–Weiss susceptibility:

$$\chi_\mathrm{CW} = \frac{C}{T - T_\mathrm{CW}}, \tag{2.16}$$

where T_CW is the Curie-Weiss temperature:

$$k_\mathrm{B}T_\mathrm{CW} = \frac{J(J+1)}{3} \sum_\mathrm{j} J_\mathrm{ij}. \tag{2.17}$$

2.2.5 Frustration

Frustration in condensed matter physics is a phenomenon in which the spatial arrangement of the magnetic moments on a lattice forbids simultaneous minimisation of the pair interaction energies. It leads to highly degenerate ground states with non-zero entropy at zero temperature. Frustration suppresses long-range order and promotes the development of short range ordered ground states quantum or classical. Prominent examples are spin glass and spin liquid states. [13] There are several types of frustration, including bond frustration (best example is water ice [14]), orbital frustration (the spin-orbital liq-

uid $FeSc_2S_4$ [15], later suggested to be spin-orbital singlet [16]) and magnetic frustration. Among these systems the most studied are the frustrated magnets, where frustration is predominantly caused by competing antiferromagnetic interactions on non-bipartite lattices. There are also other sources of magnetic frustration, for example competing anisotropy and ferromagnetic coupling as in the spin-ice material $Dy_2Ti_2O_7$. [17]

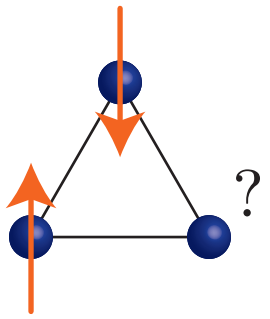

Figure 2.2: Triangle of antiferromagnetic Ising spins, due to frustration the third spin cannot satisfy both antiferromagnetic coupling.

Lattices that support frustration are often made up of triangular units, see Fig. 2.2. Frustrated lattices are for example in one dimension: the chain with nearest and next-nearest neighbour interactions, in two dimension: the triangular lattice [18, 19], kagome lattice [20, 21] and square lattice with next-nearest neighbour interactions [22], in three dimension: the pyrochlore lattice [23], hyperkagome [24] and spinel lattice. [25] Some examples are shown on Fig. 2.3.

Both α-$CaCr_2O_4$ and β-$CaCr_2O_4$ are frustrated. α-$CaCr_2O_4$ is a triangular lattice antiferromagnet and β-$CaCr_2O_4$ has spin chains with frustrated 1st and 2nd neighbour interactions.

2.2.6 Low dimensionality

According to the Mermin–Wagner theorem continuous symmetries cannot be broken spontaneously at finite temperature in systems with sufficiently short range interactions in dimensions less than three. For magnetic crystals, it means that one and two dimensional structures cannot stabilise long-range order at finite temperature. However in real (quasi low dimensional) materials there are always weak interactions which couple the magnetic ions along all three dimensions. The competition between these weak interactions and the quantum fluctuations determine whether the system is long-range ordered at low temperature. At non-zero temperatures thermal fluctuations can play important

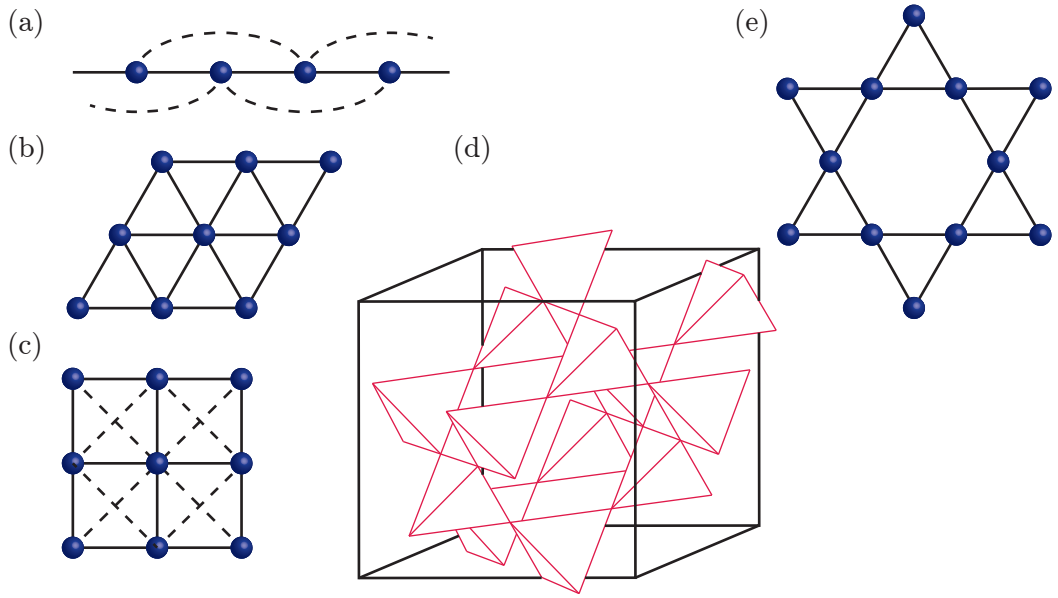

Figure 2.3: Different lattices with geometrical frustration, dashed lines denote next-nearest neighbour interactions. (a) Chain with next nearest neighbour interaction, (b) triangular lattice, (c) square lattice with next-nearest neighbour interactions, (d) pyrochlore lattice and (e) kagome lattice.

role, which can easily destroy the order in quasi low dimensional systems. This results in suppressed ordering temperature and suppressed ordered moment size.

2.3 Magnetic order

The spin Hamiltonians described in the previous sections imply different types of magnetic order at zero temperature. The magnetic order can be short range or long-range. Examples of short range ordered systems are spin dimers, spin liquids, spin glasses and spin ice. Spin-half dimers are made up of two strongly antiferromagnetically coupled $S = 1/2$ magnetic ions, which together form a unit with zero total spin. The excited triplet state is separated by an energy gap from the dimer state. Three dimensional dimer systems can undergo Bose–Einstein condensation of magnons in applied magnetic field. [26] Spin liquid is a state of matter which shows no sign of ordering down to lowest temperatures due to quantum fluctuations. [27, 28] The spin glass ground state can occur when disorder is explicitly present in the spin Hamiltonian and the system has frustrated interactions. Spin glasses have static magnetic order at low temperature but fluctuations exists at any energy scale. In spin ice, which is a type of spin liquid, the

dynamics of spins is governed by the same rules as the hydrogen atom positions in water ice. The spins are located on corner sharing tetrahedra. The ice rule, which occurs due to the single ion anisotropy, says that the energetically favourable state is when two spins point out and two spins point into the tetrahedron. This rule describes frustration because it competes with the magnetic interactions, therefore the system has residual entropy even at zero temperature. The spin ice state gained attention after the discovery that their magnetic excitations can be mapped onto magnetic monopoles. [23, 17, 29]
More commonly magnetic materials develop static long-range magnetic order. These systems are categorized by a magnetic structure which can be ferromagnetic, antiferromagnetic, ferrimagnetic, helical or more complicated.
Magnetic order can be also induced by fluctuations, either thermal or quantum. This is the so called "order by disorder" phenomena. It relates to systems, which have a degenerate ground state but thermal or quantum fluctuations lifts this degeneracy and causes the system to order. For magnetic systems with classically degenerate ground states quantum fluctuations can induce order at low temperatures. For frustrated exchange-coupled systems fluctuations usually favour collinear states. [30]
The relevant topics for the following chapters are spin dimers (Sr_2VO_4) and helical structures (α-$CaCr_2O_4$ and β-$CaCr_2O_4$), thus these will be discussed here in more detail.

2.3.1 Spin dimer

Spin dimers are strongly correlated units of two $S = 1/2$ ions. The simplest system is where the two spins are coupled via antiferromagnetic Heisenberg exchange:

$$\mathcal{H}_{\text{dimer}} = J\boldsymbol{S}_1 \cdot \boldsymbol{S}_2, \tag{2.18}$$

where $J > 0$. The energy levels can be indexed with the total spin operator: $S^2_{\text{tot}} = (\boldsymbol{S}_1 + \boldsymbol{S}_2)^2$, since it commutes with the Hamiltonian. The lowest lying eigenfunction of S^2_{tot} is antisymmetric with zero total spin S_{tot}=0 and an energy of $E_0 = -3/4J$. This wave function can be expressed in terms of the single spin wave functions: $|0,0\rangle = 1/\sqrt{2}(|\uparrow\downarrow\rangle - |\downarrow\uparrow\rangle)$, where $|\uparrow\rangle \equiv |1/2, 1/2\rangle$ and $|\downarrow\rangle \equiv |1/2, -1/2\rangle$. The excited state is a triplet, it has $S^2_{\text{tot}} = 2$ which is effectively a spin-1 object with energy of $E = 1/4J$. The three symmetric wave functions are $|1,1\rangle = |\uparrow\uparrow\rangle$, $|1,0\rangle = 1/\sqrt{2}(|\uparrow\downarrow\rangle + |\downarrow\uparrow\rangle)$, $|1,-1\rangle = |\downarrow\downarrow\rangle$. The energy difference between the excited and ground state of a dimer is J. The magnetic susceptibility as a function of temperature $\chi(T)$ can be easily calculated: [31, 32]

$$\chi(T) = \frac{N}{2}\left[p(S=0,T)\chi_0 + p(S=1,T)\chi_1\right], \tag{2.19}$$

where N is the number of dimers, χ_S is the Curie susceptibility of a spin-S ion and $p(S,T)$ is the probability that state S is occupied. This probability is given by the Boltzmann distribution:

$$p(S,T) = \frac{\exp(-E_S/k_BT)}{\exp(-E_0/k_BT) + 3\exp(-E_1/k_BT)} n(S), \tag{2.20}$$

where $n(S)$ is the degeneracy of the state. Substituting the Curie susceptibility (χ_0=0) one gets:

$$\chi_{\text{dimer}} = \frac{g^2}{8T} \frac{1}{3 + \exp(J/k_BT)}, \tag{2.21}$$

which is the susceptibility per mole magnetic ions in units of cm^3/mol.
Simple approximation can be made for interacting dimers, using mean field theory. According to Eq. 2.14 the susceptibility of weakly interacting dimers: [33, 32]

$$\chi_{\text{inter-dimer}} = \frac{\chi_{\text{dimer}}}{1 + \gamma\chi_{\text{dimer}}} = \frac{g^2}{8T} \cdot \frac{1}{3 + \exp(J/k_BT) + J'/k_BT}, \tag{2.22}$$

where J' is the sum of the inter-dimer exchange interactions per magnetic ion.

2.3.2 Long-range magnetic order

Long-range magnetic order means that the magnetic moments have non-vanishing expectation value: $\langle \boldsymbol{M}_i \rangle \neq 0$. The magnetic structures can be described by the so called magnetic (Shubnikov) groups or by irreducible representations (irrep) and basis functions. [34] The motivation to describe magnetic structures using group theory comes from the Landau theory of a second-order phase transition. In the simplest of terms it states that magnetic fluctuations at a second-order phase transition have the symmetry of only one irreducible representation. This representation describes the transformation of the magnetic moment. Even for first-order phase transitions the resulting magnetic structure is often the same as would be predicted for second-order transition. Therefore group theory calculations are useful in the determination and description of magnetic structures.
The magnetic groups are generated from the 230 crystallographic space groups plus the time inversion operator, which leaves the crystal structure unchanged but inverts the magnetic moments. With this new operator the number of possible magnetic groups is 1651, however they cannot describe all the observed magnetic structures including the helical structure.

The representation analysis of magnetic structures investigates the transformation properties of magnetic structures under the operations of the 230 crystallographic space groups. It provides a more general description than magnetic space groups. A magnetic structure is expressed as a Fourier transform: [35, 36]

$$\boldsymbol{M}_{\mathrm{i}}(\boldsymbol{l}) = \sum_{\boldsymbol{k}_{\mathrm{m}}} \boldsymbol{\psi}_{\mathrm{i}}^{\boldsymbol{k}_{\mathrm{m}}} \exp\left(-2\pi i \boldsymbol{k}_{\mathrm{m}} \cdot \boldsymbol{l}\right), \tag{2.23}$$

where $\boldsymbol{M}_{\mathrm{i}}(\boldsymbol{l})$ is the magnetic moment of the ith atom in the unit cell of the $\boldsymbol{l}$ lattice translational vector ($\boldsymbol{l} = i\boldsymbol{a} + j\boldsymbol{b} + k\boldsymbol{c}$). The summation is made over several wave vectors within the first Brillouin zone of the crystal and $\boldsymbol{\psi}_{\mathrm{i}}^{\boldsymbol{k}_{\mathrm{m}}}$ are the set of basis vectors that are projections of the magnetic moment along the $\{a, b, c\}$ crystallographic axes. The $\boldsymbol{k}_{\mathrm{m}}$ vectors are the magnetic ordering wave vectors. If the magnetic unit cell is a simple multiple of the crystallographic unit cell (the components of $\boldsymbol{k}_{\mathrm{m}}$ are rational numbers in the units of the reciprocal lattice vectors of the crystal), the magnetic structure is called commensurate, otherwise it is incommensurate. Since the components of the magnetic moments are real numbers, the right hand side of Eq. 2.23 has to be real. It is real in two cases, either all components of the $\boldsymbol{k}_{\mathrm{m}}$ vectors are half-integer or the non-zero basis functions pair up and $\boldsymbol{\psi}_{\mathrm{i}}^{-\boldsymbol{k}_{\mathrm{m}}} = \boldsymbol{\psi}_{\mathrm{i}}^{\boldsymbol{k}_{\mathrm{m}}*}$ is true for the $\boldsymbol{k}_{\mathrm{m}}$ and $-\boldsymbol{k}_{\mathrm{m}}$ pairs.

The simplest magnetic structures which can be described by Eq. 2.23 are ferromagnets and antiferromagnets on a Bravais lattice. They can be described by a single basis vector: $\boldsymbol{\psi}_1 = \boldsymbol{M}(0)$, the direction of the magnetic moment in the first unit cell and the magnetic moment: $\boldsymbol{M}(\boldsymbol{l}) = \boldsymbol{M}(0)\cos(2\pi\boldsymbol{k}_{\mathrm{m}} \cdot \boldsymbol{l})$. If $\boldsymbol{k}_{\mathrm{m}}$ is zero, the structure is a ferromagnet, if $\boldsymbol{k}_{\mathrm{m}}$ has components of zero and half the structure is an antiferromagnet.

If $\boldsymbol{k}_{\mathrm{m}}$ is not half-integer, a minimum of two basis vectors are necessary to construct real magnetic moments:

$$\begin{aligned} \boldsymbol{M}_{\mathrm{i}}(\boldsymbol{l}) &= \boldsymbol{\psi}_{\mathrm{i}}^{\boldsymbol{k}_{\mathrm{m}}} \exp\left(-2\pi i \boldsymbol{k}_{\mathrm{m}} \cdot \boldsymbol{l}\right) + \boldsymbol{\psi}_{\mathrm{i}}^{-\boldsymbol{k}_{\mathrm{m}}*} \exp\left(2\pi i \boldsymbol{k}_{\mathrm{m}} \cdot \boldsymbol{l}\right) \\ &= 2\,\mathrm{Re}\left(\boldsymbol{\psi}_{\mathrm{i}}\right) \cos\left(2\pi \boldsymbol{k}_{\mathrm{m}} \cdot \boldsymbol{l}\right) + 2\,\mathrm{Im}\left(\boldsymbol{\psi}_{\mathrm{i}}\right) \sin\left(2\pi \boldsymbol{k}_{\mathrm{m}} \cdot \boldsymbol{l}\right), \end{aligned} \tag{2.24}$$

where $\boldsymbol{\psi}_{\mathrm{i}} \equiv \boldsymbol{\psi}_{\mathrm{i}}^{\boldsymbol{k}_{\mathrm{m}}}$. This structure is the so called single-k magnetic structure. Expression 2.24 can describe sinusoidally modulated (if either $\mathrm{Im}(\boldsymbol{\psi}_{\mathrm{i}})$ or $\mathrm{Re}(\boldsymbol{\psi}_{\mathrm{i}})$ is null vector) and helical magnetic structures (if $\mathrm{Im}(\boldsymbol{\psi}_{\mathrm{i}})$ is perpendicular to $\mathrm{Re}(\boldsymbol{\psi}_{\mathrm{i}})$). Figure 2.4 shows two examples. Tab. 2.1 list the names of different helical structures.

Multi-k structures involve several $\boldsymbol{k}_{\mathrm{m}}$ vector. A typical multi-k structure is, where higher harmonics of a base $\boldsymbol{k}_{\mathrm{m}}$ vector are present. The higher order wave vectors appear for example in the case of sinusoidal structures upon cooling. To decrease the entropy, the

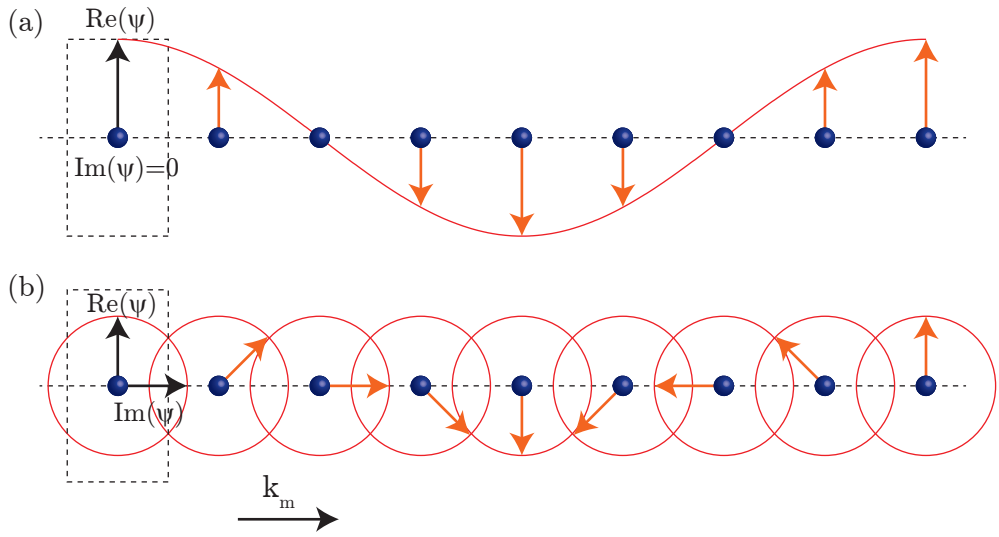

Figure 2.4: Magnetic structures described by $\boldsymbol{k}_\mathrm{m} = (a/8, 0, 0)$ and $-\boldsymbol{k}_\mathrm{m}$ ordering wavevector pair. (a) Sinusoidally modulated structure where $\mathrm{Re}(\boldsymbol{\psi}) = (0, 1, 0)$ and $\mathrm{Im}(\boldsymbol{\psi}) = 0$, (b) helical structure (cycloidal) where $\mathrm{Re}(\boldsymbol{\psi}) = (0, \sqrt{2}, 0)$ and $\mathrm{Im}(\boldsymbol{\psi}) = (\sqrt{2}, 0, 0)$.

Table 2.1: Names of single-k helical structures, where $\mathrm{Im}(\boldsymbol{\psi}_\mathrm{i})$ is perpendicular to $\mathrm{Re}(\boldsymbol{\psi}_\mathrm{i})$.

name	defining expression
circular helix	$\lvert\mathrm{Im}(\boldsymbol{\psi}_\mathrm{i})\rvert = \lvert\mathrm{Re}(\boldsymbol{\psi}_\mathrm{i})\rvert$
elliptical helix	$\lvert\mathrm{Im}(\boldsymbol{\psi}_\mathrm{i})\rvert \neq \lvert\mathrm{Re}(\boldsymbol{\psi}_\mathrm{i})\rvert$
proper screw	$\boldsymbol{k}_\mathrm{m} \parallel \mathrm{Im}(\boldsymbol{\psi}_\mathrm{i}) \times \mathrm{Re}(\boldsymbol{\psi}_\mathrm{i})$
cycloidal	$\boldsymbol{k}_\mathrm{m} \perp \mathrm{Im}(\boldsymbol{\psi}_\mathrm{i}) \times \mathrm{Re}(\boldsymbol{\psi}_\mathrm{i})$

non-equal length spins grow and the magnetic structure develops into a square wave and locks the incommensurate ordering wavevector value to the nearest commensurate value, for example in the case of Er and Tm rare earth metals. [37, 38] Since the Fourier transform of the square wave contains the higher harmonics of the base wave vector, it explains the appearance of the multiples of $\boldsymbol{k}_\mathrm{m}$ in the expansion of the magnetic structure. Both α-$CaCr_2O_4$ and β-$CaCr_2O_4$ develop helical long-range order and both have a small ellipticity.

2.3.3 Representation analysis of magnetic structures

To determine the symmetry allowed magnetic structures, first the effect of the symmetry elements of the crystallographic space group G_0 on the propagation vector $\boldsymbol{k}_\mathrm{m}$ has to be considered. Each symmetry element can be separated into rotational and translational part, $g = \{g_\mathrm{r}, \boldsymbol{g}_\mathrm{t}\}$. Applying only the g_r rotational part of the symmetry elements to $\boldsymbol{k}_\mathrm{m}$ the operators are sorted into cosets. The symmetry elements which leave $\boldsymbol{k}_\mathrm{m}$ invariant are in the first coset $G_{\boldsymbol{k}_\mathrm{m}}$, the second coset $G^2_{\boldsymbol{k}_\mathrm{m}}$ contains elements which transform $\boldsymbol{k}_\mathrm{m}$ into an inequivalent vector $\boldsymbol{k}'_\mathrm{m}$ and so on. The set of these generated inequivalent wave vectors is called the "star" of the propagation vector $\boldsymbol{k}_\mathrm{m}$. The first coset is also called the "little group".

The effect of a crystal symmetry element g on the magnetic moment is twofold. It permutes the symmetry equivalent magnetic atoms and reorient the magnetic moments. The combination of these two are described by the magnetic representation Γ. [34, 39, 35]

The effect of the symmetry elements on the atom positions can be represented by the permutation representation $\Gamma^\mathrm{g}_\mathrm{perm}$. The (i, j) element of the permutation matrix is unity if $g(\boldsymbol{d}_\mathrm{j}) = \boldsymbol{d}_\mathrm{i}$, where $\boldsymbol{d}_\mathrm{i}$ and $\boldsymbol{d}_\mathrm{j}$ are the atomic positions within the unit cell of the ith and jth magnetic atoms respectively. However if the symmetry operation results in an atomic position outside the zeroth unit cell, the (i, j) element has to be multiplied by a phase factor:

$$\delta = -2\pi \boldsymbol{k}_\mathrm{m} \cdot \boldsymbol{l}. \tag{2.25}$$

The effect of g on the magnetic moment direction can be described by the axial vector representation $\Gamma^\mathrm{g}_\mathrm{axial}$. Its matrices are $R^\mathrm{g} \det(R^\mathrm{g})$, where R^g is the 3x3 rotation matrix of g_r rotation operation and $\det(R^\mathrm{g})$ is $+1$ for proper and -1 for improper rotation.

The Γ magnetic representation describes the effect of symmetry operations on the atomic positions and on the magnetic moments. Since these effects are independent, the mag-

netic representation is given by the direct product of their representations:

$$\Gamma = \Gamma_{\text{axial}} \times \Gamma_{\text{perm}}. \tag{2.26}$$

This is equivalent to the Kronecker product of the matrices of the representations. The magnetic representation Γ can be decomposed into contributions from the irreducible representations of the little group $G_{\boldsymbol{k}_\text{m}}$: [40]

$$\Gamma = \sum_\nu n_\nu \Gamma_\nu, \tag{2.27}$$

where Γ_ν are the irreducible representations, which appear n_ν-times in Γ.

The $\boldsymbol{\psi}_\lambda^{\boldsymbol{k}_\text{m}\nu}$ basis vectors that belong to the d_ν dimensional irreducible representation Γ_ν can be calculated. The vectors are projected out of the D^ν matrix of the irrep using a series of test functions $\psi_{\text{j}\beta}^{\boldsymbol{k}_\text{m}}$, where $\beta \in \{x, y, z\}$ and j is the index of the atom in the crystal unit cell. The test function is a column vector with zero values, except the jth atom β component is one. The equation is called the projection operator formula:

$$\boldsymbol{\psi}_\lambda^{\boldsymbol{k}_\text{m}\nu} = \sum_{g \in G_{\boldsymbol{k}_\text{m}}} D_{\lambda\mu}^{*\boldsymbol{k}_\text{m}\nu}(g) \hat{T}(g) \psi, \tag{2.28}$$

where the summation runs over the elements of the little group $G_{\boldsymbol{k}_\text{m}}$. $D_{\lambda\mu}^{*\boldsymbol{k}_\text{m}\nu}(g)$ is the (λ, ν) element of the matrix of the g symmetry element that belongs to the Γ_ν irrep. ψ is one of the test functions and $\hat{T}(g)$ is an operator which transforms the magnetic moment and permutes the atom. The $\hat{T}(g)$ transforms the test functions according to the following:

$$\hat{T}(g)\psi_{\text{j}\beta}^{\boldsymbol{k}_\text{m}} = \sum_{\text{i}\alpha} \exp\left(-i\boldsymbol{k}_\text{m} \cdot (\boldsymbol{d}_{g\text{i}} - \boldsymbol{d}_\text{i})\right) \det(R^g) R_{\alpha\beta}^g \delta_{\text{i},g\text{j}} \psi_{\text{i}\alpha}^{\boldsymbol{k}_\text{m}}, \tag{2.29}$$

where $R_{\alpha\beta}^g$ it the (α, β) element of the rotation matrix, $\delta_{\text{i,j}}$ is the Kronecker delta. The number of basis functions that belongs to the same irrep equals the dimension of the irrep times its multiplicity in the magnetic representation.

Representation analysis is performed to restrict the number of possible magnetic structures for the refinement of α-$CaCr_2O_4$ and β-$CaCr_2O_4$ neutron diffraction data using the program BasIreps. [41]

2.4 Magnetic excitations

The family of different magnetic excitations is large similarly to the number of possible magnetic ground states. Magnons, spinons, electromagnons and the massive excitations of the Haldane chain belong to this family among others. Magnons are spin-1 bosons or harmonic spin-deviations in a long-range ordered magnetic structure. Emergent particles with fractional quantum numbers is quite generic in one-dimensional conductors and magnets. One of them is the spin-1/2 excitation called spinon, which is a free domain wall on the antiferromagnetic $S = 1/2$ chain. [42, 43] It was first experimentally observed in the quasi one dimensional chain compound $KCuF_3$. [44] Electromagnons are electric dipole active magnetic excitations. [45]

2.4.1 Linear spin-wave theory

The aim of this section is to introduce a general solution to linear spin-wave theory (LSWT) with the purpose to use it in an algorithm which calculates spin-wave dispersion and correlation functions of α-$CaCr_2O_4$ and β-$CaCr_2O_4$. Since these systems are frustrated antiferromagnets with non-collinear and incommensurate structure, the assumptions on the magnetic structure and ordering wavevector will be as general as possible. Spin-wave theory for collinear antiferromagnets is based on the partition of the magnetic moments into sublattices and the assignment of a spin operator for each sublattice. This method cannot be applied to incommensurate frustrated antiferromagnets since the number of sublattices would be infinite. To solve the problem a rotating coordinate system is introduced, which rotates together with the magnetic moment. This way the direction of the spin vector-operator in the local coordinate system is the same in every crystallographic unit cell in real space. However this method has its limitations as well. The Hamiltonian has to be invariant under arbitrary lattice vector translation. This means classically that the angle between any pair of spin should be also invariant assuming only isotropic Heisenberg exchange interactions. This can be seen by examining the classical energy, which is $S_\mathrm{i}S_\mathrm{j}\cos(\varphi_\mathrm{ij})$, where φ_ij is the angle between the ith and jth spin. Apart from the $\varphi = -\varphi$ equivalence, the invariance of the cosine function means invariance of φ under lattice translations. The most general solution has arbitrary moment directions in the crystallographic unit cell (directions are determined by the spin Hamiltonian), a $\boldsymbol{k}_\mathrm{m}$ magnetic ordering wavevector and an $\boldsymbol{n}$ rotation axis. The spin are rotating in the plane perpendicular to this rotation axis:

$$\boldsymbol{S}^\mathrm{i}_{\boldsymbol{l}+\Delta\boldsymbol{l}} = \underline{R}_{\boldsymbol{n}}(\Delta\boldsymbol{l}\cdot\boldsymbol{k}_\mathrm{m})\cdot\boldsymbol{S}^\mathrm{i}_{\boldsymbol{l}}, \tag{2.30}$$

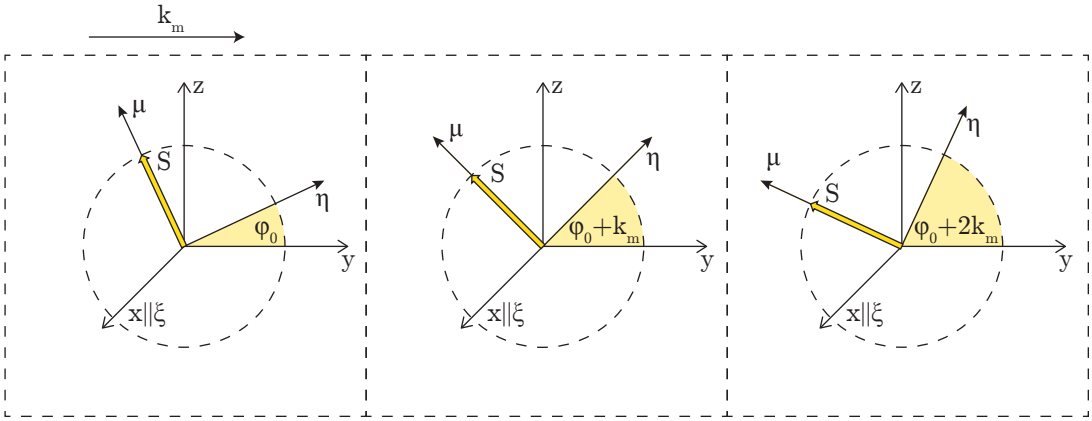

Figure 2.5: A $\xi\eta\mu$ local coordinate system is attached to every spin, dashed squares denote unit cells.

where $\underline{R}_{\boldsymbol{n}}(\alpha)$ is a rotation matrix, which describes rotation around the vector $\boldsymbol{n}$ by α angle, $\boldsymbol{l}$ and $\Delta\boldsymbol{l}$ are arbitrary lattice vectors.

In this model each spin is described by two parameters, the (θ, φ) spherical coordinates. In the following spin-wave calculation a simplified case will be analysed, when the magnetic structure is planar. In this case $\boldsymbol{n}$ is the normal vector of the plane of the spins and φ is the angle of the spin in this plane. The spin-wave theory will be developed for different type of magnetic Hamiltonians: Heisenberg exchange and Dzyaloshinskii-Moriya interactions, single ion anisotropy and for the Zeeman term. This method can also be applied to collinear structures.

2.4.1.1 Spin-wave dispersion

Two coordinate systems are going to be used in the following. The $\{x, y, z\}$ system is determined by the $\boldsymbol{n}$ normal vector of the spin plane: $\hat{\boldsymbol{x}} \parallel \boldsymbol{n}$, $\hat{\boldsymbol{y}}$ is arbitrary vector perpendicular to $\boldsymbol{n}$ and $\hat{\boldsymbol{z}} \parallel (\hat{\boldsymbol{x}} \times \hat{\boldsymbol{y}})$. The basis vectors of the rotating system $\{\xi, \eta, \mu\}$ are defined as:

$$\begin{aligned} \hat{\xi}_{\boldsymbol{l}} =& \hat{x}, \\ \hat{\eta}_{\boldsymbol{l}} =& \hat{y}\cos(\varphi_{\boldsymbol{l}}) + \hat{z}\sin(\varphi_{\boldsymbol{l}}), \\ \hat{\mu}_{\boldsymbol{l}} =& \hat{\xi}_{\boldsymbol{l}} \times \hat{\eta}_{\boldsymbol{l}}, \end{aligned} \tag{2.31}$$

where $\varphi_{\boldsymbol{l}}$ is the spin angle in the $\boldsymbol{l}$th unit cell, (see Fig. 2.5) and is given by:

$$\varphi_{\boldsymbol{l}} = \varphi_0 + \boldsymbol{k}_{\mathrm{m}} \cdot \boldsymbol{l}, \tag{2.32}$$

where φ_0 is the angle in the zeroth unit cell which minimizes the ground state energy. The transformation for the spin components between the two coordinate systems is similar (omitting the $\boldsymbol{l}$ index):

$$\begin{aligned} S^{\mathrm{x}} =& S^{\xi} \\ S^{\mathrm{y}} =& S^{\eta}\cos\varphi - S^{\mu}\sin\varphi \\ S^{\mathrm{z}} =& S^{\eta}\sin\varphi + S^{\mu}\cos\varphi, \end{aligned} \tag{2.33}$$

where the upper index of the spin denotes the spin component along the specific axis. Switching to quantum mechanics the spin vector $\boldsymbol{S}$ and each of its components S^{μ}, S^{η} and S^{ξ} become operators. The spin ladder operators are defined as the linear combination of these components:

$$\begin{aligned} S^{\mu} =& S^{\mu} \\ S^{\xi} =& \frac{1}{2}\left(S^{+} + S^{-}\right) \\ S^{\eta} =& \frac{1}{2i}\left(S^{+} - S^{-}\right), \end{aligned} \tag{2.34}$$

where S^{+} and S^{-} are the raising and lowering operators. Applying it them on a spin state one gets:

$$S^{\pm}|S, m_{\mathrm{s}}\rangle = C^{\pm}(S, m_{\mathrm{s}})|S, m_{\mathrm{s}} \pm 1\rangle. \tag{2.35}$$

The derivation of the matrix form of the spin Hamiltonian is going to be introduced through the example of the isotropic Heisenberg exchange interaction. In the first step the scalar product of two spin will be expressed in terms of the ladder operators. Index i and j are going to be used to distinguish the two interacting spins, these two spins can be in the same unit cell or in different unit cells. The scalar product of the two spins is:

$$\begin{aligned} \boldsymbol{S}_i \cdot \boldsymbol{S}_j =& \frac{1}{4}(S_i^{+}S_j^{+} + S_i^{-}S_j^{-})(1 - \cos\Delta\varphi) + \\ &+ \frac{1}{4}(S_i^{+}S_j^{-} + S_i^{-}S_j^{+})(1 + \cos\Delta\varphi) + S_i^{\mu}S_j^{\mu}\cos\Delta\varphi + \\ &+ \frac{1}{2i}\left[(S_{\mathrm{i}}^{+} - S_{\mathrm{i}}^{-})S_{\mathrm{j}}^{\mu} - S_{\mathrm{i}}^{\mu}(S_{\mathrm{j}}^{+} - S_{\mathrm{j}}^{-})\right]\sin\Delta\varphi. \end{aligned} \tag{2.36}$$

$\Delta\varphi = \varphi_i - \varphi_j$ is defined as the angle between the two spins. The $S_\mathrm{i}^+ S_\mathrm{j}^-$ and similar terms in Expr. 2.36 are responsible for the propagation of the spin deviation, the result is that one angular momentum quantum is moved from the jth spin to the ith spin. If the ordered spin moment reduction is small, as often the case for sufficiently low temperatures, the elementary excitations of the spins can be modelled as a non interacting boson gas. In this case bosonic operators can be defined, which have an unbounded spectrum. This condition can be more easily satisfied for large S. The ladder operators can be expressed using the Holstein-Primakoff transformation [46] and keeping only the first term of the Taylor series:

$$\begin{aligned} S_\mathrm{i}^\mu =& S - a_\mathrm{i}^+ a_\mathrm{i} \\ S_\mathrm{i}^+ =& \sqrt{2S}\sqrt{1 - \frac{a_\mathrm{i}^+ a_\mathrm{i}}{2S}} a_\mathrm{i} \approx \sqrt{2S} a_\mathrm{i} \\ S_\mathrm{i}^- =& \sqrt{2S} a_\mathrm{i}^+ \sqrt{1 - \frac{a_\mathrm{i}^+ a_\mathrm{i}}{2S}} \approx \sqrt{2S} a_\mathrm{i}^+, \end{aligned} \tag{2.37}$$

where a_i and a_i^+ are the bosonic annihilation and creation operators of the ith spin. Equation 2.36 can be expressed using these bosonic operators:

$$\begin{aligned} \boldsymbol{S}_i \cdot \boldsymbol{S}_j / S =& S\cos\Delta\varphi - i\sqrt{\frac{S}{2}}\left(a_\mathrm{i} - a_\mathrm{i}^+ - a_\mathrm{j} + a_\mathrm{j}^+\right)\sin\frac{\Delta\varphi}{2} + \\ &+ (a_i a_j + a_i^+ a_j^+)\sin^2\frac{\Delta\varphi}{2} + (a_i a_j^+ + a_i^+ a_j)\cos^2\frac{\Delta\varphi}{2} - (a_i^+ a_i + a_j^+ a_j)\cos\Delta\varphi, \end{aligned} \tag{2.38}$$

where the first line on the right side is the constant and one operator term. The semi-classical result of the scalar product $S(S+1)\cos\Delta\varphi$ is slightly larger than the constant term in 2.38, this is due to the zero point energy, which originates from the two operator terms. The one operator term can be seen as the torque between interacting spins in the ground state, thus this has to be zero in the proper ground state.

The a and a^+ bosonic operators represent excitations localized on magnetic moments. However in crystals where the interactions are periodic the solutions of the spin Hamiltonian are called spin-waves which are periodic in space and non localized. The spin-waves are harmonic deviations of the magnetic moments from the equilibrium position. The elementary excitation is called a magnon, which is a boson. The corresponding creation and annihilation operators can be expressed as the Fourier transformation of the

localized bosonic operators:

$$\begin{aligned} a_{\boldsymbol{k}}^{+} =& N^{-1/2} \sum_{\boldsymbol{l}} a_{\boldsymbol{l}}^{+} e^{-i\boldsymbol{k}\cdot(\boldsymbol{l}+\boldsymbol{d}_{\mathrm{a}})} \\ a_{\boldsymbol{k}} =& N^{-1/2} \sum_{\boldsymbol{l}} a_{\boldsymbol{l}} e^{i\boldsymbol{k}\cdot(\boldsymbol{l}+\boldsymbol{d}_{\mathrm{a}})}, \end{aligned} \tag{2.39}$$

where $\boldsymbol{l}$ runs over all lattice translation vectors, N is the number of unit cells in the crystal and d_{a} is the atomic position within the unit cell. The inverse transformations are:

$$\begin{aligned} a_{\boldsymbol{l}}^{+} =& N^{-1/2} \sum_{\boldsymbol{k}} a_{\boldsymbol{k}}^{+} e^{i\boldsymbol{k}\cdot(\boldsymbol{l}+\boldsymbol{d}_{\mathrm{a}})} \\ a_{\boldsymbol{l}} =& N^{-1/2} \sum_{\boldsymbol{k}} a_{\boldsymbol{k}} e^{-i\boldsymbol{k}\cdot(\boldsymbol{l}+\boldsymbol{d}_{\mathrm{a}})}. \end{aligned} \tag{2.40}$$

If there is more than one magnetic ion in the unit cell, Latin letters will denote the different spins: a, b, c etc. To Fourier transform any quadratic Hamiltonian the following two operator terms have to be transformed:

$$\begin{aligned} \sum_{\boldsymbol{l}} a_{\boldsymbol{l}} b_{\boldsymbol{l}+\Delta\boldsymbol{l}} =& \sum_{\boldsymbol{k}} a_{\boldsymbol{k}} b_{-\boldsymbol{k}} e^{-i\boldsymbol{k}\cdot(\boldsymbol{d}_{\mathrm{a}}-\boldsymbol{d}_{\mathrm{b}}-\Delta\boldsymbol{l})}, \\ \sum_{\boldsymbol{l}} a_{\boldsymbol{l}}^{+} b_{\boldsymbol{l}+\Delta\boldsymbol{l}} =& \sum_{\boldsymbol{k}} a_{\boldsymbol{k}}^{+} b_{\boldsymbol{k}} e^{i\boldsymbol{k}\cdot(\boldsymbol{d}_{\mathrm{a}}-\boldsymbol{d}_{\mathrm{b}}-\Delta\boldsymbol{l})}, \\ \sum_{\boldsymbol{l}} a_{\boldsymbol{l}} b_{\boldsymbol{l}+\Delta\boldsymbol{l}}^{+} =& \sum_{\boldsymbol{k}} a_{\boldsymbol{k}} b_{\boldsymbol{k}}^{+} e^{-i\boldsymbol{k}\cdot(\boldsymbol{d}_{\mathrm{a}}-\boldsymbol{d}_{\mathrm{b}}-\Delta\boldsymbol{l})}, \\ \sum_{\boldsymbol{l}} a_{\boldsymbol{l}}^{+} b_{\boldsymbol{l}+\Delta\boldsymbol{l}}^{+} =& \sum_{\boldsymbol{k}} a_{\boldsymbol{k}}^{+} b_{-\boldsymbol{k}}^{+} e^{i\boldsymbol{k}\cdot(\boldsymbol{d}_{\mathrm{a}}-\boldsymbol{d}_{\mathrm{b}}-\Delta\boldsymbol{l})}, \end{aligned} \tag{2.41}$$

where $\Delta\boldsymbol{l}$ is the distance of the unit cells of the two interacting moments, if they are in the same unit cell $\Delta\boldsymbol{l}$=0. The periodic form of Eq. 2.38 is the following:

$$\sum_{\boldsymbol{l}} S_{\boldsymbol{l}}^{(\mathrm{a})} S_{\boldsymbol{l}+\Delta\boldsymbol{l}}^{(\mathrm{b})}. \tag{2.42}$$

The spin on site (a) interacts with the spin on site (b) with a unit cell translation of $\Delta\boldsymbol{l}$.

Using Eq. 2.38 and Eq. 2.41 one gets:

$$\begin{aligned}\sum_{\boldsymbol{l}} S_{\boldsymbol{l}}^{(\mathrm{a})} S_{\boldsymbol{l}+\Delta\boldsymbol{l}}^{(\mathrm{b})}/S = \sum_{\boldsymbol{k}} \Big\{ &\left(a_{\boldsymbol{k}} b_{-\boldsymbol{k}} e^{-i\boldsymbol{k}\Delta\boldsymbol{r}} + a_{\boldsymbol{k}}^{+} b_{-\boldsymbol{k}}^{+} e^{i\boldsymbol{k}\Delta\boldsymbol{r}}\right) \sin^2 \frac{\Delta\varphi}{2} + \\ &+ \left(a_{\boldsymbol{k}} b_{\boldsymbol{k}}^{+} e^{-i\boldsymbol{k}\Delta\boldsymbol{r}} + a_{\boldsymbol{k}}^{+} b_{\boldsymbol{k}} e^{i\boldsymbol{k}\Delta\boldsymbol{r}}\right) \cos^2 \frac{\Delta\varphi}{2} - \\ &- \left(a_{\boldsymbol{k}}^{+} a_{\boldsymbol{k}} + b_{\boldsymbol{k}}^{+} b_{\boldsymbol{k}}\right) \cos\Delta\varphi \Big\},\end{aligned} \tag{2.43}$$

where $\Delta\boldsymbol{r} = \boldsymbol{d}_{\mathrm{a}} - \boldsymbol{d}_{\mathrm{b}} - \Delta\boldsymbol{l}$ is the distance vector separating the two spins and $\Delta\varphi$ is the angle between the two magnetic moment vectors:

$$\Delta\varphi = \varphi_0^{(\mathrm{a})} - \varphi_0^{(\mathrm{b})} - \boldsymbol{k}_{\mathrm{m}} \cdot \Delta\boldsymbol{l}. \tag{2.44}$$

To present Eq. 2.43 in a convenient matrix form, the following vectors will be introduced:

$$x_{\boldsymbol{k}} = \begin{bmatrix} a_{\boldsymbol{k}} \\ b_{\boldsymbol{k}} \\ a_{-\boldsymbol{k}}^{+} \\ b_{-\boldsymbol{k}}^{+} \end{bmatrix}, \quad x_{\boldsymbol{k}}^{\dagger} = \left[a_{\boldsymbol{k}}^{+} b_{\boldsymbol{k}}^{+} a_{-\boldsymbol{k}} b_{-\boldsymbol{k}}\right]. \tag{2.45}$$

Using these vectors, equation 2.43 can be rewritten in a matrix form:

$$\sum_{\boldsymbol{l}} S_{\boldsymbol{l}}^{(a)} S_{\boldsymbol{l}+\Delta\boldsymbol{l}}^{(b)} = \sum_{\boldsymbol{k}} \frac{S}{2} x_{\boldsymbol{k}}^{\dagger} \underline{M}_{\boldsymbol{k}} x_{\boldsymbol{k}}, \tag{2.46}$$

where $\underline{M}_{\boldsymbol{k}}$ is defined as:

$$\underline{M}_{\boldsymbol{k}} = \begin{bmatrix} A_{\boldsymbol{k}} & B_{\boldsymbol{k}} & 0 & D_{\boldsymbol{k}} \\ \overline{B}_{\boldsymbol{k}} & A_{\boldsymbol{k}} & \overline{D}_{\boldsymbol{k}} & 0 \\ 0 & D_{\boldsymbol{k}} & A_{\boldsymbol{k}} & B_{\boldsymbol{k}} \\ \overline{D}_{\boldsymbol{k}} & 0 & \overline{B}_{\boldsymbol{k}} & A_{\boldsymbol{k}} \end{bmatrix}. \tag{2.47}$$

The terms in the matrix are:

$$\begin{aligned} A_{\boldsymbol{k}} &= -\cos\Delta\varphi, \\ B_{\boldsymbol{k}} &= e^{i\boldsymbol{k}\Delta\boldsymbol{r}} \cos^2 \frac{\Delta\varphi}{2}, \\ D_{\boldsymbol{k}} &= e^{i\boldsymbol{k}\Delta\boldsymbol{r}} \sin^2 \frac{\Delta\varphi}{2}. \end{aligned} \tag{2.48}$$

The $\underline{M}_{\boldsymbol{k}}$ matrix is Hermitian and $\underline{M}_{\boldsymbol{k}} = \overline{\underline{M}}_{-\boldsymbol{k}}$.

The same matrix form can be developed for single ion anisotropy. If the magnetic ordering wavevector is incommensurate, only easy-plane anisotropy is solvable with the rotating coordinate system method. In this case the spins are lying in this easy-plane and the anisotropy energy is independent of the φ_{i} angle of the spin. The easy-plane anisotropy has the following form:

$$\mathcal{H}_{\mathrm{aniso}} = D_{\mathrm{aniso}} S^{\mathrm{x}2}, \tag{2.49}$$

where $D_{\mathrm{aniso}} > 0$. This can be expressed by the magnon operators:

$$D_{\mathrm{aniso}} \sum_{\boldsymbol{l}} S_{\boldsymbol{l}}^{(\mathrm{a})\mathrm{x}} S_{\boldsymbol{l}}^{(\mathrm{a})\mathrm{x}} / S = \frac{D_{\mathrm{aniso}}}{2} \sum_{\boldsymbol{k}} a_{\boldsymbol{k}}^2 + 2 a_{\boldsymbol{k}}^{+} a_{\boldsymbol{k}} + a_{\boldsymbol{k}}^{+2}. \tag{2.50}$$

The $\underline{M}_{\boldsymbol{k}}$ matrix of the interaction is defined as in Eq. 2.46:

$$\underline{M}_{\boldsymbol{k}} = D_{\mathrm{aniso}} \begin{bmatrix} 1 & 1 \\ 1 & 1 \end{bmatrix}. \tag{2.51}$$

The Dzyaloshinskii-Moriya interaction can be treated as well. The Hamiltonian is solvable if the DM vector is perpendicular to the spin rotation plane. In this case the interaction can be written as:

$$\mathcal{H}_{\mathrm{DM}} = D^{\mathrm{x}} (S_{\mathrm{i}} \times S_{\mathrm{j}})_{\mathrm{x}} = D^{\mathrm{x}} (S_{\mathrm{i}}^{\mathrm{y}} S_{\mathrm{j}}^{\mathrm{z}} - S_{\mathrm{i}}^{\mathrm{z}} S_{\mathrm{j}}^{\mathrm{y}}). \tag{2.52}$$

and for the lattice as a whole:

$$\mathcal{H}_{\mathrm{DM}} = D^{\mathrm{x}} \sum_{\boldsymbol{l}} \left(S_{\boldsymbol{l}}^{(a)} \times S_{\boldsymbol{l}+\Delta\boldsymbol{l}}^{(b)} \right)_{\mathrm{x}}. \tag{2.53}$$

After substitution of the magnon operators and keeping the quadratic terms only, the following matrix is obtained:

$$\mathcal{H}_{\mathrm{DM}} = \sum_{\boldsymbol{k}} \frac{S}{2} x_{\boldsymbol{k}}^{\dagger} \underline{M}_{\boldsymbol{k}} x_{\boldsymbol{k}}, \tag{2.54}$$

$$\underline{M}_{\boldsymbol{k}} = \begin{bmatrix} A_{\boldsymbol{k}} & B_{\boldsymbol{k}} & 0 & D_{\boldsymbol{k}} \\ \overline{B}_{\boldsymbol{k}} & A_{\boldsymbol{k}} & D_{\boldsymbol{k}} & 0 \\ 0 & \overline{D}_{\boldsymbol{k}} & A_{\boldsymbol{k}} & \overline{B}_{\boldsymbol{k}} \\ \overline{D}_{\boldsymbol{k}} & 0 & B_{\boldsymbol{k}} & A_{\boldsymbol{k}} \end{bmatrix}.$$

The elements of the $\underline{M_{\boldsymbol{k}}}$ matrix are:

$$\begin{aligned} A_{\boldsymbol{k}} =& -\sin\Delta\varphi, \\ B_{\boldsymbol{k}} =& \frac{1}{2}e^{i\boldsymbol{k}\Delta\boldsymbol{r}}\sin\Delta\varphi, \\ D_{\boldsymbol{k}} =& -\frac{1}{2}e^{i\boldsymbol{k}\Delta\boldsymbol{r}}\sin\Delta\varphi. \end{aligned} \tag{2.55}$$

If there are several interactions in the unit cell, the above calculated $\underline{M_{\boldsymbol{k}}}$ matrices have to be tiled together to construct the matrix form of the spin Hamiltonian $\underline{H_{\boldsymbol{k}}}$. The size of the $\underline{H_{\boldsymbol{k}}}$ matrix is twice the number of magnetic atoms in the unit cell and the x magnon operator contains the operators (a, b, c, etc.) and their complex conjugate for each magnetic atom in the unit cell. The time independent solutions can be obtained by diagonalising the Hamiltonian. This occurs through a transformation to a new basis of operators such that:

$$x = \underline{T}x', \tag{2.56}$$

where the matrix $\underline{T}$ describes the transformation to the new basis. [47] The transformation matrix is not necessarily unitary, since the new and old basis vector have to fulfil the following commutation relation:

$$\left[x, x^\dagger\right] \equiv xx^\dagger - x^{\dagger\intercal}x^\intercal = \underline{g}, \tag{2.57}$$

where $\underline{g}$ is a diagonal matrix:

$$\underline{g} = \begin{bmatrix} \mathbb{1} & 0 \\ 0 & -\mathbb{1} \end{bmatrix}. \tag{2.58}$$

$\underline{T}$ can be found by solving the following eigenvalue problem:

$$\underline{g}\underline{H}\underline{T} = \underline{T}\underline{g}\underline{H}', \tag{2.59}$$

where $\underline{H}'$ is a diagonal matrix and its diagonal elements are the magnon dispersions: $\omega_{\mathrm{i}}(\boldsymbol{k})$. Each calculated magnon mode is doubly degenerate in the absence of a magnetic field. To solve the eigenvalue problem a new matrix $\underline{V}$ is defined, which contains the

eigenvectors of $\underline{gM}$. The matrix of eigenvectors has to be normalized as follows:

$$\underline{V}' = \underline{V}\sqrt{\left(\underline{gV}^{\dagger}\underline{gV}\right)^{-1}}. \tag{2.60}$$

Then the diagonal $\underline{H}'$ can be obtained from the following equation:

$$\underline{H}' = \underline{gV}'^{-1}\underline{gHV}'. \tag{2.61}$$

It can be shown that all diagonal elements of $\underline{H}'$ are real, even though the matrix $\underline{gH}$ is not, in general, Hermitian. [47]

2.4.1.2 Dynamic correlation function

It will be shown in Eq. 3.32 of the next chapter, that neutron scattering measures directly the spin-spin correlation functions $S^{\mathrm{xx}}(\boldsymbol{k},\omega)$, $S^{\mathrm{yy}}(\boldsymbol{k},\omega)$ and $S^{\mathrm{zz}}(\boldsymbol{k},\omega)$. [48] They can be expressed using Fermi's golden rule:

$$S^{\mathrm{xx}}(\boldsymbol{k},\omega) = \sum_{\lambda} |\langle\lambda|S^{\mathrm{x}}(\boldsymbol{k})|0\rangle|^2\delta(\omega + E_0 - E_\lambda), \tag{2.62}$$

where $|0\rangle$ is the ground state, $|\lambda\rangle$ is an excited state, E_0 and E_λ are the energies of these states respectively and $S^{\mathrm{x}}(\boldsymbol{k})$ is the Fourier transform of S^{x}. The $\langle\lambda|$ state is an excited state with one magnon, e.g. $\langle 0|a'(\boldsymbol{k})$, where the operators of the normal modes are used. The lowest order operator expression in $S^{\mathrm{x}}(\boldsymbol{k})$ with non-zero expectation value are the one operator terms. $S^{\mathrm{x}}(\boldsymbol{k})$ is defined as:

$$S^{\mathrm{x}}(\boldsymbol{k}) = \sum_{\#\in\{a,b,\ldots\}} N^{-1/2}\sum S_{\boldsymbol{l}}^{(\#)\mathrm{x}} e^{i\boldsymbol{k}\cdot(\boldsymbol{l}+\boldsymbol{d}_{\#})}. \tag{2.63}$$

The first summation runs over all sites in the unit cell, shown by the sublattice symbols a, b. The S^{x} operator can be expressed by the magnon operators using Eq. 2.33, 2.34 and 2.37 and assuming two sites per unit cell:

$$S^{\mathrm{x}}(\boldsymbol{k}) = \sqrt{\frac{S}{2}}(a_{\boldsymbol{k}} + b_{\boldsymbol{k}} + a^{+}_{-\boldsymbol{k}} + b^{+}_{-\boldsymbol{k}}) = \sqrt{\frac{S}{2}}\begin{bmatrix}1 & 1 & 1 & 1\end{bmatrix}\cdot x. \tag{2.64}$$

For incommensurate structures the Fourier transform of the y and z spin components are equal up to a complex phase, since the magnetic moments are equally distributed

along y and z directions. They can be expressed with the magnon operators as well:

$$S^{\mathrm{y}}(\boldsymbol{k}) = S^{\mathrm{z}}(\boldsymbol{k}) = \frac{1}{2}\left[S^{\eta}(\boldsymbol{k}+\boldsymbol{k}_{\mathrm{m}}) + S^{\eta}(\boldsymbol{k}-\boldsymbol{k}_{\mathrm{m}})\right], \tag{2.65}$$

where $S^{\eta}(\boldsymbol{k})$ is the spin component along η direction:

$$S^{\eta}(\boldsymbol{k}) = -i\sqrt{\frac{S}{2}}(a_{\boldsymbol{k}} + b_{\boldsymbol{k}} - a^{+}_{-\boldsymbol{k}} - b^{+}_{-\boldsymbol{k}}) = -i\sqrt{\frac{S}{2}}\begin{bmatrix}1 & 1 & -1 & -1\end{bmatrix}\cdot x. \tag{2.66}$$

After substitution into Eq. 2.62 one gets:

$$S^{\mathrm{xx}}(\boldsymbol{k},\omega) = \frac{S}{2}|\sum_{i,j} T_{\mathrm{ij}}(\boldsymbol{k})|^2\delta(\omega-\omega_{\mathrm{j}}(\boldsymbol{k})), \tag{2.67}$$

where T_{ij} is the (i,j) element of the $\underline{T}$ transformation matrix. Similarly the η correlation function is:

$$S^{\eta\eta}(\boldsymbol{k},\omega) = \frac{S}{2}|\sum_{\mathrm{i,j}} -1^{\mathrm{i+1}} T_{\mathrm{ij}}(\boldsymbol{k})|^2\delta(\omega-\omega_{\mathrm{j}}(\boldsymbol{k})). \tag{2.68}$$

The inplane component of the correlation function is therefore:

$$S^{\mathrm{yy}}(\boldsymbol{k}) = S^{\mathrm{zz}}(\boldsymbol{k}) = \frac{1}{4}\left[S^{\eta\eta}(\boldsymbol{k}+\boldsymbol{k}_{\mathrm{m}}) + S^{\eta\eta}(\boldsymbol{k}-\boldsymbol{k}_{\mathrm{m}})\right]. \tag{2.69}$$

The method presented here can be readily adapted to numerically calculate spin-wave dispersion and dynamic correlation functions for any combination of the above interactions and incommensurate ordering wavevectors. For commensurate ordering wavevectors, the calculation of the correlation functions is slightly different, since $S^{\mathrm{yy}}(\boldsymbol{k})$ and $S^{\mathrm{zz}}(\boldsymbol{k})$ are not equal.

2.4.1.3 Triangular lattice

As an example of the presented numerical method for calculating spin-wave dispersion in incommensurate structures, the dispersion of the two dimensional triangular lattice is calculated. This example is important because it is the starting model for the fitting of the inelastic neutron spectra of the distorted triangular lattice α-$CaCr_2O_4$.

The spin-wave dispersion of the triangular antiferromagnet can be calculated exactly using a rotating coordinate system and a single magnetic atom in the unit cell. [49, 50] Using hexagonal lattice vectors and assuming that the triangular lattice is in the ab

plane, the single twofold degenerate mode has the dispersion of:

$$\omega(\boldsymbol{k}) = 3JS\sqrt{(1-\gamma(\boldsymbol{k}))(1+2\gamma(\boldsymbol{k}))}, \tag{2.70}$$

where $\gamma(\boldsymbol{k})$ is the Fourier transform of the interactions:

$$\gamma(\boldsymbol{k}) = \frac{1}{3}\left(\cos(2\pi k_{\mathrm{x}} + 2\pi k_{\mathrm{y}}) + \cos(2\pi k_{\mathrm{x}}) + \cos(2\pi k_{\mathrm{y}})\right. . \tag{2.71}$$

The components of $\boldsymbol{k}$ are in reciprocal lattice units. This dispersion is plotted on Fig. 2.6 as a black line.

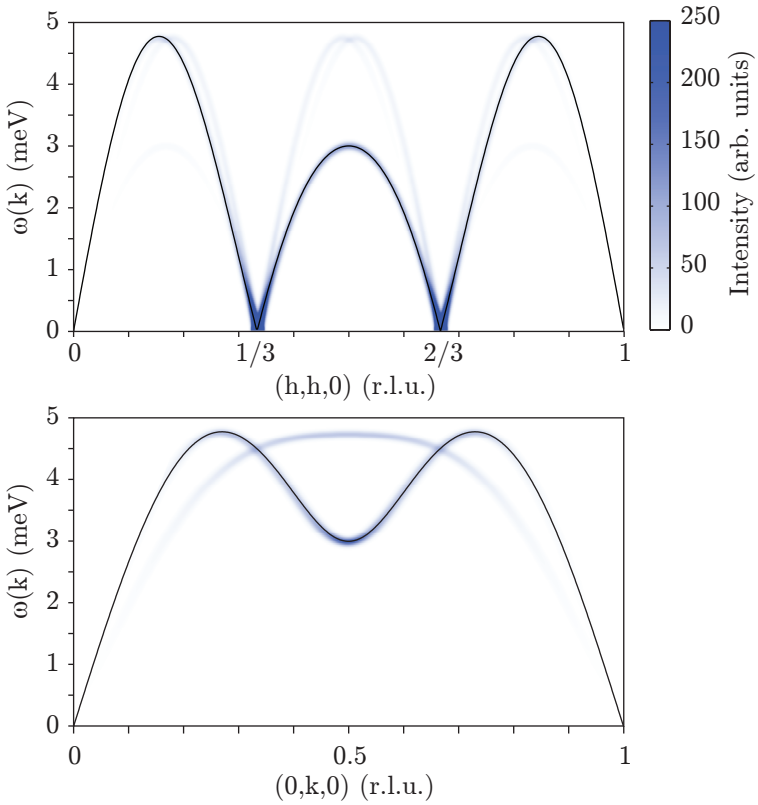

Figure 2.6: Comparison of linear spin-wave dispersion calculations for the two dimensional triangular lattice. Black line denotes the $\gamma(\boldsymbol{k})$ dispersion, blue lines denote the result of the numerical calculation and the colour gives the value of each component of the spin-spin correlation functions.

For the numerical calculation also single atom unit cell is assumed, thus the size of the $\underline{H}_{\boldsymbol{k}}$ matrix of the spin Hamiltonian is 2x2. The 4x4 matrix of the Heisenberg interaction

shrinks to 2x2, since the interacting spin are on the same site:

$$\underline{M}_{\boldsymbol{k}} = 2 \begin{bmatrix} A_{\boldsymbol{k}} + \operatorname{Re} B_{\boldsymbol{k}} & \operatorname{Re} D_{\boldsymbol{k}} \\ \operatorname{Re} D_{\boldsymbol{k}} & A_{\boldsymbol{k}} + \operatorname{Re} B_{\boldsymbol{k}} \end{bmatrix}. \tag{2.72}$$

This matrix has to be summed over the six nearest-neighbour interactions and divided by two to get the Hamiltonian. It can then be used to obtain the dispersion and correlation functions. The resulting spin-spin dynamical correlation functions are plotted on Fig. 2.6 in blue where the darkness of the shading indicates the scattering intensity. Although there is a single dispersion, the neutron structure factor reproduces it three times shifted by the ordering wavevector. The blue line which overlaps with the $\omega(\boldsymbol{k})$ dispersion is the $S^{\mathrm{xx}}(\boldsymbol{k},\omega)$ out of spiral-plane mode, the other modes polarised in the spiral-plane: $S^{\mathrm{yy}}(\boldsymbol{k},\omega)$ and $S^{\mathrm{zz}}(\boldsymbol{k},\omega)$.

3 Experimental techniques

Several experimental technique was used for the investigation of α-$CaCr_2O_4$, β-$CaCr_2O_4$ and Sr_2VO_4. The first experiments for each materials were magnetic susceptibility and heat capacity measurements. These can reveal phase transitions and the nature of the magnetic ground state. Several different types of neutron diffraction and X-ray diffraction were used to determine the crystal structure and long-range ordered magnetic structure if present. Inelastic neutron scattering was performed on each compound. It allows one to explore magnetic and lattice excitations throughout the Brillouin zone. The following sections describe the physical background and the operation of the most often used experimental techniques. Further details can be found in the following books and references therein. [51, 52, 53, 54, 55] Detailed descriptions of the specific instruments can be found in the references after each section.

3.1 Diffraction

Diffraction is a powerful method to determine crystal structures and long range ordered magnetic structures. The basic principle of diffraction is that waves (e.g. neutrons, X-ray) can scatter on localized potential (atoms, magnetic moment) without changing wavelength. It is called Rayleigh scattering for electromagnetic waves. The scattered waves from different objects with the same wavelength undergo constructive or destructive interference depending on wavelength and the positions of the potentials. In case of a periodic potential the Bragg's law gives the condition of constructive interference:

$$\begin{aligned} \boldsymbol{k}_\mathrm{f} - \boldsymbol{k}_\mathrm{i} &= \boldsymbol{\tau}, \\ |\boldsymbol{k}_\mathrm{f}| &= |\boldsymbol{k}_\mathrm{i}|, \end{aligned} \tag{3.1}$$

where $\boldsymbol{k}_\mathrm{f}$ and $\boldsymbol{k}_\mathrm{i}$ are the scattered and incident wave vectors (since they have equal magnitude k denotes the absolute value), $\boldsymbol{\tau}$ is a reciprocal lattice vector. A simple explanation for Bragg's law says that the path length difference dl between two plane waves diffracted from different crystallographic planes has to be a multiple of the wavelength λ to get constructive interference and strong scattering, see Fig. 3.1. If one changes one

of the parameters (crystal orientation, wavelength, scattering angle) strong scattering is observed when Eq. 3.1 is fulfilled, the peak in the detector as a function of the parameter is called the Bragg peak.

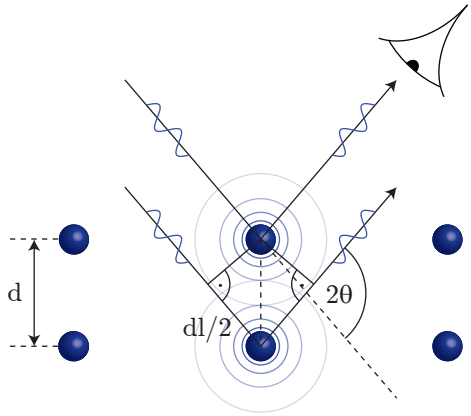

Figure 3.1: Bragg diffraction on crystallographic planes, dl denotes the path length difference between two plane wave diffracted from different crystallographic planes, d is the spacing between the two planes and 2θ is the angle between incident and reflected wave, the eye symbolizes the detector. Constructive interference happens if $dl/2 = n\lambda$.

The scattering problem can be generalized to arbitrary scattering system. The scattering cross section characterizes the interaction of the scattering system and the scattered wave. On the detector, the scattered wave amplitude appears as countable particles (photon, neutron). Suppose there is a detector measuring the number of scattered particles per second in a given direction as a function of its energy. The distance of the detector from the sample is large in comparison to the scattering system size. Using polar coordinates, the incident beam is along the polar axis and the detector measures the scattered beam along (θ, φ) direction. The partial differential cross-section is defined by the equation:

$$\frac{d^2\sigma}{d\Omega dE'} = \frac{\begin{array}{c}\text{Scattered particles per second into the solid angle } d\Omega \\ \text{in the energy range } (E', E' + dE')\end{array}}{\Phi d\Omega dE'}, \tag{3.2}$$

where Φ is the incident flux, i.e. particle number per area per time, the unit of the cross section is area. The partial differential cross-section depends on the structure of the scatterer and the type of scattering process. The scattering is elastic if the energy of the incident and scattered particles are the same, in this case the energy derivation

can be omitted.
The differential cross-section can be calculated for elastic scattering on periodic structures (crystals) at zero temperature:

$$\frac{d\sigma}{d\Omega} = N\frac{(2\pi)^3}{\nu_0}\sum_{\boldsymbol{\tau}}\delta(\boldsymbol{\kappa}-\boldsymbol{\tau})|F_{\mathrm{N}}(\boldsymbol{\kappa})|^2, \tag{3.3}$$

$$F_{\mathrm{N}}(\boldsymbol{\kappa}) = \sum_{\mathrm{d}} f_{\mathrm{d}}(\boldsymbol{\kappa})\exp(i\boldsymbol{\kappa}\cdot\boldsymbol{d}), \tag{3.4}$$

where N is the number of unit cells in the crystal, ν_0 is the volume of the unit cell, the sum runs over all $\boldsymbol{\tau}$ reciprocal lattice vectors. $\boldsymbol{\kappa} = \boldsymbol{k}_{\mathrm{i}} - \boldsymbol{k}_{\mathrm{f}}$ is the scattering vector, $F_{\mathrm{N}}(\boldsymbol{\kappa})$ is the nuclear unit cell structure factor, where the summation over d is over all the atoms in the unit cell and $f_{\mathrm{d}}(\boldsymbol{\kappa})$ is the atomic form factor of these atoms. Equation 3.3 and 3.4 not only give the direction of the Bragg scattering but also its intensity. In case of Bravais lattices, the above equations give the same condition for scattering as the Bragg's law. The atomic form factor carries all the microscopic details of the scattering and it depends on the interaction between the ion and the scatterer.

3.1.1 X-ray diffraction

X-rays are electromagnetic waves with wavelength between 0.1 Å to 100 Å, this range covers the typical atomic distances in solids. Therefore crystal structures can be investigated using X-ray diffraction. X-rays scatter strongly from the electrons. The important process here is the charge scattering, where the varying electric field of the X-ray accelerates the electrons, which then radiate X-rays of the same frequency. This radiation is the scattered wave. The atomic form factor for charge scattering is:

$$f(\boldsymbol{\kappa}) = \int \rho(\boldsymbol{r})e^{i\boldsymbol{\kappa}\cdot\boldsymbol{r}}d^3\boldsymbol{r}, \tag{3.5}$$

where $\rho(\boldsymbol{r})$ is the spatial density of electrons about the centre of mass of an atom. Since the total scattering of an atom $f(0)$ is proportional to its atomic number, X-rays scatter only weakly from light elements like hydrogen and oxygen. Besides elastic scattering, atoms absorb X-ray strongly. There are threshold energies, so called absorption edges, above which atoms absorb X-ray strongly. These edges correspond to energy differences between filled and empty electronic shells. For measuring diffraction, X-ray energies well below the first absorption edge are the most suitable. X-ray scattering cross sections for selected atoms are given in Tab. 3.1.
X-ray diffraction of α-$CaCr_2O_4$ and Sr_2VO_4 was measured on ID31 high-resolution

powder-diffraction beamline [56, 57] at the European Synchrotron Radiation Facility (ESRF), Grenoble, France. Beside a Bruker D8 type laboratory X-ray diffractometer [58] was used to determine the quality of powder samples. To orient single crystals for further experiments, a Laue apparatus with a white X-ray beam was used.

3.1.2 Neutron diffraction

The de Broglie wavelength of thermal neutrons is in the range of the interatomic distances in solids due to the specific value of the neutron mass. Therefore diffraction with thermal neutrons can yield information on the structure of solids. Neutrons have no charge, which means there is no strong Coulomb repulsion between the nucleus and the neutron, thus neutrons can approach the core close enough to interact via the short range nuclear force. Furthermore neutrons possess a magnetic dipole moment, which interacts with the magnetic field created by the electron cloud. This interaction allows the study of static magnetic properties of solids by neutron diffraction.

3.1.2.1 Nuclear scattering

The range of the interaction between the neutron and the nucleus (10^{-15} m) is much smaller than the typical wavelength of the thermal neutron thus the nuclei can be considered as point scatterer. As can be shown classically, a point scatterer has a constant form factor. For nuclear scattering of neutrons the scattering length b is defined, which is the amplitude of the scattered neutron wave, it has the dimension of length. For the chemical elements relevant for this thesis, the scattering length is a positive real number independent of the neutron energy, see Tab. 3.1. The cross section of a single nucleus can be calculated from the scattering length:

$$\sigma_{nuc} = 4\pi b^2. \tag{3.6}$$

If a crystal contains more than one isotope of a given element with random spatial distribution, the scattering length averaged over the isotopes can be used in the cross section formula, this is called coherent scattering cross section:

$$\sigma_{\mathrm{coh}} = 4\pi(\bar{b})^2. \tag{3.7}$$

Since this cross section is smaller than the sum of the cross section of individual isotopes, the incoherent scattering cross section accounts for the missing scattered intensity:

$$\sigma_{\text{inc}} = 4\pi \left[\overline{b^2} - (\overline{b})^2\right]. \tag{3.8}$$

These incoherently scattered neutrons don't show interference effects, thus the scattering is isotropic, independent of direction. The absolute values of scattering cross sections for neutrons have the same order of magnitude as that of X-ray. To determine the

Element	$\sigma^{\text{n}}_{\text{coh}}$ (barn)	$\sigma^{\text{n}}_{\text{inc}}$ (barn)	$\sigma^{\text{n}}_{\text{abs}}$ (barn)	σ^{x} (barn)
O	4.232(6)	0.000(8)	0.00019(2)	5.1
Cr	1.660(6)	1.83(2)	3.05(6)	45.7
V	0.01838(2)	5.08(6)	5.08(4)	42.0

Table 3.1: Neutron [59] and X-ray [60] scattering cross sections for elements important for this thesis. The neutron absorption cross-section is given for a wavelength of 1.798 Å, while the X-ray wavelength is assumed to be 0.4 Å.

intensity of a Bragg peak some experimental parameter has to be varied to pass through the condition $\boldsymbol{\kappa} = \boldsymbol{\tau}$. Due to the finite instrumental resolution, the δ-function in the theoretical cross section is measured as a peak with finite width as a function of the varying parameter. There are three conventional methods of measuring diffraction.

For the Laue method neutrons with a continuous range of wavelengths are incident on a single crystal. The scattered neutrons are recorded on a two dimensional position sensitive detector around the sample, Fig. 3.2 shows the schematic experimental arrangement. The angle between the $\boldsymbol{\tau}$ reciprocal lattice vector of the crystal and the incident beam is denoted by Ψ. For a fixed Ψ, there is always a k wave vector which fulfils the scattering condition:

$$k = \frac{\tau}{2\cos\Psi}. \tag{3.9}$$

The scattering angle is $2\theta = \pi - 2\Psi$. If the flux of the incident neutrons between λ and $\lambda + d\lambda$ is $\phi(\lambda)d\lambda$, then the number of neutrons per second in the scattered beam is:

$$P = \frac{V}{\nu_0}\phi(\lambda)\frac{\lambda^4}{2\sin^2\theta}|F_{\text{N}}(\boldsymbol{\tau})|^2, \tag{3.10}$$

where $V = N\nu_0$ is the volume of the crystal.

In the rotating single crystal method of measuring a Bragg peak a monochromatic beam of neutrons is incident on the crystal that is rotated around an axis perpendicular to the

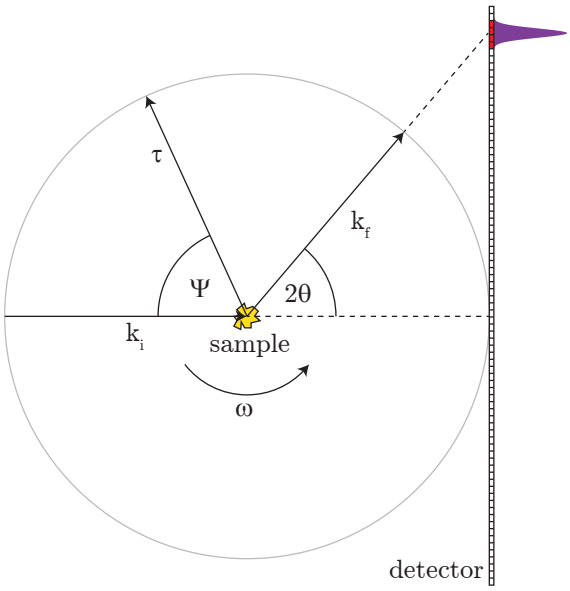

Figure 3.2: Schematic experimental arrangement for diffraction. The angle between incident $\boldsymbol{k}_\mathrm{i}$ and scattered $\boldsymbol{k}_\mathrm{f}$ beam is 2θ, the angle between incident beam and $\boldsymbol{\tau}$ reciprocal lattice vector is Ψ. The purple Gaussian is the signal on the position sensitive detector if the scattering condition $\boldsymbol{k}_\mathrm{f} - \boldsymbol{k}_\mathrm{i} = \boldsymbol{\tau}$ is fulfilled. For single crystal diffraction the sample is rotated around the vertical axis (normal to the paper) by ω angle.

scattering plane. The rotation of the crystal means the variation of the Ψ angle. The detector is positioned at a fixed 2θ angle. The scattering condition is fulfilled if $\boldsymbol{\tau}$ is in the scattering plane and:

$$\tau = 2k \sin\theta. \tag{3.11}$$

If Φ is the flux of the incident neutrons, the integrated number of scattered neutrons per second is:

$$P = \frac{V}{\nu_0} \Phi \frac{\lambda^3}{\sin 2\theta} |F_\mathrm{N}(\boldsymbol{\tau})|^2. \tag{3.12}$$

In the powder method of measuring diffraction a monochromatic neutron beam scatters from a polycrystalline sample. For a specific value of $\boldsymbol{\tau}$ the scattered neutrons lies on a cone, called the Debye–Scherrer cone. The detector is usually position sensitive in the scattering plane covering an extended range of 2θ angle. At a certain 2θ angle only those microcrystals contribute to the scattering whose $\boldsymbol{\tau}$ lie on a cone with axis along $\boldsymbol{k}_\mathrm{i}$ and

the angle between $\boldsymbol{\tau}$ and $\boldsymbol{k}_\mathrm{i}$ is $2\Psi = \pi - 2\theta$. The counting rate on the detector is:

$$P = \frac{V}{\nu_0^2}\Phi\frac{\lambda^3}{4\sin\theta}\frac{d}{2\pi r\sin 2\theta}\sum_{\boldsymbol{\tau}}|F_\mathrm{N}(\boldsymbol{\tau})|^2, \tag{3.13}$$

where d is the diameter of the detector, r is the sample detector distance. Thus the detector intercepts $d/(2\pi r\sin 2\theta)$ of the neutrons of the Debye-Scherrer cone.

3.1.2.2 Magnetic scattering

Magnetic scattering is due to the electromagnetic interaction between the magnetic moment of the neutron and the magnetic field generated by the electrons in the sample. The magnetic field in the sample originates from the intrinsic magnetic moment of the electron ($1\mu_\mathrm{B}$) and from its orbital motion. The cross section of the magnetic scattering is comparable to the cross section of an electron calculated from its classical radius $r_0 \approx 2.818\cdot 10^{-15}$ m. The proper value is given by $(\gamma r_0)^2$, where $\gamma \sim 1.913$ is the ratio between the magnetic moment of the neutron and the nuclear magneton. This gives a cross section of 0.29 barn for a single electron, which is comparable to the nuclear cross sections ranging from 0.02 to 29.3 barn for vanadium and gadolinium respectively. However for non-zero momentum transfer the magnetic intensity becomes weaker due to the momentum transfer dependence of the magnetic form factor $F_\mathrm{M}(\boldsymbol{\kappa})$. Since the atomic electrons are distributed on orbitals with sizes in the Ångstrom range, which is comparable to the wavelength of the neutron, the magnetic form factor decreases strongly over the range of a few Å^{-1}. The magnetic form factors of the two magnetic ions investigated in this thesis are plotted on Fig. 3.3.

The elastic magnetic scattering measures the static spin-spin correlation function $\langle S_0^\alpha\rangle\langle S_{\boldsymbol{l}}^\beta\rangle$, where α and β denote the $\{x, y, z\}$ components of the spin and $\boldsymbol{l}$ is a lattice translation vector. For magnetically ordered crystals, the order is characterized by the magnetic ordering wave vector $\boldsymbol{k}_\mathrm{m}$. Magnetic Bragg scattering occurs when:

$$\boldsymbol{\kappa} = \boldsymbol{\tau} \pm \boldsymbol{k}_\mathrm{m}. \tag{3.14}$$

If $\boldsymbol{k}_\mathrm{m} = 0$ the magnetic Bragg reflections overlap with the nuclear ones, if $\boldsymbol{k}_\mathrm{m} \neq 0$ the magnetic reflections appear as pair of satellites around the nuclear reflections. The operator describing the interaction between a neutron and ordered magnetic structure is $\boldsymbol{\sigma}\cdot\boldsymbol{M}_\perp(\boldsymbol{\kappa})$, where $\boldsymbol{\sigma}$ is the neutron spin operator and $\boldsymbol{M}_\perp(\boldsymbol{\kappa})$ is the magnetic interaction vector defined as the perpendicular component of the magnetic structure factor to the

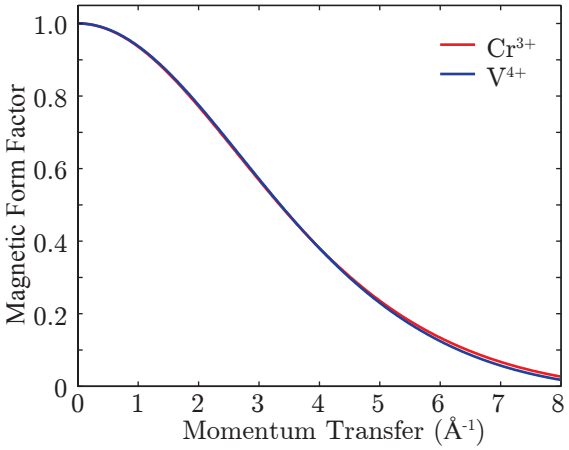

Figure 3.3: Magnetic form factor $F_{\mathrm{M}}(\boldsymbol{q})$ as a function of momentum transfer, plotted for Cr^{3+} and V^{4+}.

scattering vector $\boldsymbol{\kappa}$:

$$\boldsymbol{M}_{\perp}(\boldsymbol{\kappa}) = \hat{\boldsymbol{\kappa}} \times \boldsymbol{M}(\boldsymbol{\kappa}) \times \hat{\boldsymbol{\kappa}}. \tag{3.15}$$

$\boldsymbol{M}(\boldsymbol{\kappa})$ is the Fourier transform of the magnetisation:

$$\boldsymbol{M}(\boldsymbol{\kappa}) = \int \boldsymbol{M}(\boldsymbol{r}) \exp(-i\boldsymbol{\kappa} \cdot \boldsymbol{r}) dr^3. \tag{3.16}$$

Thus the neutron interacts only with the component of the magnetisation perpendicular to the scattering vector. For unpolarized incident neutrons, where $\langle \boldsymbol{\sigma}_{\mathrm{i}} \rangle = 0$, the scattering cross section has to be averaged over the incident neutron spins.

The elastic neutron scattering cross section can be easily calculated for different ordered structures. Since α-$CaCr_2O_4$ and β-$CaCr_2O_4$ develops helical structure at low temperatures, the cross section for this structure will be developed here. Lets assume the spins are in the xy plane, then the components of the spins are:

$$\begin{aligned} \langle S_{\boldsymbol{l}}^{\mathrm{x}} \rangle &= \langle S \rangle \cos(\boldsymbol{k}_{\mathrm{m}} \cdot \boldsymbol{l}), \\ \langle S_{\boldsymbol{l}}^{\mathrm{y}} \rangle &= \langle S \rangle \sin(\boldsymbol{k}_{\mathrm{m}} \cdot \boldsymbol{l} + \varphi_0), \\ \langle S_{\boldsymbol{l}}^{\mathrm{z}} \rangle &= 0. \end{aligned} \tag{3.17}$$

where φ_0 is zero for a helical structure and $\pi/2$ for a sinusoidally modulated structure.

The scattering cross section is:

$$\left(\frac{d\sigma}{d\Omega}\right)_{mag} = (\gamma r_0)^2 \left(\frac{1}{2} g F(\boldsymbol{\kappa})\right)^2 \exp(-2W) I, \tag{3.18}$$

$$I = \frac{N}{4} \frac{(2\pi)^3}{\nu_0} \langle S \rangle^2 (1 + \hat{\kappa}_z^2) \sum_{\boldsymbol{\tau}} \{\delta(\boldsymbol{\kappa} + \boldsymbol{k}_m - \boldsymbol{\tau}) + \delta(\boldsymbol{\kappa} - \boldsymbol{k}_m - \boldsymbol{\tau})\},$$

where W is the Debye-Waller factor, $\hat{\kappa}_z$ is the z component of the normalized $\boldsymbol{\kappa}$ vector. The $(1 + \hat{\kappa}_z^2)$ factor is doubled if $\boldsymbol{\kappa} \parallel z$ is compared to $\boldsymbol{\kappa} \perp z$ since in the first case both x and y components of the spin contributes to the magnetic scattering while in the latter case only one of the components. It can be shown that the φ_0 phase information is lost in the cross section, which means the helical and sinusoidal structures cannot be distinguished by unpolarised neutron scattering.

Single-crystal neutron diffraction of α-$CaCr_2O_4$ was measured on the E5 4-circle diffractometer [61] at HZB which utilises the rotating crystal method. It was also measured on E2 Flat-Cone Diffractometer [61] at HZB. Furthermore neutron powder diffraction of α-$CaCr_2O_4$, β-$CaCr_2O_4$ and Sr_2VO_4 was measured on different powder diffractometers: E9 fine resolution powder diffractometer [61] at HZB, D20 high-intensity two-axis diffractometer [62] at ILL, D1a high-resolution powder diffractometer [63] at ILL. This data allowed the crystal and magnetic structures of these compounds to be determined.

3.1.2.3 Spherical neutron polarimetry

It was shown in the previous section, that unpolarised neutron scattering can be utilised to determine magnetic structures. However the determination of the magnetic structure from the measured Bragg intensities is not unambiguous since the phase information is lost. This makes it difficult to directly distinguish helical and sinusoidal structures or multiple domain and single domain structures. Furthermore if the nuclear and magnetic reflections overlap, the separation of the magnetic scattering from the nuclear scattering can be also difficult.

To overcome these problems polarised neutron diffraction is developed. Polarisation analysis implies that an initially polarised beam is scattered by a sample and the polarisation of the scattered beam is measured. The extra information provided by the polarisation analysis can reveal the missing phase information of the magnetic structure and efficient separation of magnetic and nuclear scattering can be achieved. Since neutron sources produce unpolarised beam, it has to be polarised first. The most common polarisers are a Heusler alloy monochromator, ^{3}He filter and polarizing supermirror. [64] The most control over polarisation is provided by the spherical neutron polarimeter. [52]

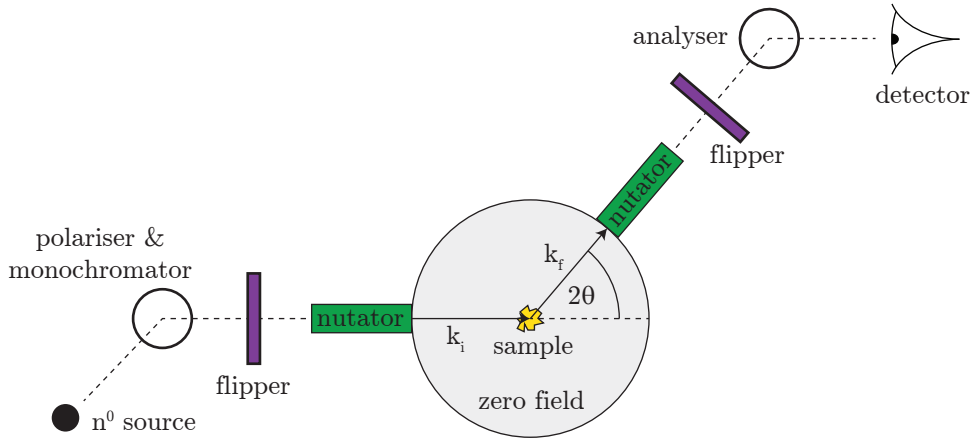

Figure 3.4: Schematic setup of a spherical neutron polarimeter. Grey region around the sample has zero magnetic field.

In this instrument the polarisation of the incident neutrons can be set to any direction and the final polarisation can be analysed along any direction. To achieve this the incident beam is polarised along a fixed direction usually vertical and afterwards magnetic fields within the nutator rotate the neutron spins to the desired direction. The sample is in a zero magnetic field chamber to avoid the uncontrolled precession of the neutron spin during the scattering process. The polarisation of the scattered neutrons is rotated again to the desired orientation and the final polarisation is measured by a fixed analyser similar to the polariser, see fig. 3.4. To measure the beam polarisation the counts are recorded in a detector for the on and off state of the spin flipper. The polarisation of the beam along a specific direction is defined as:

$$P = \frac{n^+ - n^-}{n^+ + n^-}, \tag{3.19}$$

where n^+ and n^- are the number of neutron in the beam parallel and anti-parallel (flipper on and off) to the selected direction respectively. In the following a right handed coordinate system is used, where the x axis is parallel to the momentum transfer $\boldsymbol{\kappa}$, z is vertical and y perpendicular to both. The result of the polarisation analysis can be expressed in terms of polarisation dependent cross sections, $\sigma^{\mathrm{i}\to\pm\mathrm{j}}$, where i and j denote one of the axes, $\pm$ denotes whether the beam is analysed parallel or anti-parallel to the incident beam polarisation. In general there are 36 cross sections, but only 18 measured

by using only one spin flipper. The polarisation matrix of the sample is defined as:

$$\mathsf{P}_{\mathrm{ij}} = \frac{\sigma^{\mathrm{i}\to\mathrm{j}} - \sigma^{\mathrm{i}\to-\mathrm{j}}}{\sigma^{\mathrm{i}\to\mathrm{j}} + \sigma^{\mathrm{i}\to-\mathrm{j}}}. \tag{3.20}$$

The P_{ij} elements can be measured with higher precision than the individual cross sections, since most of the non-magnetic background is cancelled out with the subtraction. For neutron diffraction, the P_{ij} matrix is determined by the nuclear and magnetic structure factors. The relation is described by the Blume-Maleev equations. [65] The polarisation of the scattered beam is:

$$\begin{aligned}\boldsymbol{P}_{\mathrm{f}} I =& \boldsymbol{P}_{\mathrm{i}}(NN^* - \boldsymbol{M}_\perp \cdot \boldsymbol{M}_\perp^*) + \boldsymbol{M}_\perp(\boldsymbol{P}_{\mathrm{i}} \cdot \boldsymbol{M}_\perp^*) \\ &+ \boldsymbol{M}_\perp^*(\boldsymbol{P}_{\mathrm{i}} \cdot \boldsymbol{M}_\perp) + \boldsymbol{M}_\perp N^* + \boldsymbol{M}_\perp^* N \\ &- i\boldsymbol{P}_{\mathrm{i}} \times (\boldsymbol{M}_\perp N^* - \boldsymbol{M}_\perp^* N) + i(\boldsymbol{M}_\perp \times \boldsymbol{M}_\perp^*),\end{aligned} \tag{3.21}$$

and the scattered beam intensity is:

$$I = NN^* + \boldsymbol{M}_\perp \cdot \boldsymbol{M}_\perp^* + \boldsymbol{P}_{\mathrm{i}} \cdot \boldsymbol{M}_\perp N^* + \boldsymbol{P}_{\mathrm{i}} \cdot \boldsymbol{M}_\perp^* N - i\boldsymbol{P}_{\mathrm{i}} \cdot (\boldsymbol{M}_\perp \times \boldsymbol{M}_\perp^*), \tag{3.22}$$

where N denotes the nuclear structure factor $F_{\mathrm{N}}(\boldsymbol{\kappa})$, $\boldsymbol{M}_\perp$ is the magnetic interaction vector $\boldsymbol{M}_\perp(\boldsymbol{\kappa})$. Using the previously defined coordinate system and assuming the incoming polarisation vector is parallel to one of the three axes and if the nuclear structure factor is zero (true if the magnetic ordering wave vector is non-integer) the polarisation matrix can be expressed as the following 3×3 matrix:

$$\mathsf{P} = \begin{bmatrix} -\frac{M_\perp^2 P_{\mathrm{x}} + J_{\mathrm{yz}}}{M_\perp^2 + P_{\mathrm{x}} J_{\mathrm{yz}}} & 0 & 0 \\ -\frac{J_{\mathrm{yz}}}{M_\perp^2} & \frac{-M_\perp^2 + R_{\mathrm{yy}}}{M_\perp^2} P_{\mathrm{y}} & \frac{R_{\mathrm{zy}}}{M_\perp^2} P_{\mathrm{y}} \\ -\frac{J_{\mathrm{yz}}}{M_\perp^2} & \frac{R_{\mathrm{zy}}}{M_\perp^2} P_{\mathrm{z}} & \frac{-M_\perp^2 + R_{\mathrm{zz}}}{M_\perp^2} P_{\mathrm{z}} \end{bmatrix}, \tag{3.23}$$

with:

$$\begin{aligned} M_\perp^2 =& \boldsymbol{M}_\perp \cdot \boldsymbol{M}_\perp^*, \\ J_{\mathrm{ij}} =& 2\Im(M_{\perp\mathrm{i}} \cdot M_{\perp\mathrm{j}}^*), \\ R_{\mathrm{ij}} =& 2\Re(M_{\perp\mathrm{i}} \cdot M_{\perp\mathrm{j}}^*). \end{aligned} \tag{3.24}$$

From this form of the polarisation matrix, some simple rules of polarised neutron scattering can be easily deduced:

1. If the magnetic structure has non-zero vector chirality: $\sum \boldsymbol{S}_\mathrm{i} \times \boldsymbol{S}_\mathrm{j} \neq 0$, which is true for helical magnetic structures, there are terms in P independent of the incoming polarisation. These terms are responsible for the polarisation of the unpolarized beam and the physical basis of producing polarised neutron beam.

2. The P_{xx} element for magnetic scattering is usually spin-flip and close to -1.

3. If $\boldsymbol{M}_\perp$ and $\boldsymbol{M}_\perp^*$ are parallel ($J_\mathrm{ij} = 0$), the $\boldsymbol{P}_\mathrm{i}$ incoming polarisation is rotated 180° around the magnetic interaction vector.

3.1.2.4 Magnetic domains

If several magnetic domains coexist in the sample, the individual cross sections for all spin processes have to be calculated independently. Each cross section is the weighed sum of the cross sections of the different domains. The polarisation matrix is then to be calculated from these cross sections. If $\boldsymbol{M}_\perp$ and $\boldsymbol{M}_\perp^*$ are parallel this is equivalent to the direct weighed addition of the polarisation matrices of the different domains. There are several different types of magnetic domains:

1. Configuration domains: "configuration domains exist whenever the propagation vector $\boldsymbol{k}_\mathrm{m}$ describing the magnetic structure is not transformed either into itself, or itself plus a reciprocal lattice vector, by all the symmetry operators of the paramagnetic group". [52]

2. 180° domains: "180° domains correspond to regions of crystal in which the moments are related by the time inversion operator". [52]

3. Orientation domains: "orientation domains occur whenever a magnetic structure cannot be described by a magnetic space group which is congruent with that describing the configurational symmetry". [52] In case of orthorhombic space groups and helical magnetic structure this means configuration domains exist if any of the two principal axis of the moment ellipsis are not parallel to the crystal axes.

4. Chirality domains: "chirality domains can occur whenever the paramagnetic space group is centrosymmetric but the ordered magnetic structure is not". [52] The magnetic structure can be non-centrosymmetric if the moments related by the centre are noncollinear. In this case, J_yz and J_zy are non-zero, and the P_{xy} and P_{xz} are non-zero and have opposite sign for the two chirality domains. If they have equal population, the two elements cancel each other.

3.1.2.5 Example polarisation matrix

This example shows, how to calculate the polarisation matrix for a 120° helical magnetic structure. This was found to be the structure of α-$CaCr_2O_4$ using spherical neutron polarimetry. It is also the structure typical of an undistorted triangular lattice. If the plane of the spins is determined by $\boldsymbol{v}$ and $\boldsymbol{u}$ orthogonal vectors, the magnetisation of this structure can be written as:

$$\boldsymbol{M}(\boldsymbol{r}) = \boldsymbol{M_v} \sin(\boldsymbol{k}_\mathrm{m} \cdot \boldsymbol{r}) + \boldsymbol{M_u} \cos(\boldsymbol{k}_\mathrm{m} \cdot \boldsymbol{r}), \tag{3.25}$$

where $\boldsymbol{M_v}$ and $\boldsymbol{M_u}$ are the projection of the magnetization. Using the standard hexagonal unit cell, the ordering wave vector is $\boldsymbol{k}_\mathrm{m} = (1/3, 1/3, 0)$ if the ab plane is the triangular plane. Assuming $|\boldsymbol{M_v}| = |\boldsymbol{M_u}| = M_0$, the Fourier transform of the magnetisation:

$$\boldsymbol{M(\kappa)} = 4\pi^3 M_0 \left[(-i\boldsymbol{u} + \boldsymbol{v})\delta(\boldsymbol{\kappa} - \boldsymbol{k}_\mathrm{m} + \boldsymbol{\tau}) + (i\boldsymbol{u} + \boldsymbol{v})\delta(\boldsymbol{\kappa} + \boldsymbol{k}_\mathrm{m} + \boldsymbol{\tau})\right]. \tag{3.26}$$

For a $\boldsymbol{\kappa} = \boldsymbol{\tau} \pm \boldsymbol{k}_\mathrm{m}$ reflection $\boldsymbol{M}(\boldsymbol{\kappa})$ vector has to be transformed to the $\boldsymbol{\kappa}$ dependent $\{x, y, z\}$ coordinate system: $\boldsymbol{M'}(\boldsymbol{\kappa})$, then the components of the magnetic interaction vector are $\boldsymbol{M}_\perp = (0, \boldsymbol{M'}(\boldsymbol{\kappa})_\mathrm{y}, \boldsymbol{M'}(\boldsymbol{\kappa})_\mathrm{z})$. For the opposite chirality domain $\boldsymbol{M}_\perp(\boldsymbol{\kappa}) = \boldsymbol{M}_\perp(\boldsymbol{\kappa})^*$. To experimentally differentiate between the helical structure and the collinear sinusoidally modulated structure, where the moment along $\boldsymbol{v}$ and $\boldsymbol{u}$ are in phase, it is enough to measure the polarisation matrix for a magnetic reflection along $\boldsymbol{\kappa} \parallel \boldsymbol{u} \times \boldsymbol{v}$. The result is:

$$\mathsf{P}^\mathrm{hel} = \begin{bmatrix} -\frac{2}{1+P_\mathrm{x}} & 0 & 0 \\ \pm 1 & 0 & 0 \\ \pm 1 & 0 & 0 \end{bmatrix}, \qquad \mathsf{P}^\mathrm{sin} = \begin{bmatrix} -\frac{2}{1+P_\mathrm{x}} & 0 & 0 \\ 0 & 0 & 0 \\ 0 & 0 & 0 \end{bmatrix}, \tag{3.27}$$

where P_x is the incoming beam polarisation along $\boldsymbol{\kappa}$, the $\pm$ sign denote the matrix element value for the two chirality domains. In case of non equal chirality populations the measurement of P enables to determine whether the magnetic structure is helical or sinusoidal. Whereas if the two chiral domains have equal population the chiral terms are averaged to zero and other reflections have to be measured. For a general $\boldsymbol{\kappa}$ vector, the magnetic interaction vectors are the following:

$$\begin{aligned} \boldsymbol{M}_\perp^\mathrm{hel} &= (0, A_1 \pm iA_2, B_1 \pm iB_2), \\ \boldsymbol{M}_\perp^\mathrm{sin} &= (0, A_1 + A_2, B_1 + B_2), \end{aligned} \tag{3.28}$$

where ± denotes the two opposite helical chirality. Assuming that the helical structure has equally populated chirality domains, the elements of P can be calculated. For example the P_{zy} element:

$$\mathsf{P}_{zy}^{hel} = \left\langle \frac{R_{zy}}{M_\perp^2} \right\rangle_{\text{chirality}} = \frac{A_1B_1 + A_2B_2}{A_1^2 + A_2^2 + B_1^2 + B_2^2}, \tag{3.29}$$

$$\mathsf{P}_{zy}^{sin} = \frac{R_{zy}}{M_\perp^2} = \frac{(A_1 + A_2)(B_1 + B_2)}{A_1^2 + A_2^2 + B_1^2 + B_2^2}, \tag{3.30}$$

this shows that we can differentiate between equally populated chiral helical structure and collinear sinusoidally modulated structure. In case of orthorhombic symmetry the sinusoidally modulated structure usually has other orientation domains. For example it is possible that the two equally populated sinusoidal domain have the interaction vector of $\boldsymbol{M}_{\perp\text{sin}} = (0, A_1 \pm A_2, B_1 \pm B_2)$, this would produce the same polarisation matrix as the helical structure.
Spherical neutron polarimetry of α-$CaCr_2O_4$ was measured on TASP triple axis spectrometer using MuPAD [66] at the Paul Scherrer Institute (PSI), Switzerland.

3.2 Neutron spectroscopy

The energy of thermal neutrons is of the same order as that of many different excitations of condensed matter systems. If a neutron during the scattering process creates or annihilates a quasi-particle e.g. phonon, the transferred energy is comparable to the initial neutron energy, thus precise measurement of this energy change and the excitation energy is possible. In comparison to photons with same energy, neutrons carry enough momentum to excite quasi-particles throughout the Brillouin zone. Because of these properties inelastic neutron scattering is the only technique able to map out the four dimensional space of energy and wave vector space in the range which is important for solid state physics.
To describe the inelastic scattering process, Bragg's law (see Eq. 3.1) has to be generalised:

$$\begin{aligned} \frac{\hbar^2}{2m}\left(\boldsymbol{k}_\text{i}^2 - \boldsymbol{k}_\text{f}^2\right) &= \hbar\omega(\boldsymbol{q}), \\ \boldsymbol{k}_\text{i} - \boldsymbol{k}_\text{f} &= \boldsymbol{\tau} + \boldsymbol{q}. \end{aligned} \tag{3.31}$$

These equations describe the process when the scattered neutron creates a quasi-particle with a momentum of $\boldsymbol{q}$ and energy of $\hbar\omega(\boldsymbol{q})$. If the energy and momentum of the incident

and scattered neutron is measured, the $\hbar\omega(\boldsymbol{q})$ dispersion can be mapped out.
The topic of this thesis is magnetism, thus the magnetic excitations of solids measured with inelastic neutron scattering will be discussed in more details here. Neutron scattering of phonons can be described with similar formalism. The excitations of magnetically ordered systems considered here are magnons. The magnetic neutron scattering measures the spin-spin correlation function:

$$\frac{d^2\sigma}{d\Omega dE} = (\gamma r_0)^2 \frac{k_\mathrm{f}}{k_\mathrm{i}} \left(\frac{1}{2} g F_\mathrm{M}(\boldsymbol{\kappa})\right)^2 \exp(-2W) \sum_{\alpha,\beta}^{\{x,y,z\}} (\delta_{\alpha\beta} - \hat{\kappa}_\alpha \hat{\kappa}_\beta)\, S^{\alpha\beta}(\boldsymbol{\kappa}, \omega). \tag{3.32}$$

This is the generalized formula of the magnetic scattering, the $k_\mathrm{f}/k_\mathrm{i}$ factor is due to the conversion from the energy dependence of the cross section to wave vector dependence. $S^{\alpha\beta}(\boldsymbol{\kappa}, \omega)$ is the space and time Fourier transform of the time-dependent spin-spin correlation function:

$$S^{\alpha\beta}(\boldsymbol{\kappa}, \omega) = \sum_{i,j} \exp\left(i\boldsymbol{\kappa} \cdot (\boldsymbol{r}_\mathrm{i} - \boldsymbol{r}_\mathrm{j})\right) \int_{\infty}^{\infty} \exp(i\omega t) \left\langle S_\mathrm{i}^{\alpha}(0) S_\mathrm{j}^{\beta}(t) \right\rangle dt. \tag{3.33}$$

In the previous chapter the spin-spin correlation function was calculated from spin-wave theory. However neutrons do not directly measure the calculated correlation functions, because the scattering cross section is non-zero only for spin waves with polarisation perpendicular to the scattering wave vector. This is expressed by the $(\delta_{\alpha\beta} - \hat{\kappa}_\alpha \hat{\kappa}_\beta)$ term in Eq. 3.32.

3.2.1 Triple-axis spectrometer

The triple-axis spectrometer (TAS) is used with steady-state neutron sources. Its construction allows independent control of the incident and scattered neutron's energy and the momentum transfer to the sample. [54] A typical TAS setup is shown on Fig. 3.5. The triple axis spectrometer consists of three arms with connections bendable in the horizontal plane. These are monochromator-sample, sample-analyser and analyser-detector. The angles between them are controlled mechanically.
The emitted "white" beam from the neutron source is transported to the monochromator by a neutron guide, which minimizes the neutron loss by reflecting them on the inside walls. The monochromator is a single crystal with large mosaic, which diffracts the different wavelength neutrons along different directions via Bragg reflection. The angle of the monochromator selects neutrons with a narrow energy and wave vector range k_i. The most common monochromator material for cold neutrons is pyrolytic graphite,

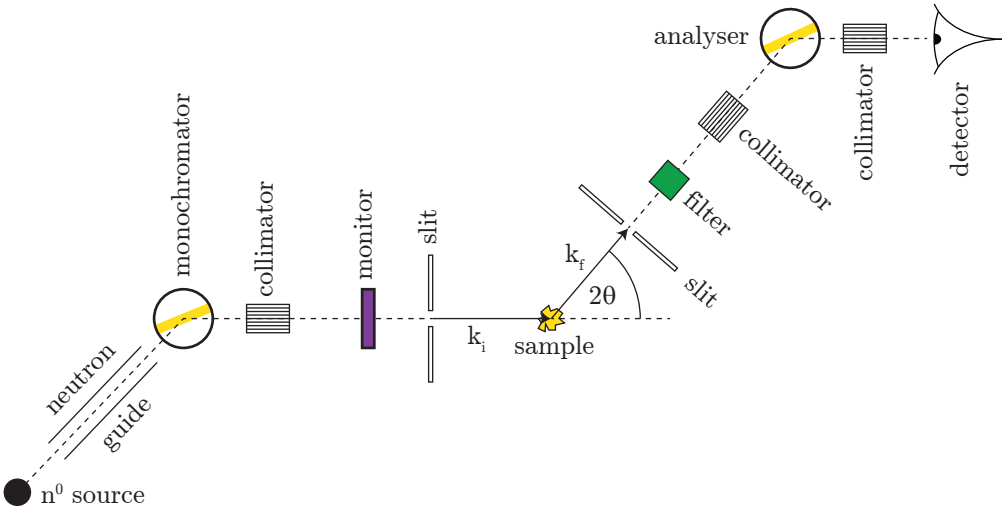

Figure 3.5: Schematic setup of a typical triple axis spectrometer, with a (−/+/−) configuration.

which has large cross section for the (0,0,2) reflection, however neutrons with $2k_\mathrm{i}$ are also scattered in the same direction, due to the non-zero (0,0,4) Bragg-reflection. The monitor after the collimator records the incident beam intensity, this is necessary since the intensity can fluctuate with time and also varies as a function of the incident neutron energy. The slit before the sample acts like an aperture, the neutrons which would miss the sample are absorbed by the slit thus the background signal on the detector is reduced. The second slit and collimator after the sample selects neutrons scattered by the sample with a selected 2θ value. The filter after the second slit absorbs the higher order neutrons which can be present in the incident beam. The analyser after the sample is similar to the monochromator, it selects the final wave vector k_f of the neutrons. An additional collimator between detector and analyser can be applied to suppress background and increase resolution. The neutrons with the selected $(k_\mathrm{i}, k_\mathrm{f}, 2\theta)$ values are counted in the detector.

The typical TAS measuring technique is the so called fixed k_f scan, when the size of k_f is kept constant and k_i is varied. This is achieved by fixing the analyser angle and simultaneously varying the monochromator angle and the sample 2θ. The most common scans are constant energy transfer and constant momentum transfer scans. For constant energy transfer, both k_f and k_i are fixed and the 2θ angle of the sample is varied along with the sample angle Ψ. For constant momentum transfer scan the energy transfer is varied, for this both k_i and the sample 2θ have to be changed in a controlled manner.

In this thesis the TAS instruments V2 (FLEX) cold neutron 3-axis spectrometer [67] at HZB and PUMA thermal triple axis spectrometer [68] at FRM2 were used to study the spin-wave spectra of α-$CaCr_2O_4$.

3.2.2 Time-of-flight spectrometer

Time-of-flight (TOF) neutron spectrometers are operated on pulsed neutron beam. The beam is either provided by a pulsed neutron source (spallation source) or by a chopper system which cuts out pulses from a continuous neutron beam. TOF spectrometers are ideal to measure isotropic samples, non-dispersive excitations and to obtain an overview of the excitation spectra in an extended volume of the four dimensional reciprocal space - energy transfer space. [53] It is also effective to measure low dimensional systems, since the directions along which the excitations are non-dispersing can be integrated out, that increases the signal to noise ratio. On the other hand it is less suitable for measuring three dimensional dispersion and for parametric studies.

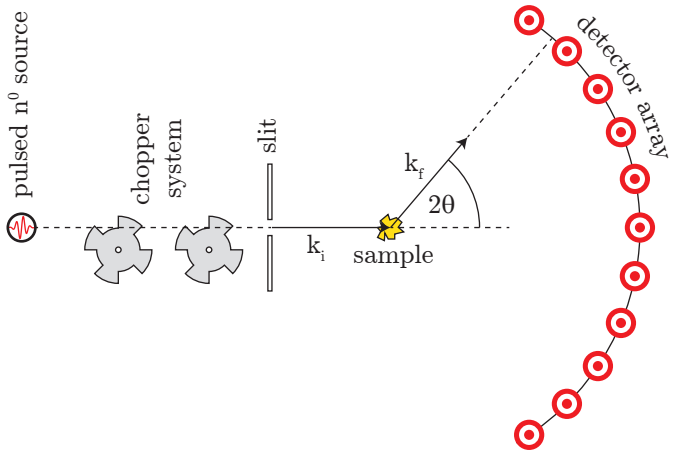

Figure 3.6: Schematic setup of a typical time-of-flight spectrometer.

The basic principle of the TOF spectrometer is the ability of measuring the energy of the neutron by measuring the time it takes to reach the detector from a reference point. By knowing the distance and the elapsed time the speed and energy of the neutron can be calculated. Precise measurement is possible since thermal neutrons are “slow”, the typical speed is 2000 m/s and flight times of the order of ms, which can be easily measured by current electronic timers. The typical TOF spectrometer consists of a chopper system which selects the incident neutron energy and bandwidth and a large evacuated detector chamber with the sample in the centre and area sensitive detectors

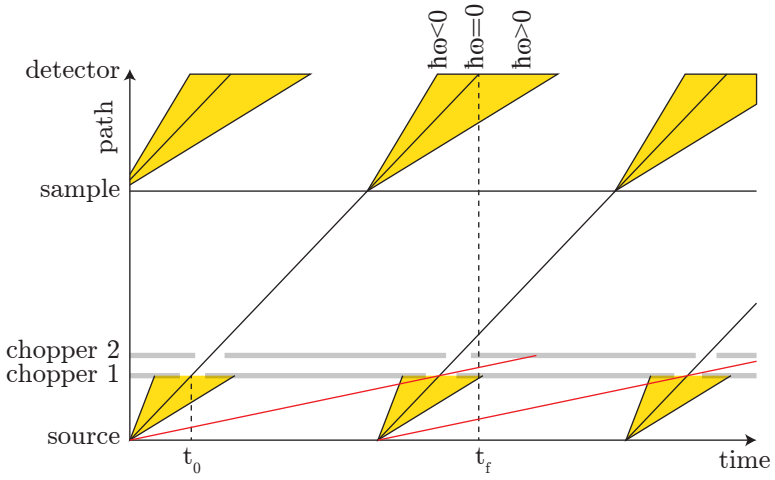

Figure 3.7: Neutron path as a function of time. Grey lines with the opening are the choppers, which lets through the neutrons periodically. Red line show neutrons from the previous pulse which are absorbed by the second chopper. Yellow triangles symbolise the broad velocity range of neutrons coming from the source and after inelastically scattered in the sample.

covering the walls, see Fig. 3.6. The choppers are fast rotating disks made of neutron absorbing material with small windows, that periodically let the neutrons pass through. Figure 3.7 shows the path of the neutrons as a function of time. The pulsed source emits thermalised neutrons with broad energy distribution. When the first chopper opens, the virtual timer starts and runs until this neutron reaches one of the detectors. The first chopper is phased with respect to the pulsed source to select neutrons with a certain speed. There is often a second chopper to prevent slow neutrons of previous pulse from getting through. There can be more choppers to precisely control the energy resolution. After the chopper system a slit is used to cut out the background. After the neutrons scatter on the sample, they are counted by the area sensitive detectors covering a large 2θ range. From the time stamp of the detection and the 2θ angle of the detector pixel, the final energy and momentum of the neutron can be calculated. The measured dataset is three dimensional, the two position coordinate of the detector pixels plus the time dimension. To measure the full reciprocal space and energy transfer, the sample has to be rotated around a vertical axis, this variable angle is the fourth dimension. The recorded dataset is then converted into reciprocal and energy transfer space. To visualise and manipulate the large dataset, advanced visualisation softwares have been developed, e.g. the Horace program. [69]

In this thesis the TOF instruments ARCS wide angular-range chopper spectrometer [70]

at SNS, CNCS cold neutron chopper spectrometer [71] at SNS, Merlin [72] at ISIS are used to measure the excitation spectra of α-$CaCr_2O_4$. Furthermore Sr_2VO_4 was measured on NEAT [73] at HZB to investigate the dimer excitation energies and β-$CaCr_2O_4$ was measured on IN4 thermal neutron time-of-flight spectrometer at ILL to determine the magnetic excitation spectra.

3.3 Magnetic susceptibility

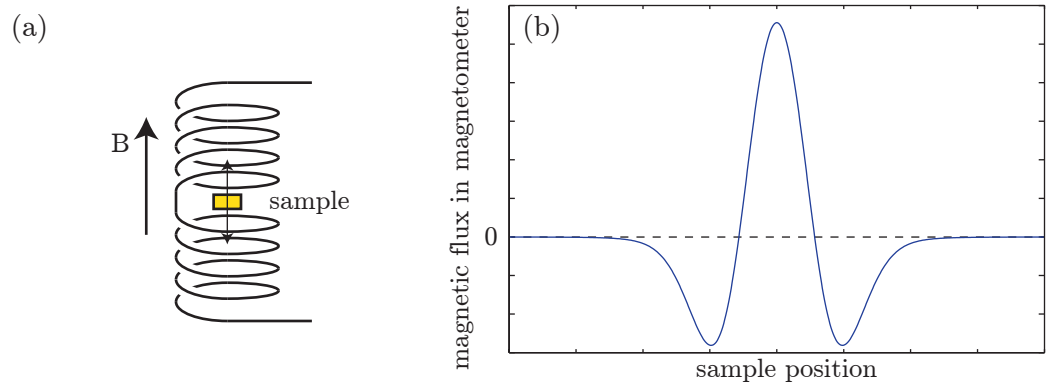

Figure 3.8: (a) Pick-up coil of a magnetometer, the sample moves vertically, while the external magnetic field is also vertical. (b) Magnetic flux in the pick-up coil as a function of sample position, assuming a magnetic dipole.

Instruments that measure temperature dependent magnetic susceptibility and field dependent magnetisation in a wide temperature and field range are commercially available and they provide valuable information about magnetic properties of novel materials. To measure magnetisation in an external magnetic field, the variation of the external field at the sample position is necessary. A special pick-up coil is used to filter out the homogeneous external field while being able to measure the inhomogeneous field of the sample. The simplest magnetometer which fulfils this task is the two coil gradient magnetometer, which has two coils wound in opposite directions, see Fig. 3.8(a). The spatially homogeneous external field would induce opposite electric field in the two coils thus cancelling each other, while a small sample which can be approximated by a magnetic dipole induces different electric fields in the two coils. The typical magnetic flux as a function of sample position is shown on Fig. 3.8(b). There are two methods of measuring the induced electric field. For small values of sample magnetisation and low temperatures the highly sensitive superconducting quantum interference device (SQUID) is coupled

inductively to the pick-up coil. The SQUID device is a superconducting ring with two Josephson junction in the two arms. When a biasing current is driven through the ring the voltage oscillates if the magnetic flux changes in the ring. One oscillation belongs to the increase of the field by one flux quantum $\Phi_0 = h/2e = 2.07 \cdot 10^{-15}$ Tm^2 in the ring. To measure the change of the sample magnetisation, the external magnetic field is swept and the change of the magnetic flux in the pick-up coil is measured via the SQUID. Another susceptibility measurement technique is the vibrating sample magnetometer (VSM). In this device the sample is resonating in the centre of the pick-up coil and the induced current in the pick-up coil is measured by a lock-in amplifier to increase the signal to noise ratio. This method is less sensitive to the magnetic moment but faster when compared to the SQUID detection.
The magnetic susceptibility of α-$CaCr_2O_4$ was measured by both methods, using the VSM option of the physical property measurement system (PPMS) and using the magnetic property measurement system (MPMS), both made by Quantum Design. Both instruments are part of the MagLab at Helmholtz-Zentrum Berlin (HZB). The MPMS can measure susceptibility in the range of 1.8 K and 400 K up to 5 T magnetic field, the VSM option of PPMS can measure from 1.8 K up to 1000 K and up to 14 T magnetic field. The combined use of the two device enable to measure magnetic susceptibility with high sensitivity and an extended temperature and magnetic field range.

3.4 Heat capacity

Heat capacity was measured in the PPMS using the adiabatic relaxation method. For the measurement the sample is glued to the microcalorimeter platform and put into high vacuum to avoid uncontrolled heat exchange. The principle of the measurement is the following. The starting point is a thermalised sample at a particular temperature. First a small heater on the platform heats the sample for fixed time. After the heater is switched off the system relaxes adiabatically back to the initial temperature and the relaxation time constant is measured. The heat capacity can be obtained from the relaxation time constant and the known heat conductivity between the sample platform and the constant temperature environment. [74] Repeating the same measurement at different temperatures of the cryostat yields the $C(T)$ temperature dependent heat capacity.

4 Nuclear and magnetic structure of α-$CaCr_2O_4$

In frustrated antiferromagnets (AF) the magnetic interactions compete and it is impossible to satisfy them all simultaneously. This competition suppresses long range magnetic order to temperatures well below the Curie-Weiss temperature [75]. Most frustrated magnets do eventually order and in the case of Heisenberg interactions a compromise is often reached where the magnetic interactions are all partially satisfied by a non-collinear arrangement of the magnetic moments. This ground state can be highly degenerate leading to exotic physical states like spin liquid behaviour or chiral order. The simplest frustrated system is the triangular lattice antiferromagnet where all magnetic interactions between nearest neighbours (J_{nn}) are equal. In their pioneering work, Anderson and Fazekas suggested that the ground state is a spin liquid with no long-range magnetic order for spin-1/2 systems. [27, 76] However, recent theoretical work implies that at T=0 it develops long-range order [77] with a helical structure, where the spin moments on nearest neighbours point 120° with respect to each other. Interactions between the planes can stabilize this ground state at finite temperatures.

Among real triangular lattice materials the 120° structure has been found in $CsFe(SO_4)_2$, $RbFe(SO_4)_2$ [78], VX_2 (X=Cl, Br, I) [79], $CuCrO_2$ [80], Ag_2NiO_2 [81] and $RbFe(MoO_4)_2$ [82]. Unfortunately, these compounds only exist in polycrystalline form or as small single-crystals limiting the possibilities of experimental investigation. Additional terms in the spin Hamiltonian can favour different magnetic structures or even destroy long range order. For example single-ion anisotropy favours collinear order ($CuFeO_2$ [83], α-$NaMnO_2$ [84]); frustrated interlayer interactions suppress order ($AgCrO_2$ [85], $NaCrO_2$ [86]) and strong exchange striction drive the system away from 120° helical magnetism (α-$NaMnO_2$ [87], $CuCrS_2$ [88, 89]).

Departures from ideal triangular crystal symmetry typically lead to spatially anisotropic exchange interactions sometimes accompanied by orbital ordering and resulting in the frustration being lifted. In most cases the spatial distortion reduces the dimensionality, so that one of the three nearest neighbour exchange interactions (J_{nn1}) is stronger than

the other two (J_{nn2}), and together the intraplanar interactions produce antiferromagnetic chains with frustrated interchain interactions, see Fig. 4.1. The magnetic structure is often helical but where the angle between nearest neighbours along the chain takes a value between 120° and 180°.

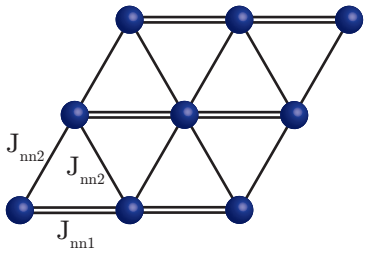

Figure 4.1: Typical spatially anisotropic triangular lattice with two different exchange interactions.

Examples of such compounds are Cs_2CuCl_4 where J_{nn2}/J_{nn1}=0.33 and the angle between intrachain neighbours is 170° [90], while for α-$NaMnO_2$ the presence of single ion anisotropy along with the ratio J_{nn2}/J_{nn1}=0.44 gives rise to collinear antiferromagnetic order. [84, 87] A third example is $CuCrO_2$, a multiferroic compound where a small lattice distortion accompanies the transition to long-range magnetic order. This along with substantial next nearest neighbour and frustrated interplane interactions, results in angles between nearest neighbours of 118° and 120°. [91, 92]

α-$CaCr_2O_4$ is a distorted triangular lattice antiferromagnet. However the distortion is very different from those investigated previously. The triangular layers of Cr^{3+}ions are only slightly distorted with four different nearest neighbour distances. They build up two zig-zag and two chain patterns running along the c-axis. This special distortion and competing next nearest neighbour interactions (as in $CuCrO_2$) makes α-$CaCr_2O_4$ a good compound for studying frustration effects on the physics of an antiferromagnet.

α-$CaCr_2O_4$ is a relatively unexplored compound. The room temperature crystal structure was determined by Pausch et al. in 1974 [93] using laboratory X-ray diffractometer. For the atomic positions see Tab. 4.2. The compound belongs to the delafossite aristotype, which has a general composition of $A^+B^{3+}O_2$, named after the delafossite mineral $CuFeO_2$. [94] The B cations build up triangular layers, which can be distorted, by being shortened one nearest neighbour direction. The oxygen atoms form edge-sharing octahedra around the B cation, while A cations lie between the BO_2 layers, see Fig. 4.2(a). The calcium in α-$CaCr_2O_4$ energetically favours the +2 ionic state, which can be achieved in the delafossite structure, if every second A cation position is vacant, see Fig. 4.2(b). This

doubles the unit cell along the a and b directions and due to the large ionic radius the hexagonal symmetry is broken. The resulting crystal symmetry is orthorhombic $Pmmn$ and each triangular layer contains 4 Cr^{3+} ions in the unit cell. Due to this extended unit cell, the atoms have more freedom in choosing their positions, thus there are four different distances between nearest neighbour Cr^{3+} ions compared to two distances in the simple "isosceles triangle-type" distortion found in delafossites. [92, 95] The interlayer distances are also different for the four magnetic atoms due to the distortion.

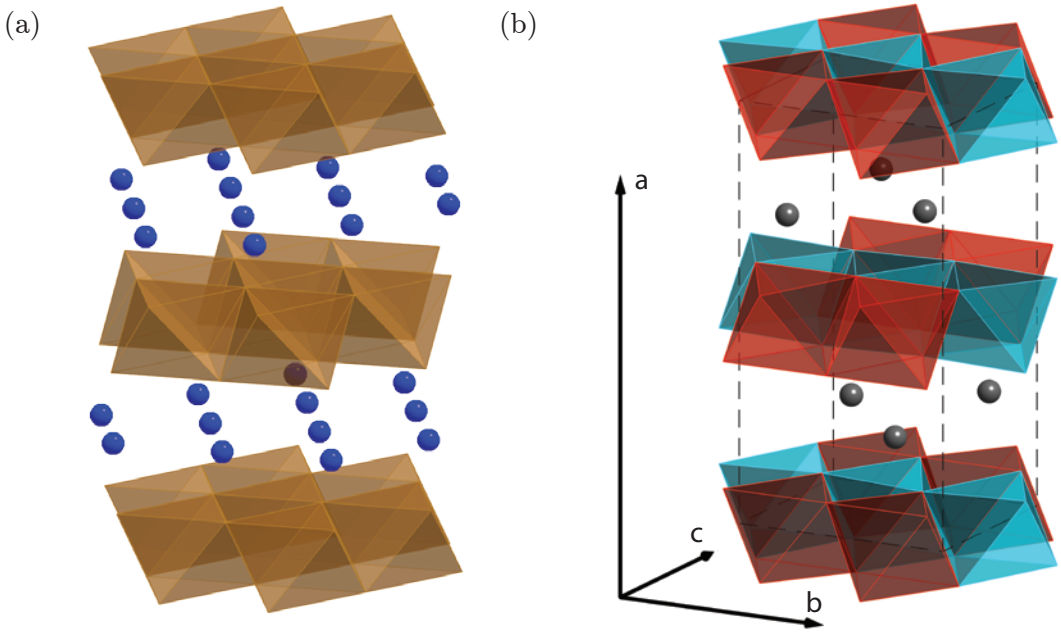

Figure 4.2: (a) $CuFeO_2$ delafossite, with $P6_3/mmc$ symmetry. (b) Crystal structure of α-$CaCr_2O_4$ ($Pmmn$) showing the triangular layers formed of two inequivalent CrO_6 octahedra coloured blue for $Cr(1)O_6$ and red for for $Cr(2)O_6$. The layers are separated by Ca^{2+} ions.

The second published work about α-$CaCr_2O_4$ was done by Chapon et al. in 2011. [96] They measured specific heat and magnetic susceptibility of α-$CaCr_2O_4$, which showed a single magnetic phase transition below room temperature at T_N=43 K and revealed the presence of strong antiferromagnetic interactions in the sample. A Curie-Weiss fit of the susceptibility in the paramagnetic phase gave J_{mean}=7.9 meV antiferromagnetic exchange between the magnetic nearest neighbour Cr^{3+} ions. Neutron powder diffraction in the magnetically ordered phase at 1.5 K showed that spins order in a proper screw structure with ordering wave vector of $\boldsymbol{k}_m$=(0,0.3317(2),0), and angles close to 120° between nearest neighbour Cr spins. They also predicted the existence of quadratic

magnetoelectric effects, based on a Landau analysis.
Pyrocurrent measurements done by Singh et al. in 2011 [97] on powder samples confirmed α-$CaCr_2O_4$ to be ferroelectric in the magnetic phase. Furthermore they verified that magnetoelectric coupling exists below T_N and the induced magnetic moment is proportional to the square of magnetic field.
In this chapter the synthesis of α-$CaCr_2O_4$ powder and single crystal samples, bulk property measurements and diffraction results will be discussed. Heat capacity was measured on single crystal samples showing a single phase transition to long-range magnetic order at T_N=42 K, in good agreement with Ref. [96]. Magnetic susceptibility was measured along all crystallographic direction and showed paramagnetic behaviour at high temperatures with Curie-Weiss temperature of T_{CW}=-564(4) K. Below 50 K the susceptibility decreases, showing the appearance of antiferromagnetic correlations. Neutron and synchrotron X-ray scattering were performed on powder and single crystal samples at several temperatures between room temperature and 4 K to search for changes in the crystal structure accompanying the magnetic phase transition. An anomaly found in the length of the a lattice constant, it has negative thermal expansion coefficient below the magnetic phase transition temperature. The magnetic structure in the ordered phase was determined unambiguously by powder and single crystal neutron diffraction and spherical neutron polarimetry. The structure is helical with spins lying in the ac plane and the ordering wave vector is $\boldsymbol{k}_m$=(0,0.3317(2),0) at 10 K. All the angles between in-plane nearest neighbours are 120°. This is the same structure as for the spatially anisotropic triangular lattice antiferromagnet. To explain the apparent contradiction between the high symmetry of the observed magnetic structure and the undistorted geometry of the underlying triangular lattice, the magnetic phase diagram was calculated as a function of the 1st neighbour and 2nd neighbour interaction strengths. This model shows that the observed magnetic structure is stable over a large range of exchange interactions and it is therefore insensitive to small deviations of the 1st neighbour in-plane distances.

4.1 Sample preparation

Both polycrystalline and single-crystal samples of α-$CaCr_2O_4$ were synthesized via a solid state reaction of CaO and Cr_2O_3.
Figure 4.3 shows the phase diagram of the CaO and Cr_2O_3 mixture in air. According to the phase diagram α-$CaCr_2O_4$ and β-$CaCr_2O_4$ are not thermodynamically stable at room temperature. To produce the desired phase the proper ratio of CaO and Cr_2O_3 has to be heated above 1480°C and quenched to room temperature to avoid decomposition.

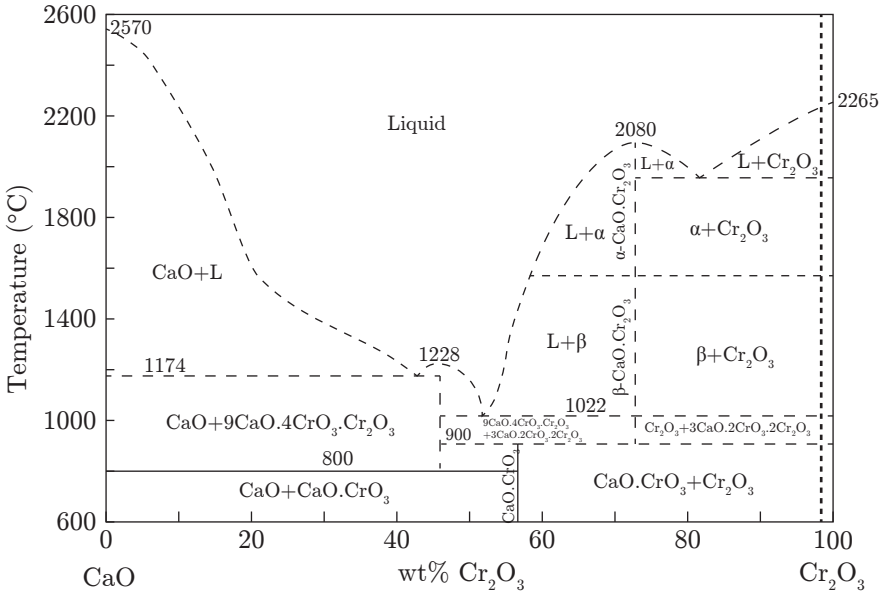

Figure 4.3: Phase diagram of the CaO-Cr_2O_3 system as a function of mass ratio and temperature in air. α-$CaCr_2O_4$ is thermodynamically stable above ∼1480 °C. Image taken from [98].

However in argon atmosphere the alpha phase appears already at 1300°C, enabling lower temperature synthesis. For both powder and single crystal samples a 1:1 molar ratio of $CaCO_3$ and Cr_2O_3 was mixed thoroughly and annealed in argon atmosphere at 1100°C for 12 hours. After the annealing the powder was re-ground. For polycrystalline sample the powder was re-annealed at 1300°C for 24 hours in argon, the quenching was unnecessary. For the single crystal growth the powder was compressed into a pellet and re-annealed at 1100°C for 12 hours. The single-crystal growth was performed using a high-temperature optical floating zone furnace at the Crystal Laboratory at Helmholtz Zentrum Berlin für Materialien und Energie (HZB), Berlin, Germany. The details of the technique will be reported elsewhere. [99]

The resulting rods contained several single crystals, see Fig. 4.4. To separate the single crystals, each specimen was measured with a custom built X-ray Laue diffractometer, in the XLab, HZB. The Laue pattern was recorded on an image plate and digitized, see Fig. 4.5. Using the OrientExpress program [100] the crystallographic orientation of the sample was determined. Several diffraction images were recorded on each side of the pieces to check whether it is single crystalline. The same Laue apparatus was used later to orient the crystals on a goniometer for neutron experiments. Due to the low resolution and the small penetration depth, the Laue machine provided only

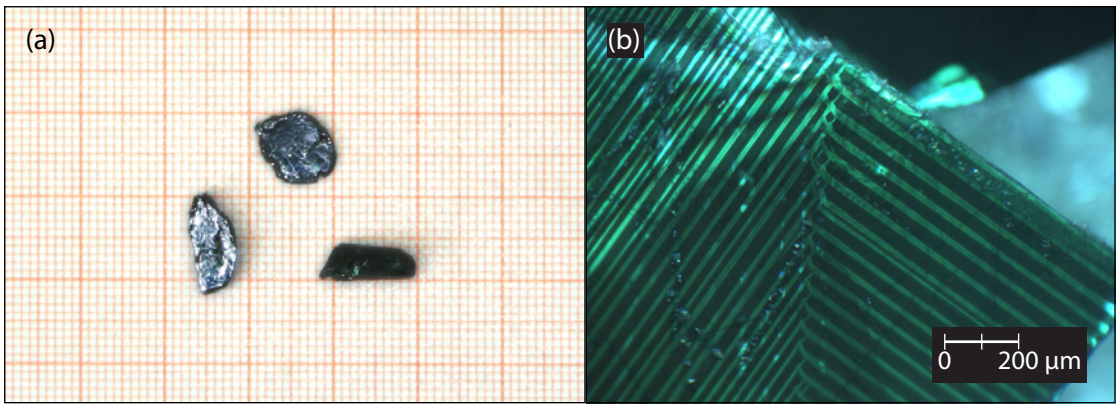

Figure 4.4: (a) Single crystal pieces after breaking the rod, (b) polarized light microscope image of a cleaved (100) surface.

limited information about the crystal quality. More reliable information was gained by single crystal neutron diffraction. Furthermore polarized light microscope was used to determine sample quality. The growth process resulted in a limited number of samples

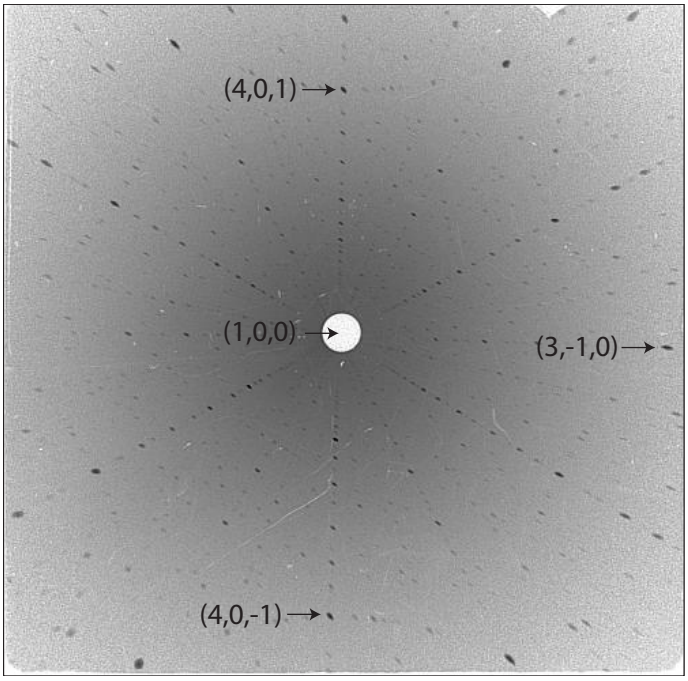

Figure 4.5: X-ray Laue image of an oriented single crystal, the plane of the image is the (100) plane.

adequate for scattering experiments. The selected single crystals are plate-like with

shiny flat surfaces perpendicular to the a-axis. The (100) planes can be cleaved easily and the resulting surface showed a striped pattern in polarized light, see Fig. 4.4(b). The different stripe directions have a domain-like structure, where there are mostly two different directions perpendicular to each other. The origin of the stripes is unknown, although they might related to the structural domains in the crystal, see 4.3.2.2.

4.2 Bulk Properties

Bulk properties measurements were performed at the Laboratory for Magnetic Measurements (MagLab), HZB. Heat capacity was measured on a small single-crystal sample of 15.6 mg using a Physical Properties Measurement System (PPMS), Quantum Design, over the temperature range of $2.1 \leq T \leq 300$ K.

Pyrocurrent was measured in the PPMS along the a axis, sample thickness was 0.75 mm. The two a sides of the sample were painted with conducting Al paint (on a surface area of 4.7 mm^2) and contacted to an electrometer (Keithley 6517B). The sample was cooled from 55 K to 4 K in 250 V polarizing electric field using the built in power supply of the electrometer. Afterwards without polarizing field the sample was heated up while measuring the pyrocurrent flowing between the two contacts with the ammeter option of Keithley. The temperature sweep was 10 K/min in both direction. The measurement was repeated with opposite poling field polarity and without applying poling field. The leakage current of the setup was about 10 fA without the sample.

High temperature DC magnetic susceptibility ($300 \leq T \leq 1000$ K) was measured in a 1 T field on an unoriented crystal using the PPMS with vibrating sample magnetometer (VSM) and oven options. The sample was fixed to the heater using Al-cement. Low temperature ($2.1 \leq T \leq 300$ K) susceptibility at 1 T as well as magnetization at 2 K up to 5 T were measured both parallel and perpendicular to the a-axis ($\chi_{\mathrm{a}\parallel}$ and $\chi_{\mathrm{a}\perp}$) using the SQUID magnetometer, Quantum Design. The single-crystal had a weight of 1.81 mg and was fixed with GE varnish to a plastic sample stick.

4.2.1 Heat Capacity

The specific heat of α-$CaCr_2O_4$ as a function of temperature is shown in Fig. 4.6. A sharp peak is observed at T_{N}=42(1) K in good agreement with Ref. [96]. It is attributed to the onset of long-range antiferromagnetic order. No other sharp features were observed in this temperature range indicating the absence of further magnetic or structural transitions.

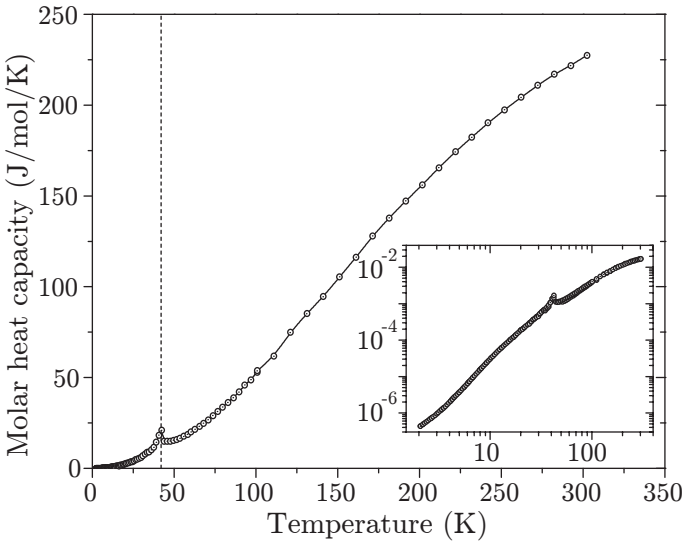

Figure 4.6: Heat capacity showing the magnetic phase transition at T_N=42(1) K. The inset shows the same data plotted on a log-log scale.

4.2.2 Electric Properties

Pyrocurrent was measured on single crystals along the *a*-axis. Attempts to measure perpendicular directions failed, because the grown crystals were thin along the *a*-axis and they fell into pieces during cutting. Figure 4.7(a) shows the measured pyrocurrent as a function of temperature using different poling electric fields upon cooling. There is a broad bump in the pyrocurrent curve around the Néel temperature, when applying poling field. All three curves show a broad background, originating from the leakage current of the measurement setup and the temperature dependent resistivity of the sample. To correct for these effects, the zero poling field measurement was used as a reference and was subtracted from the signal, see Fig. 4.7(b). The peaks at 44 K can be attributed to the breaking down of the electric polarization in the sample in correlation with the disappearance of the magnetic order. The broad peak above 47 K in the pyrocurrent curve appears probably due to small changes in the positions of ions within the unit cell. To calculate the electric polarization the peak at 44 K was integrated, which yielded an electric polarization of $\sim$0.1 μC/m^2, see Fig. 4.7(c). The measured value of polarization is much smaller than the published powder results by Singh et al. (0.6 μC/m^2). This shows that the induced polarization might be much larger in the *bc* plane.

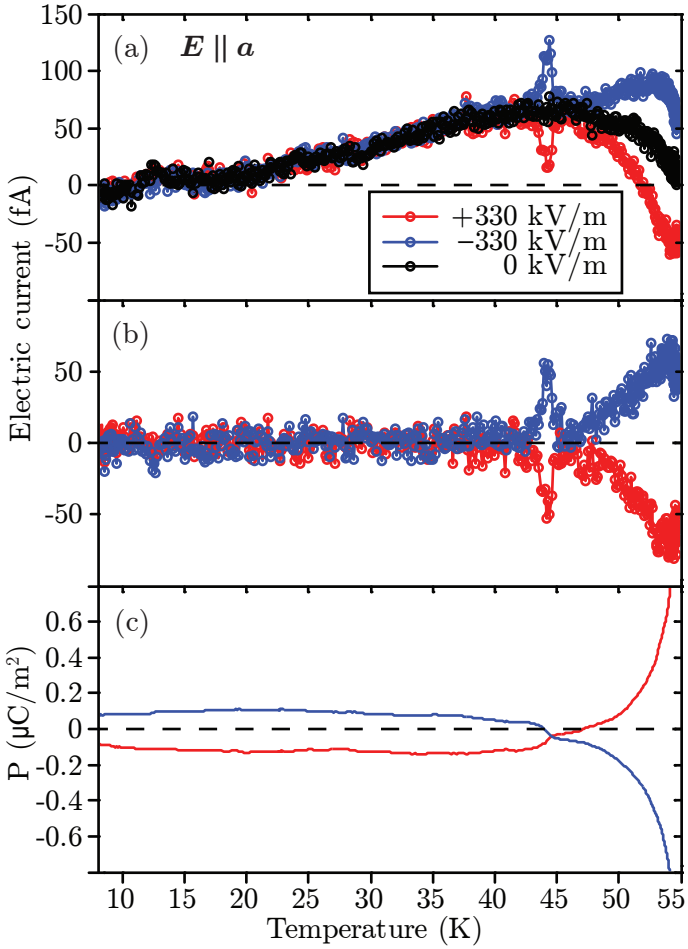

Figure 4.7: (a) Pyrocurrent measured along the a direction on α-$CaCr_2O_4$with different poling electric field, (b) zero poling field curve subtracted, (c) electric polarization of the sample assuming zero polarization at the Néel temperature.

4.2.3 Magnetic Susceptibility

Both field cooled and zero field cooled magnetic susceptibility were measured but no significant difference was observed. Figure 4.8(a) shows the high temperature susceptibility from 300 K to 1000 K, which reveals Curie-Weiss behaviour, proving that α-$CaCr_2O_4$ is paramagnetic in this temperature range. Using mean field approximation, the average interaction between the magnetic Cr^{3+} ions can be determined. The data were fitted in the temperature range 800 K to 1000 K to the Curie-Weiss law:

$$\chi_{\mathrm{CW}} = \frac{C}{T - T_{\mathrm{CW}}} + \chi_0, \tag{4.1}$$

χ_0 is a temperature independent background, which accounts for the paramagnetic Van Vleck susceptibility and diamagnetic core susceptibility as well the background from sample stick and Al-cement (which is less than 0.5% of the measured susceptibility at 1000 K). The fitted value of the Curie-Weiss temperature is T_{CW}=-564(4) K and the effective moment, given by $\sqrt{8C}\mu_{\mathrm{B}}$, was found to be $\mu_{\mathrm{eff}} = 3.68(1)\mu_{\mathrm{B}}$. This is close to the expected spin only value of Cr^{3+} $g\sqrt{S(S+1)}$=3.87μ_{B}. The average value of the exchange interactions in the triangular layers can be estimated from the Curie-Weiss temperature: $k_B\Theta = S(S+1)zJ_{\mathrm{mean}}/3$, where the number of nearest neighbours for triangular lattice is $z = 6$ if interlayer and next nearest neighbour interactions are neglected. The extracted average intralayer coupling in α-$CaCr_2O_4$ is antiferromagnetic with strength J_{mean}=6.48(5) meV.

The susceptibility at low temperatures (2.1$\leq T \leq$300 K) for an applied field parallel and perpendicular to a is shown in Fig. 4.8(b). The data deviate from the Curie-Weiss law and show a broad maximum at 50 K for both crystal orientations. This feature can be explained by the onset of low dimensional antiferromagnetic correlations in the triangular plane. The susceptibility decreases suddenly at the same temperature where heat capacity shows a phase transition. The large drop reveals the onset of long-range antiferromagnetic order and the best estimate for the transition temperature is T_{N}=43 K. The susceptibility below T_{N} drops and it is different for the two crystal orientations.

The magnetization of α-$CaCr_2O_4$ as a function of magnetic field was also measured along all three crystallographic directions, see Fig. 4.9. Up to the instrumental limit of 5.5 T the magnetization curve and it's derivative dM/dB are smooth, which reveals that no sudden spin reorientation occurs up to the maximum field. Therefore the single ion anisotropy is either very small or very large in comparison to the applied magnetic field range. A small but significant hysteresis can be observed along the b and c directions, in contrast to the a axis, see inset of Fig. 4.9.

4.3 Diffraction study

To determine the nuclear and magnetic structure of α-$CaCr_2O_4$, neutron and X-ray scattering experiments were performed on powder and single crystal samples. In the magnetic phase, the structure is found to be helical with ordering wave vector $\boldsymbol{k}_{\mathrm{m}}$=(0,0.332(3),0) and spins lying in the ac plane.

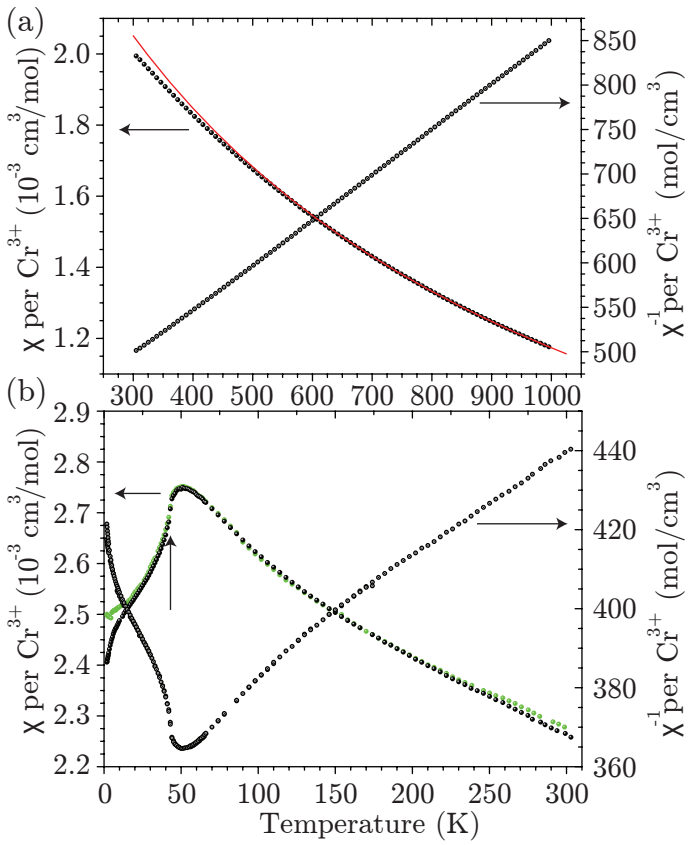

Figure 4.8: DC magnetic susceptibility per Cr^{3+} ion measured on a single-crystal sample in a 1 T magnetic field. (a) left axis: high temperature susceptibility of unoriented sample (filled data points), right axis: inverse susceptibility (open data points), the red line is the Curie-Weiss fit. (b) Low temperature magnetic susceptibility; green data points, $\chi_{a\parallel}$; black points, $\chi_{a\perp}$. The vertical arrow shows the inflection point at T_N. Right axis: inverse susceptibility ($\chi_{a\perp}^{-1}$) displayed by the open data points.

4.3.1 Experiment

X-ray powder diffraction was measured on the ID31 high-resolution powder-diffraction beamline at the European Synchrotron Radiation Facility (ESRF), Grenoble, France. A wavelength of λ=0.39983(2) Å (E=31.18 keV) was used, and data were collected at ten different temperatures in the range $10 \leq T \leq 260$ K with a measurement time of 30 min per pattern.

Neutron powder diffraction patterns were measured on two instruments. First on the D20 high-intensity two-axis diffractometer at the Institute Laue Langevin (ILL), Grenoble, France, where a Ge monochromator was used to select a wavelength of λ=1.869 Å,

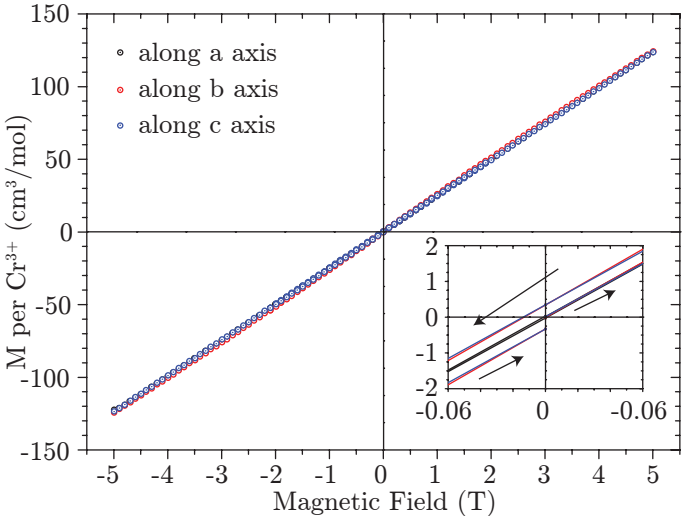

Figure 4.9: Magnetization in function of magnetic field at 4 K, inset shows the small hysteresis.

and data were collected over the temperature range of $10 \leq T \leq 42.6$ K in 1 K steps. Measurements were also performed on the E9 fine-resolution powder diffractometer at the BER II reactor, HZB. A Ge monochromator selected a wavelength of $\lambda = 1.799$ Å and data were collected at 2.1 K and 50 K.

Single-crystal neutron diffraction was performed on a large crystal using the E5 four-circle single-crystal diffractometer at the BER II reactor, HZB. The single-crystal has a weight of 340 mg and a size of $3 \times 7 \times 8$ mm^3. A pyrolytic graphite (PG) monochromator selected an incident wavelength of $\lambda = 2.36$ Å. The instrument is equipped with a two-dimensional position-sensitive ^{3}He detector consisting of 36 x 36 pixels and for each Bragg reflection a 36-step scan of the crystal angle (ω) was performed. A total of 616 magnetic and 423 nuclear Bragg reflections were collected at 6 K for a total counting time of five minutes each.

Spherical neutron polarimetry was performed on the same single-crystal using the TASP triple axis spectrometer at the Paul Scherrer Institute (PSI), Switzerland. The wavelength $\lambda = 3.2$ Å was selected by a PG monochromator and benders were used to polarize and analyse the neutron beam along the vertical z-axis of the instrument. They acted as collimators as well. The sample temperature was set to 1.5 K during the experiment. The MuPAD option was installed to control the polarization direction of the incoming neutron beam ($\boldsymbol{P}_\mathrm{i}$) and also to analyse the scattered beam along any final polarization direction ($\boldsymbol{P}_\mathrm{f}$). The beam polarization was measured to be 0.883(10) for all directions of neutron polarization. There are a total of 36 cross sections that can be measured for

every Bragg reflection, since both $\boldsymbol{P}_\mathrm{i}$ and $\boldsymbol{P}_\mathrm{f}$ can be along $\pm x$, $\pm y$ and $\pm z$. For most Bragg peaks only 18 cross sections were measured by setting the incoming beam polarization to the positive value, while for a few peaks all 36 cross sections were measured to check the presence of chirality in the magnetic structure of α-$CaCr_2O_4$. Since the measured intensities were rather small, the background was also measured for all cross sections close to each Bragg peak. The polarization matrices were calculated from the background corrected cross sections. This method has the advantage of cancelling out positioning errors and any wave vector dependent attenuation since only the ratio of the intensities matters. A total of 23 reflections was measured with the crystal oriented in three different scattering planes $(h, k, 0)$, $(h, k, 3k/2)$ and $(h, k, -3k/2)$. All cross sections were counted for three minutes each.

Single crystal diffuse scattering was measured with neutrons using the E2 flat-cone diffractometer at the BER II reactor, HZB to determine spin-spin correlations below and above the Néel temperature in reciprocal space. The instrument has four two-dimensional delay-line detectors (PSD), with horizontal and vertical resolution of 0.1°. The incident neutron wavelength of 2.36 Å was determined by the (0,0,2) reflection of the PG monochromator and collimated by a 30' collimator. No collimation was used between sample and detector. Diffuse scattering intensity was collected over a 3D volume in reciprocal space by rotating the crystal around its vertical axis and measuring the intensity pattern on the 2D detector for 1 min each step. Using the TVnexus software, the measured data was combined into a 3D intensity map. The sample was measured in two different orientations, setting the scattering plane to (1,k,l) and (h,k,0). Measurements were repeated at three different temperatures: 4 K, 44 K and 50 K.

4.3.2 Nuclear Structure

4.3.2.1 Powder diffraction

The crystal structure of α-$CaCr_2O_4$ was refined from neutron powder diffraction data (measured on E9 and D20) along with X-ray powder diffraction data (measured on ID31) collected above the antiferromagnetic phase transition temperature (Fig. 4.10). The structural refinement was performed with the FullProf software. [101] The refinement algorithm is based on the Rietveld method. [102] All the peaks could be indexed in the space group $Pmmn$ in agreement with previous powder measurements [93, 96] and no detectable impurity was observed. The strongest peak of the X-ray diffraction data is (2,0,0) at 3°, which was excluded from the refinement. Due to the strong intensity, this peak strongly influences the refinement, but contains only very little information, thus

by removing it the quality of the refinement could be improved. There is a broad bump around $2\theta = 25°$ in the neutron diffraction patterns. It is absent from the X-ray pattern which, due to the insensitivity of X-rays to magnetic moments, must be of magnetic origin. This provides further evidence for two-dimensional magnetic correlations above T_N at 50 K in agreement with the temperature of the maximum in the susceptibility, see Fig. 4.8(b).

The lineshape of the X-ray diffraction pattern is completely Lorentzian. The Bragg peaks with indices $(0, k, l)$ are broadened which was not observable in the neutron data because of the poorer resolution. To improve the X-ray data refinement anisotropic microstrain parameters had to be introduced in the model. This model assumes a distribution of the lattice parameters. The width of the Bragg peaks is modelled as a function of the hkl indices of the reflection, these width are determined by a set of S_{hkl} parameters along specific crystallographic directions. [103, 104] The largest strain values are along the (0,2,2) direction at 50 K, see Table 4.1. In a phenomenological model this means a measurable distribution of lattice parameters in the bc plane. The strain was also determined as a function of temperature, but no significant change was found below room temperature.

Table 4.1: Strain parameter values of α-$CaCr_2O_4$ at 50 K measured on ID31.

S_{400}	S_{040}	S_{004}	S_{220}	S_{202}	S_{022}
0.0036(1)	0.57(2)	0.843(1)	0.42(2)	0.3349(6)	3.05(8)

Table 4.2 lists the fitted atomic positions from the different refinements. The fitted values are in agreement with those from the previous room temperature measurement of Ref. [93]. The quality of fit is given by the R_F-factor values: $R_F = \sum |F_{OBS} - F_{CALC}| / \sum |F_{OBS}|$, where F_{OBS} and F_{CALC} are the observed and calculated structure factors. They are: 0.035 for ID31 at 50 K, 0.037 for D20 at 47 K, 0.035 for E9 at 50 K and 0.031 fr E9 at 2.1 K. The refined model confirms that α-$CaCr_2O_4$ consists of distorted triangular layers with two symmetry inequivalent Cr^{3+} ions in the (100) plane. There are a total of four intraplanar nearest neighbour distances varying between 2.889 Å and 2.939 Å at 2.1 K, see Fig. 4.11, the interplane distances are 5.529 Å for Cr(1)–Cr(1) and 5.379 Å for Cr(2)–Cr(2). The Cr–O–Cr angles vary between 91.0° and 95.7°.

The temperature dependence of the crystallographic parameters was determined by sequential refinement of the data collected on ID31 over a temperature range from 10 K to 300 K. The sequential method is based on the Rietveld refinement of individual diffraction patterns at each temperature. However the starting parameters of each refinement

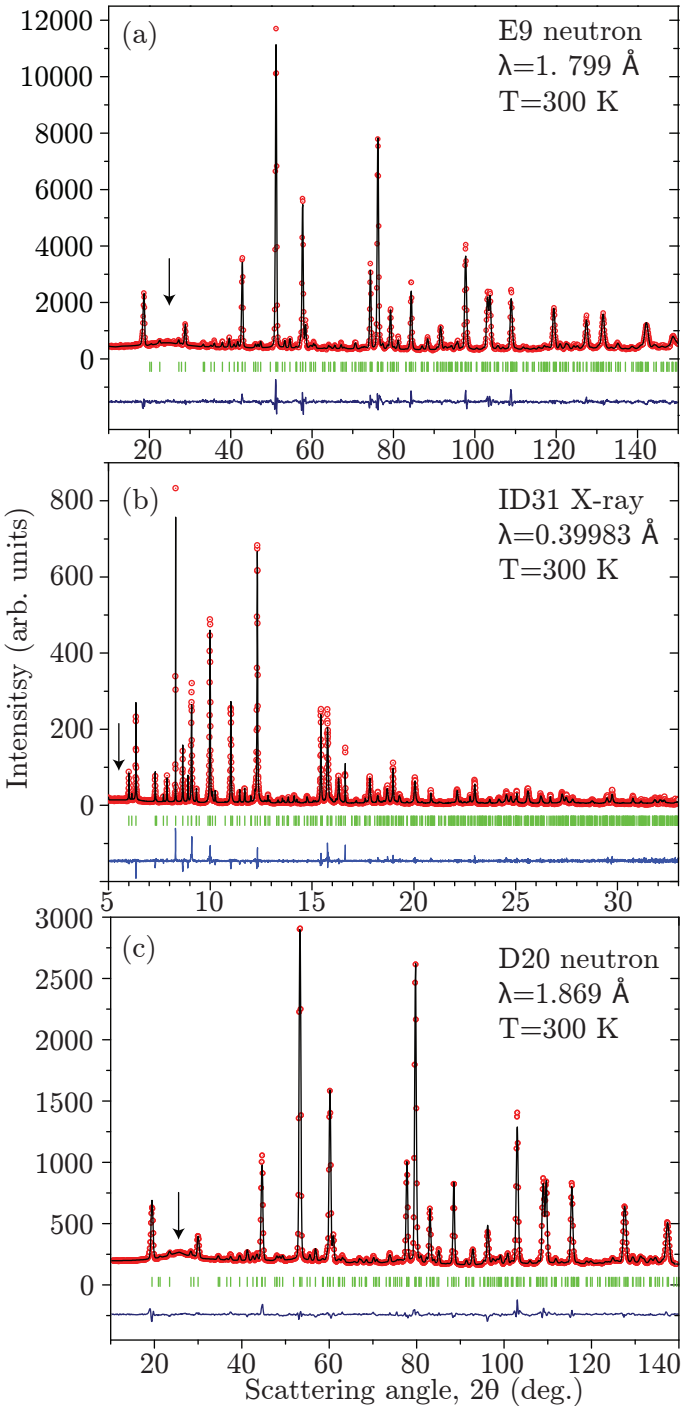

Figure 4.10: Powder diffraction patterns along with Rietveld refinements. The open red symbols are the data, the black curve is the fit, the blue line is the difference and the green bars indicate the nuclear Bragg peaks. The arrows indicate the d=4.1 Å position, where the broad bump is on the neutron data.

Table 4.2: Refined crystallographic parameters using space group *Pmmn*. The lattice parameters were determined from the high resolution ID31 X-ray powder data at 50K. The atomic position listed are; first row previously published by Pausch et al. [93], second row, ID31 powder data at 50 K; third row, refinement of D20 neutron powder data at 47 K; fourth row, refinement of E9 powder data at 50 K; fifth row, E9 powder data at 2.1 K.

Unit cell dimensions: $a = 11.0579(2)$ Å
$b = 5.8239(2)$ Å
$c = 5.0553(1)$ Å

Atom	Site	x	y	z
Ca(1)	2a	3/4	3/4	0.3519
				0.3512(4)
				0.3494(10)
				0.3521(12)
				0.3532(12)
Ca(2)	2b	1/4	3/4	0.0352
				0.0385(4)
				0.0359(8)
				0.0384(11)
				0.0410(11)
Cr(1)	4d	1/2	1/2	1/2
Cr(2)	4f	0.4922	1/4	0.0058
		0.4932(1)		0.0046(4)
		0.4921(4)		0.0050(9)
		0.4917(5)		0.0059(11)
		0.4931(6)		0.0057(12)
O(1)	4f	0.406(9)	1/4	0.338(5)
		0.4022(5)		0.3365(14)
		0.4022(4)		0.3394(6)
		0.4023(4)		0.3397(8)
		0.4024(4)		0.3410(8)
O(2)	4f	0.609(4)	1/4	0.679(9)
		0.5904(5)		0.6825(14)
		0.5891(3)		0.6771(6)
		0.5901(4)		0.6758(8)
		0.5906(4)		0.6762(8)
O(3)	8g	0.598	0.497(1)	0.170(7)
		0.5989(3)	0.4996(8)	0.1665(12)
		0.6007(2)	0.4963(5)	0.1653(5)
		0.6003(2)	0.4955(6)	0.1647(7)
		0.6003(2)	0.4966(6)	0.1657(7)

Table 4.3: Bond lengths in α-$CaCr_2O_4$ at various temperatures obtained from ID31 X-ray diffraction.

α-$CaCr_2O_4$	10 K	50 K	220 K
Cr(1)–Cr(1) d_{ch2}	2.9162(1)	2.9173(2)	2.9201(2)
Cr(1)–Cr(2) d_{zz2}	2.896(1)	2.898(2)	2.899(2)
Cr(2)–Cr(1) d_{zz1}	2.938(1)	2.937(2)	2.943(2)
Cr(2)–Cr(2) d_{ch1}	2.91102(3)	2.93706(5)	2.91435(4)
Cr(1)–Cr(1) (interplane)	5.363(2)	5.365(3)	5.356(3)
Cr(1)–Cr(1) (interplane)	5.697(2)	5.692(3)	5.706(3)
Cr(2)–Cr(2) (interplane)	5.53006(3)	5.52875(5)	5.53116(5)

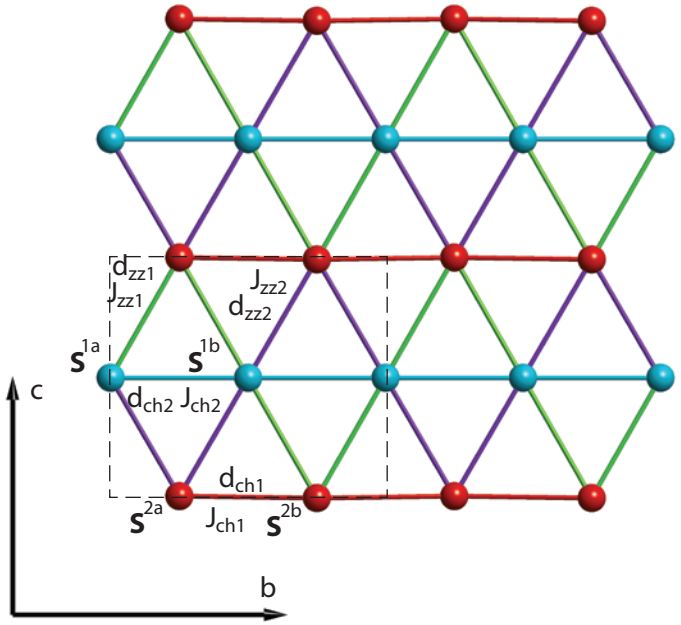

Figure 4.11: A single triangular layer showing only the Cr^{3+} ions. The four inequivalent nearest-neighbour intralayer Cr^{3+}–Cr^{3+} distances determined from the E9 powder data at 2.1 K (see Table 4.2): red d_{ch1} = 2.882 Å; blue d_{ch2} = 2.932 Å; green d_{zz1} = 2.914 Å; purple d_{zz2} = 2.910 Å. The corresponding exchange interactions are J_{ch1}, J_{ch2}, J_{zz1} and J_{zz2}, (see Sec 4.4). The dashed lines indicate the boundaries of the structural unit cell.

are taken from the refinement of the previous temperature. The resulted temperature dependent lattice parameters are plotted on Fig. 4.12. No sudden change in the relative atomic positions was observed, that would suggest a phase transition. In particular there is no sudden jump of the values at the Néel temperature. For comparison see the atomic positions at 2.1 K and 50 K determined from the E9 refinement in Table 4.2. The b and

c lattice constants increase gradually with increasing temperature, while the a lattice constant has a minimum at 70 K and shows negative thermal expansion at lower temperatures. There is no indication of any symmetry change over this temperature range, even a subtle distortion can be ruled out since the linewidths remain constant between 10 K and room temperature.

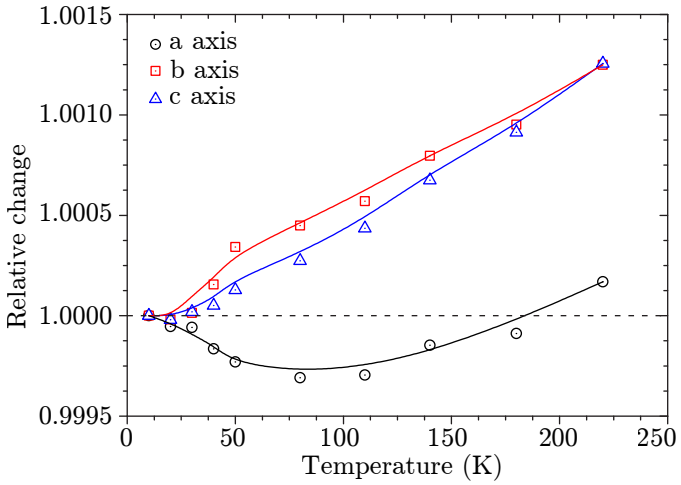

Figure 4.12: Temperature dependence of the lattice parameters obtained from ID31 data. The lines are guides to the eye.

4.3.2.2 Twinning

For the analysis of the single crystal data the problem of twinning has to be considered in detail. Due to the vacancies in the A cation site, the original threefold symmetry of the delafossite structure is broken. However the distortion is small thus during the high temperature growth process, the formation of twins is inevitable. The three twins will share the a axis but the b and c axes are rotated with respect to each other by 60°, see Fig. 4.13. In the orthorhombic setting the distortion parameter is only $\sqrt{(3)}/2 \cdot b/c$ =0.998, which is very close to the undistorted value of one, see Tab. 4.2. To parametrize the the reflections of all three twins in reciprocal space, a Cartesian coordinate system is fixed to the lattice vectors of each twin. The nuclear reflections of each twin in its own coordinate system have integer indices. The transformation between these coordinate systems is a

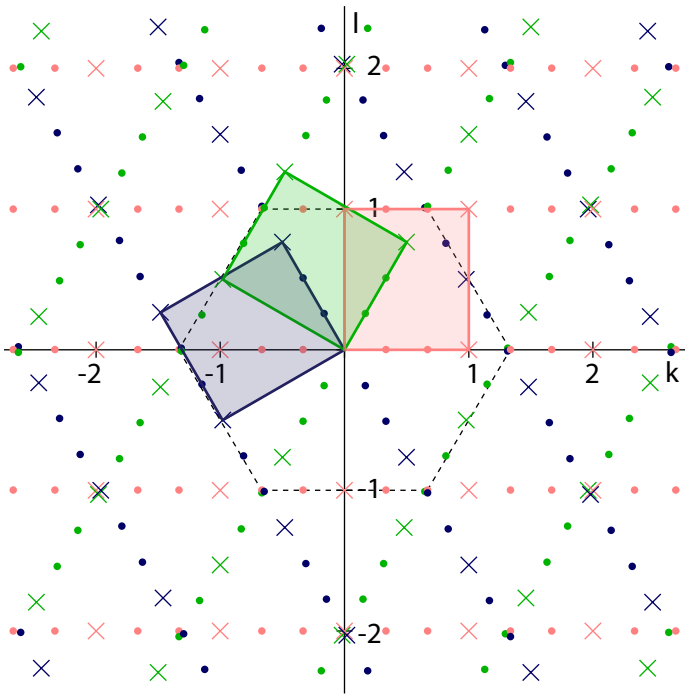

Figure 4.13: The three twins in the $(1, k, l)$ reciprocal space plane where distortion is exaggerated for better visibility. The three different colors denote the three twins, rectangles show the original and rotated reciprocal unit cells. The crosses give the position of the nuclear reflections while the dots show all possible magnetic reflections. The dashed line indicates the border of the Brillouin zone of the 120° magnetic structure.

simple 60° or 120° rotation, which gives the following:

$$\begin{aligned} Q_1 &= (h, k, l), \\ Q_2 &= (h, 1/2k - l, 3/4k + 1/2l), \\ Q_3 &= (h, -1/2k - l, 3/4k - 1/2l). \end{aligned} \tag{4.2}$$

These formulas allow to transform reciprocal coordinates from twin 1 to twin 2 and twin 3. For the analysis of inelastic neutron scattering data these formulas define a folding, by giving the equivalent coordinates. These equations distinguish two types of reflections. The first set contains reflections which have integer indices in all three coordinate systems, they are the "twinned reflections" (e.g. (1,2,1),(1,0,2) and (1,-2,1), see Fig. 4.13), because in this case the reflections of the three twins are almost overlapping. The rest of the reflections are "untwinned reflections". If the crystal distortion would disappear and

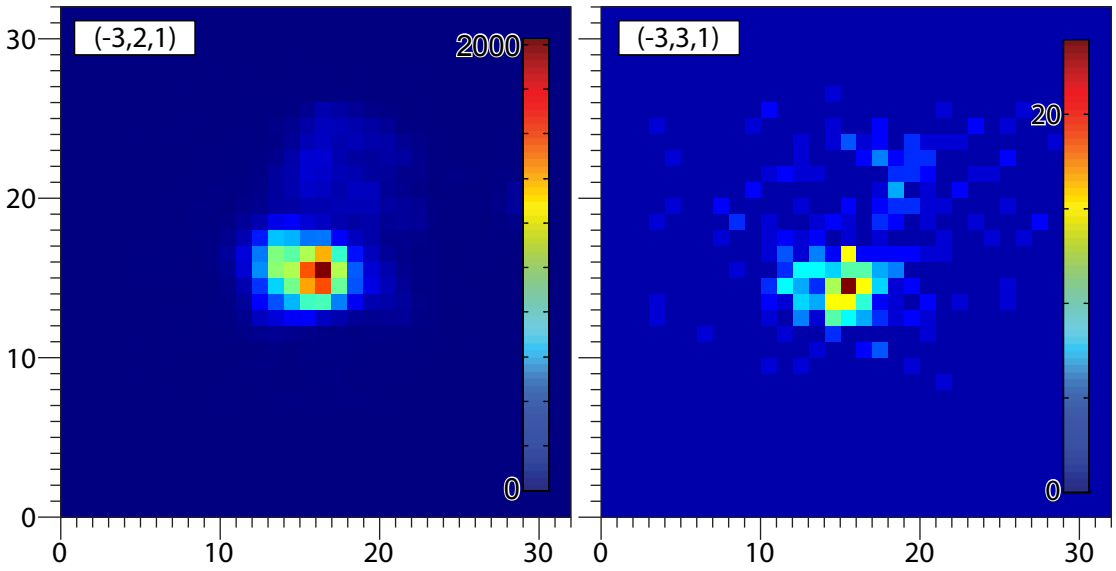

Figure 4.14: Detector image of a twinned (left) and untwinned (right) nuclear reflection on E5.

the 3-fold symmetry would be restored, the twinned reflections would become the Bragg peaks of the higher symmetry structure, while the intensity of the untwinned reflections would go to zero.

4.3.2.3 Single crystal diffraction

Single-crystal diffraction was measured on the E5 instrument to determine the nuclear Bragg peak intensities at 6 K. Each nuclear Bragg peak was measured by performing a scan of the crystal angle (ω-scan) and the scattered neutrons were collected in the area detector. Using the Racer program the collected detector counts were integrated into Bragg reflection intensities, as described in Ref. [105]. The measured sample was previously identified as a single crystal, using X-ray Laue diffraction. However the neutron diffractometer showed that several small grains exist beside the main oriented crystal and the mosaic spread of the main crystal is 2°, see Fig. 4.14. This unfortunately impacted on the data quality and the reliability of the structure determination.
Another problem that arises with the single-crystal diffraction data is the twinning discussed previously. The overlapping twinned peaks could not be resolved due to the limited resolution of the instrument see Fig. 4.14(left). For the structure determination only the sum of the overlapping intensities could be measured, which gave uncertainty. The untwinned reflections could be used to determine the volume ratio of the three twins

in the sample by simply taking the intensity ratio of equivalent reflections. To overcome the twinning problem a single intensity list was generated containing reflections of all three twins and each reflection was labelled by the twin(s) to which it belonged. One label was assigned to the untwinned peaks while three labels (twin 1, twin 2 and twin 3) were assigned to the twinned reflections. Using the atomic coordinates obtained from the E9 powder diffraction data at 2.1 K, the single crystal diffraction dataset of nuclear peaks was refined to obtain the scale factor and the volume ratios of the twins. As a result of the refinement the three twins were found to have non-equal weight (see Table 4.4). These volume ratios were essential to the magnetic structure refinement of the low temperature single crystal data which is described in the next section.

Table 4.4: Twin ratio of the single-crystal sample, determined from refinement of nuclear Bragg peaks measured on E5 at 6 K.

Twin 1	Twin 2 (+60°)	Twin 3 (+120°)
64(2)%	19(2)%	17(3)%

4.3.3 Magnetic Structure

Several different neutron diffraction techniques were necessary to determine unambiguously the magnetic structure of α-$CaCr_2O_4$, powder diffraction, single-crystal diffraction and spherical neutron polarimetry were performed on the magnetically ordered phase. In this subsection the results of each will be discussed and shown how do they provide a complete picture of the magnetic order.

4.3.3.1 Powder diffraction

The onset of magnetic order can be observed below the Néel temperature, if one compares neutron diffraction patterns measured on D20 at 10 K and 50 K. On the low temperature diffraction pattern below the Néel temperature several new peaks can be observed with non integer reciprocal lattice units, see Fig. 4.15. The strongest peak is at $d = 4.093$ Å, the position where the broad bump was found on the 50 K diffraction pattern. The new peaks were indexed using the k-search program of the FullProf suite. The determined magnetic ordering wave vector $\boldsymbol{k}_\mathrm{m}$ was found to be close to the commensurate value of $(0, 1/3, 0)$ in agreement with Ref. [96]. Table 4.5 shows the Q position of several measured magnetic peaks. Only magnetic reflections where h is odd were observed, which implies antiferromagnetic ordering between successive planes along a (since the unit cell contains two Cr^{3+} layers stacked along a). All possible magnetic reflections in

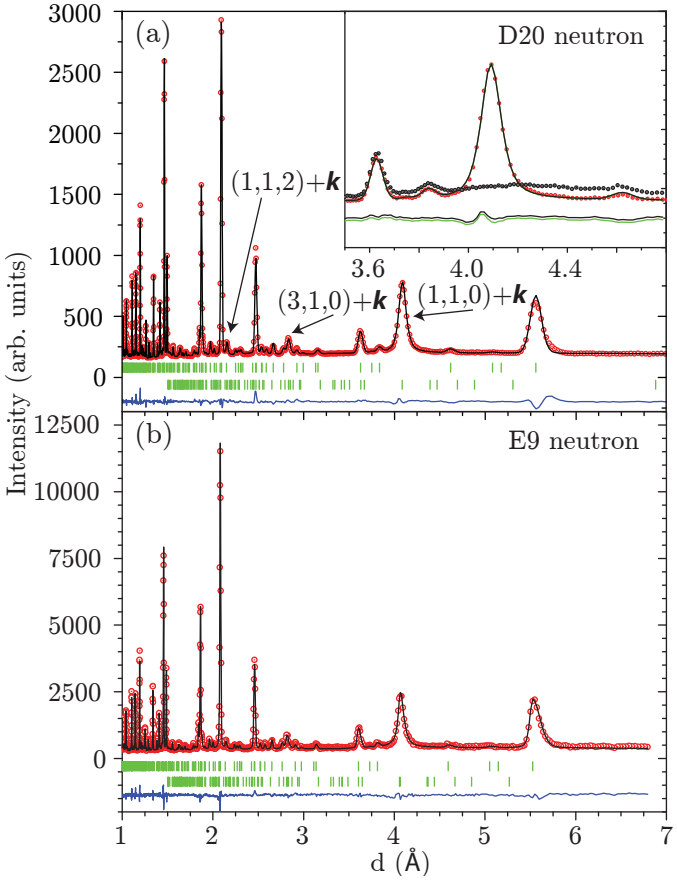

Figure 4.15: Powder diffraction data are displayed along with the Rietveld refinement assuming helical magnetic order in the (101) plane, (a) measured on D20 at 10 K and (b) on E9 at 2.1 K. The open red symbols are the data, the black curve is the fit, the upper and lower green bars indicate the nuclear and magnetic Bragg peak positions respectively, and the lower blue line gives the difference between fit and data. Inset of (a) shows details of the $(1, 1, 0) + \boldsymbol{k}$ magnetic peak along with the 50 K data (open black symbols). The green and blue solid lines are the difference between the data and the fit with $\boldsymbol{k}$ fixed to (0,1/3,0) and refined to (0,0.332(3),0) respectively.

the $(1, k, l)$ plane generated by $\boldsymbol{k}_\mathrm{m} = (0, 1/3, 0)$ are shown in Fig. 4.13. However, only magnetic peaks where the three twins overlap have measurable magnetic intensity e.g. $(1, 4/3, 0)$; this makes the magnetic refinement challenging.

Besides the identified magnetic ordering k-vector, the orientation of the spins have to be determined for a complete description of the magnetic structure. Each spin in the unit cell can be described by three continuous variables: magnetic moment and a Θ

Table 4.5: The magnetic peaks indexed assuming $\boldsymbol{k} = (0, 1/3, 0)$ are listed along with their observed and calculated d-spacings.

d_{obs} (Å)	index	d_{cal} (Å)
4.093	$(1,1,0) + \boldsymbol{k}$	4.084
2.833	$(3,1,0) + \boldsymbol{k}$	2.832
2.154	$(1,3,0) - \boldsymbol{k}$	2.154
1.642	$(1,3,3) - \boldsymbol{k}$	1.645

and φ angle in a spherical coordinate system. Having four spins per unit cell means 12 parameters to be determined. Considering the low number of measurable magnetic reflections on the D20 and E9 low temperature powder patterns, the number of fitted parameters have to be reduced. Analysing the symmetry of the possible magnetic structure can reduce the number of fitted parameters, see Section 2.3.3. The Landau theory of second order phase transitions says that the first ordered magnetic phase below the ordering temperature can be described by a single irreducible magnetic representation (irrep) of the crystal symmetry. Since the magnetic phase transition of α-$CaCr_2O_4$ is of first order, this rule does not apply rigorously to the system, see Ref. [96]. Still it gives a possibility to simplify the fitting problem. The Γ_{m} magnetic representation of the crystal symmetry, assuming $\boldsymbol{k}_{\mathrm{m}} = (0, 1/3, 0)$, consists of four irreps as listed in Table 4.6, where $\eta = \exp(2\pi i/6)$. Each irrep consists of four basis functions. According to the Landau theory a general magnetic structure contains a linear combination of basis functions belonging to the same irrep, the prefactors are complex. In case of a first order magnetic phase transition the magnetic structure can be described by a linear combination of basis functions from different irreps. The previously recognized antiferromagnetic order along the a-axis restricts the number of possible basis functions. The magnetic structure can be described only by the ones which change sign under the $m(1/4, y, z)$ symmetry operation (this operation exchanges the magnetic atoms between the two triangular layer in the unit cell). With this restriction still many different magnetic structures are possible including helical, cycloidal, ellipsoidal and sinusoidal arrangements.

To determine the magnetic structure from the powder diffraction data using symmetry analysis, the prefactors of the basis functions were refined. The best fit was given by the use of two basis function $\Gamma_1\psi_1$ and $\Gamma_2\psi_3$ to compose the magnetic moment orientation of Cr(1), see Tab. 4.7. In this case, the spin component along (1,0,0) transforms according to $\Gamma_1\psi_1$ and the component along $(0, 0, 1)$ transforms according to $\Gamma_2\psi_3$. The basis function of the Cr(2) site are found by taking the complex conjugate of them. These two basis functions describe a magnetic structure with spins lying in the ac plane. Depending

Table 4.6: Irreducible representations for $\boldsymbol{k}_\mathrm{m} = (0, 1/3, 0)$ in the $Pmmn$ group, where $\eta = \exp(2\pi i/6)$. The magnetic representation Γ_m consists of four irreps each occurring three times: $\Gamma_\mathrm{m} = 3\Gamma_1 \oplus 3\Gamma_2 \oplus 3\Gamma_3 \oplus 3\Gamma_4$.

	1	$2_1(0, y, 0)$	$n(x, y, 0)$	$m(¼, y, z)$
Γ_1	1	η	$-\eta$	-1
Γ_2	1	η	η	-1
Γ_3	1	$-\eta$	$-\eta$	-1
Γ_4	1	$-\eta$	η	-1

on the phase difference of the complex prefactors of $\Gamma_1\psi_1$ and $\Gamma_2\psi_3$, the generated structure can be a proper screw or sinusoidally modulated.

Table 4.7: The two basis function of the two different irreducible representations which describe the magnetic structure best. The listed functions describe the magnetic moment of Cr(1), their complex conjugate describe the Cr(2) site.

	Cr-1 (x, y, z)	Cr-2 $(-x, y{+}½, -z)$	Cr-3 $(x{+}½, y{+}½, -z)$	Cr-4 $(-x{+}½, y, z)$
Γ_1 ψ_1	(1,0,0)	($-\eta^*$,0,0)	(η^*,0,0)	($-$1,0,0)
Γ_2 ψ_3	(0,0,1)	(0,0,$-\eta^*$)	(0,0,η^*)	(0,0,$-$1)

Table 4.8: Refinement of the magnetic structure for spins pointing in various directions or planes for the two data sets (D20 and E5). The column headings define the axes along which the magnetic moment is non-zero and m_x, m_y and m_z are the moment sizes along these axes. All moment lengths are in units of μ_B. The R-factors are also included in order to compare the quality of the fits, R_B is determined from the integrated intensities: $R_B = \sum |I_\mathrm{OBS} - I_\mathrm{CALC}| / \sum |I_\mathrm{OBS}|$. Helical and sinusoidal models give the same R-factors.

	D20 data ($T = 10$ K)				E5 data ($T = 6$ K)			
	m_x	m_y	m_z	R_B	m_x	m_y	m_z	R_B
ab	2.62(5)	1.39(11)		0.045	2.63(8)	1.63(13)		0.138
	2.18(1)	$= m_x$		0.066	2.15(3)	$= m_x$		0.135
ac	2.50(4)		1.88(7)	0.032	2.58(3)		1.98(4)	0.089
	2.24(2)		$= m_x$	0.068	2.31(2)		$= m_x$	0.108
bc		2.40(8)	2.23(10)	0.212		2.24(12)	2.14(15)	0.212
		2.35(2)	$= m_y$	0.209		2.20(4)	$= m_y$	0.214
a	2.88(2)			0.067	3.02(4)			0.173
b		3.11(2)		0.190		2.89(7)		0.222
c			3.30(3)	0.255			3.06(8)	0.329

Since the two Cr^{3+} ions in the unit cell are unrelated by symmetry, there can be an arbitrary phase between them. Altogether the number of refinable parameters are reduced to five: the prefactors of two basis function per Cr site and the phase between the two Cr sites. The refined phase between the Cr(1) and Cr(2) sites was close to $-2\pi/3$, which was afterwards fixed to this value for all the refinements. For comparison the prefactors of several other combination of basis functions were refined as well, see Table 4.8. The magnetic moments on the different sites can be calculated from the refined coefficients of the basis functions, see Sec. 2.3.3. The table shows the magnetic moment components along the three crystallographic axes for the different structures. The coefficients of the two inequivalent Cr^{3+} sites were refined independently, but found to have the same size within standard deviation. Therefore they were constrained to be equal for all subsequent refinements. As can be observed, the results of the refinement are ambiguous since several structures have similar R-values. The powder data favours models where the spins point either in the ab or ac planes; however in these cases it is not possible to distinguish between helical or sinusoidal order because the phase difference between the two prefactors cannot be refined. Nevertheless the sinusoidal structures can probably be excluded indirectly as shown in Ref. [96]. For example the refined moment lengths for the ac structure are m_x=2.50(4)μ_B and m_z=1.88(7)μ_B. Assuming sinusoidally modulated order, the maximum moment length would exceed the spin only magnetic moment of Cr^{3+}: $\sqrt{m_x^2 + m_z^2} > gS$. On the other hand the maximum size of the moment in the helical structure would be the x component 2.50μ_B.
The refined value of the ordering wave vector was $(0, 0.332(3), 0)$ from D20 at 10 K and $(0, 333(5), 0)$ from E9 at 2.1 K. According to the refinement the k-vector is equal to $(0, 1/3, 0)$ within standard deviation, the difference between the diffraction patterns generated by these two $\boldsymbol{k}_m$ values is negligible (see inset of Fig. 4.15(a)). These results are also in agreement with the more precise incommensurate value of (0,0.3317(2),0) published previously by Chapon et al. [96] In the case of helical structures, the phase of $-2\pi/3$ together with $\boldsymbol{k}_m = (0, 1/3, 0)$ means that the angle between all intraplanar nearest neighbour spins is 120°. This structure is expected only for the ideal triangular lattice where all nearest neighbour exchange interactions are equal and Heisenberg. It is therefore surprising to find it on the distorted triangular lattice of α-$CaCr_2O_4$.

4.3.3.2 Single crystal diffraction

As a complementary study, single-crystal diffraction was performed at 6 K in the magnetic phase. For the magnetic structure determination the twin ratio and scale factor were fixed to the values obtained from fitting the single-crystal nuclear peak intensities.

The data were refined with the same set of possible magnetic structures as for the neutron powder diffraction refinements. The R_F-factors and resulting magnetic components are listed in Table 4.8. The single-crystal data is also unable to distinguish between the helical and sinusoidal models. The measurable $|M(Q)|^2$, the absolute value squared of the magnetic structure factor, is identical for a helical structure and a sinusoidal structure with same moment components due to the orthorhombic crystal symmetry. In the case of *ac* sinusoidal structure, two magnetic S-domains can exist in the sample. If the two domains have equal weight the resulting magnitude of the structure factor is the same as in the case of the helical structure. For the orientation of the spin-plane, the best fit gives the *ac* plane in agreement with the powder diffraction.
The temperature dependence of two magnetic peaks (1,2/3,-1) and (1,4/3,0) were measured on the single-crystal sample in the temperature range $6 \leq T \leq 50$ K, see Fig. 4.16. The intensity is proportional to the square of the magnetization which is the magnetic order parameter and can be fitted with $I(T) = C \cdot ((T - T_N)/T_N)^{2\beta}$, where C is an overall constant and β is the critical exponent. The data were fitted between 32 K and 48 K and gave a transition temperature of T_N=42.6(1) in agreement with the heat capacity data. The exponent is $\beta = 0.1815(9)$ for both peaks. Although the function fits well, according to theory the magnetic phase transition of a stacked triangular lattice is first order, and the value of β is not universal. [106] Several noncollinear easy axis antiferromagnets have a sinusoidal phase just below T_N which precedes the helical phase, e.g. $CuCrO_2$ [107] and β-$CaCr_2O_4$. [108] However there is no sign of such a phase in α-$CaCr_2O_4$, the temperature dependence of the two measured Bragg peaks is smooth and the ordering wave vector remains constant up to T_N (Fig. 4.16 (b)).

4.3.3.3 Spherical neutron polarimetry

Spherical neutron polarimetry was used to produce additional information to complement the previous neutron diffraction techniques. A number of different overlapping magnetic Bragg peaks were measured for all three twins. For example the strongest magnetic Bragg peak, (1,4/3,0) indexed in the coordinate system of twin 1, overlaps with (1,2/3,1) from twin 2 and (1,-2/3,1) from twin 3. The (1,4/3,0) peak was also measured for twins 2 and 3, where it is described as (1,2/3,1) and (1,-2/3,1) respectively in the coordinate system of twin 1 (see Fig. 4.13). The polarization matrices for these three peaks labelled using the coordinate system of twin 1 are displayed in the first three rows of Table 4.9.
The observed data show strong depolarization of the scattered beam when polarization of the incoming beam was polarised along y or z due to the presence of structural twins.

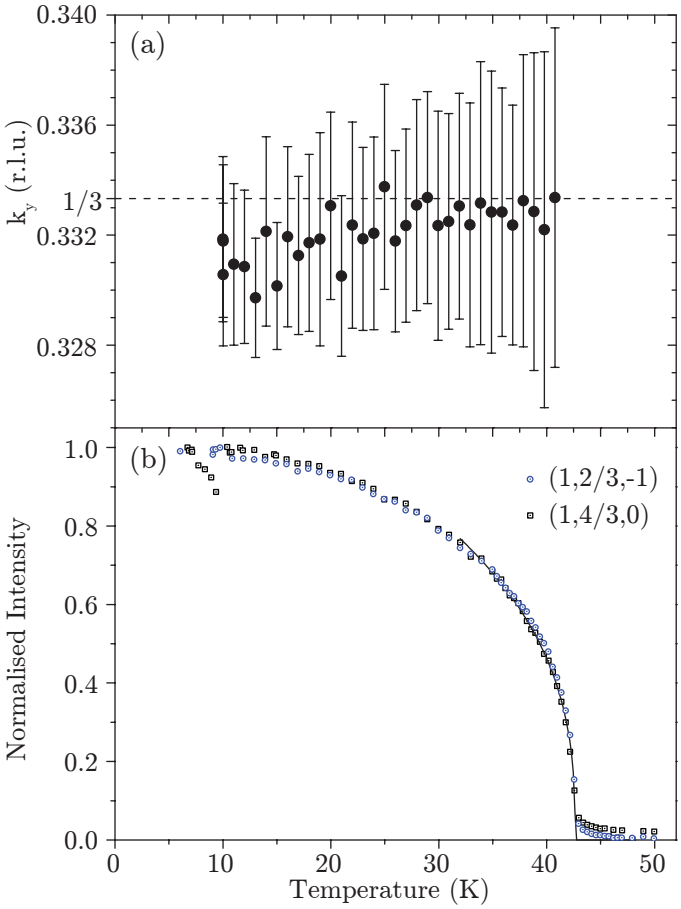

Figure 4.16: (a) Temperature dependence of k_y refined from D20 powder data, (b) temperature dependence of the (1,2/3,-1) and (1,4/3,0) magnetic reflections of the single-crystal sample, measured on E5. The black line is the fit described in the text.

This makes it difficult to draw conclusions about the axis of the spin helix by simply inspecting the data. Therefore, simulations were performed of the different models of magnetic ordering and compared to the data. The polarization matrices were calculated using Blume–Maleev equations [52] assuming the phase difference between Cr(1) and Cr(2) is $-2\pi/3$ and the ordering wave vector is (0,1/3,0).

Polarization matrices of three possible spin structures (helical order in the *ab*, *ac* and *bc* planes) were simulated for all three twins for the (1,4/3,0) magnetic reflection in the coordinate system of twin 1, see Table 4.10. The corresponding sinusoidal structures would produce the same matrices because of the orthorhombic symmetry, similarly to the single crystal unpolarized case. For the helical models the issue of chirality also

Table 4.9: Polarization matrices measured using TASP at 1.5 K for the three strongest magnetic reflections (rows 1-3) and results of the refinement which yields a helical structure with spins lying almost entirely within the *ac* plane (rows 4-6).

		$\boldsymbol{P}_\mathrm{i}^x$	$\boldsymbol{P}_\mathrm{i}^y$	$\boldsymbol{P}_\mathrm{i}^z$	$\boldsymbol{P}_\mathrm{i}^x$	$\boldsymbol{P}_\mathrm{i}^y$	$\boldsymbol{P}_\mathrm{i}^z$
(1,4/3,0)	$\boldsymbol{P}_\mathrm{f}^x$	-0.907(3)	-0.083(9)	-0.136(9)	-0.887	0.000	0.000
	$\boldsymbol{P}_\mathrm{f}^y$	-0.086(9)	0.086(9)	-0.029(9)	0.000	0.098	-0.022
	$\boldsymbol{P}_\mathrm{f}^z$	0.013(9)	-0.037(9)	-0.100(9)	0.000	-0.022	-0.098
(1,2/3,1) (+60°)	$\boldsymbol{P}_\mathrm{f}^x$	-0.880(5)	0.054(9)	0.043(9)	-0.887	0.000	0.000
	$\boldsymbol{P}_\mathrm{f}^y$	-0.048(10)	0.372(8)	0.082(9)	0.000	0.352	0.081
	$\boldsymbol{P}_\mathrm{f}^z$	0.033(10)	0.063(9)	-0.369(9)	0.000	0.081	-0.352
(1,−2/3,1) (+120°)	$\boldsymbol{P}_\mathrm{f}^x$	-0.903(4)	-0.001(9)	-0.014(9)	-0.887	0.000	0.000
	$\boldsymbol{P}_\mathrm{f}^y$	-0.036(10)	0.400(9)	-0.092(9)	0.000	0.407	-0.112
	$\boldsymbol{P}_\mathrm{f}^z$	0.004(10)	-0.110(9)	-0.402(9)	0.000	-0.112	-0.407

needs to be addressed. In these cases the centrosymmetry of the paramagnetic space group is broken in the magnetically ordered phase, allowing the appearance of two chiral domains for each twin with opposite vector chirality. The polarization matrix of the chiral domains differs only in the $\mathcal{P}_{\mathrm{yx}}$ and $\mathcal{P}_{\mathrm{zx}}$ terms, which change sign with opposite chirality, see Table 4.10. Because the measured values for these two elements are rather small (less than 0.136(9)), it is assumed that the population of the two chiral domains are equal for all three twins. Fitting the weight of the chiral domains also don't improve the data significantly. In this case the measured $\mathcal{P}_{\mathrm{yx}}$, $\mathcal{P}_{\mathrm{zx}}$ would be zero because they cancel each other out. This, together with the presence of structural twins, explains the strong depolarization when the incident beam has y and z polarization. In order to make a comparison with the measured (1,4/3,0) reflection, the contributions of the three twins weighted by their volume ratios were added together and multiplied by the beam polarization and are listed in the last three columns of table 4.10. Comparison of the simulated matrices to the experimental matrix in the first three rows of Table 4.9 under $(1, 4/3, 0)$, clearly show that the *ac* helical structure describe the data best.

To precisely determine the orientation of the spin rotation plane, the polarization matrices of several other reflections were also considered: (3,4/3,0), (5,4/3,0), (1,8/3,0) for all three twins. A computer code was written to fit these matrices to both sinusoidal structures with arbitrary spin direction and helical structures with arbitrary spin rotation plane. Spherical coordinates (θ, φ) were used to parametrize the spin direction in

Table 4.10: Calculation of the polarization matrices of the $(1, 4/3, 0)$ reflection for helical order in the ab, ac and bc planes. The $\pm$ sign is for the two opposite vector chiral domains. The contributions of all three structural twins are listed. Columns 10–12 give the combined contribution weighted by the ratio of the twin volumes and assuming equal chiral domain ratios, the last three columns are multiplied by the finite instrumental polarization.

		Twin 1			Twin 2 (+60°)			Twin 3 (+120°)			Together			$\mathcal{P}_{xx}$ corrected		
		$\boldsymbol{P}_\mathrm{f}^x$	$\boldsymbol{P}_\mathrm{f}^y$	$\boldsymbol{P}_\mathrm{f}^z$	$\boldsymbol{P}_\mathrm{f}^x$	$\boldsymbol{P}_\mathrm{f}^y$	$\boldsymbol{P}_\mathrm{f}^z$	$\boldsymbol{P}_\mathrm{f}^x$	$\boldsymbol{P}_\mathrm{f}^y$	$\boldsymbol{P}_\mathrm{f}^z$	$\boldsymbol{P}_\mathrm{f}^x$	$\boldsymbol{P}_\mathrm{f}^y$	$\boldsymbol{P}_\mathrm{f}^z$	$\boldsymbol{P}_\mathrm{f}^x$	$\boldsymbol{P}_\mathrm{f}^y$	$\boldsymbol{P}_\mathrm{f}^z$
	$\boldsymbol{P}_\mathrm{i}^x$	-1.000	0.000	0.000	-1.000	0.000	0.000	-1.000	0.000	0.000	-1.000	0.000	0.000	-0.883	0.000	0.000
ab	$\boldsymbol{P}_\mathrm{i}^y$	0.000	1.000	0.000	$\mp$0.977	0.090	0.193	$\pm$0.977	0.090	-0.193	0.000	0.562	0.005	0.000	0.496	0.005
	$\boldsymbol{P}_\mathrm{i}^z$	0.000	0.000	-1.000	$\mp$0.977	0.193	-0.090	$\pm$0.977	-0.193	-0.090	0.000	0.005	-0.562	0.000	0.005	-0.496
	$\boldsymbol{P}_\mathrm{i}^x$	-1.000	0.000	0.000	-1.000	0.000	0.000	-1.000	0.000	0.000	-1.000	0.000	0.000	-0.883	0.000	0.000
ac	$\boldsymbol{P}_\mathrm{i}^y$	$\mp$0.997	-0.072	0.000	$\pm$0.765	0.589	-0.262	$\pm$0.765	0.589	0.262	0.000	0.105	-0.004	0.000	0.093	-0.003
	$\boldsymbol{P}_\mathrm{i}^z$	$\mp$0.997	0.000	0.072	$\pm$0.765	-0.262	-0.589	$\pm$0.765	0.262	-0.589	0.000	-0.004	-0.105	0.000	-0.003	-0.093
	$\boldsymbol{P}_\mathrm{i}^x$	-1.000	0.000	0.000	-1.000	0.000	0.000	-1.000	0.000	0.000	-1.000	0.000	0.000	-0.883	0.000	0.000
bc	$\boldsymbol{P}_\mathrm{i}^y$	$\mp$0.647	-0.762	0.000	$\pm$0.647	-0.762	0.000	$\mp$0.647	-0.762	0.000	0.000	-0.762	0.000	0.000	-0.673	0.000
	$\boldsymbol{P}_\mathrm{i}^z$	$\mp$0.647	0.000	0.762	$\pm$0.647	0.000	0.762	$\mp$0.647	0.000	0.762	0.000	0.000	0.762	0.000	0.000	0.673

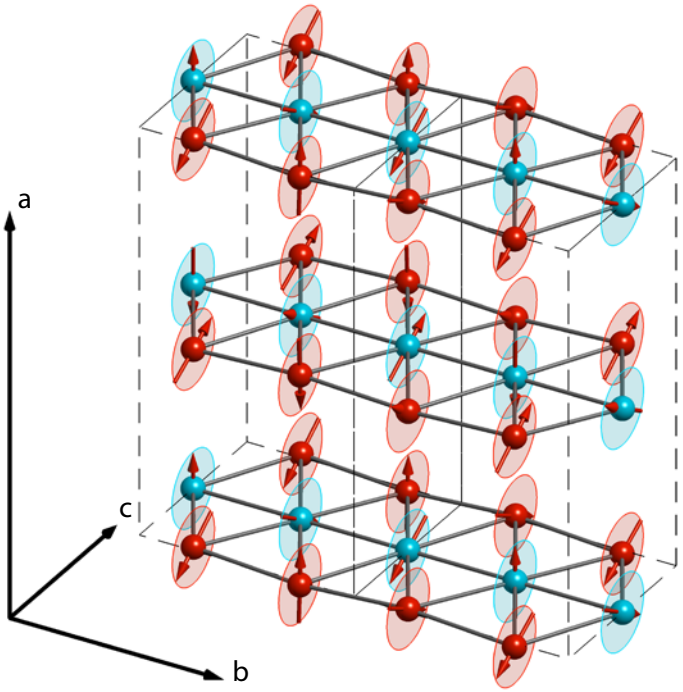

Figure 4.17: Magnetic structure of α-$CaCr_2O_4$, determined from spherical neutron polarimetry. Cr(1) and Cr(2) are represented by the blue and red spheres respectively.

the case of sinusoidal structures, or the vector $\boldsymbol{n}$ normal to the rotation plane in the case of helical structures (where the c axis corresponds to $\theta = 0°$). The equally populated S-domains were generated from the magnetic structure by applying one of the mirror planes (m_{yz} and m_{xz}) or the glide plane ($n_{xy}(1/2,1/2,0)$) and the contribution from all domains were averaged. The other fitted parameters were the beam polarization ($\mathcal{P}_{xx}$) and the ellipticity of the spin helix (ratio of the moment length along the two main axis of the ellipsoid, where $\mu = m_{\mathbf{v}}/m_{\mathbf{u}}$, $\mathbf{u} = \mathbf{n} \times (\mathbf{c} \times \mathbf{n})$ and $\mathbf{v} = \mathbf{u} \times \mathbf{n}$). Fitting was performed by minimizing the function $R_w^2 = \sum w|\mathcal{P}_{OBS} - \mathcal{P}_{CALC}|^2 / \sum w\mathcal{P}_{OBS}^2$, where $w = 1/\sigma^2$ and σ is the counting error and the summation was over all elements of all measured polarization matrices.

By fitting this general model to all the measured polarization matrices the magnetic structure was found to be helical with spins rotating in the ac plane; the resulting polarization matrices are listed in the last three rows of Table 4.9. The extracted parameters are: $\mathcal{P}_{xx} = 0.887$, $\theta = 87°$, $\varphi = 91°$, $m_a/m_c = 0.99$. With these parameters excellent agreement with the data could be achieved ($R_w = 0.074$). To check how sensitive the refinement is to the spin-plane orientation, the values of θ and φ were fixed to other

directions. All other possible structures (ab and bc helical, a, b and c sinusoidal) give a value of R_{w} that is more than four times larger. According to the result the spin components along a and c are close to equal in agreement with Ref. [96], whereas the unpolarized single crystal and powder refinements show larger a component by a factor of 1.3.

Using spherical neutron polarimetry it has been possible to prove unambiguously that α-$CaCr_2O_4$ has a 120° helical magnetic structure with spin moments rotating in the ac plane perpendicular to the ordering wave vector $\boldsymbol{k}_{\mathrm{m}} = (0, 1/3, 0)$. The magnetic structure is illustrated in Fig. 4.17.

4.3.3.4 Diffuse scattering

To learn more about the nature of the magnetic phase transition, diffuse scattering was measured on the E2 flat cone neutron diffractometer. Measurements were carried out at base temperature (4 K) and at two temperatures above the Néel temperature (44 K and 50 K). Figure 4.18 shows the (1,k,l) plane measured at T=44 K. The plot is a cut from the measurement with the $(0, k, l)$ crystal orientation. It is the plane of the strongest magnetic reflections. Although the temperature is above T_{N}, still magnetic Bragg peaks can be observed. This might be due to the improper sample temperature control. Beside the magnetic Bragg peaks several sharp nuclear Bragg peaks can be observed as well, several of them consists of 3 peaks. These come from grains, slightly misaligned in the (100) plane. Beside grains some of the peaks are twinned, as shown on Fig. 4.13. The non-integer peaks belong to one of the two rotated crystallographic twins. The magnetic Bragg peaks look broader than the instrumental resolution

The crystal was measured in the $(h, k, 0)$ orientation as well, to determine interplane correlations, see Fig. 4.19. The two measured magnetic Bragg peaks are (1,4/3,0) and (3,4/3,0). Upon heating the sample through the transition temperature, the peak width perpendicular to the triangular planes increases rapidly. At 50 K rod-like scattering can be observed, which is characteristic of 2D magnetic correlations.

To understand the nature of the magnetic peak broadening, several cuts were extracted from the (h,k,0) plane data, see Fig. 4.20. At 4 K the magnetic Bragg peaks are approximately isotropic and have Gaussian line shape. The width is larger than the instrumental resolution. At 44 K the peaks consists of two Gaussians with different width. The narrower component is slightly broader then the peaks at 4 K. At 50 K the sharp peaks disappeared and only the broad component is visible.

To explain the measured data the temperature has to be corrected. The temperature of the 44 K measurement has to be below the Néel temperature. Using this assumption the

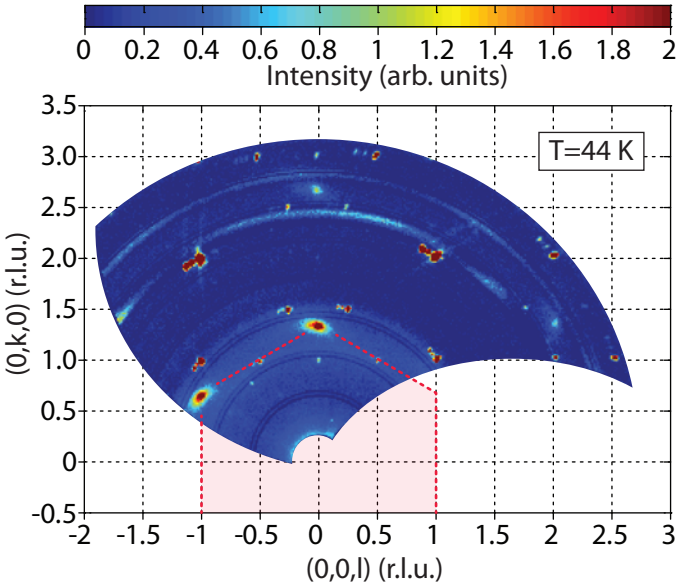

Figure 4.18: The (1,k,l) reciprocal plane measured on E2 just below the Néel temperature (see text). Pink hexagon shows the twinned magnetic reflections.

narrower component of the magnetic peaks can be identified as Bragg peaks, showing static magnetic correlations. Static correlations disappear above the Néel temperature, therefore no sharp peak is visible at 50 K. Measuring close to the Néel temperature, phonons can excite magnons in the system and the neutrons can scatter on these magnons while loosing or gaining energy. This diffuse scattering is visible as a broad peak centered at the magnetic Bragg peak. The elastic scattering can be separated by applying an analyser, which filters out the inelastically scattered neutrons. The quantitative analysis of the data is unfortunately not possible since the unreliable temperature and data quality. The extracted peak widths are varying from peak to peak. Reliable measurement is possible on a triple axis spectrometer.

4.4 Simulation of the Magnetic Ground State

The 120° helical magnetic structure of α-$CaCr_2O_4$ is exactly the structure expected for an ideal triangular antiferromagnet with Heisenberg nearest neighbour interactions that are all equal. This is a surprising result given that the triangular plane is in fact distorted with two inequivalent Cr^{3+} ions and four independent nearest neighbour exchange interactions. Other distorted triangular antiferromagnets that have been investigated so far all show departures from ideal triangular behaviour with ordering wave vectors that de-

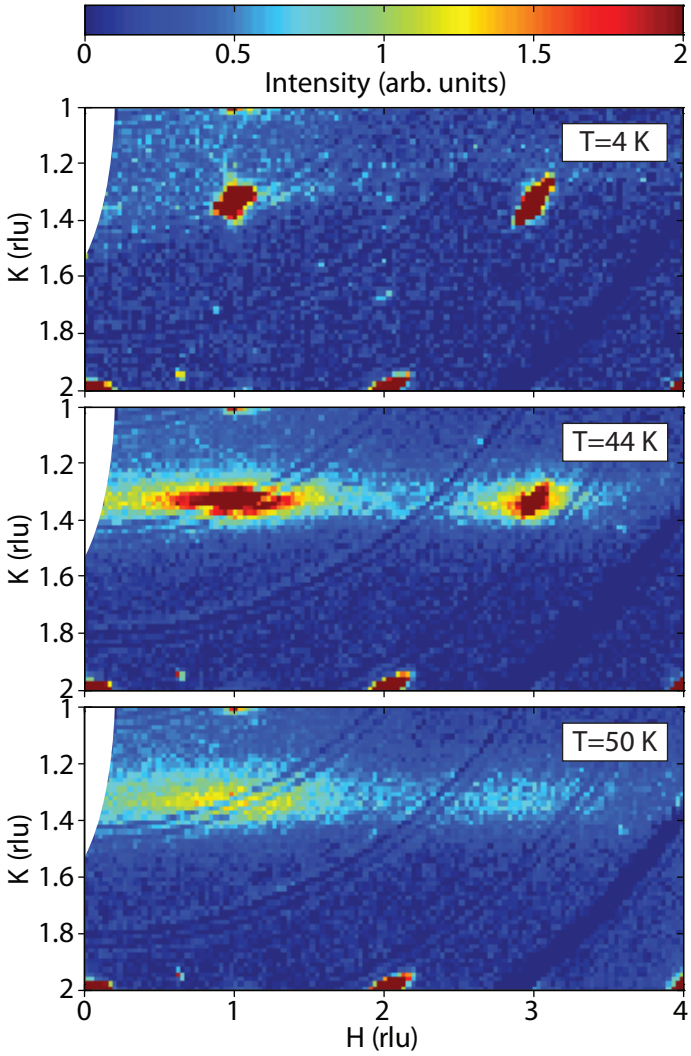

Figure 4.19: The $(h, k, 0)$ reciprocal plane measured on E2 at three different temperatures after the subtraction of aluminium powder lines. Two magnetic Bragg peaks are visible, (1,4/3,0) and (3,4/3,0).

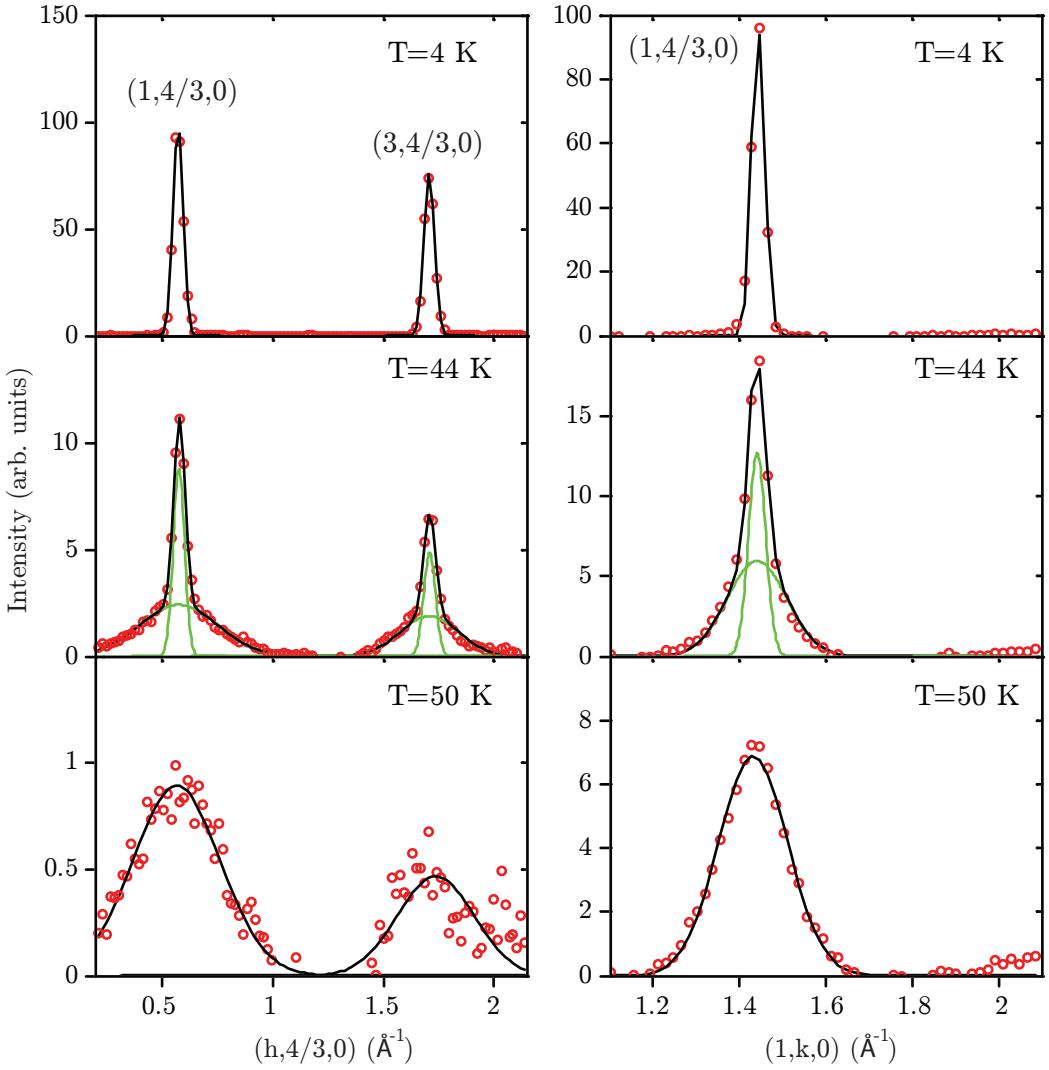

Figure 4.20: Intensities of (1,4/3,0) and (3,4/3,0) magnetic Bragg peaks at different temperatures measured on E2 neutron diffractometer after subtracting a linear background and the aluminium powder lines. Red circles depict data points, black curve is the fit, which might be composed of two Gaussian functions shown as green curves.

viate from (0,1/3,0). Good examples are Cs_2CuCl_4 with $\boldsymbol{k}_m$=(0,0.472,0) [109], $NaMnO_2$ with $\boldsymbol{k}_m$=(1/2,1/2,0) [84] and $CuCrO_2$ with $\boldsymbol{k}_m$=(0,0.329,0) [95]. In this section this apparent contradiction is solved by investigating how the ordering wave vector and relative orientation of the spin moments in α-$CaCr_2O_4$ vary as a function of the exchange interactions.

To determine the ground state of α-$CaCr_2O_4$ one needs to know the effective Hamiltonian which describes the interactions between magnetic moments. The possible interactions between the magnetic moments can be constrained by considering the surrounding crystal structure. The strongest interaction is expected between the in-plane nearest neighbours due to the short distance between magnetic Cr^{3+} ions. Figure 4.11 shows the location of the Cr^{3+} ions on the triangular plane. There are four different nearest neighbour Cr^{3+}–Cr^{3+} distances: d_{ch1}, d_{ch2}, d_{zz1} and d_{zz2} identified by the different coloured lines. Their values are ranging from 2.882 Å to 2.932 Å at 2.1 K. The neighbouring CrO_6 octahedra are edge-sharing and the Cr–O–Cr angle between nearest neighbour Cr atoms are close to 90°, thus the superexchange interactions through oxygen atoms are expected to be weak. On the other hand significant antiferromagnetic direct exchange interactions are expected due to the short distances. [110] Since the interaction depends on the direct overlap of electronic orbitals localized on different atoms, the strength of the interaction is expected to be highly sensitive to the interatomic distance of nearest neighbour Cr^{3+} ions. Therefore for the four different nearest neighbour distances four different values of the direct exchange interactions are expected. The interactions are labelled as the nearest neighbour distances: J_{ch1}, J_{ch2}, J_{zz1} and J_{zz2}, see Fig. 4.11. These interactions are expected to be Heisenberg with little anisotropy.

Although there are two triangular layers per unit cell, they are in fact symmetry related due to the the $m(1/4, y, z)$ reflection plane of the $Pmmn$ space group. The antiferromagnetic stacking of the magnetic layers along the a-axis can be explained by assuming antiferromagnetic interactions between the Cr layers. These interactions are unfrustrated and do not influence the in-plane components of the ordering wave vector. Thus the problem of the magnetic order can be reduced to the determination of the magnetic structure of a single Cr layer. The three-dimensional magnetic structure can be reproduced by stacking these layers antiferromagnetically along a.

The model Hamiltonian will be evaluated on a single triangular layer. To extend the generality of the Hamiltonian, isotropic next nearest neighbour Heisenberg exchange interactions are included as well. It will be shown in Chapter 5 that indeed 2nd neighbour interactions have significant effect. The effective Hamiltonian of the magnetic moments in α-$CaCr_2O_4$ will be expressed as the sum of nearest neighbour and next nearest neigh-

bour interactions on a triangular lattice:

$$\mathcal{H} = \mathcal{H}_{\mathrm{nn}} + \mathcal{H}_{\mathrm{nnn}}. \tag{4.3}$$

The nearest neighbour Hamiltonian has the form:

$$\begin{aligned}\mathcal{H}_{\mathrm{nn}} = \sum_{\mathrm{nm}} & J_{\mathrm{ch1}} \boldsymbol{S}^{2a}_{\mathrm{nm}} \cdot \left(\boldsymbol{S}^{2b}_{\mathrm{nm}} + \boldsymbol{S}^{2b}_{\mathrm{(n\text{-}1)m}} \right) \\ & + J_{\mathrm{ch2}} \boldsymbol{S}^{1a}_{\mathrm{nm}} \cdot \left(\boldsymbol{S}^{1b}_{\mathrm{nm}} + \boldsymbol{S}^{1b}_{\mathrm{(n\text{-}1)m}} \right) \\ & + J_{\mathrm{zz1}} \boldsymbol{S}^{2a}_{\mathrm{nm}} \cdot \left(\boldsymbol{S}^{1a}_{\mathrm{n(m\text{-}1)}} + \boldsymbol{S}^{1b}_{\mathrm{n(m\text{-}1)}} \right) \\ & + J_{\mathrm{zz1}} \boldsymbol{S}^{2b}_{\mathrm{nm}} \cdot \left(\boldsymbol{S}^{1a}_{\mathrm{(n+1)m}} + \boldsymbol{S}^{1b}_{\mathrm{nm}} \right) \\ & + J_{\mathrm{zz2}} \boldsymbol{S}^{2a}_{\mathrm{nm}} \cdot \left(\boldsymbol{S}^{1a}_{\mathrm{nm}} + \boldsymbol{S}^{1b}_{\mathrm{nm}} \right) \\ & + J_{\mathrm{zz2}} \boldsymbol{S}^{2b}_{\mathrm{nm}} \cdot \left(\boldsymbol{S}^{1a}_{\mathrm{(n+1)(m\text{-}1)}} + \boldsymbol{S}^{1b}_{\mathrm{n(m\text{-}1)}} \right), \end{aligned} \tag{4.4}$$

where $\boldsymbol{S}^{i}_{\mathrm{nm}}$ is the spin of the Cr^{3+} site (i$\in \{1a, 1b, 2a, 2b\}$), and n and m are the indices of the unit cell along the b and c axes respectively. The next nearest neighbour Hamiltonian has the form:

$$\begin{aligned}\mathcal{H}_{\mathrm{nnn}} = J_{\mathrm{nnn}} \sum_{\mathrm{nm}} & \boldsymbol{S}^{2a}_{\mathrm{nm}} \cdot \left(\boldsymbol{S}^{2a}_{\mathrm{(n+1)m}} + \boldsymbol{S}^{1a}_{\mathrm{(n+1)m}} + \boldsymbol{S}^{1a}_{\mathrm{(n+1)(m\text{-}1)}} \right) \\ & + \boldsymbol{S}^{2b}_{\mathrm{nm}} \cdot \left(\boldsymbol{S}^{2b}_{\mathrm{(n+1)m}} + \boldsymbol{S}^{1b}_{\mathrm{(n+1)m}} + \boldsymbol{S}^{1b}_{\mathrm{(n+1)(m\text{-}1)}} \right) \\ & + \boldsymbol{S}^{1a}_{\mathrm{nm}} \cdot \left(\boldsymbol{S}^{1a}_{\mathrm{(n+1)m}} + \boldsymbol{S}^{2b}_{\mathrm{n(m+1)}} + \boldsymbol{S}^{2b}_{\mathrm{nm}} \right) \\ & + \boldsymbol{S}^{1b}_{\mathrm{nm}} \cdot \left(\boldsymbol{S}^{1b}_{\mathrm{(n+1)m}} + \boldsymbol{S}^{2a}_{\mathrm{(n+1)m}} + \boldsymbol{S}^{2a}_{\mathrm{(n+1)(m+1)}} \right), \end{aligned} \tag{4.5}$$

where a single J_{nnn} exchange constant is assumed for all nnn interactions.

The above Hamiltonian can be used to explore the possible magnetic ground states of α-$CaCr_2O_4$ as a function of the exchange interaction strengths. In order to do this all the spins are treated as classical vectors of the same length and are restricted to be coplanar based on the observed magnetic structure of α-$CaCr_2O_4$. The aim is to understand how the in-plane wave vector(both k_{y} and k_{z} components) and the directions of the spin moments $\varphi^{i}_{\mathrm{nm}}$ (for the i-th spin in the (n, m)-th unit cell) depend on the magnetic interactions. $\varphi^{i}_{\mathrm{nm}}$ can be written in terms of φ^{i}, the angle of spin $\boldsymbol{S}^{i}$ in the first unit cell and the ordering vector: $\varphi^{i}_{\mathrm{nm}} = \varphi^{i} + \boldsymbol{k}_{\mathrm{m}} \cdot \boldsymbol{r}_{\mathrm{nm}}$, where $\boldsymbol{r}_{\mathrm{nm}}$ is the position of the unit cell. The Hamiltonian can be re-expressed in terms of $\boldsymbol{k}_{\mathrm{m}}$ and φ^{i} by rewriting the dot

product of the spins, for example:

$$\boldsymbol{S}^{i}_{\mathrm{nm}} \cdot \boldsymbol{S}^{i'}_{\mathrm{n'm'}} = S^2 \cos\left[\left(\varphi^{i'} - \varphi^{i}\right) + \boldsymbol{k}_{\mathrm{m}} \cdot (\boldsymbol{r}_{\mathrm{n'm'}} - \boldsymbol{r}_{\mathrm{nm}})\right]. \tag{4.6}$$

φ^{1a} can be set to zero due to the $O(3)$ invariance of the Heisenberg Hamiltonian.
A linear transformation was performed on the exchange constants, which was found to give more insight into the results as will be explained later:

$$\begin{aligned}
J_{\mathrm{nn}} &= \frac{1}{4}(J_{\mathrm{ch1}} + J_{\mathrm{ch2}} + J_{\mathrm{zz1}} + J_{\mathrm{zz2}}),\\
\Delta_1 &= \frac{1}{2J_{\mathrm{nn}}}(J_{\mathrm{zz1}} - J_{\mathrm{zz2}}),\\
\Delta_2 &= \frac{1}{2J_{\mathrm{nn}}}(J_{\mathrm{ch1}} - J_{\mathrm{ch2}}),\\
\Delta_3 &= \frac{1}{4J_{\mathrm{nn}}}[(J_{\mathrm{ch1}} + J_{\mathrm{ch2}}) - (J_{\mathrm{zz1}} + J_{\mathrm{zz2}})].
\end{aligned} \tag{4.7}$$

J_{nn} gives the overall energy scale and does not affect the zero temperature ground state structure, thus together with J_{nnn} there are four parameters to vary. Finally, to determine the ground state, values of $\boldsymbol{k}_{\mathrm{m}}$, φ^{1b}, φ^{2a} and φ^{2b} for a given set of exchange interactions Δ_1, Δ_3, Δ_3 and J_{nnn} the energy of the system was minimized by performing a constrained linear optimization using a simplex minimization algorithm.
Figure 4.21 (a-c) shows the in-plane wave vector as a function of Δ_1, Δ_2 and J_{nnn} with Δ_3 fixed to zero. The reason for the linear transformation of the exchange constants become clear from these plots. They show that the magnetic structure is the 120° helical structure over a large volume of Δ_1, Δ_2 and J_{nnn} parameter space. In this region the ordering wave vector is $\boldsymbol{k}_{\mathrm{m}}$=(0,1/3,0) and the spin-angles inside the unit cell are: φ^{1a}=0, φ^{1b}=240°, φ^{2a}=120° and φ^{2b}=0°. Figure 4.21(d) shows the 120° structure which belongs to the square on the phase diagram on Fig. 4.21(b). Although the crystal structure is distorted, the nature of the distortion is such that when Δ_3 is constrained to zero, commensurate 120° magnetic order is stabilized unless the magnitude of Δ_1, Δ_2 and J_{nnn} are much greater than zero. Surrounding the central phase there is a shaded region where the magnetic ground state structure is a multi-k structure, which is beyond the simplifications of the present model. To determine the precise structure in this region, a Monte Carlo calculation is necessary on an extended unit cell. Beyond the multi-k region the present model becomes valid again and it predicts structures with ordering wave vector of $\boldsymbol{k}_{\mathrm{m}} = (0, 0, k_{\mathrm{z}})$, where k_{z} is a function of the Δ parameters. In this region the relative moment angles inside the unit cell are varying as well. Figure 4.21(e) shows the magnetic structure for a selected point in this region of the phase diagram (circle

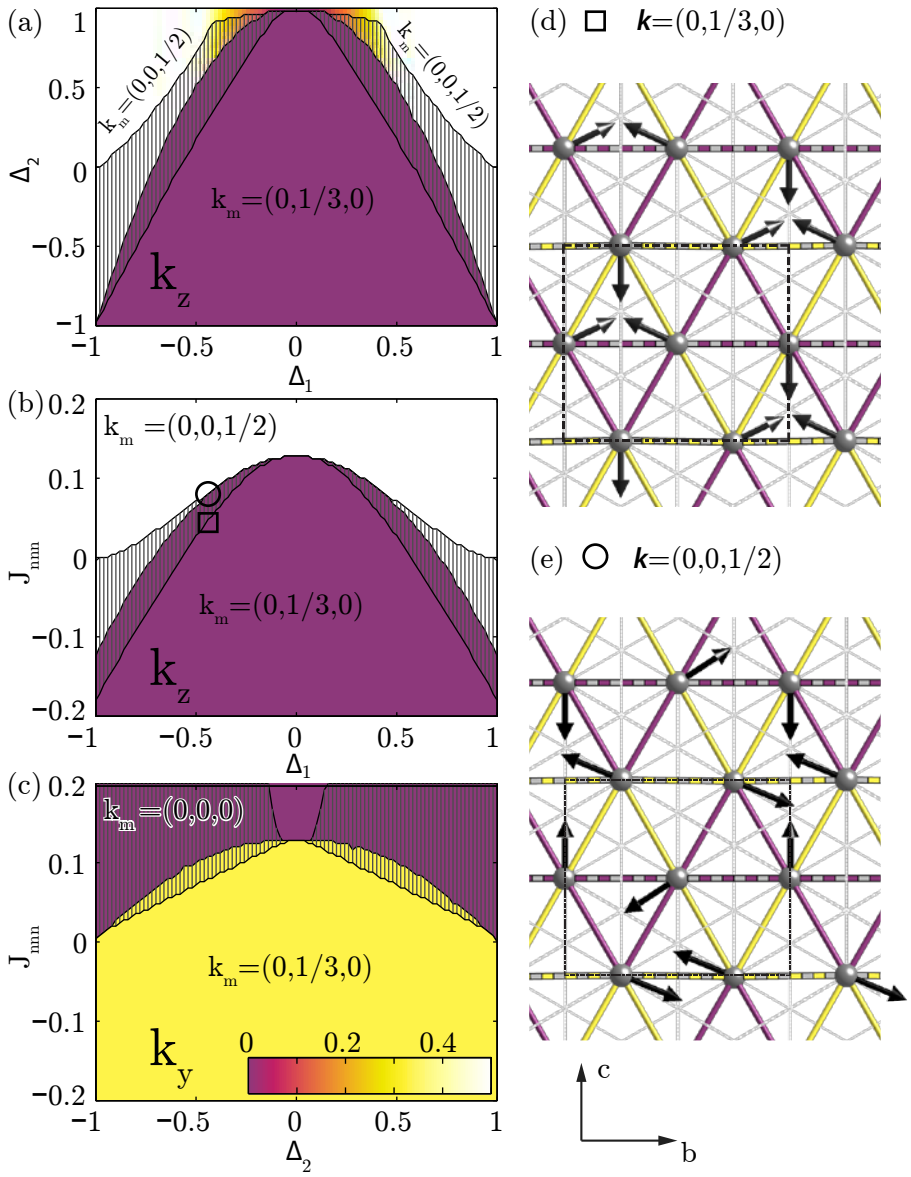

Figure 4.21: (a-b) Ordered magnetic structure of single triangular layer of Cr^{3+} ions, arrows represent the magnetic moments and spins are rotated to the *bc* plane for better visibility. The structures on (a) and (b) belong to the points on the (d) phase diagram marked by square (k_m=(0,1/3,0)) and circle (k_m=(0,0,1/2)) symbol respectively. The solid purple and yellow lines represent J_{zz1} and J_{zz2}, the dashed lines are J_{ch1} and J_{ch2} respectively. Thin gray lines depict next nearest neighbour interactions.(c-e) Magnetic ordering wave vector as a function of Δ_1, Δ_2 and J_{nnn} for $\Delta_3 = 0$, the colours indicate the size of the components of k_m, in the shaded region the magnetic ground state has multi-k structure.

symbol on Fig. 4.21(b)).

If Δ_3 is varied, while the other variables are fixed to zero the value of the ordering wave vector changes continuously, as shown in Fig. 4.22. Even a slight deviation of Δ_3 from zero drives $\boldsymbol{k}_\mathrm{m}$ incommensurate. The slope of k_y at the point $\Delta_3 = 0$ is -0.74, this can be used to estimate the value of Δ_3 for α-$CaCr_2O_4$. From powder diffraction data the upper limit for the difference between k_y and the commensurate 1/3 value is $\mathrm{d}(k_\mathrm{y}) < 0.004$. This means, $|\Delta_3| < |1/(-0.74)| \cdot d(k_\mathrm{y}) \sim 0.005$. Therefore the only condition for the observed magnetic structure is that $|\Delta_3| < 0.005$. Comparison of the different Cr^{3+}–Cr^{3+} nearest neighbour distances reveal that the average of d_{zz1} and d_{zz2} (2.907 Å) is almost the same as the average of d_{ch1} and d_{ch2} (2.912 Å). This explains why the direct exchange interactions appear to obey $(J_{\mathrm{zz1}} + J_{\mathrm{zz2}}) \approx (J_{\mathrm{ch1}} + J_{\mathrm{ch2}})$.

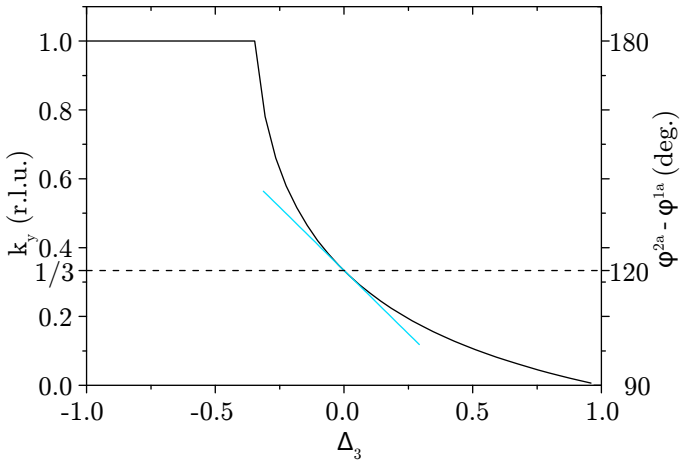

Figure 4.22: Dependence of the y component of the magnetic ordering wave vector $\boldsymbol{k}$ on Δ_3 ($\Delta_1 = \Delta_2 = J_{\mathrm{nnn}} = 0$), right scale shows the phase difference between $\boldsymbol{S}^{1a}$ and $\boldsymbol{S}^{2a}$. At $\Delta_3 = 0$ the tangent of the slope (blue line) is -0.74.

Although α-$CaCr_2O_4$ is distorted from ideal triangular symmetry with two inequivalent Cr^{3+} ions and four different exchange interactions, the nature of the distortion is such that the average of the exchange interactions along any direction are approximately equal. On larger length scales the Hamiltonian is in fact spatially isotropic providing an explanation for the observed 120° helical magnetic ordering.

4.5 Conclusions

In this chapter a detailed investigation of the crystal structure and the magnetic order in α-$CaCr_2O_4$ is presented. The crystal consist of slightly distorted triangular layers of

magnetic Cr^{3+} ions in octahedral oxygen environment stacked along the a-axis. The layers are separated by Ca^{2+} ions. There are four slightly different nearest neighbour Cr^{3+} in-plane distances, which are organized into zig-zag and chain patterns. The magnetic order sets on below T_N=42.6 K. The magnetic structure was determined by utilizing neutron powder diffraction, single crystal diffraction and spherical polarimetry. The structure could be unambiguously identified as a helical structure with ordering wave vector $\boldsymbol{k}_m$=(0,0.332(3),0) and spins lying in the ac plane. It was pointed out that the expected main exchange interactions are direct exchanges between nearest neighbours in the triangular planes. This reveals the intriguing relation between crystal structure and it's ordered magnetic structure. Due to the different nearest neighbour Cr–Cr distances, the strength of the direct exchange interactions are expected to be different, this is seemingly in contradiction with the highly symmetric 120° magnetic structure. Using a classical model and assuming a single-k magnetic structure, the magnetic phase diagram was drawn up. It showed that a single constrain on the magnetic interactions is enough to make the 120° magnetic structure the ground state. This single constrain gives the relation between the value of the nearest neighbour interactions. The average value of the zig-zag interactions have to be the same as the average value of the chain interactions. This indeed can be supported be the crystal structure. The two chain distances have a difference of 0.050 Å and in case of the zig-zag patterns it is 0.004 Å. However the difference between the average of the chain distances and the average of the zig-zag distances is only 0.005 Å.

It is interesting to compare α-$CaCr_2O_4$ to other Cr triangular layer compounds. There are two known isostructural compounds, where the Ca is substituted by either Ba or Sr. The characterization of the magnetic structure is done only on the latter. [111] α-$SrCr_2O_4$ has the same crystal symmetry as α-$CaCr_2O_4$, the atomic positions are very close to that of α-$CaCr_2O_4$. The spacing between triangular layers in α-$SrCr_2O_4$ is larger than in α-$CaCr_2O_4$ by 5% because the larger ionic radius of Sr^{2+} compared to Ca^{2+}. The b and c lattice parameters are also larger by 1%. The four nearest neighbour Cr^{3+} distances of α-$SrCr_2O_4$ are shown in Table 4.5. In comparison with α-$CaCr_2O_4$, the difference between d_{zz1} and d_{zz2} of α-$SrCr_2O_4$ is smaller, the Cr triangles are closer to being equilateral. The magnetism of α-$SrCr_2O_4$ is also very similar to α-$CaCr_2O_4$. α-$SrCr_2O_4$ develops magnetic order below T_N=43 K with an incommensurate wave vector $\boldsymbol{k}_m$=(0,0.3217(8),0). The y component of the ordering k-vector defers only by 0.01 rlu units from the one in α-$CaCr_2O_4$. The size of the ordered magnetic moment in α-$SrCr_2O_4$ at 12 K is 2.34(3)μ_B, which is also very close to α-$CaCr_2O_4$.

Another interesting comparison is provided by $CuCrO_2$. Its magnetic properties re-

Table 4.11: Bond length in α-$SrCr_2O_4$ at 12 K, [111] $CuCrO_2$ at room temperature [112] and α-$CaCr_2O_4$ at 10 K.

	d_{zz1}	d_{zz2}	d_{ch1}	d_{ch2}
α-$SrCr_2O_4$	2.954(4)	2.932(4)	2.936(0)	2.938(0)
$CuCrO_2$	2.975	2.975	2.975	2.975
α-$CaCr_2O_4$	2.938(1)	2.896(1)	2.91102(3)	2.9162(1)

ceived interest since the discovery of its multiferroic behaviour. [107, 113, 114] It has delafossite structure with rhombohedral $R\bar{3}m$ symmetry. The triangular Cr^{3+} layers are undistorted above 24 K with equal interplane nearest neighbour Cr^{3+} ion distances and the stacking pattern of the layers is ABC type. The magnetic structure below T_{N1}=23.6 K is commensurate 120° helical structure with ordering wave vector of $\boldsymbol{k}_m$=(0.3298(1),0.3298(1),0). [80, 95, 115] Upon cooling a small distortion of the triangular layers happen around the Néel temperature ∼24 K [92] which is believed to be driven by spin-lattice coupling. Due to the stacking pattern the interplane 1st neighbour antiferromagnetic interactions are also frustrated and that influences the size of the in-plane components of the k-vector.

The triangular layers of Cr^{3+} ions with the surrounding oxygen octahedra are very similar in the three compounds: α-$SrCr_2O_4$, $CuCrO_2$ and α-$CaCr_2O_4$. Also in the ordered phase the magnetic structure is very similar. The differences between most of the observed properties are the result of the different stacking of the triangular layers. This explains the very weak induced electric polarization upon cooling in magnetic field in α-$CaCr_2O_4$ and α-$SrCr_2O_4$ in comparison of $CuCrO_2$. In the first two due to the unfrustrated antiferromagnetic stacking of the Cr^{3+} sheets the induced electric polarization has opposite sign in adjacent layers and only higher order perturbation terms give nonvanishing electric response to magnetic fields. In contrast the polarization of the triangular sheets in $CuCrO_2$ have the same sign in magnetic field.

5 Magnetic excitations in α-$CaCr_2O_4$

In the previous chapter, the nuclear and magnetic structure of α-$CaCr_2O_4$ were discussed. Using neutron and X-ray diffraction it was shown that the magnetic Cr^{3+} ions build up distorted triangular layers. The magnetic structure is the same as that of the classical Heisenberg triangular lattice antiferromagnet with angles of 120° between nearest neighbours. Although the distortion of the triangular layers are small, the four exchange interactions between nearest neighbour Cr^{3+} spins are expected to differ significantly in value, due to the strong sensitivity of the direct exchange interaction on the spin-spin distances. To determine the strength of the magnetic interactions and to investigate quantum effects on the spin wave excitation spectra, inelastic neutron scattering was measured on powder and single crystal samples of α-$CaCr_2O_4$.

The magnetic excitations of an ordered spin-3/2 system are expected to be well modelled by linear spin wave theory (LSWT). For the spatially isotropic triangular Heisenberg antiferromagnet one sinusoidal, doubly degenerate mode is predicted. However the excitation spectrum for spin-1/2 is expected to strongly deviate from linear spin wave theory; downward renormalization of up to 33% and damping of excitations are expected over large regions of the Brillouin zone, [116, 117, 50] see Fig. 5.1. These quantum effects decrease as the spin moment increases, however even for spin-3/2 a downward renormalization of $\sim$10% is predicted. [118]

The introduction of antiferromagnetic next-nearest neighbour interactions also modifies the excitation spectra and drives the magnetic structure from helical to collinear when the ratio of next nearest to nearest neighbour interactions is greater than a critical value of 0.125. [119] Before the helical to collinear transition LSWT predicts softening of the magnon dispersion at wavevectors around the magnetic Bragg-peaks of the collinear structure. Theoretical studies including quantum fluctuations showed strong deviations from LSWT and predicted that the stripe magnetic order is selected by the fluctuation from the classically degenerate manifold. [119]

It will be shown in this chapter that despite the high symmetry of the magnetic structure the magnetic excitations of α-$CaCr_2O_4$ are highly complex. Furthermore, a significant softening of the spin waves was found around wavevectors such as (0,2,0) and (0,0,1)

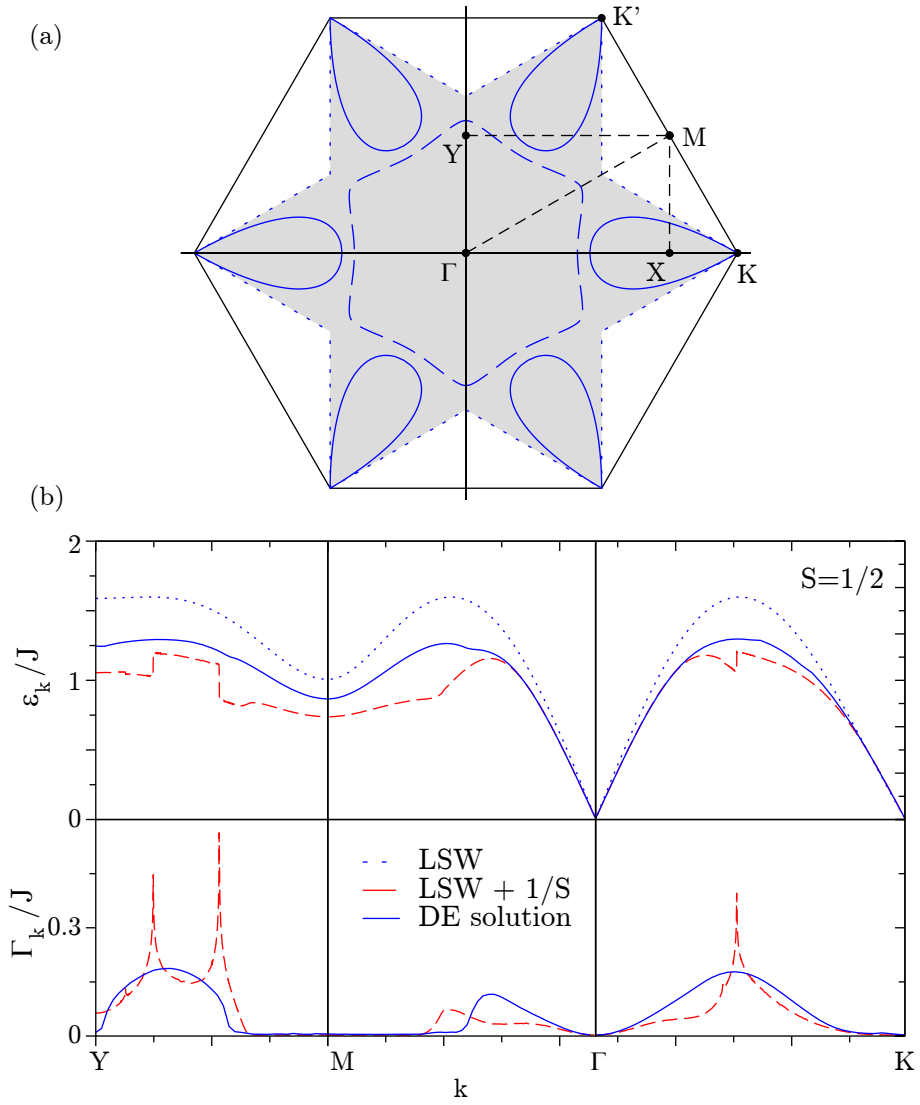

Figure 5.1: (a) reciprocal space of the Brillouin zone of the triangular lattice. (b) predicted dispersion and linewidth for spin-1/2 spatially isotropic triangular lattice Heisenberg antiferromagnet using different theories from Ref. [50]. Dashed blue and red line are linear spin wave theory without and with $1/S$ corrections, the solid blue line is the solution of the Dyson equation. This figure is taken from Ref. [50].

suggesting that it is close to an instability away from the simple 120° structure towards the formation of a new magnetic structure, which is as yet unexplored. This softening is very similar to the one predicted on the triangular lattice close to the helical-collinear phase transition in the presence of next-nearest-neighbour interactions. The extracted exchange constants show a dependence on Cr^{3+}–Cr^{3+}separation that agrees with the trend shown in other chromium oxide triangular antiferromagnets with direct exchange interactions.

5.1 Experiment

Inelastic neutron scattering was measured on both polycrystalline and single-crystal samples of α-$CaCr_2O_4$. The polycrystalline sample has a mass of 3.5 g, same as the one used for neutron diffraction. The single-crystal sample consists of two coaligned pieces with a mosaic spread of 2° which together weighed 416 mg.

Powder inelastic neutron scattering was measured on the Wide Angular-Range Chopper Spectrometer (ARCS) [70] at the Spallation Neutron Source (SNS), Oak Ridge, U.S.A. Incident energies of 40 meV and 60 meV were used providing a resolution of 1.64 meV and 2.35 meV at the elastic line respectively. The sample was cooled in a closed cycle cryostat and measurements took place at base temperature (4.2 K) in the magnetically ordered state and in the paramagnetic phase at 55 K. The background was measured with an empty aluminium sample can and the strong isotropic incoherent scattering of a vanadium reference was used to calibrate the detectors.

To map out the excitations along all reciprocal space directions, a single crystal experiment was performed on the Merlin [72] chopper spectrometer at the ISIS facility, Rutherford Appleton Laboratory, U.K. The incident energy was set to 50 meV, chopper speed 300 Hz and sample temperature 5 K. The crystal was rotated over 120° in 1° steps about the vertical a axis and data was collected for 1 hour at each angle. The data was then transformed in units of energy and wavevector, combined and integrated over h direction using the Horace software. [69] Scattering intensity was normalized using a vanadium reference and the background was subtracted using an empty cryostat plus aluminium rod scan.

Similar data with higher resolution were collected on the Cold Neutron Chopper Spectrometer (CNCS) at SNS. The α-$CaCr_2O_4$ sample with $(0, k, l)$ orientation was measured at T=2.1 K with incident neutron energies of 12 meV and 18 meV providing a resolution of 0.46 meV and 0.83 meV at the elastic line respectively. The sample was rotated around the vertical axis in 1° steps and in total 72 steps were measured for 30 minutes each (1.5

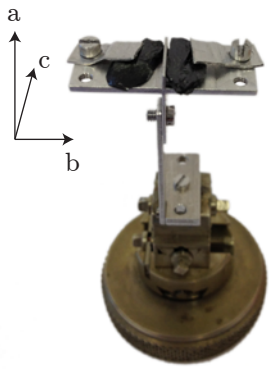

Figure 5.2: Two aligned single crystal samples on the holder attached to the goniometer. The horizontal plane of the sample is the *bc* plane, the screw below the sample can be turned so that the *ab* plane is in the horizontal scattering plane.

C proton charge). Due to the lack of measurement time, no detector normalization and background measurement was performed.

Single crystal experiments were also performed on the Puma Thermal Triple Axis Spectrometer at Forschungs-Neutronenquelle Heinz Maier-Leibnitz (FRM2), Munich. The setup was optimized for high signal by using horizontal and vertical monochromator and vertical analyser focusing. The final neutron wavelength was fixed to $k_F = 2.662$ Å^{-1}, and horizontal collimation of $45'$ was used between monochromator and analyser giving a resolution of 0.75 meV. To measure the magnetic excitations the sample was cooled to 3.5 K, while to separate phonon and magnon signal several scans were repeated above the magnetic phase transition temperature at 280 K.

To determine the strength of the weak interplane coupling and check for an anisotropy gap, scans were performed on the cold neutron high resolution V2/FLEX triple axis spectrometer at HZB. Measurements were performed with two instrument settings, first optimized for neutron intensity using fixed final neutron wavevector $k_F = 1.55$ Å^{-1}, giving an energy resolution of 0.41 meV, the second optimized for energy resolution using final wavevector of $k_F = 1.20$ Å^{-1} (resolution $dE = 0.093$ meV). In both cases horizontal collimation of $60'$ was used between monochromator and sample and a Be filter was applied before the analyser to filter out higher harmonics in the incident beam.

5.2 Results

5.2.1 Powder spectra

Inelastic neutron scattering on powder samples are best performed on time of flight instruments. Since the scattering intensity depends on the absolute value of momentum transfer and energy transfer, the signal of the area-detectors can be combined giving good counting statistics.

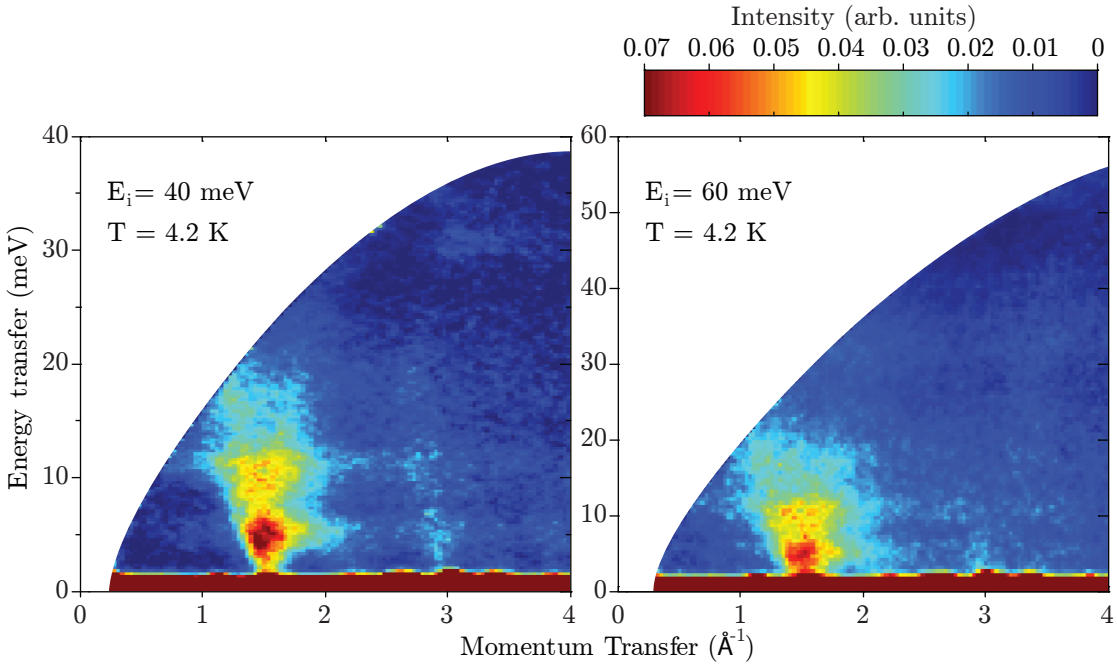

Figure 5.3: Energy and wavevector dependence of ARCS powder spectra of α-$CaCr_2O_4$ for E_i=40 meV (left) and E_i=60 meV (right) measured at T=4.2 K.

The powder spectra of α-$CaCr_2O_4$ measured on ARCS at 4.2 K shows strong inelastic intensity centered around Q=1.54 Å^{-1} at the position of the (1,4/3,0) magnetic Bragg-peak (1.55 Å^{-1}), see Fig. 5.3. Starting from this Q-point the characteristic V-shaped dispersion is visible without any sign of a gap. Van Hove singularities are observed at 5, 11, 17 and 33 meV indicating energies where the dispersion is flat, however no strong singularity is observed at the top of the dispersion, as one would naively expect from spin wave theory of spatially isotropic triangular lattice, see Fig. 5.5. Beside the singularity at the top of the dispersion, LSWT predicts one additional singularity at about 2/3 of the largest spin wave energy and another at lower energy if there is an antiferromagnetic interlayer coupling.

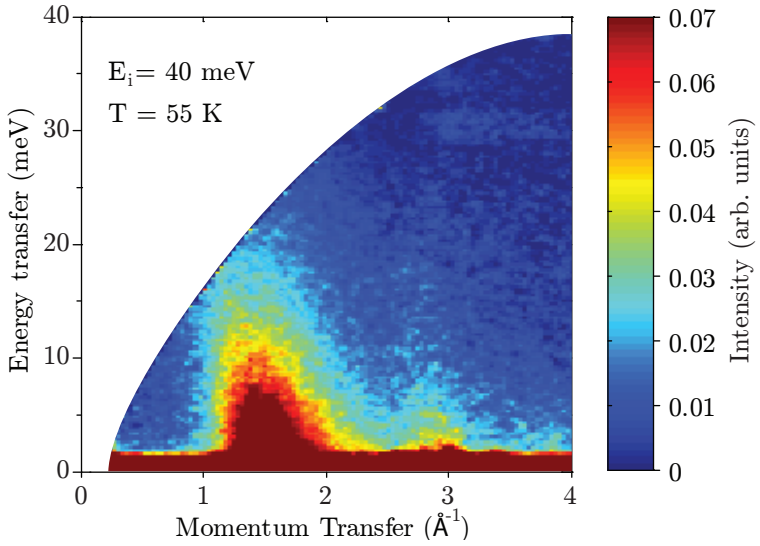

Figure 5.4: Energy and wavevector dependence of ARCS powder spectra of α-$CaCr_2O_4$ in the paramagnetic phase.

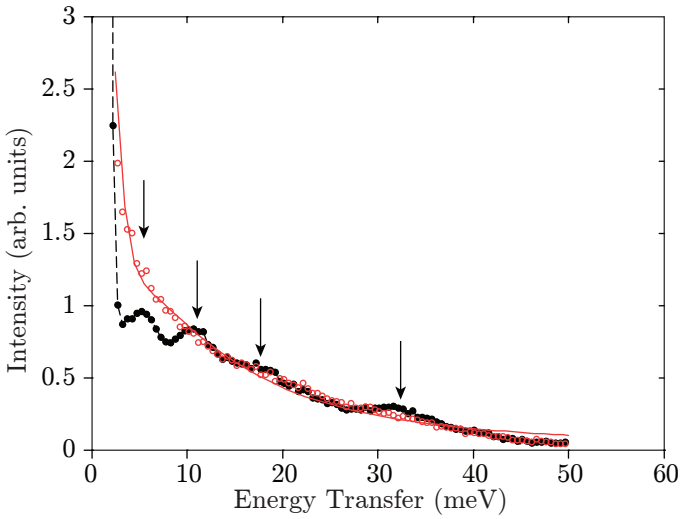

Figure 5.5: Energy cut between 1.5$\leq Q \leq$3.3 Å of ARCS spectra, measured with $E_i = 60$ meV. Sample temperature was 4.2 K (black dots) and 55 K (red circles). Red line is a Lorentzian plus Gaussian function (elastic line) fit to the high temperature data. Arrows indicate the Van Hove singularities at 4.2 K.

Data was also collected at 55 K, see Fig. 5.4. It shows a similar bandwidth as the low temperature scan, but the features of the spectra are smoothed. The energy transfer cut between $1.5 \leq Q \leq 3.3$ Å can be well fitted with a Lorentzian (Gaussian is added to describe the elastic line), see Fig. 5.5. The strong inelastic scattering at low wavevectors indicates that magnetic correlations are present at this temperature.

5.2.2 Single crystal spectra

The full complexity of the spectra of α-$CaCr_2O_4$ is revealed by the inelastic neutron scattering measured on single crystal samples. Using both time of flight instruments and triple axis instruments, the scattering intensity in the 4-dimensional space (3 reciprocal space directions and energy transfer) was explored. Time of flight instruments provide a broad overview of the inelastic spectra since they measure an extended volume in the 4 dimensional scattering space during a single experiment. To measure the scattering intensity at specific reciprocal space points the ideal tool is the triple axis spectrometer. It allows better signal to noise ratio and better resolution at a limited number of important points.

The inelastic neutron scattering experiment on the single crystal sample using Merlin provides an overview of the excitation spectra. Based on the powder inelastic spectra the incident neutron energy was fixed to 50 meV to get an overview of the full range of the excitations. The sample temperature was set to 5 K during the whole experiment. Inelastic scattering was observed up to 37 meV, with several broad dispersive modes in the $(0,k,l)$ plane. The dispersion along the $(h,0,0)$ direction is weak, and practically no dispersion was observed above 10 meV energy transfer. Therefore integrating the measured spectra along the h direction affects the data quality only below 10 meV energy transfer by smearing out features. The following plots are cuts along high symmetry directions from the 3 dimensional scattering space (k,l,E) after integration along the h directions in the range of $-10<h<10$.

The scattering intensity integrated between 10 and 12 meV energy transfer is plotted on Fig. 5.6. In the $(0,k,l)$ reciprocal plane circles of strong scattering are visible. They are centered around the magnetic Bragg peaks. Cuts at higher energy transfer values show, these circles are cones in the (k,l,E) space. It is worth noting that the scattering intensity varies around the cone. At higher momentum transfer rings of constant $|Q|$ are visible, which are aluminium powder lines and could not be completely removed by subtracting the aluminium background.

Several other representative cuts were taken along high symmetry reciprocal space directions, see Fig. 5.7. The plots show that the cone shaped dispersion goes up to 37 meV.

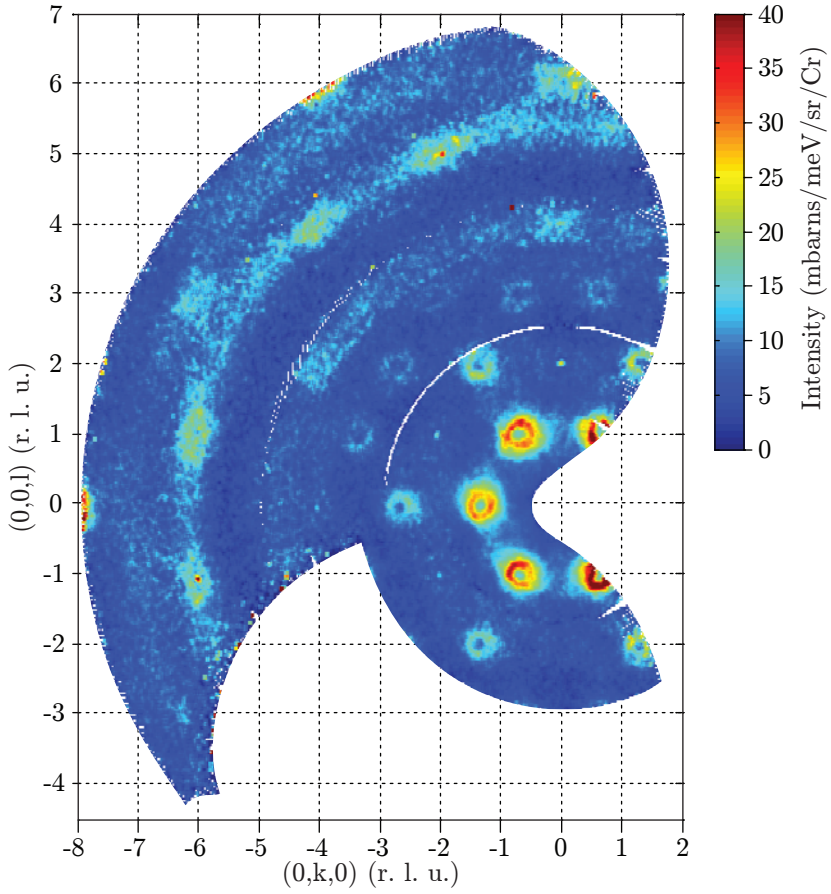

Figure 5.6: Cut of the Merlin data in the $(0, k, l)$ plane, integrated in energy between 10 meV$<E<$12 meV and along h between -10$<h<$10. Scale is in absolute units.

Furthermore at least two other sets of modes can be distinguished between the cones at ∼10 meV and ∼20 meV. There is no scattering intensity above 37 meV, suggesting this is the top of the magnon dispersion.

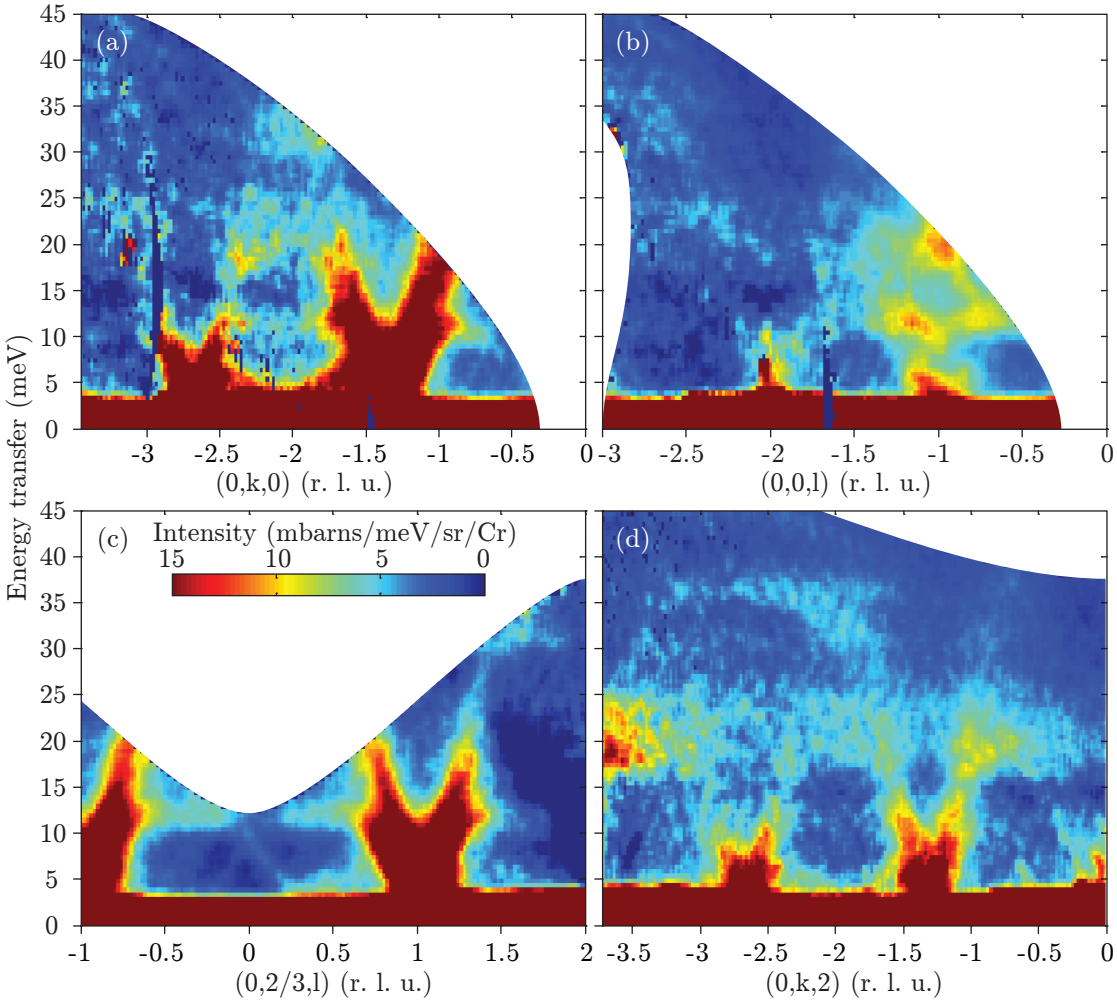

Figure 5.7: Merlin data measured at 5 K, scale in absolute units, aluminium background signal subtracted. Scans were integrated along h between -10<h<10 and (a) along l between -0.05<l<0.05, (b) along k between -0.1<k<0.1, (c) along k between -0.1<$k-2/3$<0.1 and (d) along l between -0.1<$l-2$<0.1.

To gain more insight into the low energy part of the excitations, time of flight inelastic neutron scattering experiment was performed on CNCS. Using low energy incident neutrons the excitations of α-$CaCr_2O_4$ could be mapped out below 10 meV energy transfer, see Fig. 5.8. Fig. 5.8(a) shows constant energy cut in the (0,k,l) plane, data integrated between 1 meV and 5 meV and between -0.2 and 0.2 along h. The inelastic spots are cen-

tered at the magnetic Bragg peaks. Fig. 5.8(b) shows the data integrated between -0.2 and 0.2 along h and l directions. It shows that the excitations are gapped at (0,4/3,0) and (0,8/3,0), and a low energy mode can be observed below 6 meV connecting the two cones. Fig. 5.8(c) is the plot of the (0,k,1) direction, integrated along h between -0.4<h<0.4 and l between -0.2<l − 1<0.2. It shows a similar pattern as the (0,k,0) plot with a low energy mode visible between the cones. Fig. 5.8(d) shows the (0,0,l) reciprocal space direction, integrated along h between -0.2<h<0.2 and along k between -0.2<k<0.2. It shows a very distinctive dispersion which looks like a crossing of two modes at (0,0,1) and 8 meV.

To measure specific directions with better statistics and the temperature dependence at chosen Q points, an inelastic neutron scattering experiment was performed on the Puma triple axis spectrometer. The first measurement was at the (0,k,1) direction, where the CNCS experiment showed low energy modes. Figure 5.9(a) shows the measured spectra with the cone shaped dispersion and two low energy modes on both sides. The soft modes on the left side have a local minima at (0,0,1) and at energies of 7.5 meV and 3.5 meV. The broadness of the cone dispersion is larger than the instrumental resolution convolved with the crystal mosaicity. This suggests it consists of several spin wave modes with slightly different dispersion. At higher Q values (k>1.3) and above 15 meV energy transfer a broad mode is visible. At the (0,2,1) magnetic zone centre the magnetic scattering intensity is expected to be zero, thus the observed intensity indicates phonon scattering. The crossing of modes at (0,0,1) was measured again, along the (0,0,l) direction. Both modes were found, interestingly the 7.5 meV mode is at a maximum point along (0,0,l), thus being a saddle point in the (0,k,l plane. The lower 3.5 meV mode has a local minima for both k and l directions at (0,0,1). This local minima is not related to the magnetic ordering wavevector. Instead it suggests a competing magnetic ground state. At the (0,0,2) magnetic zone centre strong modes are visible, which were remeasured at 280 K. The modes become stronger with increasing temperature in accordance with Bose-Einstein statistics of phonons, this indicates that the broad signal at 20 meV around the (0,0,2) magnetic zone centre is phonon scattering.

Another series of scans were performed along the (4.25,k,0) direction, the h value was chosen to be large enough to allow high energy transfers to be measured. Figure 5.10(a) shows strong scattering with intensity centered around (4.25,4/3,0) and a broad background. This broad background is present at (4.25,0,0) between 12 meV and 25 meV, where the magnetic scattering intensity is expected to be zero. Thus the broad background can be identified as predominantly phonon scattering. To separate the magnetic signal, several scans were repeated at 280 K. Figure 5.10(b) shows two selected scans.

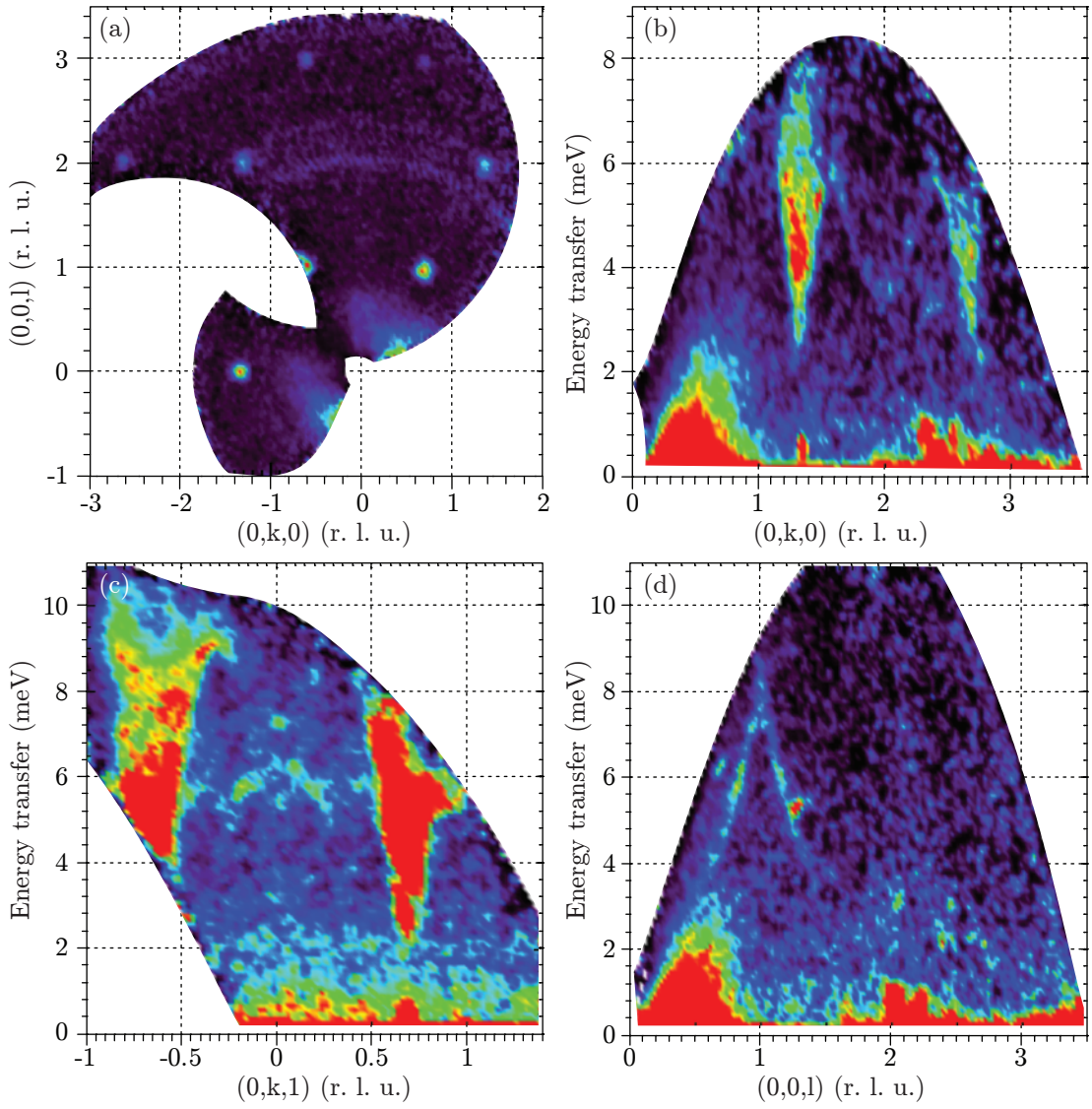

Figure 5.8: Several cuts plotted from CNCS time of flight neutron data. (a) constant energy cut, integrated between 1 meV and 5 meV, (b-d) Q-cuts along specific directions.

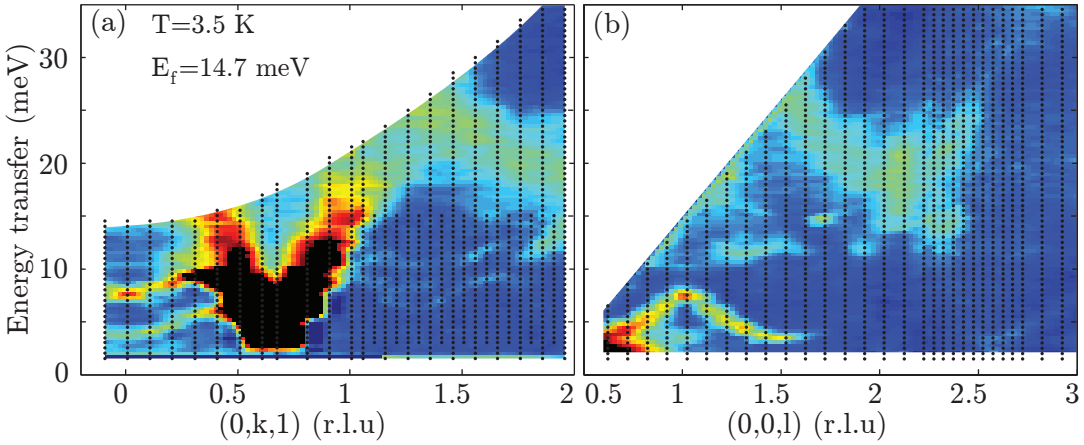

Figure 5.9: Spectra measured on Puma along (a) (0,k,1) and (b) (0,0,l) directions, intensities are in arbitrary units.

The low temperature and high temperature scans have almost identical intensity. This is a very surprising result. Since the magnetic intensity close to the zone centre in the (0,k,l) plane has to vanish therefore the signal should follow Bose–Einstein statistics of phonons, which predicts increasing scattering intensity with increasing temperature. Another explanation can be the mixing of magnetic and phonon scattering, when the intensity decrease of the magnetic scattering compensates for the increase of the phonon scattering with temperature. With this assumption the two signals can be separated by comparing the low and high temperature scans. The intensity of the high temperature scan was scaled back to low temperature assuming phonon scattering only and the scaled intensity was subtracted from the low temperature scan. Thus the phonon background could be eliminated from the low temperature scans. Red diamonds on Fig. 5.10 show the low temperature magnetic scattering intensity after this phonon subtraction. The corrected magnetic intensity decreases as k goes from 4/3 to 0, nevertheless some magnetic intensity remains at k=0.

To observe the temperature dependent evolution of the magnetic excitations, two scans were performed at several different temperature, see Fig. 5.11. The position of the two modes at (0,0,1) are mostly unaffected by increasing temperature, only the intensity decreases as the temperature gets close to the Néel point. Above 42 K a broad inelastic magnetic signal appears. At the (0,4/3,0) point, the gap is smoothly decreasing with increasing temperature up to the Néel temperature scaling approximately with the magnetic order parameter, see Fig. 5.12. This is expected, since the gap is induced by the mean field of the two neighbouring triangular planes. The intensity smoothly increases

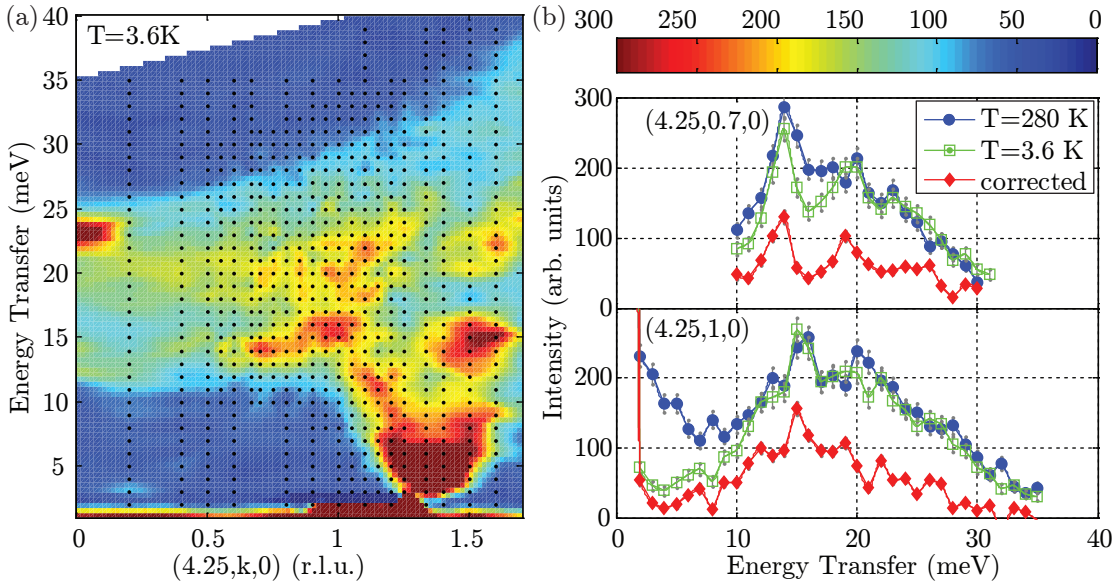

Figure 5.10: (a) inelastic neutron scattering measured on Puma in the (4.25,k,0) plane. (b) specific scans were repeated at 280 K, red line shows the magnetic scattering intensity at 3.6 K after the phonon intensity was subtracted.

as the gap is closing.

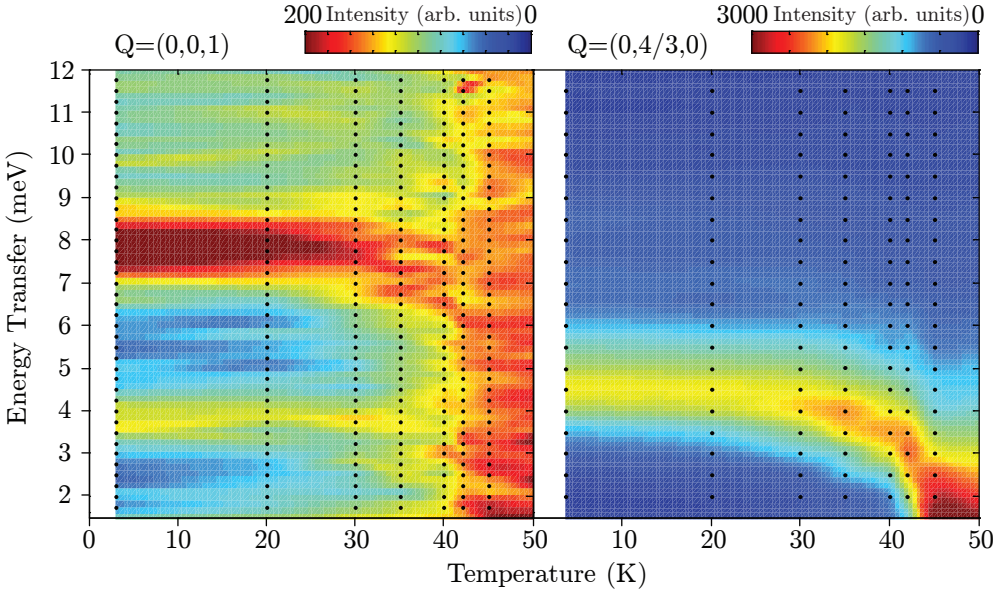

Figure 5.11: Temperature dependence of the inelastic scattering at (0,0,1) and (0,4/3,0) measured on Puma.

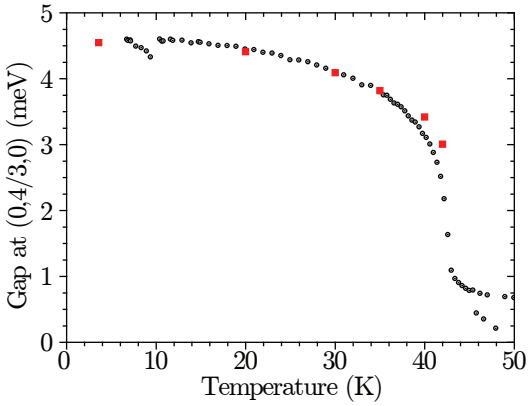

Figure 5.12: Temperature dependence of the gap at (0,4/3,0) measured on Puma, shown by red squares. For comparison the staggered magnetisation (square root of the magnetic peak intensity measured on E5) is scaled to the zero temperature value of the gap, shown by black circles.

In order to probe the interplane coupling, energy scans at the zone centre were repeated at different values of out-of-plane wavevector using the V2 triple axis neutron spectrometer with the high intensity setting. Figure 5.13(a) shows the scan along (h,4/3,0). At the (1,4/3,0) magnetic Bragg peak no gap was observed revealing that the anisotropy is negligible. Even with the high energy-resolution setting, no gap was observed, see Fig. 5.13(b). However the magnetic excitations at (2,4/3,0) where there is no Bragg peak have a gap of $\Delta_{(0,4/3,0)}$=4.0(1) meV revealing a small but significant interaction between adjacent Cr^{3+} triangular planes.

5.3 Discussion

The low temperature inelastic neutron scattering data reveals that the excitation spectra of α-$CaCr_2O_4$ has many features. The powder spectra reveals more Van Hove singularities than the number expected for isotropic TLA, besides there is no definitive top of the dispersion. Single crystal data reveals a complex pattern of several dispersive modes in the triangular plane, some being broad suggesting unresolved structure. The strongest modes correspond to the spin waves in isotropic TLA. Besides soft modes were observed with local minima at reciprocal space points different from the magnetic Bragg peaks. The size of the gap at these local minima points is independent of temperature up to the Néel temperature. The dispersion perpendicular to the triangular planes is simple antiferromagnetic, with a gap at even h values which scales with the order parameter as the temperature increases.

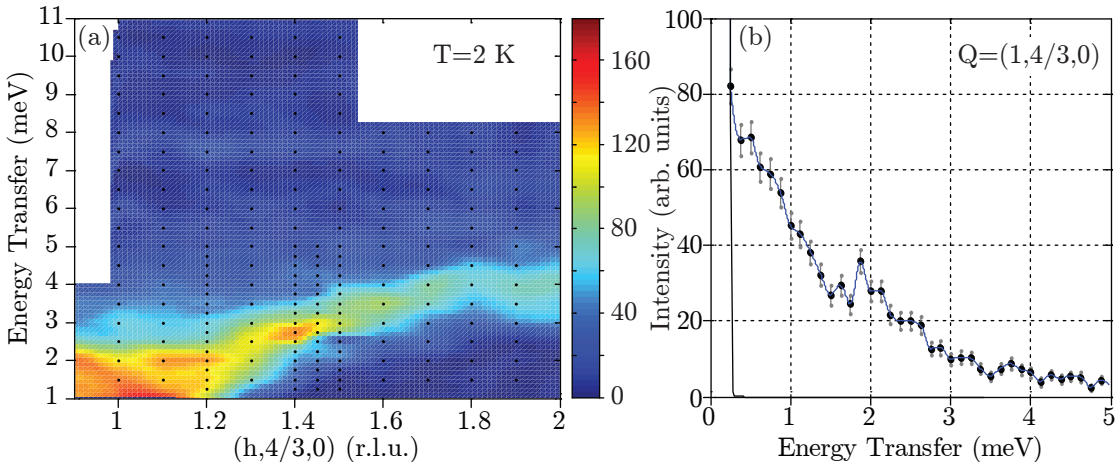

Figure 5.13: (a) dispersion along the h direction, measured on Flex triple axis spectrometer with high intensity setting. (b) measured inelastic intensity at the magnetic Bragg peak using high resolution setting on the Flex, black line shows the fitted Bragg peak.

This rich spectra hints of a microscopic Hamiltonian with several different interaction terms with different strengths. Furthermore the fact that no gap is observed points to vanishing or easy-plane anisotropy. The magnetic ions have a relatively large spin size of 3/2 suggesting that the linear spin wave theory (LSWT) could provide a good description of the inelastic spectra at low temperatures. In subsection 5.3.1, the best fitting microscopic Hamiltonian will be introduced including step by step the necessary terms by comparing the LSWT spectra and cross section with the measured data. Besides magnetic excitations at several Q points, phonon excitations were found. The most surprising result is the continuous development from phonon scattering in the magnetic zone centre to magnetic scattering at the zone boundary. This accompanies the strange temperature evolution of the scattering intensities. The scattering intensity is almost the same at base temperature and at room temperature. In subsection 5.3.2 the magnon-phonon coupling as the possible explanations will be discussed. Subsection 5.3.3 will introduce the possible effects of quantum fluctuations on the observed spectra, which could be enhanced by frustration and competing ground states.

5.3.1 Spin wave analysis

To understand the low temperature inelastic data, linear spin wave theory is applied. A step by step construction of the microscopic Hamiltonian will be introduced here, explaining all the necessary interactions using the constraints developed in Sec. 4.4.

Following the arguments of section 4.4, the magnetic interactions are assumed to be isotropic Heisenberg type.

The 120° low temperature magnetic structure is the same as that of the classical ground state of the spatially isotropic Heisenberg antiferromagnetic Hamiltonian on the triangular lattice. A nearest neighbour antiferromagnetic inplane interaction plus antiferromagnetic interplane interaction is the simplest model which produces the observed magnetic structure. The nearest neighbour interaction strength can be estimated with the J_{mean}=6.48 meV mean field value, determined from the magnetic susceptibility in the paramagnetic state (see Section 4.2.3). The weak antiferromagnetic interplane coupling can be determined from the gap at (0,4/3,0). According to LSWT, the size of the gap is $\Delta_{(0,4/3,0)} = 3S\sqrt{2J_{\mathrm{mean}}J_{\mathrm{int}}}$, thus the deduced interplane coupling strength is 0.061 meV. Using these parameters the spin wave dispersion is calculated as shown in Fig. 5.14. This calculation can be done in two different ways. Due to the symmetry of the magnetic structure and the interactions, the spin wave calculation can be done in a hexagonal unit cell with a single magnetic atom using the rotating coordinate system rather than 3 sublattices. When doing the calculation in the orthorhombic unit cell with 8 magnetic atoms there are however 8 doubly degenerate modes. This multiplicity disappears, when one calculates the correlation function, which reveals that only one mode has non zero intensity.

Although there is a single magnon mode, neutrons see three modes since the measured spin-spin correlation functions contain also the $\omega(\boldsymbol{k}\pm\boldsymbol{k}_{\mathrm{m}})$ expressions, shifting the spectra by $\pm\boldsymbol{k}_{\mathrm{m}}$. Figure 5.15 shows the powder averaged result of the spatially isotropic model. The dispersion has three Van Hove singularities at 4 meV, 19.5 meV and 31.2 meV, less than the number observed in the ARCS spectra, see Fig. 5.3. Furthermore the bandwidth of the excitations is smaller than the observed 37 meV.

The clear discrepancies between the observed and calculated spectra justifies the introduction of a more complicated Hamiltonian. The obvious generalization is to vary the strength of the symmetry inequivalent nearest neighbour couplings. The observed magnetic structure gives restrictions to the possible values of the inplane interactions, see Section 4.4. Since the stacking sequence of the layers is AA, the nearest neighbour interplane interactions are unfrustrated and do not influence the triangular plane magnetic order. To reproduce the observed spectra J_{mean}, Δ_1, Δ_2 and J_{int} were varied. The results were compared to the Puma scans (Fig. 5.9). The main difficulty was to reproduce the two low energy modes, seen at (0,0,1). The best fitting spectra is calculated from the Hamiltonian with J_{mean}=7.5 meV, $\Delta_1 = \pm 0.545$, Δ_2=0.03 and J_{int}=0.05 meV, see Fig. 5.16. Since the zig-zag nearest-neighbour exchange pattern breaks the hexagonal

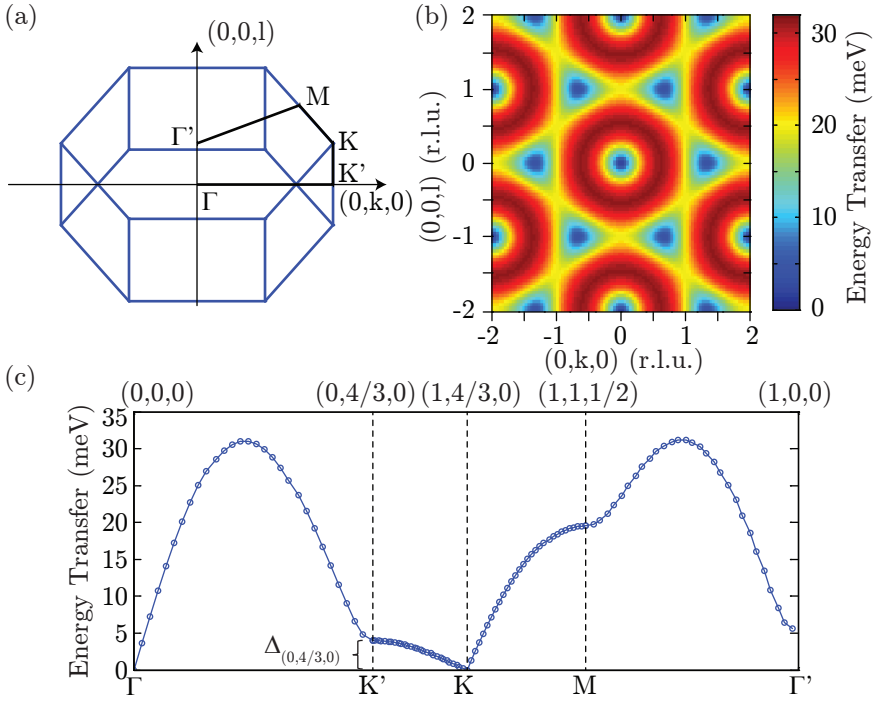

Figure 5.14: (a) blue lines denoting the edges of the magnetic Brillouin zone showing high symmetry points. (b) calculated magnon dispersion of the stacked isotropic triangular lattice in the $(0,k,l)$ plane. (c) dispersion along high symmetry directions.

symmetry, the maximum number of spin wave modes is equal to the number magnetic atoms in the unit cell, when still using the rotating coordinate system. Thus the number of different dispersion curves observable with neutrons are 24, since 8 atoms are in the magnetic unit cell and each mode is tripled by the $\pm\boldsymbol{k}_{\mathrm{m}}$ shift. Furthermore the observed spectra contains contributions from three twins, according to the rules defined in Section 4.3.2.2. Although the above Hamiltonian reproduced some of the characteristics of the observed spectra, e.g. low energy modes, it produces only one low energy mode at (0,0,1) instead of the observed two. Due to the orthorhombic symmetry twin 2 and twin 3 have the same dispersion along $(0,0,l)$ with a single low energy mode at (0,0,1) and with the above Hamiltonian, twin 1 has no low energy mode at this point. Since the breaking of the orthorhombic symmetry is not probable, the second observed low energy mode could originate from twin 1 by introducing more interactions. The main cone shaped dispersion around (0,4/3,0), (1,4/3,0) and equivalent points now contains several modes running close to each other, explaining the observed broadening. On the other hand the calculated low energy mode is a single mode explaining the observed relative sharpness

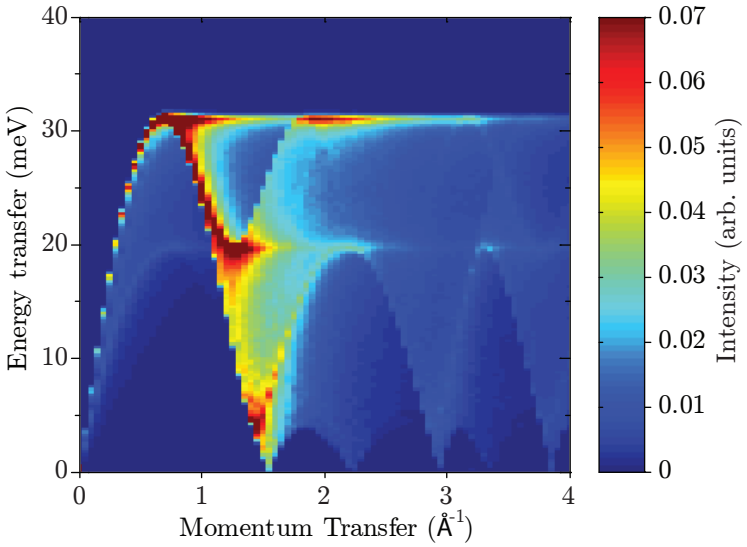

Figure 5.15: Calculated powder spectra of the isotropic triangular lattice, using $J_{\text{mean}} = 6.48$ meV and $J_{\text{int}} = 0.061$ meV.

of this mode.

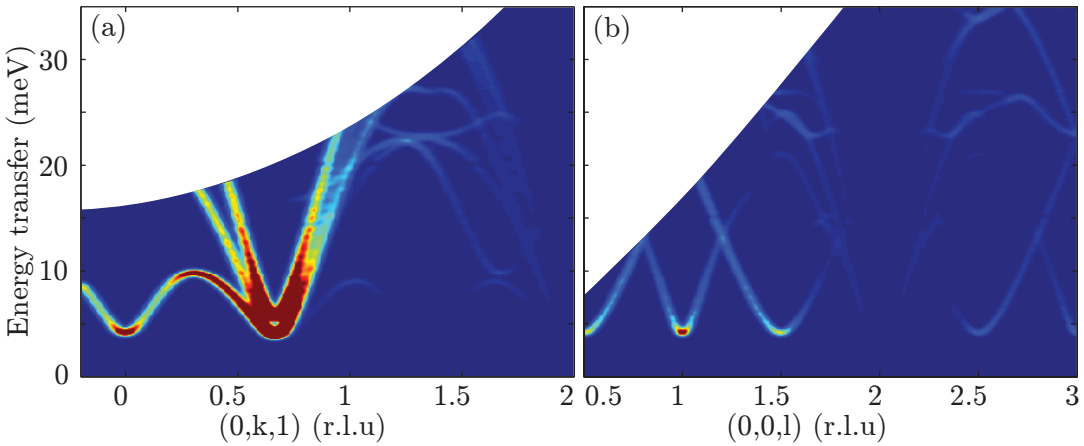

Figure 5.16: Best fitting calculated spin-wave spectra using only nearest neighbour interactions overlapped for all three twins with values: J_{mean}=7.5 meV, $\Delta_1 = \pm 0.545$, Δ_2=0.03 and J_{int}=0.05 meV.

To model the two non-overlapping low energy modes, additional terms are included in the Hamiltonian. The straightforward choice is to consider 2nd neighbour interactions in the triangular plane. There are four different symmetry inequivalent paths connecting 2nd neighbours, see Fig. 5.17.

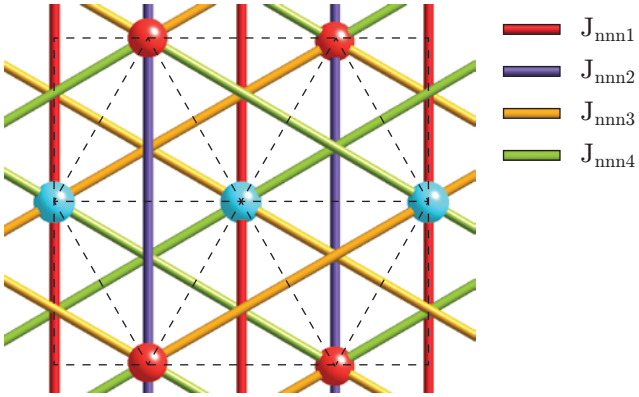

Figure 5.17: Next nearest neighbour interactions in the triangular plane denoted by four different colours, dashed line indicates the unit cell and the nearest neighbour interactions.

Including these four additional interactions, the number of fitted parameters rises to 8: J_{mean}, Δ_1, Δ_2, J_{int}, J_{nnn1}, J_{nnn2}, J_{nnn3} and J_{nnn4}. To achieve the best fit, a least square fitting algorithm was developed. The code has to include heuristics due to the large number of magnetic modes. The Puma, Flex and Merlin data were fitted together. Since the data contains broad modes and several spurious features, e.g. phonons, only energy scans at selected Q points were fitted. For each chosen energy scan, regions were selected where the modes are well defined. In these regions the spin wave intensity was fitted with a sum of Gaussian functions and a constant background. Figure 5.18 shows two selected scans with the fitted curves. In addition a weight was assigned to each peak and more weight was given to measured peaks which are better defined. The selected energy scans with the range, fitted peak positions, weight and intensity is shown in Tab. 5.1. The spin wave dispersion was calculated at the selected Q points using the rotating coordinate system method and a neutron scattering cross section was assigned to each mode. At each selected Q point all the modes were omitted which are out of the energy range (see second column of Tab. 5.1). The remaining modes were binned with 1 meV steps, which is the smallest observed signal full width at half maximum. The bins with the largest intensity were kept and they were sorted according to the energy positions into increasing order. Then an R_{i} value were calculated for each scan, which is the difference between the energy of the observed peak and the position of the calculated energy bin at the same Q point according to the following equation:

$$R_{\mathrm{i}} = \sum_{\mathrm{j}} w_{\mathrm{i,j}} \left(\omega_{\mathrm{i,j}}^{\mathrm{calc}} - \omega_{\mathrm{i,j}}^{\mathrm{fit}} \right)^2 , \tag{5.1}$$

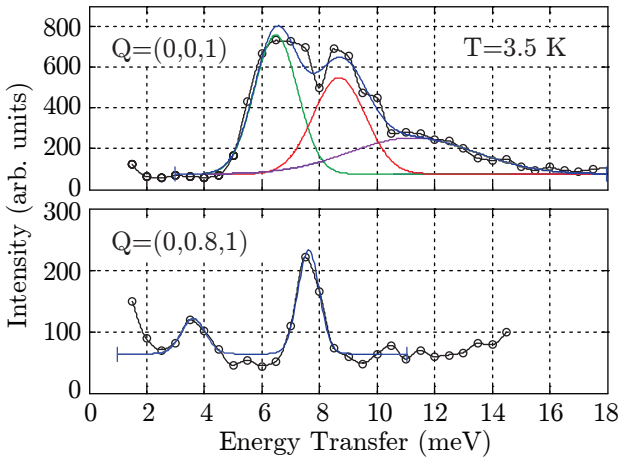

Figure 5.18: Two selected energy scans measured on Puma with the fitted Gaussians plotted separately (red, green blue and purple lines). Blue line shows the fit and the ticks on the end of the line give the range used for the least square fitting of the spin wave dispersion.

where i, and j are the index of the energy scan (row in Tab. 5.1) and the index of the mode in that energy scan (1,2 or 3) respectively. The sum of these R_i values were minimised using the simplex algorithm. While minimising 5.1 the parameters were driven out of the 120° phase. Since during the calculation, the 120° ground state structure was assumed, when the parameters left this phase the spin wave dispersion had non-zero imaginary values. To avoid this, a large R_imag value was added to the R_i sum if the dispersion has imaginary values.

The best fit was obtained with the following values: $J_\mathrm{nn} = 8.8(8)$ meV, $\Delta_1 = \pm 0.34(4)$, $\Delta_2 = 0.03(6)$ and the average next-nearest neighbour strength $J_\mathrm{nnn} = 0.69$ meV. Since the four inequivalent next-nearest-neighbour interaction parameter are strongly correlated no unique set of values were found, a good solution is shown in Tab. 5.2. The values of Δ_1 and Δ_2 correlate well with the Cr^{3+}–Cr^{3+} distances determined by neutron powder diffraction. The larger Δ_1 value arises from the difference between the two zigzag interactions, where the difference between their distances is 0.050 Å. In contrast the difference between the two chain distances is only 0.004 Å thus explaining the small Δ_2 value. The sign of Δ_1 is undetermined, because it does not affect the spin wave spectra, to make the shorter coupling stronger Δ_1 has been set negative.

The fitted dispersion is shown in Fig. 5.19(d,e,f). For the colour plots, the instrumental resolution is convolved with the calculated spectra, using the resolution ellipsoid obtained from Rescal [120]. It uses Popovici's method. [121] To reproduce all the observed modes,

Table 5.1: Selected energy scans, fitted with a maximum of three Gaussians. Range shows the energy range used for the dispersion fitting, E_i and I_i are the centre, intensity of the ith Gaussian, w_i is the weight assigned to each peak according to its quality.

(h,k,l) (r.l.u.)	Range (meV)	I_1 (arb.u.)	E_1 (meV)	w_1	I_2 (arb.u.)	E_2 (meV)	w_2	I_3 (arb.u.)	E_3 (meV)	w_3
(1.50,1.33,0.00)	1-12	42	2.1	2	83	3.4	2			
(2.00,1.33,0.00)	1-12	71	4.0	1						
(0.00,0.00,1.00)	1-11	57	3.6	4	168	7.6	4			
(0.00,0.00,1.50)	1-11	180	3.7	4						
(0.00,0.00,1.20)	1-11	103	5.5	2						
(0.00,0.20,1.00)	1-11	100	4.7	2	128	8.8	2			
(0.00,0.40,1.00)	1-12	135	5.9	2	369	9.0	2			
(0.00,2.00,2.00)	10-35	21	21.9	1						
(0.00,1.50,1.00)	14-30	30	25.0	1						
(0.00,2.00,0.00)	9-28	30	11.0	1	30	19.0	1			
(0.00,3.33,0.00)	13-40	30	18.5	1	30	23.5	1	30	35.0	3
(0.00,1.33,1.00)	15-30	30	19.0	1						
(0.00,0.80,1.00)	3-18	30	6.6	1	30	8.6	1	30	11.4	1
(0.00,0.66,1.00)	2-18	30	3.8	1						
(0.00,1.20,1.00)	3-15	30	6.5	1	30	8.0	1	30	11.0	1
(0.00,0.80,1.00)	3-18	30	8.5	1	30	11.0	1			
(0.00,0.00,1.10)	2-10	30	4.0	1	30	7.0	1			
(0.00,0.00,1.20)	2-15	30	5.5	1	30	12.0	1			
(0.00,0.00,1.30)	2-15	30	4.5	1	30	11.5	1			
(0.00,0.00,1.40)	2-13	30	4.0	1	30	12.0	1			
(0.00,0.00,0.70)	3-8	30	4.0	1						
(0.00,0.00,0.80)	3-9	30	5.0	1						
(0.00,0.00,0.90)	3-10	30	4.0	1	30	6.5	1			
(1.00,2.00,0.00)	2-10	30	3.5	1						

Table 5.2: Values of the fitted exchange parameters, for definition see text.

Name	J_{zz1}	J_{zz2}	J_{ch1}	J_{ch2}	J_{int}
Value (meV)	5.8(6)	11.8(14)	9.1(10)	8.6(15)	0.027(1)
Cr–Cr dist. (Å)	2.939	2.889	2.911	2.907	5.529
Name	J_{nnn1}	J_{nnn2}	J_{nnn3}	J_{nnn4}	
Value (meV)	0.11	0.31	0.96	0.90	

the dispersion of the three crystallographic twins were combined and weighted by their experimentally determined volume fractions. The fit of the spectra agrees well with the measured data. The soft modes could be modelled adequately, the two observed modes at

(0,0,1) are coming from different twins. The cone shaped dispersion with broad modes is also adequately modelled, although there is some discrepancy with the intensities along (0,k,1). Other discrepancy comes from the convergence of the fitting. The fitted parameters had to be restricted into the 120° phase, otherwise the spin wave fit would drive the system out of the 120° phase. As a result, the fitted exchange parameters put the system at the phase boundary of the 120° structure in parameter space, see Fig. 4.21. This shows that either more terms are necessary in the Hamiltonian (e.g. third nearest neighbour interactions) or that the LSWT is not adequate in describing the excitations and the neglected quantum fluctuations modify the spectra significantly.

Plotting the fitted exchange parameters on the magnetic phase diagram, (open square in Fig. 4.21 (b)), shows that the parameters are at the boundary between the $\boldsymbol{k}_{\mathrm{m}}$=(0,1/3,0) and the multi-k magnetic phase. The stronger the next nearest neighbour interactions, the smaller the gap of the low energy mode at the ordering wavevectors of the new structure (e.g. (0,0,1)) and the closer the system moves towards the phase boundary. Above a critical value, the magnetic structure changes, and these points become the Bragg peaks of the new structure. A further small increase of J_{nnn} puts the system beyond the multi-k region into a new structure (open circle in Fig. 4.21 (b)). Here the angles between nearest neighbours along J_{zz2} and J_{ch2} is 120°, while along the weakly coupled J_{zz1} zig-zag they have the energetically unfavourable angle of 60° and along the J_{ch1} chain the angles are 180°, see Fig. 4.11(e).

The fitted nearest neighbour exchange constants of α-$CaCr_2O_4$ can be compared with those of several other chromium oxide delafossites: $CuCrO_2$ [91, 115], $AgCrO_2$ [122], $NaCrO_2$ [123], $LiCrO_2$ [124], $KCrO_2$ [125], $DCrO_2$, $HCrO_2$ [126] and $PdCrO_2$. [127] The fitted exchange constants J_{zz1}, J_{zz2}, J_{ch1} and J_{ch2} are plotted as a function of Cr^{3+}–Cr^{3+} distance in Figure 5.20. They agree well with the trend of the related compounds. This provides further evidence for the validity of the linear spin wave model and shows that the exchange mechanism between nearest neighbours is mainly due to direct overlap of the electronic $t_{2\mathrm{g}}$ wave functions. [128]

Wulferding et al. [129] measured Raman scattering and high-field EPR on α-$CaCr_2O_4$. These techniques probe the magnetic dynamics similarly to inelastic neutron scattering but with different length and time scales. The Raman spectra shows broad two magnon scattering with three peaks observed below the 50 meV experimentally accessible maximum Raman shift. These peaks correspond to the first three Van Hove singularities seen on the inelastic powder spectra of α-$CaCr_2O_4$. The clear anomaly of the integrated signal at the Néel temperature confirms its magnetic origin. The EPR linewidth below $T*$=24 K follows a power law as a function of temperature. This is the sign of a vortex

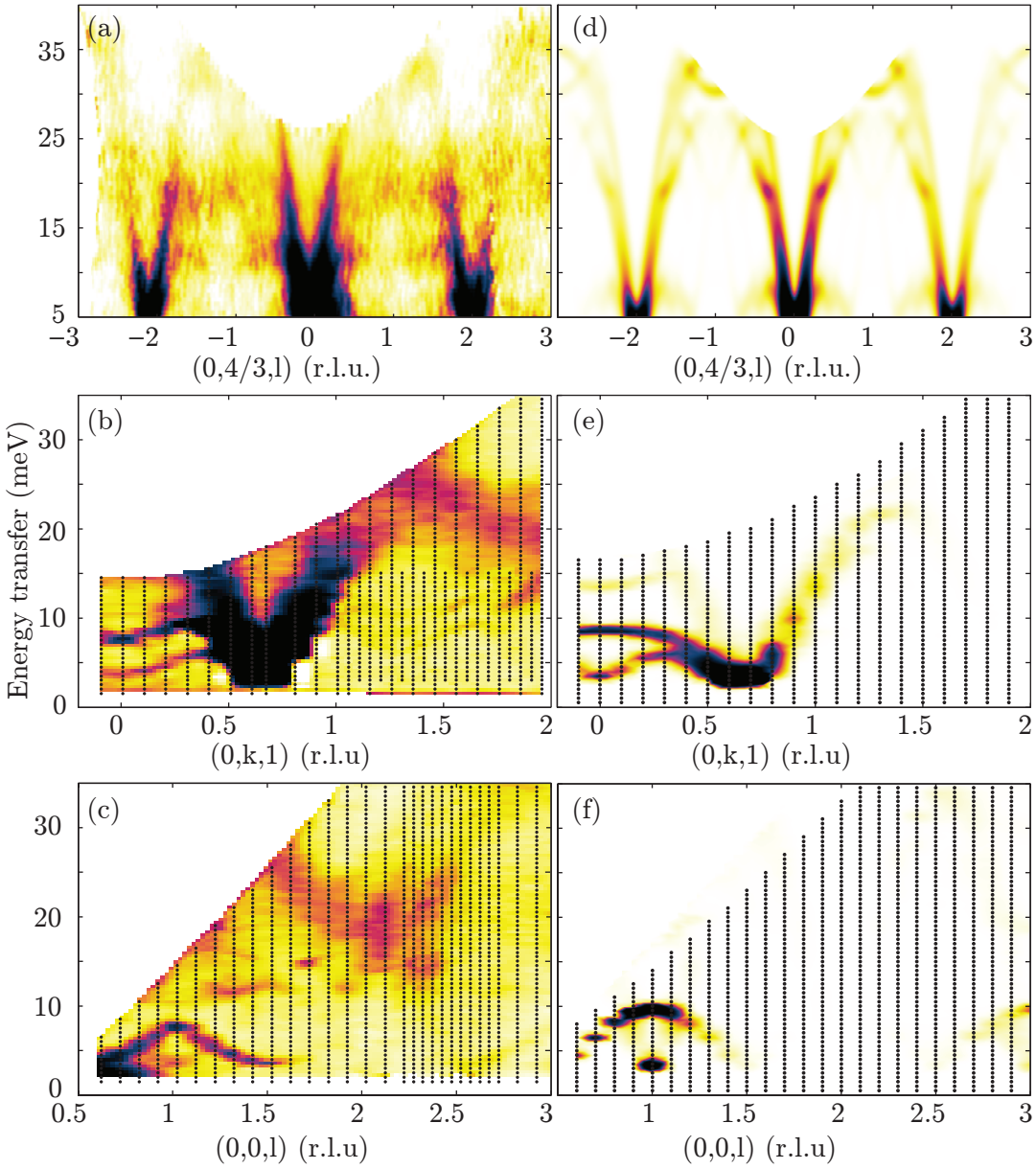

Figure 5.19: (a) spectra measured on Merlin, (b-c) spectra measured on Puma, black dots denote measurement points. (d-f) calculated spin wave spectra using the best fit parameters. Intensities are in arbitrary units.

melting or Kosterlitz-Thouless (KT) transition. However due to the slow dynamics and low energy scale, this KT transition is invisible even for cold neutron inelastic scattering. The EPR signal above the Néel temperature shows a resonance with average g-factor of $g = 1.98$ and critical broadening with a critical exponent comparably smaller than for

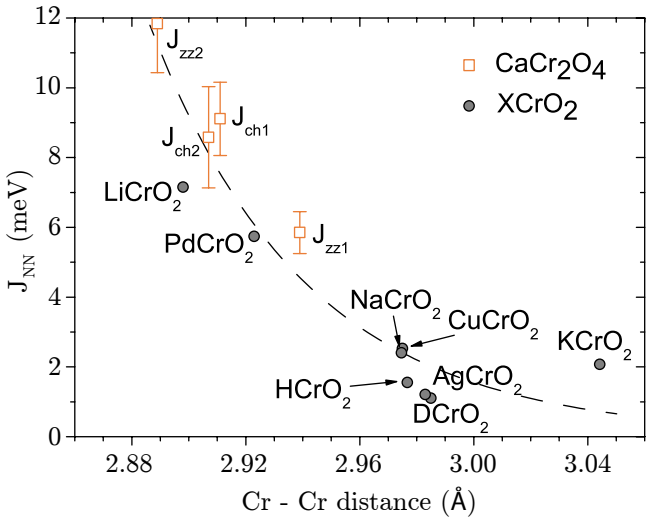

Figure 5.20: The exchange interaction strength as a function of Cr^{3+}–Cr^{3+} distance for several chromium oxide delafossite compounds. The dashed line is a guide to the eye with functional form $A \cdot x^B$ and B=-52(8).

other triangular antiferromagnets. This is ascribed to the proximity of this system to a quantum critical point.

5.3.2 Understanding phonons

On the inelastic neutron scattering spectra of α-$CaCr_2O_4$ unexpectedly strong phonon scattering was observed. Broad bands of scattering were measured up to 280 K and the temperature dependence of the scattering intensity follows Bose-Einstein statistics. This excludes a magnetic origin, since magnetic scattering intensity is expected to decrease with temperature. Another surprising result is that at certain Q points this scattering is continuously connected to magnetic scattering, e.g. along the $(4.25, k, 0)$ line. In these overlapping regions the scattering intensity is almost independent of temperature. The aluminium can and sample holder can be excluded as a source of the non-magnetic scattering, since the spectra of aluminium powder has no sharp upper and lower bounds and covers the whole energy range between 0 meV and 40 meV. [130]

A possible explanation for the observed overlapping magnon and phonon scattering is that a coupling exists between the two types of excitation. This can be exchange striction type, where the magnetic exchange strength varies strongly with the ion–ion distance. This may be the case for α-$CaCr_2O_4$ since the inplane nearest neighbour coupling between Cr^{3+} ions is mainly direct exchange and it is very sensitive to the inter-

ion distance which can be modulated by the phonons. The coupling can be expressed as an additional term in the spin Hamiltonian:

$$\mathcal{H}_{\text{mag-phon}} = -J_{\text{c}} \sum_{<ij>} \hat{\boldsymbol{e}}_{\text{ij}} \cdot (\boldsymbol{u}_{\text{j}} - \boldsymbol{u}_{\text{i}}) \boldsymbol{S}_{\text{i}} \cdot \boldsymbol{S}_{\text{j}}, \tag{5.2}$$

where J_{c} is the magnon-phonon coupling constant, $\hat{\boldsymbol{e}}_{\text{ij}}$ connects the centres of the magnetic ions i and j, $\boldsymbol{u}_{\text{i}}$ is the displacement vector of the i-th magnetic ion from the equilibrium position. The calculation of the 2 dimensional excitation spectra and correlation functions for the isotropic triangular lattice was done by Jung et al. [131] for different values of J_{c}. The calculated dispersion contains two modes which are mixed magnon and phonon modes, see Fig. 5.21(a). The low energy mode appears if the magnon-phonon coupling reaches the 0.32 critical value, where the dispersion has zero energy at (0,0,1) and symmetry equivalent points, see Fig. 5.21(b). This agrees qualitatively with the measured spectra of α-$CaCr_2O_4$ and in particular with the observed mode softening.

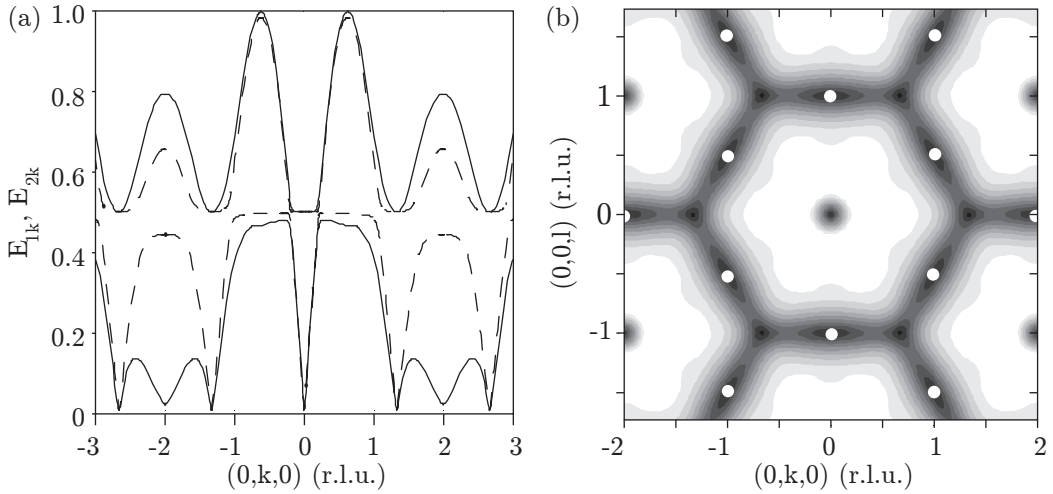

Figure 5.21: (a) dispersion along $(0, 0, l)$ direction of the coupled magnon-phonon spectrum of the triangular lattice with S=1/2 for two choices of spin-phonon coupling, J_{c}=0.1 (dashed), J_{c}=0.32 (solid). Low energy modes can be observed at $(0, 0, \pm 2)$. (b) contour plot of the low energy branch $E_{2\text{k}}$ for J_{c}=0.32, white dots indicate the k points, where $E_{2\text{k}}$ reaches zero at the critical spin-phonon coupling. Plots are taken from the paper of Jung et al. [131].

Comparing the theoretical spectra of the magnon-phonon coupled Hamiltonian with the measured data suggests that beside the orthorhombic distortion and next nearest neighbour interactions the magnon-phonon coupling can have a significant effect on the

spin wave and phonon spectra of α-$CaCr_2O_4$.

5.3.3 Quantum Fluctuations

In section 5.3.1 a detailed spin wave analysis is presented, which gives a good fit to the observed low temperature excitation spectrum of α-$CaCr_2O_4$. The least square fit of the observed spectra using LSWT drives the parameters to the phase boundary of the 120° magnetic phase in the exchange parameter space. An additional constraint had to be included in the fitting to prevent the fit from taking the system out of the 120° phase in contradiction to the diffraction results. This problem suggests that the LSWT has to be improved. This can be done either by including additional terms in the spin Hamiltonian like magnon-phonon coupling or by including the quantum fluctuations (QF) in the calculation. Quantum fluctuations arise from higher order terms in the Hamiltonian, neglected by LSWT. They describe the interaction between magnons and can have several effects. QF can stabilize exotic ground states without magnetic order, there are many possibilities proposed theoretically such as chiral spin liquid [132], spin nematic [133] and spin-Peierls or valence-bond-crystal [134] states. But what is interesting in the context of this thesis is, that QF can affect the magnetically ordered phase as well by modify the classical ground state and the excitations.
To get the reasonably good fit to the inelastic data the interaction parameters are at the phase boundary of the 120° structure. Being close to the phase boundary causes some spin wave modes to be softened. At the reciprocal space points of (0,0,±1) and (0,±1,±1/2) these calculated soft modes have roton like local minima in the $(0, k, l)$ plane and the correlation function is non-zero. Softening of modes at the same Q positions happens in the isotropic triangular lattice model with next nearest neighbour interactions when the ratio of next-nearest to nearest-neighbour-interactions is close to the critical value of 1/8, see Fig. 5.22. In the collinear phase which occurs when this ratio is greater than 1/8, quantum fluctuations lift all but one of the gapless modes at the equivalent position of (0,±1,1/2) thus selecting an antiferromagnetic stripe order from a classically degenerate set of ground state structures [119, 135] - a process known as order by disorder. The strong effect of quantum fluctuations on the low energy modes is connected to the classical degeneracy of the collinear ground state, which does not exist in the helical phase. However the low energy modes are similar in both phases of α-$CaCr_2O_4$, thus it would be interesting to see if QF also alter the observed low energy modes in the 120° phase and adjust to the fitted exchange parameters.
Another effect of quantum fluctuations is to change the ordered magnetic structure close to a phase transition boundary by shifting the boundary away from its classical posi-

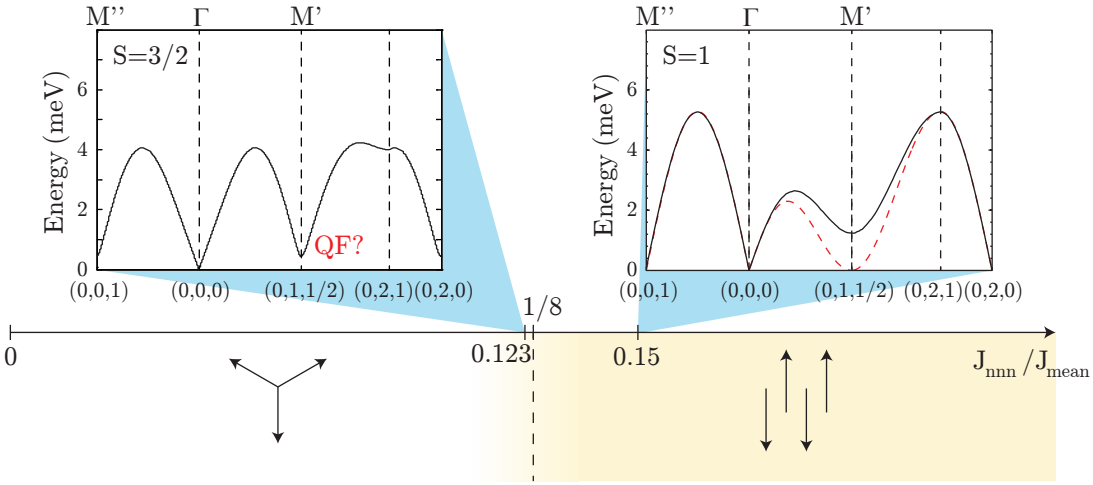

Figure 5.22: Spin-wave dispersion of the isotropic triangular lattice with nnn interactions. Black line shows the result of LSWT, red dashed line shows the 1/S corrections.

tion. This was shown for the triangular lattice antiferromagnet with first second and third nearest neighbour interactions and easy axis anisotropy in magnetic field by Fishman. [136] In general QF favour collinear spin arrangements, but in case of α-$CaCr_2O_4$, the phase boundary separates two non-collinear structures, thus no statement can be made about the direction of the shift without the specific calculation being performed.
It was shown that quantum fluctuations can also renormalise the high energy LSWT excitation spectra of the triangular lattice antiferromagnet. [116, 117, 50] The strongest effect is an overall downscale of the spectra by ∼30% for spin-1/2 and by ∼10% [118] for spin-3/2 isotropic triangular lattice. This shift also produces inaccuracies in the fitted exchange parameters when the data is compared to LSWT.
Single crystal diffraction showed that the staggered magnetisation along the a and c axis have different values, the calculated ellipticity is 1.3, which is either caused by different lengths of spin components along the two axes or by changing the spin angles away from the 120°towards the a axis. To explain the observed ellipticity classically, anisotropy has to be introduced in the form of either single ion term or anisotropic exchange into the Hamiltonian, QF can also influence this ellipticity. [137]

5.4 Conclusions

The measured excitation spectra of α-$CaCr_2O_4$ is rather complex. This complexity stems from the frustrated antiferromagnetic interaction and the large unit cell with at

least nine different isotropic exchange interaction strengths. The orthorhombic distorted triangular layers of Cr^{3+} ions allow four different in-plane nearest-neighbour exchange interaction. Although the distortion is very small the magnitude of the interactions differs significantly due to their direct exchange nature. The spatial pattern of these interactions makes the system frustrated and low dimensional. The frustration can be understood in the framework of classical physics. It causes a helical magnetic ground state and together with the orthorhombic distortion gives rise to a complex spin wave spectra. Using LSWT the measured excitation spectra could be adequately fitted, revealing the values of the exchange interactions. Further confirmation of the results is given by comparing the fitted exchange strengths with other Cr^{3+} delafossites. It reveals that the strength of the nearest-neighbour exchange interactions depend strongly on the inter-ion distance and the fitted nearest-neighbour exchange values of α-$CaCr_2O_4$ fit well into this trend. Besides the LSWT fit showed that significant next-nearest-neighbour interactions are also present.

As a combined effect the fitted exchange parameters put α-$CaCr_2O_4$ at the phase boundary of the 120° magnetic structure. The neighbouring phase is unexplored but expected to be a multi-k magnetic structure. The vicinity of the new phase is revealed experimentally by the observed soft modes in the spectra at reciprocal space positions away from the magnetic Bragg peaks of the 120° structure. This together with discrepancies in the fitting suggest that the observed spectra cannot be explained with LSWT alone. Theoretical calculations which consider higher order terms than LSWT suggest that even for spin-3/2 triangular systems quantum fluctuations renormalise and dampen the dispersion significantly. Another source of quantum effects can arise from quantum fluctuations, due to the system being close to a magnetic phase boundary. The observed softening of certain spin wave modes are similar to the one predicted for antiferromagnetic isosceles triangular lattice with nearest and next-nearest-neighbour interactions. According to this model, on the other side of the phase boundary the magnetic structure is collinear and quantum fluctuations have strong effect on the low energy modes however currently the triangular phase is unexplored. Thus it is interesting to see if quantum fluctuations due to the vicinity of the phase boundary also modifies the excitation spectra of α-$CaCr_2O_4$.

6 Magnetic structure and excitations of β-$CaCr_2O_4$

The simplest frustrated spin model is the zig-zag (J_1-J_2) chain model where spins along the chain are coupled to nearest neighbours (J_1) and next-nearest neighbours (J_2) via Heisenberg exchange interactions, see Fig. 6.1. The frustrated antiferromagnetic chain has been recently studied for ferromagnetic J_1 coupling [138], motivated by the discovery of edge-sharing cuprate chain compounds. One of the best studied chain compound is $LiCuVO_4$ [139], where the ratio of exchange constants is $J_1/J_2 = -0.7$ (J_1 is antiferromagnetic). The excitation spectra is similar to the spinon continuum found in a uniform spin-1/2 Heisenberg antiferromagnetic chain but with strongly reduced dynamic correlations at wavevectors $k > \pi$. The properties of this model are of fundamental interest. For $\alpha \equiv J_1/J_2 = 0$ the model consists of two decoupled antiferromagnetic chains. The excitations are gapless spinons for the spin-1/2 system while integer spin systems have gapped magnons as discovered by Haldane. [140] For large S systems the excitations are spin waves with $|\sin(k)|$ dispersion along the chain if magnetic order is stabilized by interchain couplings. Introducing small ferromagnetic $J_1 < 0$ coupling drives the antiferromagnetic order to helical order in the classical case, while bosonization predicts incommensurate spin correlations and an exponentially small gap in the quantum spin-1/2 case. [141] For strong ferromagnetic J_1 the structure is ferromagnetic, this ferromagnetic phase is separated from the helical phase by a quantum critical point. [142] β-$CaCr_2O_4$ is related to α-$CaCr_2O_4$ and it is stable at lower temperatures, see Fig. 4.3. It consists of spin-3/2 zig-zag chains of Cr^{3+} ions. The crystal structure of β-$CaCr_2O_4$ is calcium ferrite type, first determined by Ford et al. [143] The Cr^{3+} ions similarly to α-$CaCr_2O_4$ are in a distorted octahedral oxygen environment. The three $3d$ electrons occupy the three low lying t_{2g} levels without degeneracy, thus no orbital degeneracy is expected and the interactions between spins can be well approximated by isotropic Heisenberg interactions. The shortest Cr^{3+} distances designate chains running along the c axis. These chains couple to nearest neighbour chains in a zig-zag manner forming a honeycomb lattice in the ab plane. The short Cr^{3+}–Cr^{3+} distance along the legs

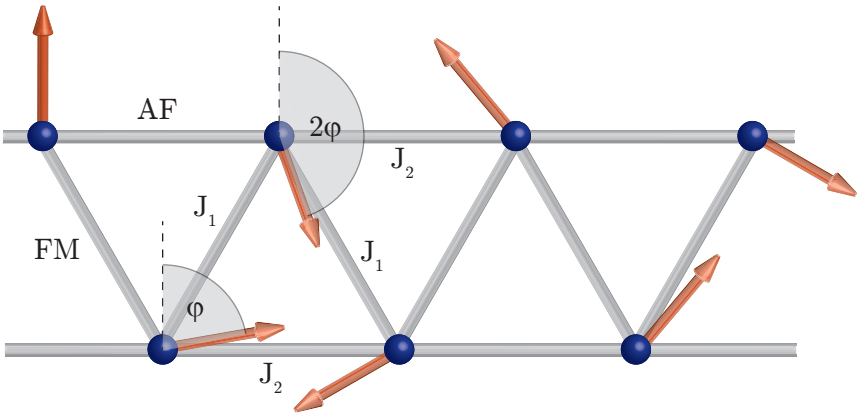

Figure 6.1: Zig-zag chain with weak ferromagnetic J_1 and antiferromagnetic J_2 coupling ($\alpha < 0$). Orange arrows denote the magnetic moment direction minimizing the classical energy.

gives the strongest direct exchange coupling, while along the zig-zag rungs much weaker interactions are expected. Thus the magnetism in β-$CaCr_2O_4$ is expected to be described by zig-zag chains with weak J_1 and stronger antiferromagnetic J_2 couplings.

Damay et al. [108, 144] reported heat capacity and muon spin polarisation measurements on β-$CaCr_2O_4$ as a function of temperature. They found two peaks in the heat capacity at $T_{N1} = 21$ K and T_{N2}=16 K. Muon spin polarisation shows that magnetic order develops at T_{N1}. The nature of the T_{N2} transition is unclear. It might be a sinusoidal to helical transition. They also determine the magnetic structure, which agrees with the results presented here. Inelastic neutron scattering results are also reported. Their data show a pseudogap feature at all temperatures and by fitting the data in the ordered phase to linear spin wave theory, exchange parameters were extracted. Their model does not include DM interactions although they are necessary to explain the magnetic structure.

Dutton et al. [145] report bulk property measurements on doped β-$CaCr_2O_4$. They synthesize hole-doped β-$Ca_{1-y}Cr_2O_4$ for $0.075 \leq y \leq 0.15$ and non-magnetic Ga^{3+} ion doped β-$CaCr_{2-2x}Ga_{2x}O_4$ compounds for $0.02 \leq x \leq 0.25$. They report divergent effects where hole doping disturbs the magnetic system more strongly than the non-magnetic impurity. They observe enhanced ferromagnetic correlations with increasing doping level.

The aim of this chapter is to determine the magnetic structure and the microscopic spin Hamiltonian of β-$CaCr_2O_4$ and to look for novel quantum phenomena. To reach this goal bulk property measurements, neutron diffraction and inelastic scattering were performed on powder samples. The interaction between magnetic Cr^{3+} ions are determined from

the experimental results. According to this β-$CaCr_2O_4$ consists of weakly coupled zig-zag chains, but significant Dzyaloshinskii-Moriya (DM) interactions are present along the rungs with opposite direction along neighbouring zig-zag chains. This decouples the zig-zag chains. The magnetically ordered phase has a helical structure with spins lying in the *ac* plane below T_{N1}=21 K. In this phase the excitation spectra has a pseudogap below 3 meV which is explained by the DM interaction and single-ion easy-plane anisotropy. In the paramagnetic phase significant scattering intensity is observed with a maxima at non-zero energy transfer ($\sim$8 meV) which is the sign of low dimensionality and also suggests a gapped excitation spectra in the paramagnetic phase. The nature of this gap is unknown, calculations of the J_1-J_2 model predict a vanishingly small gap for small ferromagnetic J_1.

6.1 Sample preparation

β-$CaCr_2O_4$ powder samples were prepared by S. A. J. Kimber by the solid state reaction of CaO and Cr_2O_3 in air. To ensure that no α-$CaCr_2O_4$ impurity is formed in the process the annealing temperature was chosen to be 1200°C, which is below the β-$CaCr_2O_4$/α-$CaCr_2O_4$ transition temperature, see Fig. 4.3. The sample was slowly cooled then reground every 24 hours for a total of one-week reaction time. Single crystal growth of this compound is very difficult, synthesis of small needle shaped β-$CaCr_2O_4$ crystals is reported by Nisino et al. [146] and Hashimoto et al. [147]

6.2 Bulk properties

The magnetic susceptibility of powder β-$CaCr_2O_4$ was measured as a function of temperature between 4.2 K and 300 K, using the MPMS instrument at HZB with 1 T magnetic field, see Fig. 6.2. The susceptibility shows paramagnetic behaviour close to room temperature, where the $1/\chi$ inverse susceptibility curve is straight. Below 150 K, the susceptibility strongly deviates from the paramagnetic curve. Below 25 K, the susceptibility drops, which is a sign of antiferromagnetic correlations. The susceptibility in the paramagnetic phase was fitted to obtain the Curie-Weiss temperature. The result of the fit is: T_{CW}=187(2) K and the paramagnetic moment size is 4.13 μ_B/Cr^{3+} ion, which is slightly larger than the expected spin only value of 3.87 μ_B. For a more reliable fit, one has to measure magnetic susceptibility up to several times the Curie-Weiss temperature. The inadequate temperature range of the fitting can explain the deviation of the magnetic moment size therefore the fitted Curie-Weiss temperature is

only expected to be approximate. These results are comparable to previously published magnetic susceptibility measurement of Damay et al. [108]. They reported T_{CW}=239(5) K and paramagnetic moment size of 3.89(5)μ_B, the difference is probably due to the different fitting range.

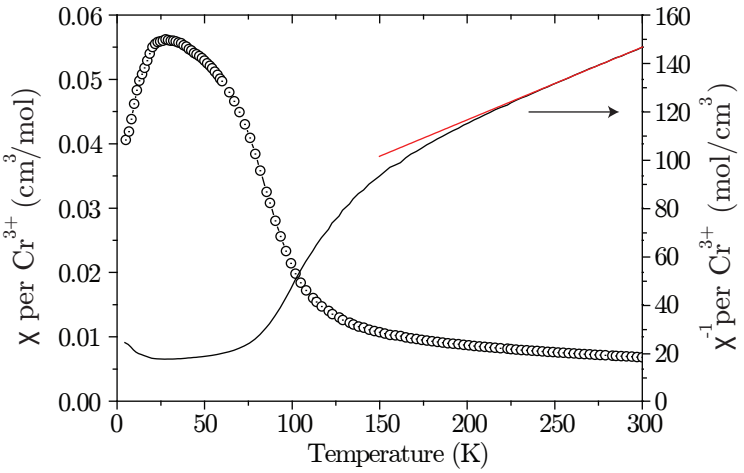

Figure 6.2: Magnetic susceptibility of β-$CaCr_2O_4$ measured in 1 T magnetic field. Red line shows the linear fit in the paramagnetic phase between 250 K and 300 K.

6.3 Diffraction study

6.3.1 Experiment

Neutron diffraction on a powder sample was measured on the D1a high-resolution powder diffractometer at ILL by S. A. J. Kimber and C. Ritter. Using a low resolution (λ=1.3887 Å) setting, measurements were carried out at 3.5 K, 14 K, 20 K and from 50 K to 300 K in 25 K steps. In the high resolution setting (λ=2.9905 Å) the temperatures were 1.7 K, 4.3 K, 9.4 K, from 13.3 K to 24.3 K in 1 K steps and at 50 K. The incident monochromatic beam has 0.073% contamination of $\lambda/3$ wavelength neutrons.

6.3.2 Nuclear structure

The room temperature crystal structure was first described by Ford et al. [143] It has a calcium ferrite type structure [148] with orthorhombic space group *Pbnm*. Each unit cell contains 4 formula units of β-$CaCr_2O_4$. To check the published crystal structure, the room temperature powder diffractogram measured on D1a was refined using Full-

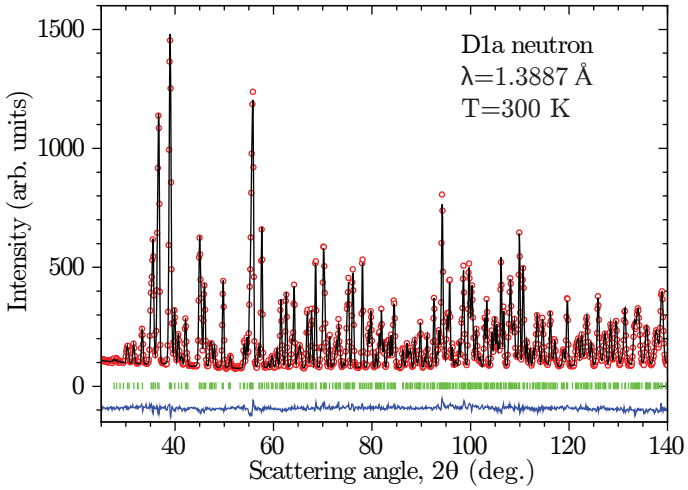

Figure 6.3: Room temperature powder diffraction pattern along with Rietveld refinement. The open red symbols are the data, the black curve is the fit, the blue line is the difference and the green bars indicate the nuclear Bragg peaks.

Prof. [101] The data was refined in the 25° to 140° 2θ range. The quality of the fit is very good, the R_{F} factor is 0.028. The results agree well with the latest published crystal structure by Damay et al. [108], see Tab. 6.1.

The room temperature structure contains two inequivalent Cr^{3+} ions in a distorted octahedral oxygen environment, see Fig. 6.4. The shortest Cr^{3+}-Cr^{3+} distance is along the c axis and equal to the c lattice constant. The associated exchange interactions are denoted by J_{1-1} and J_{1-2} for Cr(1) and Cr(2) respectively and they couple the Cr^{3+} ions into chains along c. These chains form a distorted honeycomb lattice of Cr^{3+} ions in the ab plane. The nearest neighbour chains are shifted by $c/2$ along z and the corresponding inter-chain interactions are denoted by J_{2-1}, J_{2-2}, J_{a} and J_{b}. They form a network of zig-zag chains, see Fig. 6.5. There are two types of zig-zag chains. The first type will be referred to as the J_2 zig-zag, where the rungs are denoted by J_{2-1} or J_{2-2}. They are built up by Cr(1) and Cr(2) atoms respectively and the two legs are related by inversion symmetry. In the J_2 zig-zag chains the CrO_6 octahedra are edge sharing along the rungs. The J_{a} and J_{b} type zig-zag chains are the ones where the rung interactions are J_{a} and J_{b}. Their legs are unrelated by symmetry and the CrO_6 octahedra are corner sharing along the rungs. The Ca^{2+} ions are located at the centre of the voids within the honeycomb lattice.

To look for any temperature dependent structural changes, neutron powder diffraction

Table 6.1: Refined crystallographic parameters using space group *Pbnm*. The lattice parameters are the room temperature values. The atomic position listed: first and second row are D1a powder data at 3.5 K and 300 K respectively, third row shows previously published room temperature data by Damay et al. [108] All z atomic positions are restricted on the c Wyckoff site to 1/4.

Unit cell dimensions: $a = 10.6172(2)$ Å
$b = 9.0777(2)$ Å
$c = 2.9661(1)$ Å

Atom	Site	x	y
Ca(1)	4c	0.6594(1)	0.7597(1)
		0.6591(2)	0.7596(2)
		0.6590(2)	0.7598(2)
Cr(1)	4c	0.6127(1)	0.4401(1)
		0.6129(2)	0.4400(2)
		0.6126(2)	0.4398(2)
Cr(2)	4c	0.1005(1)	0.4165(2)
		0.1002(2)	0.4166(3)
		0.1009(2)	0.4165(2)
O(1)	4c	0.1603(1)	0.2027(1)
		0.1602(1)	0.2027(1)
		0.1599(1)	0.2026(1)
O(2)	4c	0.4752(1)	0.1172(1)
		0.4757(1)	0.1168(1)
		0.4758(1)	0.1165(1)
O(3)	4c	0.7852(1)	0.5270(1)
		0.7853(1)	0.5270(1)
		0.7853(1)	0.5267(1)
O(4)	4c	0.4273(1)	0.4174(1)
		0.4272(1)	0.4181(2)
		0.4270(1)	0.4180(1)

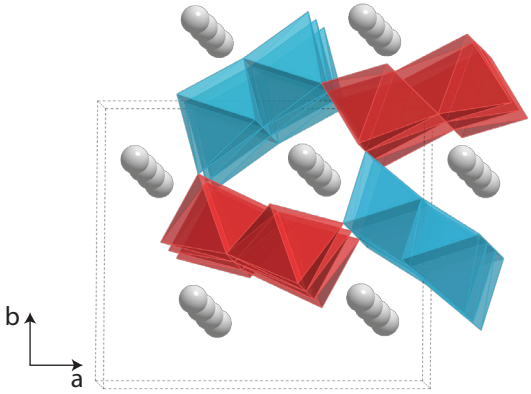

Figure 6.4: Crystal structure of β-$CaCr_2O_4$. Red and blue polyhedra are the Cr(1) and Cr(2) octahedra respectively, grey spheres denote Ca atoms.

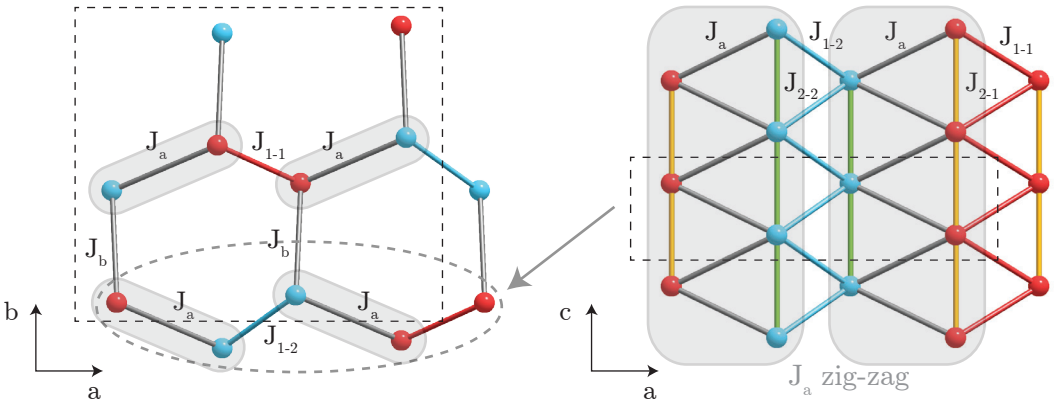

Figure 6.5: Cr^{3+} ion positions of β-$CaCr_2O_4$ in the ab and ac planes at room temperature. Red and blue spheres denote Cr(1) and Cr(2) atoms respectively, dashed black rectangles denote the unit cell. Different colours denote different inter-ionic distances, the naming convention of the exchange interactions follows Damay et al. [108]. Each zig-zag chain is defined and named by the rung coupling, e.g. the J_a zig-zag is shown by grey square.

was measured at several temperatures below room temperature. No changes of the crystal symmetry were found down to 1.7 K. Figure 6.6 shows the temperature evolution of the lattice parameters. The a and b parameters show negative thermal expansion up to 100 K nevertheless the crystal volume follows the Debye model. [149]

The Cr^{3+}-Cr^{3+} inter-ion distances show very small temperature variation (see Tab. 6.3.2), no sign of change is visible in the magnetic phase. The Cr-O-Cr angles along the superexchange paths also vary very little with the temperature.

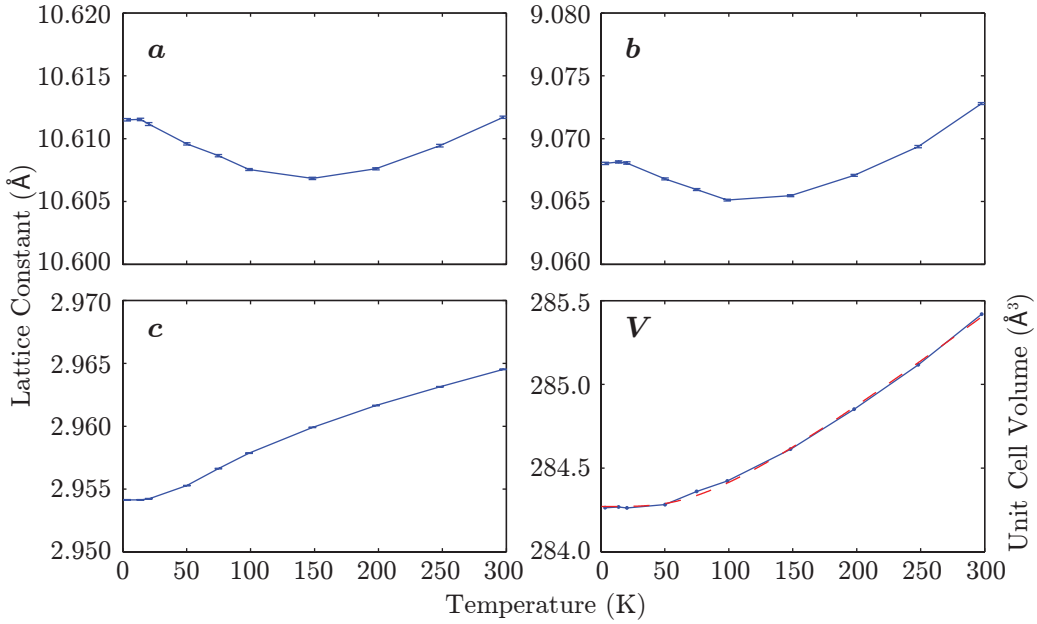

Figure 6.6: Refined lattice parameters and unit cell volume of β-$CaCr_2O_4$ as a function of temperature. The red dashed line is the fit using the Debye-model.

Table 6.2: Cr^{3+}-Cr^{3+} nearest neighbour distances of β-$CaCr_2O_4$ at different temperatures.

	300 K	50 K	3.5 K
Cr(1)–Cr(1) (J_{1-1})	3.025(3)	3.016(2)	3.016(2)
Cr(2)–Cr(2) (J_{1-2})	3.002(3)	3.003(2)	3.005(2)
Cr(1)–Cr(1) (J_{2-1})	2.96453(3)	2.95524(2)	2.95417(3)
Cr(2)–Cr(2) (J_{2-2})	2.96453(3)	2.95524(2)	2.95417(3)
Cr(1)–Cr(2) (J_a)	3.629(3)	3.626(2)	3.625(2)
Cr(1)–Cr(2) (J_b)	3.557(3)	3.555(2)	3.554(2)

6.3.3 Magnetic structure

On the neutron powder diffraction pattern of β-$CaCr_2O_4$ below 21 K new Bragg peaks appear at incommensurate positions. This together with the drop in the susceptibility reveals the onset of long range magnetic order. Since all the observable magnetic Bragg peaks are at low Q, diffraction patterns were collected below 50 K with a longer wavelength (2.9907 Å) to better resolve the low Q magnetic Bragg peaks. In the 1.7 K base temperature scan all the new peaks could be indexed with the ordering wavevector of $\boldsymbol{k}_m$=(0,0,0.4789(1)), see Fig. 6.7.

The magnetic structure was refined using the irreducible representations (irreps) of the

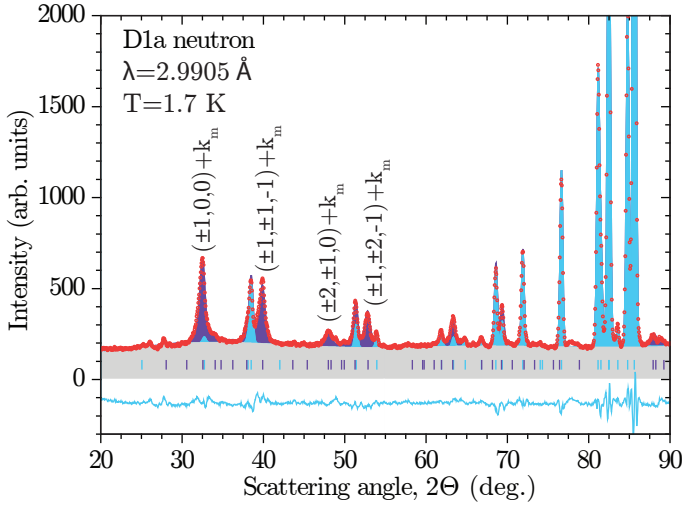

Figure 6.7: Neutron diffraction pattern of β-$CaCr_2O_4$ at 1.7 K. Red circles denote measured intensity, grey, purple and blue shading denote the background, calculated magnetic and calculated nuclear scattering respectively. Purple and blue lines denote the magnetic and nuclear Bragg peaks respectively. Blue line at the bottom denotes the difference between calculated and measured intensity.

magnetic space group, the tables were produced by the BasIreps program. The Γ_m magnetic representation consists of four irreps, each with three basis functions, see Tab. 6.3. The base temperature diffraction pattern was refined fitting the prefactors of the basis functions. This method was repeated for each representation. The best fit was achieved using the basis functions of Γ_1, see Tab. 6.4. This fit reproduced all observed magnetic Bragg peaks with the correct intensity. The moment components on the two inequivalent Cr^{3+} ions are listed in Table 6.5. The components of the magnetisation on the two Cr sites were almost equal and they were fixed to the same value for the final refinement. Also the phase between the two Cr sites was refined, however it was close to zero, thus it was fixed to zero afterwards. The R_B factor of the best fit was 6.4%, revealing good agreement. For all other irreps, the agreement was worse than 30%. The results presented here are in general agreement of Damay et al. [108], although the b component of the magnetic structure is non-zero here. If the magnetic moments are restricted to the ac plane the R_B value is 7.4%

Assuming that the b component of the moment is zero, the magnetic structure can be either helical or sinusoidal. The helical structure is described by $\Psi = m_x\Psi_1 + im_z\Psi_3$, with the maximum moment size equal to m_x. The magnetic structure is sinusoidal if the two basis function are combined with real prefactors: $\Psi = m_x\Psi_1 + m_z\Psi_3$, in this case the

Table 6.3: Irreducible representations for $\boldsymbol{k}_\mathrm{m} = (0, 0, 0.4789)$ in the *Pbnm* group, where $\eta = \exp(\pi i \cdot 0.4789)$. The magnetic representation Γ_m consists of four irreps each occurring three times: $\Gamma_\mathrm{m} = 3\Gamma_1 \oplus 3\Gamma_2 \oplus 3\Gamma_3 \oplus 3\Gamma_4$.

	1	$2_1(0,0,z)$	$b(¼,y,z)$	$n(x,¼,z)$
Γ_1	1	η	1	η
Γ_2	1	η	-1	$-\eta$
Γ_3	1	$-\eta$	1	$-\eta$
Γ_4	1	$-\eta$	-1	η

Table 6.4: The basis functions of the irreducible representation Γ_1 which describe the magnetic structure best (spins in the *ac* plane).

	Cr-1 (x,y,z)	Cr-2 $(-x,-y,z{+}½)$	Cr-3 $(-x{+}½,y{+}½,z)$	Cr-4 $(x{+}½,-y{+}½,z{+}½)$
ψ_1	(1,0,0)	($-\eta^*$,0,0)	(-1,0,0)	(η^*,0,0)
ψ_2	(0,1,0)	($-\eta^*$,0,0)	(0,1,0)	($-\eta^*$,0,0)
ψ_3	(0,0,1)	(0,0,η^*)	(0,0,1)	(0,0,η^*)

Table 6.5: Refined prefactors of the basis-functions of the Γ_1 irrep, third line is from [108].

m_x	m_y	m_z	R_B
2.32(2)	0.32(5)	0.93(2)	6.4
2.33(2)	-	0.93(2)	7.4
2.88(7)	-	1.27(13)	4.7

maximum moment size is $\sqrt{m_\mathrm{x}^2 + m_\mathrm{z}^2}$. The two structures cannot be distinguished from each other by neutron powder diffraction. Intuitively at lowest temperatures the helical structure is expected, since for fixed spin length it has a lower ground state energy than the sinusoidal structure. The expected helical structure is in agreement with that of Damay et al. [108] and is plotted on Fig. 6.8. The magnetic order on the chains along c is almost antiferromagnetic implying antiferromagnetic exchange interactions along this direction. The surprising result is that the J_2 zig-zag chains have different vector chirality along the two legs. It is shown on Fig. 6.8, where plus and minus signs denote the two chiralities. The chirality is defined as $sgn((\boldsymbol{r}_\mathrm{i} - \boldsymbol{r}_\mathrm{j}) \cdot \boldsymbol{S}_\mathrm{i} \times \boldsymbol{S}_\mathrm{j})$, this definition does not depend on the numbering of the spins. The identical chirality chains build up the J_a zig-zag chain and appear to be coupled ferromagnetically along J_a. These zig-zags consist of Cr(1)-Cr(2) ions and are surrounded by nearest neighbour chains with opposite chirality in a square lattice pattern. For neighbouring incommensurate helices

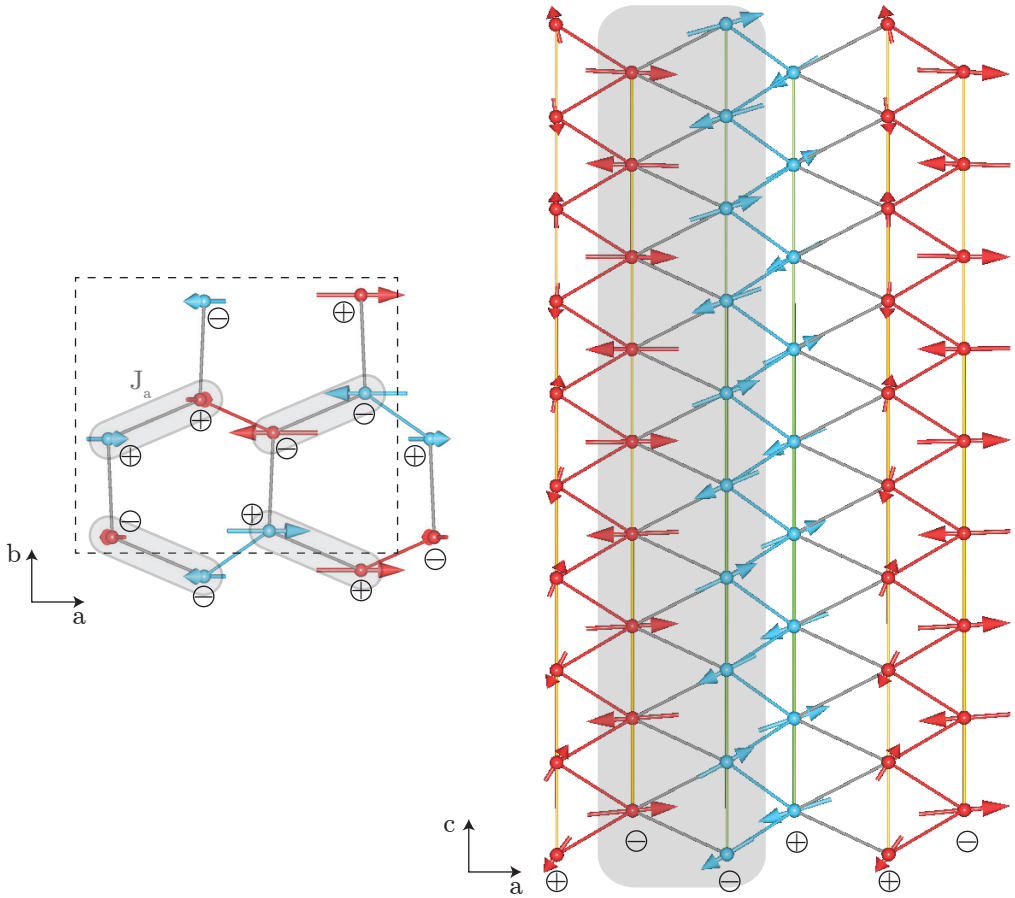

Figure 6.8: Magnetic structure of β-$CaCr_2O_4$, shown in the ab and bc planes. Plus and minus signs denote the chirality of the Cr^{3+} chains along the z axis. Grey shading indicates the J_a zig-zag chains.

running along c with opposite chirality, the angles between neighbouring spins on the two chains are distributed uniformly in the 0-2π range.

As the temperature of the sample was increased from 1.7 K up to T_{N1} the intensity of the magnetic reflections decreased continuously, see Fig. 6.9 and Fig. 6.10(a). The ordering wavevector shows a sudden jump at T_{N2}, see Fig. 6.10(b).

6.3.4 Discussion

Due to the quenched orbital angular momentum, all exchange interactions are expected to be isotropic. Based on the crystal symmetry the strongest interaction is expected along the legs of the zig-zag chains. J_{2-1} and J_{2-2} mainly originate from direct overlap

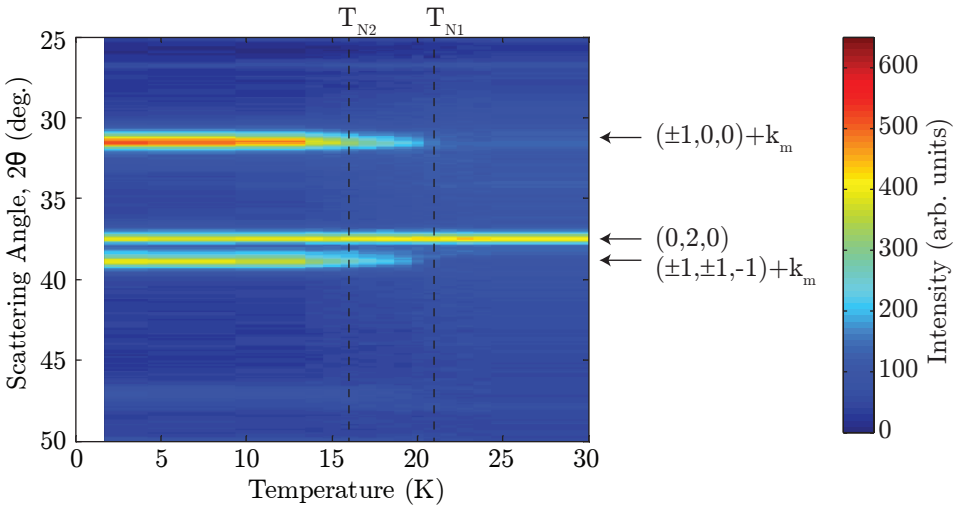

Figure 6.9: Temperature dependence of the diffraction pattern after a constant background was subtracted.

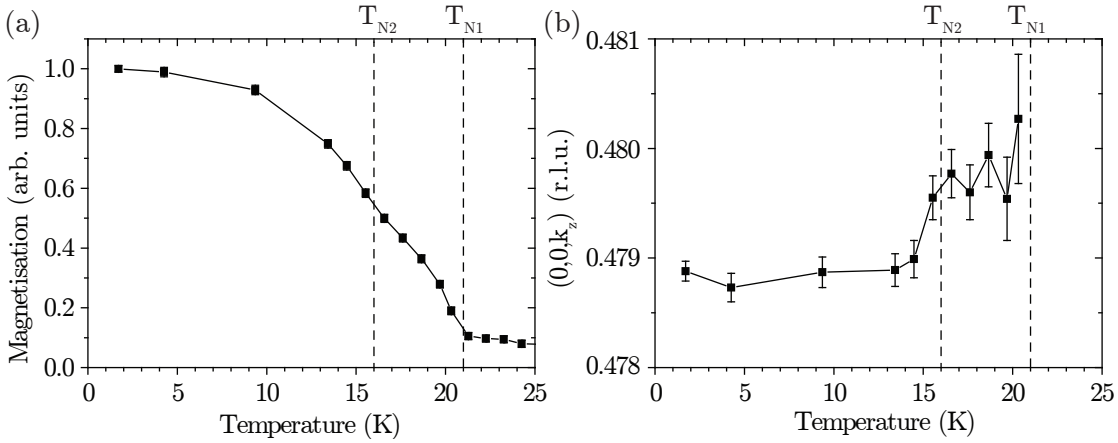

Figure 6.10: (a) Staggered magnetisation of β-$CaCr_2O_4$ as a function of temperature. (b) Magnetic ordering wavevector as a function of temperature.

of t_{2g} orbitals because of the short Cr^{3+}-Cr^{3+} separation (2.954 Å at 3.5 K). According to Fig. 5.20, the expected strength of these direct exchange interactions is ∼4 meV. The J_{1-1} and J_{1-2} interactions are mediated through the two common oxygen ions of the edge-sharing oxygen octahedra. The Cr-O-Cr angles are 98.24° and 97.37° for Cr(1) and Cr(2) respectively and the Cr^{3+}–Cr^{3+} distance are 3.016 Å and 3.005 Å at 3.5 K. The strength of these interactions are depending on the competition between antiferromagnetic direct exchange and ferromagnetic super exchange. Although the inter-ionic distances are over 3 Å, the directexchange interaction can be still significant

when compete with a weak ferromagnetic super exchange. [10, 11, 150, 151] Therefore the expected interaction is weak, the sign cannot be predicted by this simple argument. The J_a and J_b interactions are mediated through a single common oxygen ion of the corner sharing oxygen octahedra. The Cr-O-Cr angles are 131.72° and 121.94° for J_a and J_b respectively. According to the Cr^{3+} perovskite series, where Cr–O–Cr angles are ranging between 140° and 150° and Cr–Cr distances are between 3.7 Å and 3.9 Å, the superexchange interaction is ferromagnetic below 135° Cr^{3+}–O^{2-}–Cr^{3+} angle and antiferromagnetic above it. [152] According to this trend the J_a and J_b interactions are expected to be weak ferromagnetic.

The observed magnetic structure consists of a helical spin arrangement on the J_a zig-zag chains while neighbouring J_a zig-zags have opposite chirality. The observed opposite chirality is unusual. If all interactions are isotropic exchange interactions, all of the zig-zag chains would have the same chirality. This suggests, that Dzyaloshinskii-Moriya (DM) interactions are present. [153, 154, 155, 156] The DM interactions have the following form:

$$\mathcal{H}_{\mathrm{DM}} = \boldsymbol{D}_{12} \cdot \boldsymbol{S}_1 \times \boldsymbol{S}_2. \tag{6.1}$$

It has two effects on the magnetic structure, first it creates an easy-plane anisotropy perpendicular to the $\boldsymbol{D}$ vector and second it favours a particular chirality (opposite to the DM vector). Since the magnetic moment is mainly in the *ac* plane, only the D^{y} component of the DM vector couples to the spins, since $\boldsymbol{S}_{\mathrm{i}} \times \boldsymbol{S}_{\mathrm{j}}$ is always parallel to the *b* axis. To force two neighbouring Cr(1) or Cr(2) chains to have opposite chirality, the DM interaction has to compete with the J_{1-1}, J_{1-2} and J_b interactions. There is a minimum value of $\boldsymbol{D}$ depending on the rung coupling which wins over the zig-zag isotropic exchange interaction.

The DM interactions present in the sample have to be compatible with the crystal symmetry. [157, 158] Since the energy of the DM interaction is invariant under the symmetry operations of the crystal, the $\boldsymbol{D}$ vector has to be an axial vector, since the $\boldsymbol{S}_{\mathrm{i}} \times \boldsymbol{S}_{\mathrm{j}}$ expression gives an axial vector (axial vector × axial vector = axial vector) and the scalar product is invariant under transformations if it acts on the same type of vectors. The symmetry operations also transform the magnetic ions and since in the cross product the order of the atoms is important, if the position of the two interacting ions is exchanged by symmetry, $\boldsymbol{D}$ gains a factor of -1. Using these arguments some constraints for $\boldsymbol{D}$ can be obtained. $\boldsymbol{D} = 0$ if an inversion centre coincides with the bisecting point of the line connecting the two interacting magnetic ions. This rule prevents DM interactions

along the J_{1-1} and J_{1-2} rungs ($\boldsymbol{D}_1$=0). $\boldsymbol{D}$ has to be parallel to the mirror plane, if it bisects the line connecting the two interacting ions. This rule constrains $\boldsymbol{D}_2^z = 0$ for the interaction along the legs of the zig-zag chains due to the $m(x, y, 1/4)$ mirror plane. General DM interactions are allowed along the J_a and J_b rungs, since the interacting atoms are not related by symmetry. The transformation of the allowed components of the DM interaction along the chain are shown on Fig. 6.11. It can be seen, that only the b component of the $\boldsymbol{D}_2$ vector produces the observed chirality of the zig-zag chains. The $\boldsymbol{D}$ vector along the J_a and J_b rungs ($\boldsymbol{D}_\mathrm{a}$ and $\boldsymbol{D}_\mathrm{b}$) follow the same transformation. This shows that the spin chirality and the plane of the spins are coupled, since the observed staggered chirality is only possible for ac plane magnetic spins assuming it is induced by DM interactions. In the following $\boldsymbol{D}_\mathrm{b}$ will be neglected, since the legs of the J_b zig-zags have opposite chirality thus the contribution of $\boldsymbol{D}_\mathrm{b}$ to the classical ground state is cancelled out.

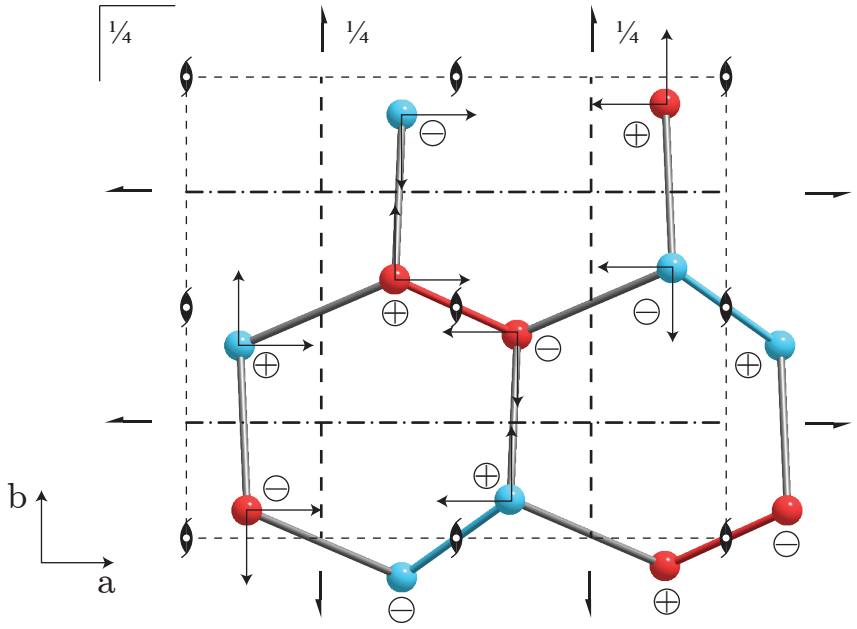

Figure 6.11: Transformation of the Dzyaloshinskii-Moriya vector. Black arrows on the magnetic ions denote the x and y components of the $\boldsymbol{D}_2$ DM interaction which acts along the legs of the zig-zag chains. The symmetry elements of the *Pbnm* space group are overlaid, for the meaning of the symbols see [159].

By examining the classical energy of the magnetically ordered ground state, the orders of magnitude of the magnetic interactions can be determined. Assuming an elliptical

magnetic structure with components m_{x} and m_{z} along the a and c axes respectively, the energy of the ground state can be written as:

$$\begin{aligned} E_{\mathrm{GS}} =& \frac{1}{4}\left(J_{2-1}+J_{2-2}\right)\left(m_{\mathrm{x}}^2+m_{\mathrm{z}}^2\right)\cos(k_{\mathrm{z}}) \\ &+\frac{1}{2}J_{\mathrm{a}}\left(m_{\mathrm{x}}^2+m_{\mathrm{z}}^2\right)\cos(k_{\mathrm{z}}/2)+\frac{1}{2}J_{\mathrm{b}}\left(m_{\mathrm{x}}^2-m_{\mathrm{z}}^2\right)\cos(k_{\mathrm{z}}/2) \\ &+\frac{1}{4}\left(J_{1-1}+J_{1-2}\right)\left(m_{\mathrm{x}}^2-m_{\mathrm{z}}^2\right)\cos(k_{\mathrm{z}}/2) \\ &-D_2 m_{\mathrm{x}} m_{\mathrm{z}}\sin\left(k_{\mathrm{z}}\right)-D_{\mathrm{a}} m_{\mathrm{x}} m_{\mathrm{z}}\sin\left(k_{\mathrm{z}}/2\right), \end{aligned} \tag{6.2}$$

where D_2 and D_{a} are the scalar b component of the DM interaction along the legs and along J_{a} rungs respectively. This ground state competes with the structure, where each leg has the same chirality. The energy of the equal chirality structure is:

$$E'_{\mathrm{GS}}=\frac{1}{4}\left(m_{\mathrm{x}}^2+m_{\mathrm{z}}^2\right)\left(\left(J_{2-1}+J_{2-2}\right)\cos(k'_{\mathrm{z}})+\left(2J_{\mathrm{a}}+2J_{\mathrm{b}}+J_{1-1}+J_{1-2}\right)\cos(k'_{\mathrm{z}}/2)\right). \tag{6.3}$$

By comparing the two equations, one can see that the DM interactions are competing with the rung exchanges J_{b}, $J_{1\text{-}1}$ and $J_{1\text{-}2}$. It can be also seen, that the D_{a} interaction has a larger influence on the magnetic structure, than D_2 by a factor of $\sin(k_{\mathrm{z}}/2)/\sin(k_{\mathrm{z}}) \approx 8$. Using the mean-field fit of the magnetic susceptibility and the observed ordering wavevector, the value of the interactions can be estimated. The value of the magnetic ordering wavevector is mostly determined by the ratio of $J_2 = 1/2(J_{2-1}+J_{2-2})$ and J_{a}, neglecting other interactions the equation of the magnetic ordering wavevector is the following:

$$\cos\left(k_{\mathrm{z}}/2\right)=-\frac{J_{\mathrm{a}}}{4J_2}. \tag{6.4}$$

Substituting the observed wavevector, one gets $J_2 = -3.8J_{\mathrm{a}}$, thus the magnetic zig-zag chains in β-$CaCr_2O_4$ are in the strong leg regime. In the paramagnetic phase, the mean-field can be determined from the Curie-Weiss temperature:

$$k_{\mathrm{B}}\cdot T_{\mathrm{CW}}=\frac{1}{3}S(S+1)\left(2J_{\mathrm{a}}+2J_2\right). \tag{6.5}$$

Since T_{CW}=187 K the expected exchange constants are J_2=8.8 meV and J_{a}=-2.3 meV.

6.4 Inelastic neutron scattering

6.4.1 Experiment

Inelastic neutron scattering of a powder β-$CaCr_2O_4$ sample was measured on the IN4 thermal neutron TOF spectrometer at ILL by S. A. J. Kimber, B. Lake and H. Mutka. Data were collected with incident neutron energies of 16.8 meV (λ=2.21 Å) and 67 meV (λ=1.10 Å) at several temperatures between 1.6 K and 125 K for 2 hours each. The FWHM of the resolution at zero energy transfer are 0.6 meV and 2.8 meV respectively. A vanadium reference was measured upon cooling with incident neutron energy of 16.8 meV for the detector efficiency calibration. All collected data are corrected for the $k_\mathrm{i}/k_\mathrm{f}$ factor.

6.4.2 Results

The inelastic neutron scattering data of β-$CaCr_2O_4$ measured on IN4 with E_i=16.8 meV at base temperature shows a broad inelastic signal centered around Q=1.2 Å^{-1}. This is close to the strongest magnetic Bragg peak $(1, 0, k_\mathrm{m}) \approx 1.08$ Å^{-1}, see Fig. 6.12(a). The strongest intensity is centered approximately around 4 meV energy transfer. Below 3 meV the intensity decreases continuously, giving a pseudogap feature. A constant Q cut at 2.2 ± 0.8 Å^{-1} shows three peaks, two at low energies (3 meV and 5 meV) and one at 13.5 meV. These three peaks could be Van Hove singularities. Upon heating the sample above the magnetic ordering temperature (Fig. 6.12(b)), the pseudogap like feature disappears and the centre of the scattering intensity moves downwards to lower energies.

To gain a more detailed picture of the gap, inelastic spectra were measured at several temperatures up to 120 K. To determine the temperature dependence of the gap, a constant Q cut at 1.17 ± 0.10 Å^{-1} was extracted from each spectra. These cuts are plotted on Fig. 6.13(a-b). The line at 1.6 K shows, that the scattering intensity increases continuously with increasing energy transfer up to 3 meV like a pseudogap. This pseudogap disappears at the Néel temperature while the scattering intensity increases. The collapse of the pseudogap scales similarly to the magnetic order parameter, compare with Fig. 6.10(a). Above the magnetic ordering temperature the excitations become broader and a broad maximum in energy can be observed up to 80 K at Q=1.17 Å^{-1} momentum transfer. This broad maximum is typical for low-dimensional antiferromagnets while for three dimensional antiferromagnets, above the Néel temperature, the inelastic intensity has a Lorentzian distribution as a function of energy transfer centered at zero energy due to the overdamped magnon spectra.

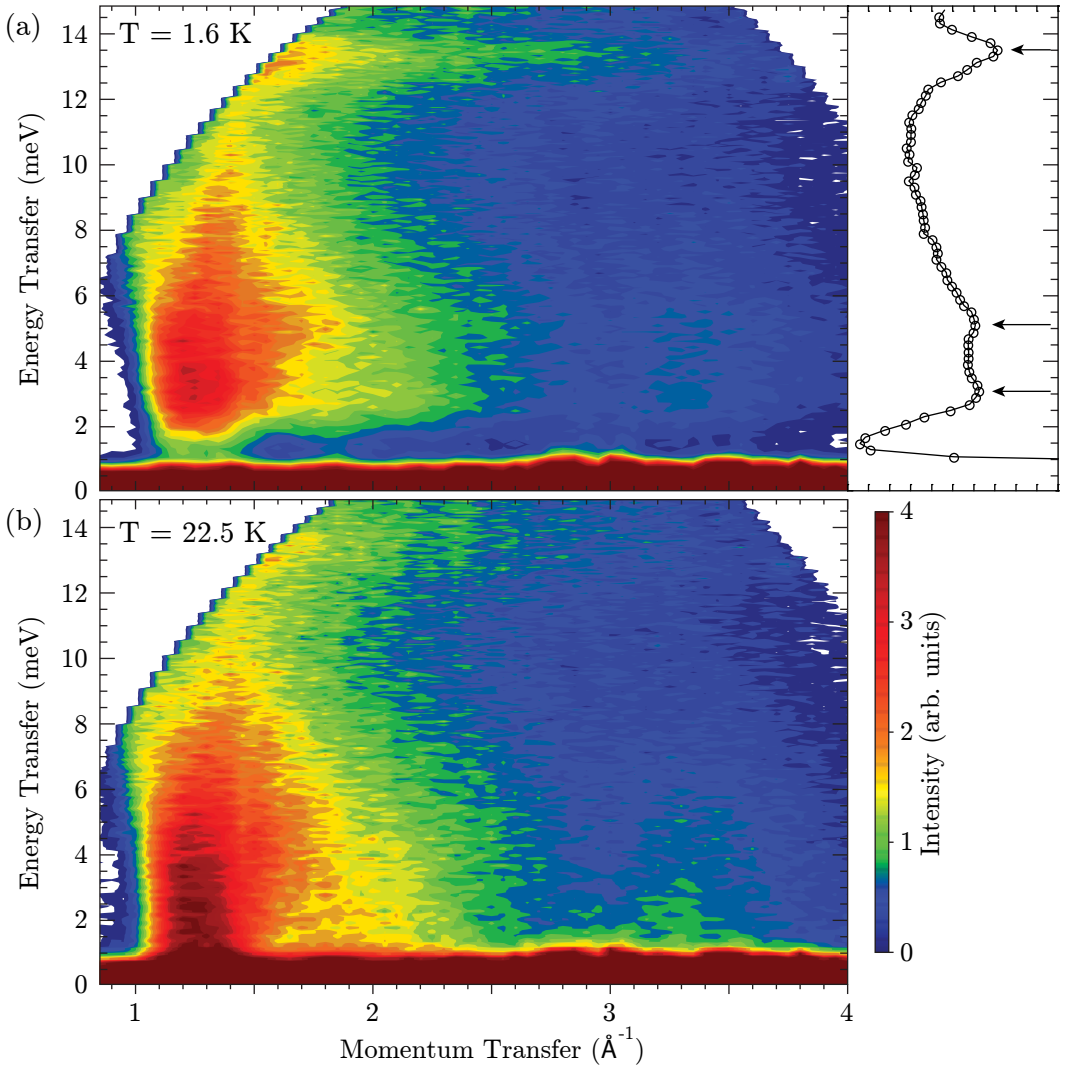

Figure 6.12: Inelastic neutron scattering measured on IN4 at (a) base temperature and (b) around the Néel temperature T_{N2} measured with neutron incident energy of E_i=16.8 meV. The black circles on the upper right plot are a constant Q cut at 2.2 ± 0.8 Å^{-1}, arrows denote possible Van Hove singularities.

Data were also collected with E_i=67 meV neutrons to explore the magnetic scattering at higher energy transfers. Fig. 6.14 shows cuts taken at Q=2.5 Å^{-1}±0.8 Å^{-1} for different temperatures compared to the high Q background. It reveals that magnetic intensity extends up to 25 meV, although due to the smooth decrease it is difficult to give a reliable upper bound. The features in the energy dependence are also broadened by the low instrumental energy resolution. After subtracting the background (Fig. 6.14(b)) the

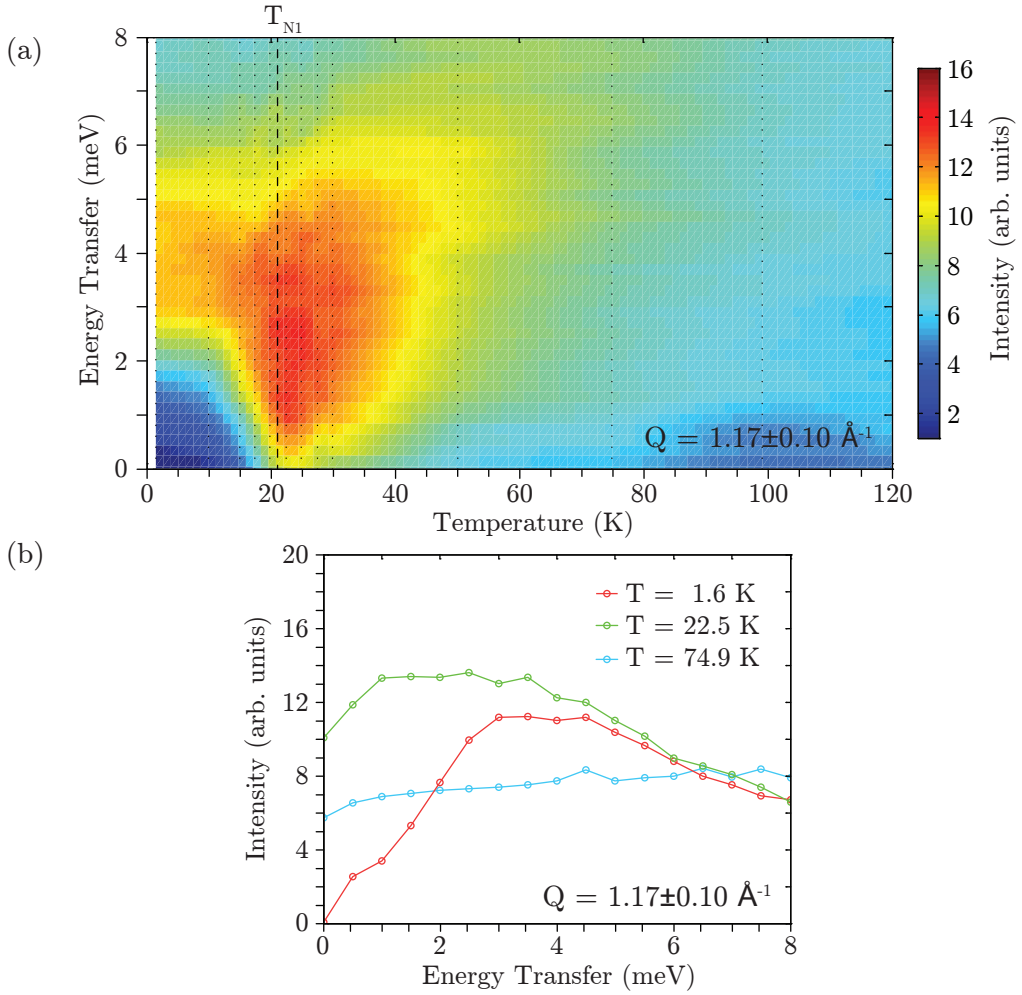

Figure 6.13: (a) Temperature dependence of the gap at $Q = (1, 0, k_{\mathrm{m}}) = 1.17 \pm 0.10$ Å, dotted lines denote the temperatures, where data were collected, the dashed line denotes the Néel temperature T_{N1}, incident neutron energy was E_{i}=16.8 meV. (b) Plot of selected scans as a function of energy transfer at different temperatures. Elastic line was subtracted.

magnetic scattering appears to be temperature independent above 15 meV up to 100 K. Below 15 meV the curve becomes smoother with increasing temperature and a well pronounced maximum is visible around 5 meV. The gap below 3 meV is the artefact of oversubtraction of the incoherent scattering.

Several constant energy cuts were plotted on Fig. 6.15 to check the Q dependence of the scattering intensity. The curves at different energy cuts were also scaled together, see Fig. 6.15. The cuts up to 20 meV scale together well over the whole Q range. The

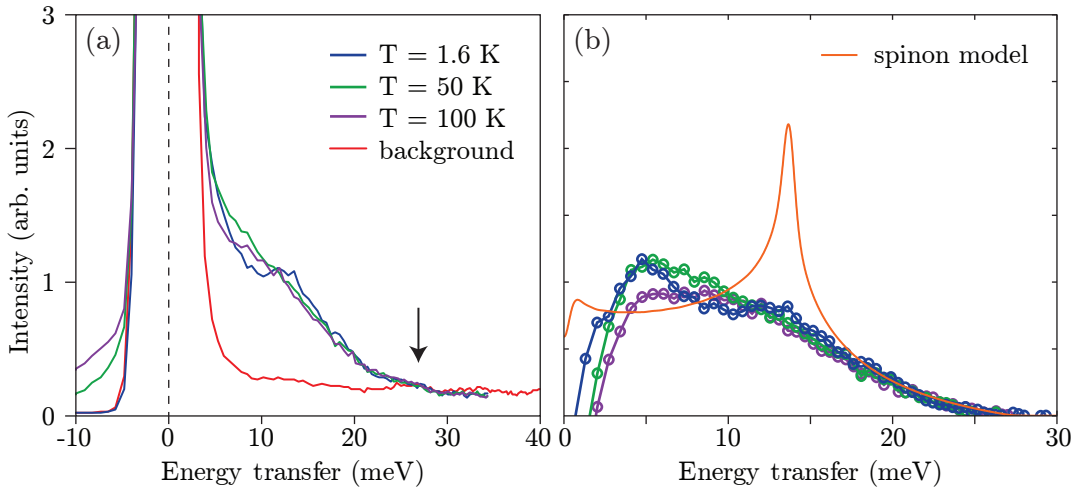

Figure 6.14: Constant Q cuts of the inelastic spectra measured with E_i=67 meV neutrons, around the magnetic signal 2.5 Å^{-1}±0.8 Å^{-1} at different temperatures (a) compared to the background cut (red line) at 5.0 Å^{-1}±0.8 Å^{-1} and (b) after subtracting the background. The orange line shows the result of the spinon model of spin-1/2 antiferromagnetic chain. The arrow shows the top of the magnetic signal.

intensity decreases with increasing momentum transfer, which confirms its magnetic origin. The cuts at 25 and 30 meV are almost constant as a function of momentum transfer giving the background noise of the measurement. No sign of phonon scattering can be seen.

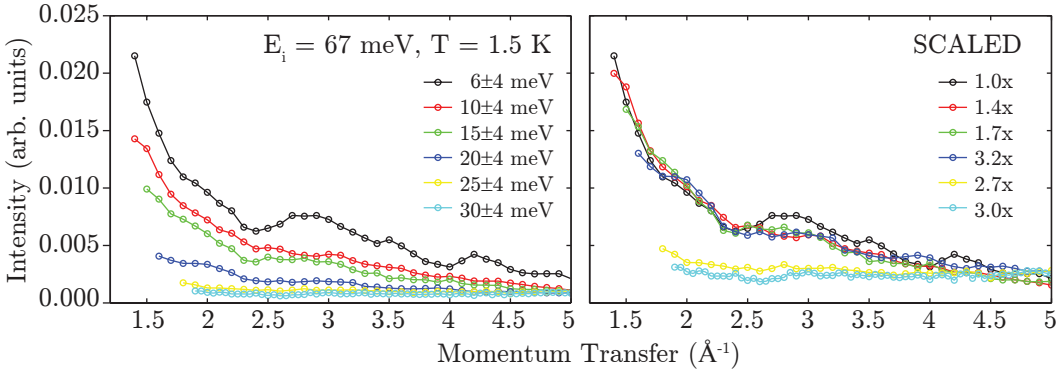

Figure 6.15: Constant energy cuts centered at different energy transfers of the IN4 data collected with E_i=67 meV. On the right side the curves are scaled together, note that the cuts at 25 and 30 meV are almost constant, giving the non-magnetic background.

Damay et al. [144] published very similar inelastic neutron scattering data. It shows the broad inelastic scattering signal centered around Q=1.17 Å^{-1} and at 4 meV energy transfer at base temperature. They claim that a pseudogap feature exists in the spectra up to 60 K and the position of the maximum intensity at Q=1.17 Å^{-1} is independent of temperature below 60 K. However they did not measure the extended scattering above 15 meV. Besides there are slight differences in the two data sets that can be attributed to the different instrumental resolution.

6.4.3 Discussion

6.4.3.1 Spin wave analysis

The observed low temperature excitations of β-$CaCr_2O_4$ are expected to be well modelled using linear spin wave theory due to the rather classical spin value of 3/2. However the Hamiltonian obtained from LSWT approximation is still hard to solve. The reason is the combination of an incommensurate structure and zig-zag chains with opposite chirality. Hamiltonians of systems with an incommensurate wavevector and the same chirality can be easily diagonalized using a rotating coordinate system. If the same technique is applied to β-$CaCr_2O_4$ the rotating coordinate system has to be fixed to one of the two observed chain chiralities. In this case the expression describing the interactions with the opposite chirality chain would contain umklapp terms [160]. These terms couple the bosonic creation and annihilation operator a_k and $a_\mathrm{k}^\dagger$ with $a_{\mathrm{k}\pm\mathrm{k_m}}$ and $a_{\mathrm{k}\pm\mathrm{k_m}}^\dagger$. Therefore the usual Bogoliubov transformation cannot be applied. The effect of these umklapp terms can be seen in an extended magnetic Brillouin zone where they make gaps at Q positions related to multiples of k_m. After folding back to the magnetic Brillouin zone these gaps will smear out the dispersion, causing broadening of the spin wave modes. To make a simpler model, these umklapp terms can be avoided by neglecting the interactions between opposite chirality zig-zags. In this case J_{1-1}, J_{1-2} and J_b have to be neglected and uncoupled zig-zag chains remain with J_{2-1} and J_{2-2} leg coupling and J_a rung coupling with additional DM interaction along the legs and/or rungs. Another difficulty arises from the reduced moment size. The magnetic structure determined from neutron diffraction is strongly elliptical, the moment component along a and c are strongly reduced from the saturation value and the reduction is almost 70% along c. This changing moment length with position along the helix gives umklapp terms when combined with incommensurate ordering wavevector. Therefore to simplify the calculation a fully ordered moment was assumed with $m_\mathrm{x} = m_\mathrm{z} = gS\mu_\mathrm{B}$. Altogether the simplest solvable model would include the J_a zig-zag chains with equal chirality

and a helical magnetic structure with a fully ordered moment. The starting parameters are chosen to be $J_{2-1} = J_{2-2}$= 4 meV and J_a=-1.05 meV. These give the right pitch angle along the zig-zag chains and the observed top of the dispersion of 13.5 meV. In this model the gap is missing below 3 meV. To produce the observed pseudogap below 3 meV additional terms are necessary in the Hamiltonian. Single ion anisotropy and DM interactions can produce a gap in some of the spin wave modes. Since the magnetic structure is helical, there are three spin wave modes which can be measured by neutrons. The $\omega(\boldsymbol{k})$ dispersion calculated from the Hamiltonian corresponds to the variation of the pitch angle along the chain direction, which is the in-plane rotation of the spins (in the *ac* plane). This mode is called the phason [49] and it is gapless in case of inplane anisotropy or DM interaction. There are two other modes $\omega(\boldsymbol{k} \pm \boldsymbol{k}_m)$ which are the collective tilting of the spins perpendicular to the spiral plane (along *a* and *c* axes). They acquire a gap in the case of anisotropy. So the pseudogap can be explained by having a gapless mode and two gapped modes which give non-zero scattering intensity down to zero energy transfer and a peak in intensity at 3 meV.

In Sec. 6.3.4 the necessity of a DM interaction was discussed to produce the observed low temperature magnetic structure of β-$CaCr_2O_4$. The *y* component of the DM interaction is allowed along the legs and rungs of the zig-zag chains. Both interactions would produce a gap, which for the DM interaction has the size:

$$\Delta_{DM} = 2S\sqrt{D^y J_2 \sin\alpha}, \tag{6.6}$$

where D^y is the *y* component of the DM interaction, α is the angle between the two coupled moments. Since the α angle along the legs are close to 180°, while along the rungs close to 90°, to produce the same 3 meV gap the DM interaction along the leg (D_2^y=1.9 meV) has to be 8-times larger than along the rungs (D_a^y=0.25 meV). This large DM value along the legs would reduce the ordering wavevector to smaller values, that the J_a and J_2 ratio cannot compensate. Thus if the gap is caused by the DM interaction, it has to be along the rungs.

The gap can also be caused by single ion anisotropy with the expression:

$$\mathcal{H}_{aniso} = \sum_i D^y_{aniso} S_i^{y2}. \tag{6.7}$$

If D^y_{aniso} is negative it gives an easy-axis anisotropy along *y*, if D^y_{aniso} is positive it gives easy-plane anisotropy in the *ac* plane. In case of a positive value this term does not change the spin angles or the ordering wavevector and produces the following gap for

the two tilting modes:

$$\Delta_{\text{aniso}} = 2S\sqrt{D^{\text{y}}_{\text{aniso}} J_2}. \tag{6.8}$$

To reproduce the observed gap, $D^{\text{y}}_{\text{aniso}}$=0.25 meV is necessary.

The above proposed Hamiltonian describes uncoupled zig-zag chains, thus the powder spectra contains sharp resonances constant in energy which are Van Hove singularities of the spin wave dispersion smoothed by resolution. The observed resonances in the β-$CaCr_2O_4$ spectra are broader than resolution. This broadening can be explained in two ways in the framework of LSWT. The previously discussed umklapp terms, due to chains of opposite chirality and varying moment length, are expected to broaden the spectra. Besides coupling between zig-zag chains of the same chirality in the *ac* plane would also broaden the resonances by introducing dispersion in the *ac* plane. The latter can be modelled easily by introducing J' ferromagnetic coupling in the *ac* plane connecting the nearest neighbour identical chirality zig-zag chains. The shortest distance is 4.878 Å and it connects magnetic ions with the same z coordinates, see Fig. 6.16.

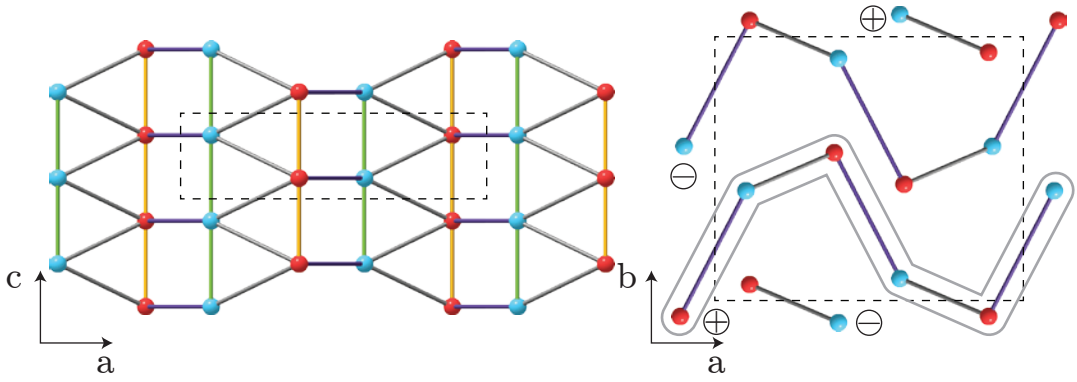

Figure 6.16: The same chirality J_a zig-zag chains (atoms connected with grey lines) coupled through the shortest interchain distance (lilac line) to build up 2 dimensional layers.

The numerical calculation was done on a unit cell with two zigzag chain with the same chirality and same J_2 and J_a and DM interaction values. They were coupled into a planar structure via J'. Due to the incommensurate structure there are two high energy Van Hove singularities from two dispersion maxima. However only one of these can be observed in the data measured with E_i = 16.8 meV, thus the higher one should be above the measurable energy transfer. This would imply an increase of the chain couplings to J_2=4.9 meV and J_a=-1.29 meV. Then the top of the dispersion is at 16.5

meV and the second maximum would agree with the observed peak at 13.5 meV. After fixing these values, several combinations of single ion anisotropy and DM interaction were compared to the data, see Fig. 6.17(a). The best fit value was the combination of single ion anisotropy and DM interaction, both equal to 0.1 meV.

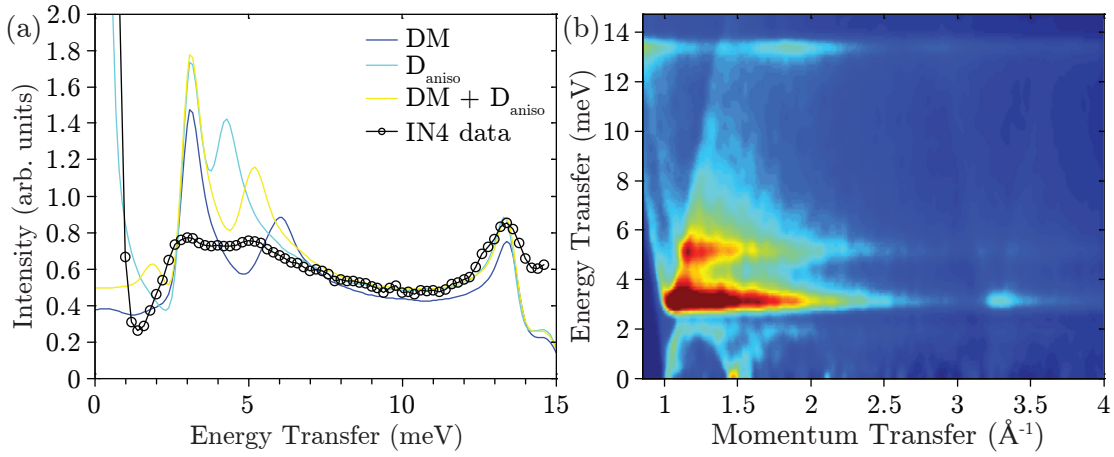

Figure 6.17: (a) Constant Q cuts at 2.2 ± 0.8 Å^{-1} of measured and simulated data. Coloured lines showing LSWT simulation result including DM interaction (dark blue, D^{y}_{a}=0.2 meV), single ion anisotropy (light blue, D^{y}_{aniso}=0.2 meV) and both of them (yellow, D^{y}_{a}=D^{y}_{aniso}=0.1 meV), black circles denote IN4 data measured with E_i=16.8 meV at base temperature. (b) Powder averaged LSWT result using J_a=-1.29 meV, J_2=4.9 meV, D^{y}_{a}=0.1 meV and D^{y}_{aniso}=0.1 meV.

The introduction of J' interchain coupling slightly broadened the Van Hove singularities, but for $J' > 0.05$ meV a new peak at 2-3 meV energy transfer was introduced which was not observed experimentally.

Using the optimum values the final fit shows good agreement with the data, see Fig. 6.17(b). Although the intensity distribution is different, the scattering intensity below 7 meV is strongly suppressed in the measured data when compared to the simulation. Furthermore the features of the measured spectra are broader, which can be attributed to the umklapp terms in the bosonic Hamiltonian and weak couplings between same chirality zig-zag chains.

Damay et al. [144] use a similar LSWT model to fit the base temperature inelastic neutron scattering data of β-$CaCr_2O_4$, for the comparison of the fitted values see Tab. 6.6. However they do not include DM interaction, which is necessary for the opposite chirality chains. Furthermore their fitted ratio of J_2 and J_a is different which gives different magnetic ordering wavevector value than observed. To determine more accurately the

Table 6.6: Comparison of the fitted values of the LSWT model with the results of Damay et al. [144].

parameter	this thesis (meV)	Damay et al. (meV)
J_a	-1.29	-1.5
J_2	4.9	5.0
D^y_{aniso}	0.1	0.2
D^y_a	0.1	-
J'	>-0.05	-0.05

small non-isotropic energy terms in the spin Hamiltonian single crystal data is necessary.

6.4.3.2 Two magnon scattering

The IN4 inelastic data of β-$CaCr_2O_4$ measured with E_i=67 meV shows magnetic scattering above the top of the spin wave dispersion from 16.5 meV up to 25 meV. This featureless scattering cannot be explained by LSWT. However two-magnon scattering processes can contribute to the magnetic scattering up to twice the spin wave energy and they would not produce a singularity at the upper edge in agreement with the data. The two magnon scattering is due to fluctuations in the longitudinal spin component and its integrated intensity increases with the low temperature reduction in the ordered moment. In the case of β-$CaCr_2O_4$ neutron diffraction shows a strong reduction of the magnetic moment from the maximum value of $gS\mu_B$. The expected intensity of the two-magnon scattering at low temperature can be estimated from the measured ordered moment size according to Ref. [161]. Since the magnetic structure is helical with very different m_x and m_z components, the average spin size is estimated as $\sqrt{(m_x^2+m_y^2)/2}/(g\mu_B)$=0.89, the moment reduction is ΔS=0.61 (while the values of Ref. [108] give ΔS=0.39). The total scattering $\langle S_x^2+S_y^2+S_z^2\rangle = S(S+1)$ can be separated into three terms (neglecting 3 magnon scattering and higher orders): elastic or Bragg-scattering $\sim (S-\Delta S)^2$, 1 magnon scattering or spin wave intensity $\sim (S-\Delta S)(2\Delta S+1)$ and 2 magnon scattering $\sim \Delta S(\Delta S+1)$, the values are listed in Tab. 6.7. As can be seen from the table, two magnon scattering is expected to contribute up to 25% of the inelastic scattering and can explain the inelastic intensity observed above 17 meV energy transfer. Since the two magnon scattering is expected to be strongest around the top of the spin wave dispersion, it may also explain the relatively weak scattering below 7 meV.

Table 6.7: The total sum rules for the different components of the scattering, evaluated for S=3/2 and ΔS=0.61, in brackets the values are calculated from ΔS=0.39 [108].

Component	Integrated intensity
$S(\boldsymbol{Q},\omega)$	$S(S+1)$=3.75
$S^{zz}(\boldsymbol{Q},\omega)_{\text{elastic}}$	$(S-\Delta S)^2$=0.79 (1.23)
$S^{xx}(\boldsymbol{Q},\omega)+S^{yy}(\boldsymbol{Q},\omega)$	$(S-\Delta S)(2\Delta S+1)$=1.98 (1.98)
$S^{zz}(\boldsymbol{Q},\omega)_{\text{inelastic}}$	$\Delta S(\Delta S+1)$=0.98 (0.54)

6.4.3.3 Spinon model

Besides two magnon scattering the additional intensity above the spin wave dispersion of β-$CaCr_2O_4$ can be explained by the presence of fractional excitations, known as spinons. In the case of the unfrustrated spin-1/2 antiferromagnetic chain, the elementary excitations are spin-1/2 spinons. During the neutron scattering process, the selection rule $\Delta S = 1$ does not allow the creation of single spinons, therefore they are created always in pairs. Thus in the neutron scattering spectra, a continuum of scattering is observed, see Fig. 6.18. The continuum extends up to πJ_2 with enhanced scattering at $\pi J_2/2$. The comparison with the measured data is shown on Fig. 6.14. In β-$CaCr_2O_4$ the magnetic ions have spin-3/2, which implies more classical behaviour than the spin-1/2 chain. Thus the spinon continuum scattering intensity is expected to be much more strongly weighted to lower energies for β-$CaCr_2O_4$. In β-$CaCr_2O_4$ the two legs are weakly coupled ferromagnetically. According to simulations, the frustrated weakly coupled spin-1/2 chains have a similar continuum as the uncoupled ones, except that the scattering intensity is reduced for increasing Q [142].

6.5 Conclusions

In this chapter the magnetic structure and excitation spectra of β-$CaCr_2O_4$ were analysed. It was found that the system behaves quasi one-dimensionally. It orders magnetically below 21 K. The magnetic structure is helical with spins lying in the ac plane. The surprising result of the neutron diffraction is that different magnetic Cr^{3+} chains have opposite chirality. Chains of the same chirality build up zig-zag chains along the c axis with weak ferromagnetic coupling along the rungs. The two different chirality zig-zag chains are organised into a checker-board pattern, if the next-nearest neighbour interactions are taken into account between chains. Although the inter-zig-zag interactions are expected to be comparable to the intra-zig-zag interactions, the opposite

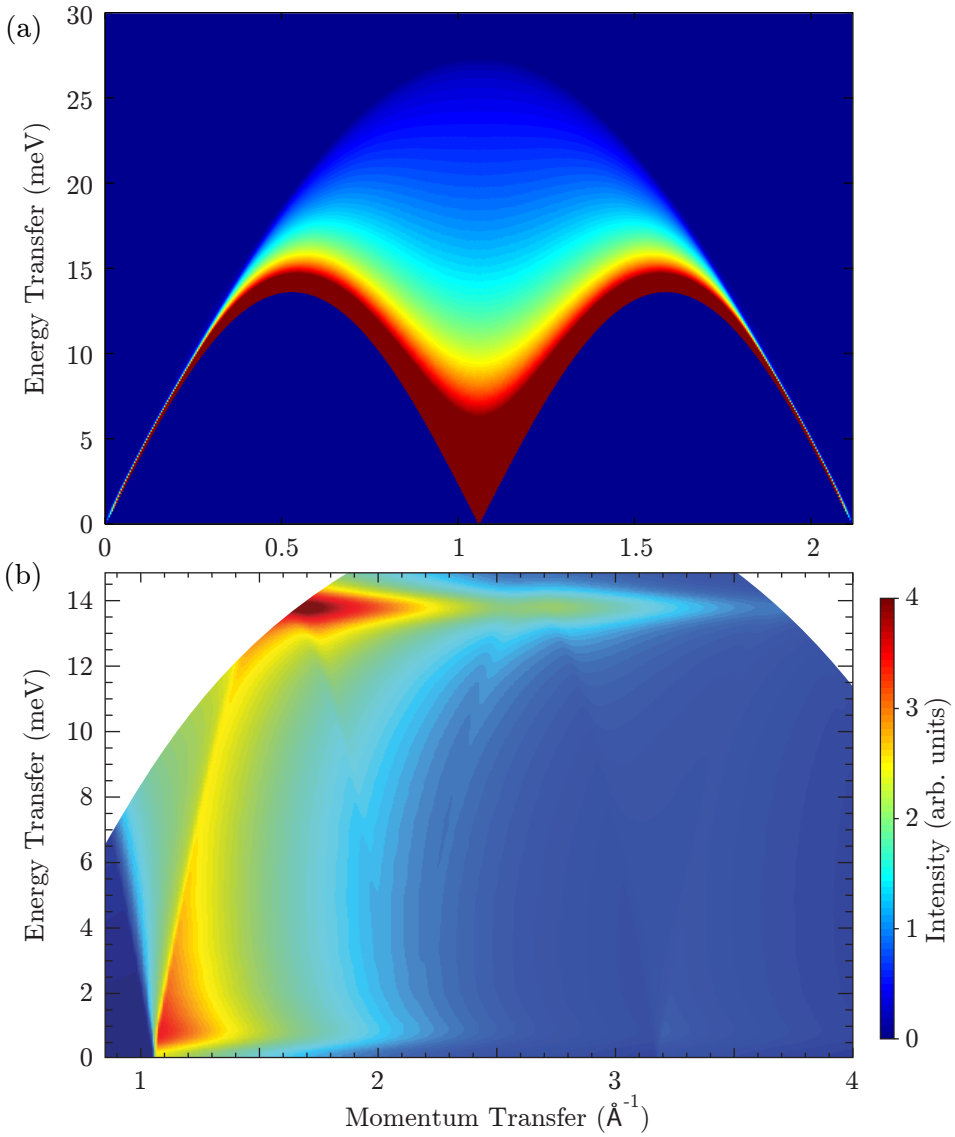

Figure 6.18: (a) Spinon continuum of the spin-1/2 chain along c direction scaled to the measured data using J_2=2.9 meV, calculated by Caux et al. [162] (b) powder averaged and convoluted with the instrumental resolution.

chirality of the neighbours cancels out these interactions by making the angles between neighbouring spins random. This appears in LSWT as umklapp terms, causing the broadening of the spin wave modes. The observed chirality pattern can be explained by Dzyaloshinskii-Moriya interaction. It was shown by applying the crystal symmetry to the b component of the DM vector, that the checker-board pattern of the chain chirality can be explained. The neutron powder inelastic spectra of β-$CaCr_2O_4$ shows broad inelastic

scattering with pseudogap feature below 3 meV and extended scattering above the spin wave dispersion. The spectra could be fitted well assuming uncoupled zig-zag chains, easy-plane single-ion anisotropy and DM interaction. The strongest antiferromagnetic interaction is along the legs and has a value of 4.9 meV, this value fits well to the trend of the direct exchange strength of Cr^{3+} ions as a function of distance, see Fig. 5.20. The high energy scattering could be explained by two-magnon process, which are expected to be strong due to the large ordered moment reduction at base temperature. Besides it could be due to a spinon continuum as observed in spin-1/2 antiferromagnetic chains. The spinon continuum is also predicted for the spin-3/2 system although the continuum intensity is strongly suppressed. In conclusion the results on β-$CaCr_2O_4$ are interesting since they show how frustration and chiral magnetic order can reduce dimensionality. Future experiments should address the questions of precise values of the DM interaction and the nature of the extended scattering continuum.

7 Magnetism of Sr_2VO_4

Dimerized antiferromagnets are systems, where antiferromagnetic interactions create strongly correlated pairs of $S = 1/2$ ions. These pairs are called dimers and have a singlet ground state: $1/\sqrt{2}(|\uparrow\downarrow\rangle - |\downarrow\uparrow\rangle)$ with $S = 0$. The excited states are threefold degenerate triplet states with $S = 1$ and $S_z \in \{-1, 0, 1\}$. Dimer systems have attracted lots of interest since in some cases they show Bose-Einstein condensation of magnons above a critical magnetic field. In magnetic field the triplet state splits due to the Zeeman energy and when the lowest excitation band reaches zero energy an ordered magnetic structure emerges. At this quantum critical point magnons condense into the ground state. Depending on the symmetry conditions of the system, this condensation can be identical to Bose-Einstein condensation, Wigner crystallization or supersolidity. [163, 164]

Interest in orthorhombic Sr_2VO_4 has been renewed since the discovery of unusual orbital ordering in tetragonal Sr_2VO_4. [165] This material was previously studied by Gong et al. [166] who describe the powder preparation and determine the crystal structure using x-ray and neutron powder diffraction and measure the low temperature magnetic susceptibility. The orthorhombic Sr_2VO_4 shows evidence of a dimerized magnetic ground state. It crystallizes in the $Pna2_1$ symmetry with 8 formula units per unit cell [166]. It is isostructural to Sr_2CrO_4. [167] The structure contains isolated VO_4^{4-} distorted tetrahedra. The V^{4+} ions have $3d_1$ electronic configuration in the outer shell with $S = 1/2$ spin and quenched magnetic moment. The single d shell electron occupies one of the two low lying e orbitals $d_{x^2-y^2}$ or d_{z^2} depending on the details of the distortion of the tetrahedron. The interactions between V^{4+} ions are expected to be weak, due to the complex exchange pathways passing through at least two oxygen atoms. The two shortest V^{4+}-V^{4+} distances build up zig-zag chains along the b axis.

Heat capacity was measured by Deisenhofer et al [168], the data shows a Schottky anomaly (broad peak) centered at 95 K. The maximum in the heat capacity is the sign of an energy gap in the system and confirms the dimerized ground state. According to the position of the maximum the excited triplet state energy is ~ 8 meV. Electron spin resonance (EPR) measurement below room temperature show a constant g-factor value

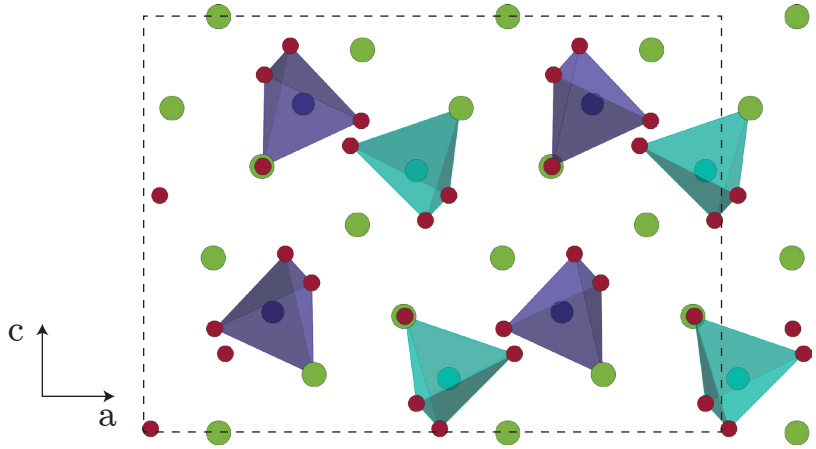

Figure 7.1: Crystal structure of Sr_2VO_4 at base temperature. Purple and green tetrahedra denote the VO_4^{4-} units, where red dots are oxygen atoms. Green dots are Sr^{2+} ions.

of 1.89 down to 31 K, where the g-factor jumps to 1.94 and at the same temperature the EPR line width drops. The sudden change of the g-factor indicates changes in the orbital ordering of V^{4+}.

Although there are no obvious dimer units in the crystal, the magnetic susceptibility measurement suggests a weakly coupled dimer system. In this chapter the crystal structure and magnetic properties of orthorhombic Sr_2VO_4 are revisited using synchrotron high resolution x-ray diffraction, DC susceptibility and inelastic neutron diffraction. The crystal structure is determined with higher accuracy than previously and the dimerized nature of the magnetic ground state is confirmed.

7.1 Magnetic susceptibility

The magnetic susceptibility of Sr_2VO_4 was measured with the SQUID, Quantum Design at HZB. The powder sample has a weight of 235.5 mg and a magnetic field of 1 T was used. Temperature was swept between 1.8 K and 300 K. The measured susceptibility was normalized to 1 mole of V^{4+}. The measured curve shows a smooth broad maximum around 50 K with Curie-Weiss behaviour at higher temperatures and a Curie tail presumably due to impurities at low temperatures, see Fig. 7.2. The measured data is similar to the previously published susceptibility by Gong et al. [166], however the measured broad peak has only half the height as previously published. This was independently confirmed by another research group. [168]

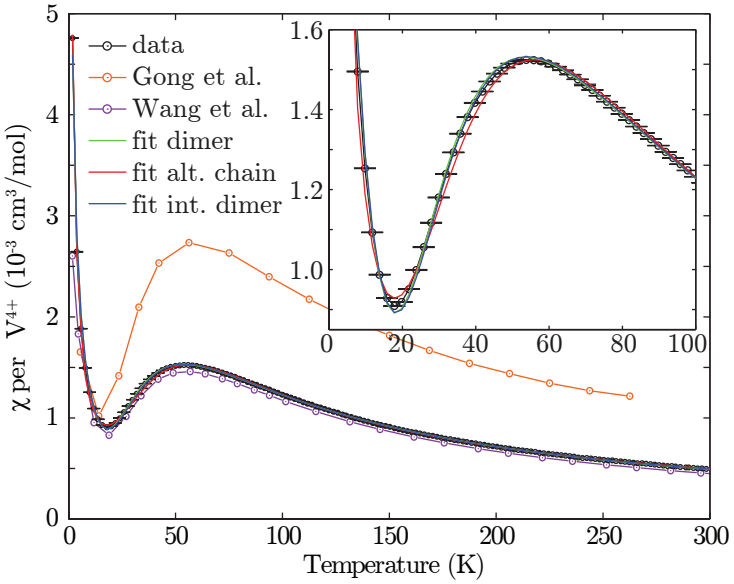

Figure 7.2: Magnetic susceptibility of Sr_2VO_4 measured in 1 T magnetic field. Green, red and blue lines denote fit to the data using non-interacting dimers, alternating chain model and interacting dimers, see text.

The broad peak can be well fitted using the theoretical susceptibility of non-interacting dimers, see Eq. 2.21:

$$\chi_{\text{dimer}} = \frac{\bar{g}^2 n_{\text{D}}}{8T} \frac{1}{3 + \exp(J/k_{\text{B}}T)}, \tag{7.1}$$

where χ_{dimer} is the susceptibility per mole of V^{4+} (in units of cm^3/mol), J is the intra-dimer exchange interaction, $\bar{g}$ is the g-value of the V^{4+} ions and n_{D} is the fraction of dimers per $2V^{4+}$. The g-value of V^{4+} in Sr_2VO_4 is fixed to 1.89, as measured by Deisenhofer et al. [168] using EPR technique.

To fit the susceptibility in the full temperature range the paramagnetic signal of the impurities had to be included together with a constant term to account for the Van Vleck paramagnetism and diamagnetic core susceptibility.

$$\chi_{\text{fit}} = \chi_0 + \chi_{\text{dimer}} + \frac{C_{\text{imp}}}{T - \theta_{\text{imp}}}. \tag{7.2}$$

In the weak coupling limit using mean field approximation the interacting dimers sus-

ceptibility can be determined in the weak coupling limit, see Eq. 2.22:

$$\chi_{\text{int-dimer}} = \frac{\bar{g}^2 n_{\text{D}}}{8T} \frac{1}{3 + \exp(J/k_{\text{B}}T + J'/k_{\text{B}}T}, \tag{7.3}$$

where J' is the sum of the inter-dimer exchange couplings.
Since the two shortest V^{4+}-V^{4+} distances build up chains, an AF alternating chain model could provide a good description of the susceptibility as well. The data were fitted to the model of alternating antiferromagnetic chains of Johnston et al. [169] with J and J' being the alternating exchange couplings. The model gives a Padé series for $\chi(\alpha, t)$, where $\alpha = J'/J$, $t = k_{\text{B}}T/J$ and $J,\ J' \geq 0$. The Padé series was fitted to the result of combined Quantum Monte Carlo (QMC) and transfer-matrix density renormalisation group (TMRG) calculations.
For the results of the three fits see Tab. 7.1. For all three fits, the constant background is small, $\chi_0 < 4 \times 10^{-5}$ cm^3/mol and the paramagnetic impurity is less than 7 n/n% assuming it is spin-1/2.

Table 7.1: Fitted parameters of different models to the measured magnetic susceptibility. J and J' are the exchange interactions, n_{D} is the fraction of dimers per $2V^{4+}$, reduced χ^2 gives the goodness of the fit and Δ is the excitation gap.

model	J (meV)	J' (meV)	n_{D}	Reduced χ^2	Δ (meV)
dimer	8.30(2)	-	0.46(1)	100%	8.3
interacting-dimer	8.33(2)	-2.1(4)	0.44(1)	86%	7.3
alternating AF chain	3.19(3)	2.18(3)	0.42(1)	94%	0.6

The interacting dimer model gives the best fit, but the alternating AF chain model also shows reasonable improvement compared to the non-interacting dimer model. The alternating chain model only gives a gap of 0.57 meV. When the dimer fit is compared to the result of Gong et al. [166], their fitted exchange coupling is slightly stronger (9.0 meV). However the measured susceptibility is only about half of what expected for 1 dimer per $2V^{4+}$ ion, see the n_{D} column of Tab. 7.1.

7.2 Diffraction

To confirm the crystal structure and extract temperature dependent changes X-ray powder diffraction was measured on Sr_2VO_4. The instrument used was ID31, the high-resolution powder-diffraction beamline at ESRF. It has angular resolution better than 0.005°, which enables precise determination of the peak positions and even the positions

of the weakly scattering oxygen atoms can be determined precisely. The advantage over neutron diffraction is that the strong incoherent neutron scatterer vanadium can be also easily measured with X-ray. The positions of the magnetic vanadium ions are crucial to understand the magnetism of Sr_2VO_4.

For the experiment the X-ray wavelength was fixed to 0.354134(11) Å. The powder sample was filled into a capillary with diameter of 0.5 mm. Measurements were done at 4.3 K and between 50 K and 300 K with 50 K steps. Fig. 7.3 shows the recorded powder pattern at 4.3 K. The diffraction pattern has a few very weak impurity peaks (B on figure). The attempt to identify them with SrO, $SrVO_3$, $Sr_3V_2O_8$ or tetragonal Sr_2VO_4 failed. Besides two weak and relatively broad peaks appear at 6.55° and 7.22°(A on figure).

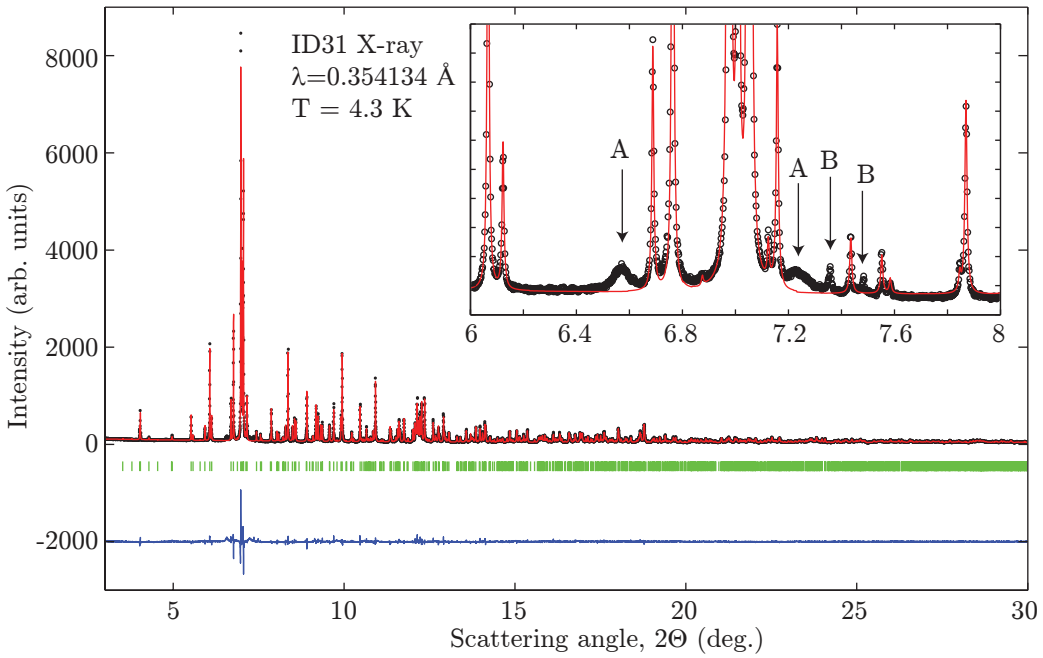

Figure 7.3: Powder spectra of Sr_2VO_4 at base temperature. Inset shows a detailed view, black arrows denote unindexed impurity peaks (A and B).

The diffraction patterns were refined using FullProf at each temperature. The starting parameters for the refinement were taken from the work of Gong et al. [166]. The ID31 data confirms the $Pna2_1$ symmetry down to 4.3 K. There are small differences in the atomic positions, see Tab. 7.2 when compared to previously published result. The largest deviations are in the oxygen positions like $O(4)_z$, where the deviation is 0.013. These deviations can be explained by the low resolution of the lab X-ray used for the previous

experiment and the relatively weak sensitivity of X-rays to oxygen.

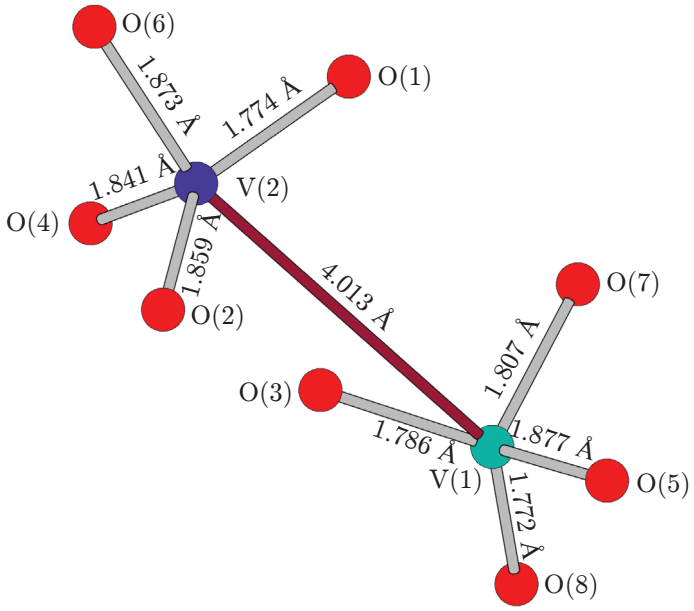

Figure 7.4: The two $V(1)O_4^{4-}$ and $V(2)O_4^{4-}$ tetrahedra with all interatomic distances labelled at base temperature.

The crystal structure consists of VO^{4-} tetrahedra separated by Sr^{2+} ions. The tetrahedra are distorted, see Fig. 7.4. The V-O distances range between 1.772 Å and 1.877 Å. There is no obvious sign of dimer pairs with the new low temperature data either, the structural changes between room temperature and 4.3 K are small. The possible dimer pairs are shown on Fig. 7.5 and are denoted by d_n. The intra-dimer distance increases with n. The d_1 and d_2 distances building up a zig-zag chain along the b axis, these zig-zag chains are coupled via the longer d_3 and d_4 in the ac plane. Each d_n distance can be associated with an exchange interaction J_n that couples the V^{4+} ions into pairs (rather than chains or planes) and therefore is potentially responsible for the dimerisation.

The temperature dependence of the lattice parameters are shown on Tab. 7.3 and plotted on Fig. 7.6(a). The c lattice parameter shows negative thermal expansion below 100 K, this might be due to magnetostriction. The unit cell volume follows the Debye-model.

Comparing the temperature dependence of the atomic positions, the largest change is 0.01 in the relative atomic positions below room temperature. The largest changes are in the oxygen positions, but the standard deviation of the fitted positions at room temperature is also larger relative to strontium and vanadium. Fig. 7.6(b) shows the temperature dependence of the possible V^{4+}-V^{4+} dimer pairs. The d_1 distance shrinks

Table 7.2: Lattice constants and atomic positions of Sr_2VO_4measured with ID31 at 4.3 K and 300 K shown on first and second row, each atom lies at Wyckoff site 4*a*. Every third line is the room temperature position published by Gong et al. [166]. Isotropic displacement parameter was fixed for identical atoms.

Atom	x	y	z	B_{iso}
Sr(l)	0.1305(2)	0.2278(3)	0	0.02(1)
	0.1307(2)	0.2281(4)	0	0.50(2)
	0.132(2)	0.236(2)	0	
Sr(2)	0.2055(2)	0.1924(3)	0.6413(4)	
	0.2064(2)	0.1934(4)	0.6406(5)	
	0.207(1)	0.204(3)	0.643(3)	
Sr(3)	0.3789(2)	0.1912(3)	0.9190(2)	
	0.3789(2)	0.1931(4)	0.9177(2)	
	0.381(1)	0.180(3)	0.922(2)	
Sr(4)	0.4503(2)	0.2311(4)	0.2782(4)	
	0.4511(2)	0.2314(5)	0.2790(5)	
	0.444(1)	0.228(3)	0.275(3)	
V(1)	0.0271(4)	0.7743(6)	0.1283(6)	0.24(4)
	0.0256(4)	0.7719(7)	0.1261(7)	0.53(5)
	0.021(1)	0.778(3)	0.120(3)	
V(2)	0.2769(4)	0.6968(6)	0.7874(7)	
	0.2757(4)	0.7006(7)	0.7875(8)	
	0.282(2)	0.701(3)	0.791(2)	
O(1)	0.1196(11)	0.3549(25)	0.2494(15)	1.31(10)
	0.1170(12)	0.3439(30)	0.2510(18)	2.18(12)
	0.122(2)	0.360(4)	0.234(4)	
O(2)	0.2469(9)	0.0003(21)	0.4236(19)	
	0.2470(10)	0.9920(24)	0.4239(23)	
	0.243(1)	0.001(4)	0.410(3)	
O(3)	0.1356(11)	0.8766(26)	0.1936(15)	
	0.1298(13)	0.8806(30)	0.1898(18)	
	0.137(2)	0.889(4)	0.190(4)	
O(4)	0.2949(13)	0.1353(21)	0.1492(19)	
	0.2959(16)	0.1396(25)	0.1499(23)	
	0.302(2)	0.142(3)	0.137(3)	
O(5)	0.4546(11)	0.7706(28)	0.2742(17)	
	0.4559(14)	0.7722(34)	0.2719(21)	
	0.453(2)	0.767(3)	0.262(3)	
O(6)	0.2895(10)	0.4554(22)	0.3510(15)	
	0.2888(11)	0.4615(25)	0.3472(18)	
	0.289(2)	0.459(4)	0.367(2)	
O(7)	0.9741(10)	0.0334(22)	0.0641(16)	
	0.9746(11)	0.0229(26)	0.0580(20)	
	0.975(1)	0.034(3)	0.054(3)	
O(8)	0.0162(9)	0.5576(22)	0.0118(16)	
	0.0146(10)	0.5606(25)	0.0146(19)	
	0.011(1)	0.574(3)	0.010(3)	

Table 7.3: Lattice parameters of Sr_2VO_4 at different temperatures.

Temperature (K)	a (Å)	b (Å)	c (Å)
4.3	14.03893(7)	5.79235(3)	10.09900(5)
300	14.10107(9)	5.81212(4)	10.10413(6)

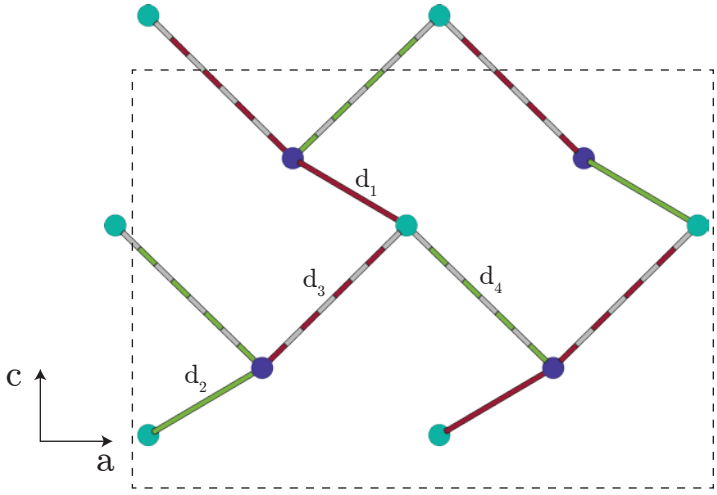

Figure 7.5: Shortest V–V pathways, red, green, red dashed and green dashed represent the d_1, d_2, d_3 and d_4 distances respectively. The red and green couplings build up alternating chains along the b axis.

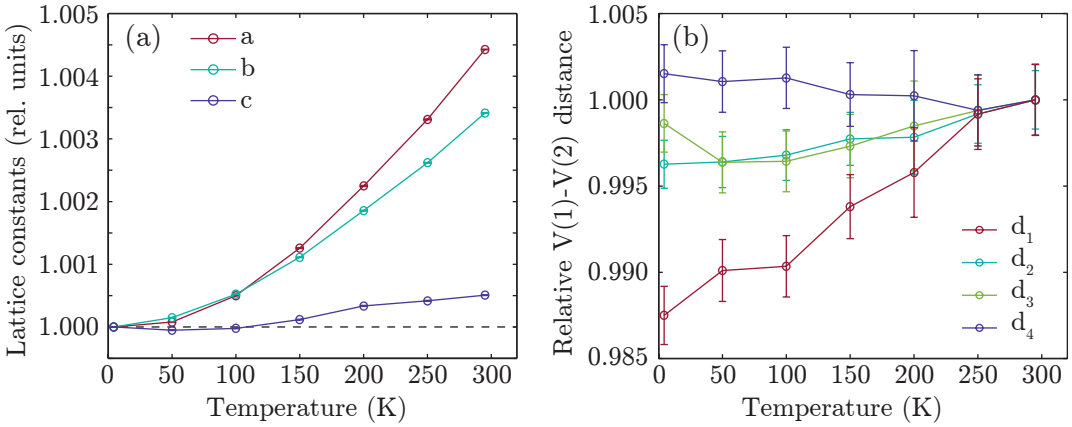

Figure 7.6: (a) Temperature dependence of lattice parameters, (b) temperature dependence of different V(1)-V(2) distances.

significantly compared to the other distances, this might due to magnetostriction as the dimer correlations become stronger.

7.3 Inelastic neutron scattering

Inelastic neutron scattering was measured on Sr_2VO_4 using the V3 time-of-flight spectrometer (NEAT) at HZB. The powder sample had a mass of 6.763 g and was loaded into an aluminium can under 1 bar helium atmosphere to provide heat exchange. The sample temperature was set to 1.7 K throughout the experiment. Spectra were collected with several incoming neutron wavelengths, 1.9 Å, 2.2 Å, 2.4 Å, 3.0 Å, 4.0 Å and 4.75 Å. The reason for so many wavelengths is that the lower energy region of the spectra contained spurious scattering which was checked by remeasuring it with lower energy neutrons. The magnetic signal was collected with λ=2.2 Å neutrons, see Fig. 7.7(a). The overall integration time was 46 hours. In addition the empty can and vanadium reference was measured and used for background subtraction and detector calibration. Absolute units were not used, due to the uncertainty of the vanadium mass in the beam. The FWHM energy resolution at the elastic line was 0.834(9) meV for λ=2.2 Å.

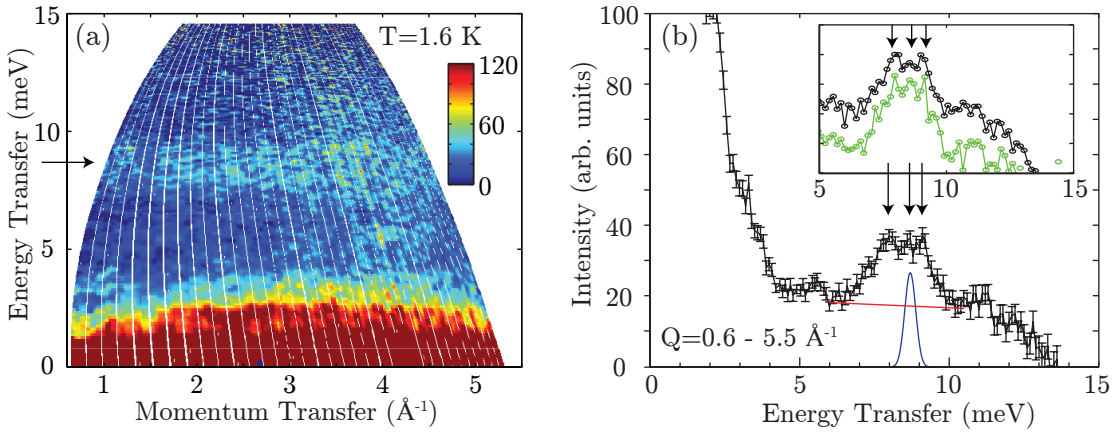

Figure 7.7: (a) Inelastic spectra of Sr_2VO_4 at base temperature, the arrow denotes the non-dispersing excitations centered at ∼8 meV. (b) Spectra integrated over all Q, the three arrows denote the fine structure of the inelastic peak, red line marks the non-magnetic background, blue curve denotes the Gaussian resolution function at 8.7 meV. Inset shows spectra integrated over $Q = 0-2$ Å^{-1} and $Q = 2-4$ Å^{-1}, denoted by green and black lines respectively.

The measurement reveals gapped excitations, forming a narrow band centred at 8.5 meV, no magnetic signal was observed below 7 meV or above 10 meV. This signal is characteristic of a dimer system with non-dispersing triplet excitations. The scattering intensity is however much weaker than expected. To calculate the expected scattering cross section, the magnon intensity was compared to the nuclear Bragg peak intensity of

Sr_2VO_4. But the elastic signal was also weak, which suggests that the sample was not fully in the beam.

To extract the non-dispersing inelastic peak position, the measured data were summed over all Q values. Figure 7.7(b) shows the result. The inelastic peak is clearly visible between 7.2 meV and 9.4 meV. The red line on the figure shows the non-magnetic background. The width of the signal is larger than the instrumental resolution (see blue curve) which is 0.43 meV FWHM at 8.7 meV energy transfer. This broadening is a sign of inter-dimer interactions, which modulate the flat dispersion giving it a finite width. On the broad peak fine structure can be recognised with three peaks at 8.0 meV, 8.7 meV and 9.1 meV respectively. This fine structure can be observed independently at different Q values, see inset of Fig. 7.7(b) which shows energy transfer cuts integrated in the Q=0...2 Å^{-1} and Q=2...4 Å^{-1} range. The observed width and position of the inelastic signal agrees very well with the interacting dimer model. The interacting dimer model predicts inelastic scattering in the range of $J - J'/2 < E < J + J'/2$, the 2.2 meV width of the inelastic peak agrees well with the $J' = 2.1(4)$ inter-dimer interaction strength extracted by fitting the susceptibility.

7.4 Conclusion

Sr_2VO_4 has the rare ionic state of vanadium, the spin-1/2 V^{4+} with a single $3d$ valence electron. Although there are no obvious V^{4+} pairs visible in the crystal structure, several independent measurements confirm that the magnetic ground state is dimerized. The measured heat capacity corresponds to a gapped system with energy gap of 8 meV. The magnetic susceptibility can be well fitted with the interacting dimer model where the dimer gap is 7.3 meV. The intriguing result is that the measured powder sample had only half of the magnetic susceptibility as expected for a fully dimerized ground state and half of that was measured by Gong et al. [166] The missing susceptibility can be explained by assuming half of the V^{4+} ions are non-magnetic, however X-ray diffraction shows no sign of oxygen deficiency. Inelastic neutron scattering shows a broad non-dispersing magnetic mode centered at 8.3 meV with a width of 2.2 meV. The flat mode corresponds to the triplet excitations of the dimer ground state and the broadening is due to non-zero inter-dimer interactions in agreement with the susceptibility.

Further inelastic neutron scattering measurement with better signal to noise ratio would make it possible to identify the dimer units in the crystal via fitting the dimer structure factor, furthermore the absolute value of the inelastic neutron scattering intensity would give an independent verification of the number of dimers in the system. Ab initio

band structure calculations based on the measured crystal structure are taking place to theoretically predict the dimer units.

8 Conclusion and Perspectives

In this thesis a detailed experimental investigation of three quantum magnets are presented. The main focus was on the properties of the magnetic ground state and the magnetic excitations. Several experimental technique were utilised, such as heat capacity and magnetic susceptibility measurements, neutron diffraction, inelastic neutron scattering and X-ray diffraction.

The first compound α-$CaCr_2O_4$ is a Mott insulator with spin $S = 3/2$ magnetic Cr^{3+} ions. The synthesis of single crystal α-$CaCr_2O_4$ was accomplished for the first time at the crystal growth lab of HZB, which enabled detailed neutron scattering investigation of the compound. The crystal structure and the magnetic order of α-$CaCr_2O_4$ revealed an interesting interplay between the crystal symmetry and the magnetic interactions. [170] The Cr^{3+} ions have no orbital degeneracy, due to the crystal field splitting, the only electronic degree of freedom is the direction of the spin. Therefore α-$CaCr_2O_4$ is a Heisenberg antiferromagnet on a triangular lattice with a small orthorhombic distortion. The inplane nearest neighbour distances of Cr^{3+} ions form a complex pattern with the shortest and longest distances forming chains along b and the two intermediate distances forming interpenetrating zig-zags along b. Below T_N=42.6 K long-range magnetic order develops. The magnetic structure is helical with ordering wavevector of $\boldsymbol{k}_m = (0, 1/3, 0)$ and spins lying in the ac plane, the angle between nearest neighbour spins is 120°. Despite the distorted crystal structure, this magnetic structure is the same is that of the classical Heisenberg antiferromagnet on a spatially isotropic triangular lattice. By calculating the classical ground state of the distorted lattice with nearest neighbour and next nearest neighbour interactions, it is found that the only necessary condition for the 120° structure is that the average value of the zig-zag interactions and the average value of the chain interactions have to be the same.

An inelastic neutron scattering study of α-$CaCr_2O_4$ revealed spin-wave excitations in the ordered phase. [171] The excitation spectra around the magnetic Bragg peaks corresponds to that of the isotropic triangular lattice. However at higher energies and away from the Bragg peaks, strong deviations revealing the underlying complex exchange pattern. Due to the short distance between Cr^{3+} ions, the dominant interactions are

antiferromagnetic direct exchange between nearest neighbours furthermore significant antiferromagnetic next-nearest neighbour superexchange is also present. The strong interionic distance sensitivity of the direct exchange amplifies the small structural distortion and the four interaction strengths are very different. The fitted exchange values are consistent with the 120° structure. However soft spin-wave modes with roton like minima at reciprocal space points different from magnetic Bragg peak positions reveal the instability of the 120° structure. The nearby phase is an unexplored multi-k structure.

The magnetic susceptibility, neutron diffraction and inelastic neutron scattering can be explained consistently. However discrepancies with the spin-wave fit may reveal quantum effects. Quantum fluctuations are expected to renormalise the spectra and might affect the soft modes due to the phase instability. The present results also suggest the possible direction of further investigations. Besides the magnon spectra, inelastic neutron scattering reveals strong phonon scattering which overlaps with the spin-wave spectra. Preliminary inelastic X-ray scattering results show temperature dependent changes in the low energy phonon spectra alongside the development of magnetic order. This together with the observed weak multiferroicity suggests the interplay between magnons, phonons and electric charge should be investigated. The instability of the 120° magnetic order implies that the magnetic interactions may be tunable by pressure or substitution to drive the system out of the 120° phase allowing investigation of the properties of the magnetic phase transition. One possibility is to substitute for the interlayer Ca^{2+} ion, which would alter the intralayer interactions.

The second compound β-$CaCr_2O_4$ has the same stoichiometry and Cr^{3+} magnetic ion as α-$CaCr_2O_4$. The completely different magnetic ground state properties and excitation spectra of these two compounds show how frustration can lead to different properties if the geometry changes. β-$CaCr_2O_4$ contains zig-zag chains of magnetic ions which are arranged on a honeycomb lattice. At low temperature it develops long-range magnetic order. It has incommensurate helical magnetic order with spins lying in the ac plane. The surprising result is that the neighbouring zig-zag chains have opposite chirality, which implies the presence of a staggered Dzyaloshinskii-Moriya interaction. Further experiments are planned to investigate the magnetic ordering wavevector which appears to change suddenly at an intermediate temperature.

Powder inelastic neutron scattering in the ordered phase of β-$CaCr_2O_4$ reveals almost one dimensional excitation spectra, with only weak dispersion between the zig-zag chains and significant Dzyaloshinskii-Moriya interaction along the legs of the zig-zag chains. The neighbouring zig-zag chains are coupled by superexchange via edge-sharing oxygen

octahedra. Therefore the small dispersion perpendicular to the zig-zag chains is not due to the weakness of the inter zig-zag interactions, but due to frustration and chiral order. Since nearest neighbour zig-zag chains have opposite chirality the spin angles between neighbouring zig-zags are effectively random thus there is no energy cost in rotating the spins of neighbouring zig-zag chains relative to each other. This reduction of dimensionality deserves further investigation. The observation of soft spin-wave modes between zig-zag chains is expected. Furthermore β-$CaCr_2O_4$ has an extended excitation continuum above the spin-wave modes. To determine whether it is a multimagnon or multispinon continuum further experimental and theoretical work necessary. However these experiments require single crystals of β-$CaCr_2O_4$, which are not available at present.

Sr_2VO_4 is a magnetic insulator, which shows dimerised ground state of the magnetic V^{4+}ions. However the crystal structure shows no obvious dimer units, all possible V^{4+}–V^{4+} exchange pathways involves at least two oxygen atoms. The orientation of the single valence electron orbital might play a role. Ab-initio calculations are currently taking place to determine the exchange pathways in this material.

Bibliography

[1] J. Brooke, D. Bitko, T. F. Rosenbaum, and G. Aeppli, Science **284**, 779 (1999).

[2] M. N. Leuenberger and D. Loss, Nature **410**, 789 (2001).

[3] S. Ghosh, R. Parthasarathy, T. F. Rosenbaum, and G. Aeppli, Science **296**, 2195 (2002).

[4] M. Gajek, M. Bibes, S. Fusill, K. Bouzehouane, J. Fontcuberta, A. Barthélémy, and A. Fert, Nature **6**, 296 (2007).

[5] S. Blundell, *Magnetism in Condensed Matter* (Oxford University Press, Oxford, 2001) p. 251.

[6] N. Majlis, *The Quantum Theory of Magnetism* (Worl Scientific, Singapore, 2000).

[7] R. Skomski, *Simple Models of Magnetism* (Oxford University Press, New York, 2008).

[8] A. Auerbach, *Interacting electrons and Quantum Magnetism* (Springer-Verlag, New York, 1994) p. 267.

[9] P. Anderson, Physical Review **79**, 350 (1950).

[10] J. B. Goodenough and Y. Car, Physical Review **100**, 564 (1955).

[11] J. Kanamori, Journal of Physics and Chemistry of Solids **10**, 87 (1959).

[12] K. Buschow, *Handbook of Magnetic Materials*, Vol. 10 (North Holland, 1997) p. 612.

[13] L. Balents, Nature **464**, 199 (2010).

[14] L. Pauling, J. Am. Chem. Soc. **57**, 2680 (1935).

[15] V. Fritsch, J. Hemberger, N. Büttgen, E.-W. Scheidt, H.-A. Krug von Nidda, A. Loidl, and V. Tsurkan, Physical Review Letters **92**, 116401 (2004).

[16] G. Chen, L. Balents, and A. Schnyder, Physical Review Letters **102**, 096406 (2009).

[17] D. J. P. Morris, D. A. Tennant, S. A. Grigera, B. Klemke, C. Castelnovo, R. Moessner, C. Czternasty, M. Meissner, K. C. Rule, J.-U. Hoffmann, K. Kiefer, S. Gerischer, D. Slobinsky, and R. S. Perry, Science **326**, 411 (2009).

[18] S. Nakatsuji, Y. Nambu, H. Tonomura, O. Sakai, S. Jonas, C. Broholm, H. Tsunetsugu, Y. Qiu, and Y. Maeno, Science **309**, 1697 (2005).

[19] S. Yamashita, T. Yamamoto, Y. Nakazawa, M. Tamura, and R. Kato, Nature communications **2**, 275 (2011).

[20] M. P. Shores, E. A. Nytko, B. M. Bartlett, and D. G. Nocera, Journal of the American Chemical Society **127**, 13462 (2005).

[21] J. S. Helton, K. Matan, M. P. Shores, E. A. Nytko, B. M. Bartlett, Y. Yoshida, Y. Takano, A. Suslov, Y. Qiu, J.-H. Chung, D. G. Nocera, and Y. S. Lee, Physical Review Letters **98**, 107204 (2007).

[22] H. T. Diep, *Frustrated Spin Systems* (World Scientific, Singapore, 2004) p. 624.

[23] C. Castelnovo, R. Moessner, and S. L. Sondhi, Nature **451**, 42 (2008).

[24] Y. Okamoto, M. Nohara, H. Aruga-Katori, and H. Takagi, Physical Review Letters **99**, 137207 (2007).

[25] D. Fiorani and S. Viticoli, Physical Review B **30**, 2776 (1984).

[26] C. Rüegg, N. Cavadini, A. Furrer, H.-U. Güdel, K. Krämer, H. Mutka, A. R. Wildes, K. Habicht, and P. Vorderwisch, Nature **423**, 62 (2003).

[27] P. Anderson, Materials Research Bulletin **8**, 153 (1973).

[28] B. Sriram Shastry and B. Sutherland, Physica B+C **108**, 1069 (1981).

[29] T. Fennell, P. P. Deen, A. R. Wildes, K. Schmalzl, D. Prabhakaran, A. T. Boothroyd, R. J. Aldus, D. F. McMorrow, and S. T. Bramwell, Science **326**, 415 (2009).

[30] C. Henley, Physical Review Letters **62**, 2056 (1989).

[31] B. Bleaney and K. D. Bowers, Proceedings of the Royal Society A: Mathematical, Physical and Engineering Sciences **214**, 451 (1952).

[32] D. C. Johnston and K. H. J. Buschow, *Handbook of Magnetic Materials*, Vol. 10 (North-Holland, 1997).

[33] Y. Singh and D. Johnston, Physical Review B **76**, 012407 (2007).

[34] E. F. Bertraut, Acta Cryst. **24**, 217 (1968).

[35] A. Wills, J. Phys. IV France **11**, 133 (2001).

[36] J. Rodríguez-carvajal and F. Bourée, EPJ Web of Conferences **22**, 00010 (2012).

[37] M. Habenschuss, C. Stassis, S. Sinha, H. Deckman, and F. Spedding, Physical Review B **10**, 1020 (1974).

[38] W. Koehler, J. Cable, E. O. Wollan, and M. Wilkinson, Physical Review **126**, 1672 (1962).

[39] E. Bertaut, Journal of Magnetism and Magnetic Materials **24**, 267 (1981).

[40] Y. Izyumov and V. Naish, Journal of Magnetism and Magnetic Materials **12**, 239 (1979).

[41] J. Rodríguez-carvajal, unpublished .

[42] L. Faddeev and L. Takhtajan, Physics Letters A **85**, 375 (1981).

[43] F. D. M. Haldane, Physical Review Letters **66**, 1529 (1991).

[44] D. A. Tennant, T. G. Perring, R. A. Cowley, and S. E. Nagler, Physical Review Letters **70**, 4003 (1993).

[45] A. B. Sushkov, R. Valdés Aguilar, S. Park, S.-W. Cheong, and H. D. Drew, Physical Review Letters **98**, 027202 (2007).

[46] T. Holstein, Physical Review **58**, 1098 (1940).

[47] S. R. White, M. Sparks, and I. Ortenburger, Physical Review **139**, A450 (1965).

[48] R. Coldea, *Neutron Scattering Studies of Two Magnetic Phase Transitions*, Ph.D. thesis, University of Oxford (1997).

[49] R. Coldea, D. A. Tennant, and Z. Tylczynski, Physical Review B **68**, 134424 (2003).

[50] A. Chernyshev and M. E. Zhitomirsky, Physical Review B **79**, 144416 (2009).

[51] G. L. Squires, *Introduction to the Theory of Thermal Neutron Scattering* (Dover, Mineola, 1996).

[52] T. Chatterji, *Neutron Scattering From Magnetic Materials* (Elsevier, 2005) p. 572.

[53] F. Hippert, E. Geissler, J. L. Hodeau, E. Lelievre-Berna, and J. R. Regnard, *Neutron and X-ray Spectroscopy* (Springer, Dordrecht, 2005) p. 566.

[54] G. Shirane, S. M. Shapiro, and J. M. Tranquada, *Neutron Scattering with a Triple-Axis Spectrometer* (Cambridge University Press, Cambridge, 2004) p. 273.

[55] G. L. Albert-José Dianoux and G. Lander, *Neutron Data Booklet* (Institute Laue-Langevin, 2003).

[56] J.-L. Hodeau, Proceedings of SPIE **3448**, 353 (1998).

[57] J. P. Wright, G. B. M. Vaughan, and Andy N. Fitch, IUCr Computing Commission Newsletter **1**, 92 (2003).

[58] "Bruker D8 X-ray powder diffractometer webpage," .

[59] V. F. Sears, Neutron News **3**, 26 (1992).

[60] C. T. Chantler, Journal of Physical and Chemical Reference Data **24**, 71 (1995).

[61] "E5 single crystal diffractometer webpage," .

[62] T. C. Hansen, P. F. Henry, H. E. Fischer, J. Torregrossa, and P. Convert, Measurement Science and Technology **19**, 034001 (2008).

[63] A. Hewat and I. Bailey, Nuclear Instruments and Methods **137**, 463 (1976).

[64] L. Cussen, D. Goossens, and T. Hicks, Nuclear Instruments and Methods in Physics Research Section A: Accelerators, Spectrometers, Detectors and Associated Equipment **440**, 409 (2000).

[65] M. Blume, Physical Review **130**, 1670 (1963).

[66] M. Janoschek, S. Klimko, R. Gähler, B. Roessli, and P. Böni, Physica B: Condensed Matter **397**, 125 (2007).

[67] M. Skoulatos and K. Habicht, Nuclear Instruments and Methods in Physics Research Section A: Accelerators, Spectrometers, Detectors and Associated Equipment **647**, 100 (2011).

[68] P. Link, G. Eckold, and J. Neuhaus, Physica B: Condensed Matter **276-278**, 122 (2000).

[69] T. G. Perring, R. A. Ewings, and J. V. Duijn, "Horace," (2009).

[70] D. L. Abernathy, M. B. Stone, M. J. Loguillo, M. S. Lucas, O. Delaire, X. Tang, J. Y. Y. Lin, and B. Fultz, The Review of scientific instruments **83**, 015114 (2012).

[71] G. Ehlers, A. A. Podlesnyak, J. L. Niedziela, E. B. Iverson, and P. E. Sokol, The Review of scientific instruments **82**, 085108 (2011).

[72] R. Bewley, R. Eccleston, K. McEwen, S. Hayden, M. Dove, S. Bennington, J. Treadgold, and R. Coleman, Physica B: Condensed Matter **385-386**, 1029 (2006).

[73] R. Lechner, R. Melzer, and J. Fitter, Physica B: Condensed Matter **226**, 86 (1996).

[74] J. S. Hwang, K. J. Lin, and C. Tien, Review of Scientific Instruments **68**, 94 (1997).

[75] A. P. Ramirez, *Handbook of magnetic materials*, Vol. 13 (Elsevier Science, 2001) p. 423.

[76] P. Fazekas and P. Anderson, Philosophical Magazine **30**, 423 (1974).

[77] L. Capriotti, A. E. Trumper, and S. Sorella, Physical Review Letters **82**, 3899 (1999).

[78] H. Serrano-González, S. Bramwell, K. Harris, B. Kariuki, L. Nixon, I. Parkin, and C. Ritter, Physical Review B **59**, 14451 (1999).

[79] K. Hirakawa, H. Kadowaki, and K. Ubukoshi, Journal of the Physics Society Japan **52**, 1814 (1983).

[80] H. Kadowaki, H. Kikuchi, and Y. Ajiro, Journal of Physics: Condensed Matter **2**, 4485 (1990).

[81] H. Nozaki, J. Sugiyama, M. Janoschek, B. Roessli, V. Pomjakushin, L. Keller, H. Yoshida, and Z. Hiroi, Journal of Physics: Condensed Matter **20**, 104236 (2008).

[82] L. Svistov, A. Smirnov, L. Prozorova, O. Petrenko, L. Demianets, and A. Shapiro, Physical Review B **67**, 094434 (2003).

[83] S. Mitsuda, H. Yoshizawa, N. Yaguchi, and M. Mekata, Journal of the Physics Society Japan **60**, 1885 (1991).

[84] M. Giot, L. C. Chapon, J. Androulakis, M. Green, P. Radaelli, and A. Lappas, Physical Review Letters **99**, 247211 (2007).

[85] Y. Oohara, S. Mitsuda, H. Yoshizawa, N. Yaguchi, H. Kuriyama, T. Asano, and M. Mekata, Journal of the Physics Society Japan **63**, 847 (1994).

[86] D. Hsieh, D. Qian, R. Berger, R. J. Cava, J. Lynn, Q. Huang, and M. Hasan, Physica B: Condensed Matter **403**, 1341 (2008).

[87] A. Zorko, S. El Shawish, D. Arčon, Z. Jagličić, A. Lappas, H. van Tol, and L. Brunel, Physical Review B **77**, 024412 (2008).

[88] M. Winterberger and Y. Allain, Solid State Communications **64**, 1343 (1987).

[89] C. J. Rasch, M. Boehm, C. Ritter, H. Mutka, J. Schefer, L. Keller, G. Abramova, A. Cervellino, and J. Löffler, Physical Review B **80**, 104431 (2009).

[90] R. Coldea, D. A. Tennant, A. M. Tsvelik, and Z. Tylczynski, Physical Review Letters **86**, 1335 (2001).

[91] M. Poienar, F. Damay, C. Martin, J. Robert, and S. Petit, Physical Review B **81**, 104411 (2010).

[92] K. Kimura, T. Otani, H. Nakamura, Y. Wakabayashi, and T. Kimura, Journal of the Physical Society of Japan **78**, 113710 (2009).

[93] V. H. Pausch and H. Mueller-Buschbaum, Zeitschrift fuer anorganische und allgemeine Chemie **405**, 113 (1974).

[94] A. F. Rogers, American Journal of Science **35**, 290 (1913).

[95] M. Poienar, F. Damay, C. Martin, V. Hardy, A. Maignan, and G. André, Physical Review B **79**, 014412 (2009).

[96] L. C. Chapon, P. Manuel, F. Damay, P. Toledano, V. Hardy, and C. Martin, Physical Review B **83**, 024409 (2011).

[97] K. Singh, C. Simon, and P. Toledano, Physical Review B **84**, 064129 (2011).

[98] Y. Lee and C. L. Nassaralla, Metallurgical and Materials Transactions B **28**, 855 (1997).

[99] A. T. M. N. Islam, S. Toth, and B. Lake, unpublished (2012).

[100] L. Jean and B. Bochu, "LMGP-Suite Suite of Programs for the interpretation of X-ray Experiments," .

[101] J. Rodríguez-carvajal, Physica B **192**, 55 (1993).

[102] H. M. Rietveld, Journal of Applied Crystallography **2**, 65 (1969).

[103] J. Rodríguez-carvajal, M. T. Fernandez-Diaz, and J. L. Martinez, Journal of Physics: Condensed Matter **3**, 3215 (1991).

[104] A. Leineweber, Zeitschrift für Kristallographie **226**, 905 (2011).

[105] C. Wilkinson, H. W. Khamis, R. F. D. Stansfield, G. J. McIntyre, I. Laue-langevin, and G. Cedex, Journal of Applied Crystallography **21**, 471 (1988).

[106] V. Ngo and H. Diep, Physical Review E **78**, 031119 (2008).

[107] K. Kimura, H. Nakamura, K. Ohgushi, and T. Kimura, Physical Review B **78**, 140401 (2008).

[108] F. Damay, C. Martin, V. Hardy, A. Maignan, G. André, K. Knight, S. R. Giblin, and L. C. Chapon, Physical Review B **81**, 214405 (2010).

[109] R. Coldea, D. A. Tennant, R. A. Cowley, D. F. McMorrow, B. Dorner, and Z. Tylczynski, Journal of Physics: Condensed Matter **8**, 7473 (1996).

[110] J. Goodenough, Physical Review **117**, 1442 (1960).

[111] S. E. Dutton, E. Climent-Pascual, P. W. Stephens, J. P. Hodges, A. Huq, C. Broholm, and R. J. Cava, Journal of Physics: Condensed Matter **23**, 246005 (2011).

[112] O. Crottaz, Journal of Solid State Chemistry **122**, 247 (1996).

[113] K. Kimura, H. Nakamura, S. Kimura, M. Hagiwara, and T. Kimura, Physical Review Letters **103**, 107201 (2009).

[114] H. Yamaguchi, S. Ohtomo, S. Kimura, M. Hagiwara, K. Kimura, T. Kimura, T. Okuda, and K. Kindo, Physical Review B **81**, 033104 (2010).

[115] M. Frontzek, J. Haraldsen, A. A. Podlesnyak, M. Matsuda, A. Christianson, R. Fishman, A. Sefat, Y. Qiu, J. Copley, S. Barilo, S. Shiryaev, and G. Ehlers, Physical Review B **84**, 094448 (2011).

[116] O. Starykh, A. V. Chubukov, and A. Abanov, Physical Review B **74**, 180403 (2006).

[117] W. Zheng, J. Fjæ restad, R. Singh, R. H. McKenzie, and R. Coldea, Physical Review Letters **96**, 057201 (2006).

[118] A. Chernyshev, private communication (2009).

[119] E. M. Wheeler, R. Coldea, E. Wawrzyńska, T. Sörgel, M. Jansen, M. M. Koza, J. Taylor, P. Adroguer, and N. Shannon, Physical Review B **79**, 104421 (2009).

[120] D. A. Tennant and D. F. McMorrow, "Rescal code," .

[121] M. Popovici, Acta Crystallographica Section A **31**, 507 (1975).

[122] E. Kan, H. Xiang, Y. Zhang, C. Lee, and M.-H. Whangbo, Physical Review B **80**, 104417 (2009).

[123] D. Hsieh, D. Qian, R. Berger, R. J. Cava, J. Lynn, Q. Huang, and M. Hasan, Journal of Physics and Chemistry of Solids **69**, 3174 (2008).

[124] N. Moreno, C. Israel, P. Pagliuso, A. Garcia-Adeva, C. Rettori, J. Sarrao, J. Thompson, and S. Oseroff, Journal of Magnetism and Magnetic Materials **272-276**, E1023 (2004).

[125] C. Delmas, G. Le Flem, C. Fouassier, and P. Hagenmuller, Journal of Physics and Chemistry of Solids **39**, 55 (1978).

[126] R. Meisenheimer and J. Swalen, Physical Review **123**, 831 (1961).

[127] H. Takatsu, H. Yoshizawa, S. Yonezawa, and Y. Maeno, Physical Review B **79**, 104424 (2009).

[128] I. Mazin, Physical Review B **75**, 094407 (2007).

[129] D. Wulferding, K.-Y. Choi, P. Lemmens, A. N. Ponomaryov, J. van Tol, A. T. M. N. Islam, S. Toth, and B. Lake, unpublished (2012), arXiv:1205.3640 .

[130] M. B. Stone, M. J. Loguillo, and D. L. Abernathy, The Review of scientific instruments **82**, 055117 (2011).

[131] K. Jung and H. Jung, Physical Review B **76**, 054431 (2007).

[132] X.-G. Wen, F. Wilczek, and A. Zee, Physical Review B **39**, 11413 (1989).

[133] P. Chandra, P. Coleman, and A. I. Larkin, Journal of Physics: Condensed Matter **2**, 7933 (1990).

[134] N. Read and S. Sachdev, Physical Review Letters **66**, 1773 (1991).

[135] A. V. Chubukov and T. Jolicoeur, Physical Review B **46**, 11137 (1992).

[136] R. S. Fishman, Physical Review B **84**, 052405 (2011).

[137] R. Fishman, Physical Review B **85**, 024411 (2012).

[138] R. Bursill, G. A. Gehring, D. J. J. Farnell, J. B. Parkinson, T. Xiang, and C. Zeng, Journal of Physics: Condensed Matter **7**, 8605 (1995).

[139] M. Enderle, B. Fåk, H.-J. Mikeska, R. K. Kremer, A. Prokofiev, and W. Assmus, Physical Review Letters **104**, 237207 (2010).

[140] F. D. M. Haldane, Physical Review Letters **50**, 1153 (1983).

[141] A. A. Nersesyan, A. O. Gogolin, and F. H. L. Eßler, Physical Review Letters **81**, 910 (1998).

[142] J. Ren and J. Sirker, Physical Review B **85**, 140410 (2012).

[143] W. F. Ford and W. J. Rees, Trans. Brit. Ceram. Soc. **48**, 291 (1949).

[144] F. Damay, C. Martin, V. Hardy, A. Maignan, C. Stock, and S. Petit, Physical Review B **84**, 020402 (2011).

[145] S. Dutton, C. Broholm, and R. J. Cava, Journal of Solid State Chemistry **183**, 1798 (2010).

[146] T. Nisino and K. Moteki, Journal of the Ceramic Association, Japan **69**, 130 (1961).

[147] S. Hashimoto, A. Yamaguchi, and Y. Takahashi, Materials Research Bulletin **32**, 1593 (1997).

[148] P. M. Hill, H. S. Peiser, and J. R. Rait, Acta Crystallographica **9**, 981 (1956).

[149] C. Kittel, *Introduction to solid State Physics*, 8th ed. (John Wiley & Sons, 2004).

[150] G. Rado and H. Suhl, eds., *Magnetism* (Academic Press, New York, 1963) pp. 25–83.

[151] J. B. Goodenough, *Magnetism and the Chemical Bond* (Interscience Publisher, New York, 1963).

[152] K. Motida and S. Miyahara, Journal of the Physical Society of Japan **28**, 1188 (1970).

[153] I. E. Dzyaloshinskii, Zh. Éksp. Teor. Fiz. **32**, 1547 (1957).

[154] I. Dzyaloshinsky, Journal of Physics and Chemistry of Solids **4**, 255 (1958).

[155] T. Moriya, Physical Review Letters **4**, 228 (1960).

[156] T. Moriya, Physical Review **120**, 91 (1960).

[157] D. Coffey, K. S. Bedell, and S. A. Trugman, Physical Review B **42**, 6509 (1990).

[158] V. E. Dmitrienko, E. N. Ovchinnikova, J. Kokubun, and K. Ishida, JETP Letters **92**, 383 (2010).

[159] T. Hahn, H. Wondratschek, U. Müller, U. Shmueli, E. Prince, A. Authier, V. Kopský, D. B. Litvin, M. G. Rossmann, E. Arnold, S. R. Hall, and B. McMahon, in *International Tables for Crystallography*, Vol. A (Springer, 2006) Chap. 1.4, pp. 7–11.

[160] S. Maleyev, Physical Review B **73**, 174402 (2006).

[161] D. A. Tennant, S. Nagler, D. Welz, G. Shirane, and K. Yamada, Physical Review B **52**, 13381 (1995).

[162] J.-S. Caux and R. Hagemans, Journal of Statistical Mechanics: Theory and Experiment **2006**, 12013 (2006).

[163] T. Giamarchi, C. Rüegg, and O. Tchernyshyov, Nature Physics **4**, 198 (2008).

[164] K.-K. Ng and T. Lee, Physical Review Letters **97**, 127204 (2006).

[165] H. Zhou, B. Conner, L. Balicas, and C. Wiebe, Physical Review Letters **99**, 136403 (2007).

[166] W. Gong, J. E. Greedan, G. U. O. Liu, and M. Bjorgvinsson, Journal of Solid State Chemistry **95**, 213 (1991).

[167] G. Liu, J. Greedan, and W. Gong, Journal of Solid State Chemistry **105**, 78 (1993).

[168] J. Deisenhofer, "private communication," .

[169] D. C. Johnston, R. Kremer, M. Troyer, X. Wang, A. Klümper, S. Bud'ko, A. Panchula, and P. Canfield, Physical Review B **61**, 9558 (2000).

[170] S. Toth, B. Lake, S. A. J. Kimber, O. Pieper, M. Reehuis, A. T. M. N. Islam, O. Zaharko, C. Ritter, A. H. Hill, H. Ryll, K. Kiefer, D. N. Argyriou, and A. J. Williams, Physical Review B **84**, 054452 (2011).

[171] S. Toth, B. Lake, K. Hradil, T. Guidi, K. C. Rule, M. B. Stone, and A. T. M. N. Islam, accepted for publication in Physical Review Letters (2012), arXiv:1206.1795 .

List of Publications

Parts of the work presented in this thesis have been published in scientific journals:

- *120° helical magnetic order in the distorted triangular antiferromagnet* α-$CaCr_2O_4$, S. Toth, B. Lake, S. A. J. Kimber, O. Pieper, M. Reehuis, A. T. M. N. Islam, O. Zaharko, C. Ritter, A. H. Hill, H. Ryll, K. Kiefer, D. N. Argyriou and A. J. Williams, Phys. Rev. B **84**, 054452 (2011)

- *Magnetic soft modes in the locally distorted triangular antiferromagnet* α-$CaCr_2O_4$, S. Toth, B. Lake, K. Hradil, T. Guidi, K. C. Rule, M. B. Stone and A. T. M. N. Islam, arXiv:1206.1795 [cond-mat.str-el] (2012), accepted for publication in Phys. Rev. Lett.

- *Anomalous magnetic excitations in the* $S = 3/2$ *distorted triangular antiferromagnet* α-$CaCr_2O_4$, D. Wulferding, K.-Y. Choi, P. Lemmens, Al. N. Ponomaryov, Johan van Tol, A. T. M. N. Islam, S. Toth and Bella Lake, arXiv:1205.3640 [cond-mat.str-el] (2012), submitted to Phys. Rev. B

Eidesstattliche Versicherung

Hiermit versichere ich an Eides Statt, dass ich meine Dissertation mit dem Titel:

"Magnetism of $3d$ Frustrated Magnetic Insulators: α-$CaCr_2O_4$, β-$CaCr_2O_4$ and Sr_2VO_4"

selbstständig verfasst habe. Alle benutzten Hilfsmittel und Quellen sind in der Arbeit aufgeführt.

Berlin, den 12.06.2012 Sándor Tóth